Imperial College of Science, Technology and Medicine
Department of Earth Science and Engineering

Isotopic and Molecular Weight Fractionation of Shale Gas; the Influences of Shale Geochemistry

Ruth Jennifer Davey

Submitted in part fulfilment of the requirements for the degree of Doctor of Philosophy in Earth Science and Engineering of the University of London and the Diploma of Imperial College, December 2019

Declaration of Originality

This is to certify that my thesis which has been submitted for my PhD degree, embodies my own course of laboratory research, data analysis ad interpretation. The words used are my own and all externally sourced materially has been referenced correctly. My work has been reviewed by both internal supervisors before submission.

Copyright Declaration

The copyright of this thesis rests with the author and is made available under a Creative Commons Attribution Non-Commercial No Derivatives licence. Researchers are free to copy, distribute or transmit the thesis on the condition that they attribute it, that they do not use it for commercial purposes and that they do not alter, transform or build upon it. For any reuse or redistribution, researchers must make clear to others the licence terms of this work.

Abstract

Shale gas has the potential to be a bridging fuel, facilitating change to a low-carbon economy whilst meting the World's energy demands. Whilst shale gas is by no means "new" fuel, it's proliferation in the USA in recent years has brought it to the attention of other countries, including the UK. Many of the shale gas plays in the USA, such as the Bakken, Eagle Ford and Monterrey Shales cover a large areal extent in areas of relative tectonic inactivity. The grid-pattern and infill drilling seen in these plays would not be viable in places such as the UK where the shales have been more heavily deformed and placing well pads are more strictly controlled by legislation. In order to maximise the efficiency of a shale gas well and inform future drilling decisions, many factors must be known; the volume of gas stored within the shale, the percentage of total volume extracted, how the gas is stored and if the well is draining from a large volume of shale or a small volume of shale. Whilst much research has been carried out on shales to determine these factors, often in isolation of one another, there is no consensus in the literature about how they can be calculated. Numerically modelled production decline curve analysis is a commonly used technique but does not factor in the specific geochemistry of a shale which has been shown to influence gas storage and the degassing production rate. There are few geochemical signatures related to shale gas but change in the stable carbon isotope fractionation and changing molecular weight with gas extraction has been seen in production data. Often these changes are attributed to adsorption-desorption processes and are used as a proxy for volume of gas stored in the adsorbed phase. There is however a large body of evidence suggesting that diffusion processes also influence the Δ gas geochemistry thus cannot be used as a direct proxy for adsorbed gas.

In order to move away from numerical modelling and work towards empirical studies based on experimental work on shale geochemistry, understanding what the change in gas geochemistry relates to is necessary to develop a geochemical index for degassing shales. Production

modelling would be greatly informed by understanding how shale geochemistry and composition influences changing gas geochemistry with gas extraction. This research measures the change in stable carbon isotope fractionation of methane and the change in methane – ethane ratio with gas extraction to see how the degassing profile changes from 100% gas in place to 100% gas extracted, building idealised volume-based production decline curves related to, initially, isolated shale components then whole shales with varying volumes and types of total organic carbon and levels of maturation. The data was collected on a custom-built sample cell coupled with either a Gas Chromatographer – Combustion - Isotope Ratio Mass Spectrometer or Gas Chromatographer – Flame-Ionizing Detector which allowed calculation of the molar volume of gas stored in the sample, the volume of gas extracted and the residual gas that could not be extracted. The cell design allowed for volume-based geochemical curves to be generate for the individual shale components and whole shale samples. The results indicate that changing the shale geochemistry influences the gas geochemistry with gas extraction and the shale composition is a key component for generating a geochemical index for volume-based production decline curves.

This technique allows quantitative assessment of not only total GIP but the percentage total volume of gas extracted over given period of time, advancing from current empirical techniques to quantitative analysis. As such, it will replace current generic mathematically calculated decline curve models with a shale/site specific decline curve which is dictated by the mineralogy/TOC content of the shale. This technique facilitates:

1. Verification and calibration of original GIP estimates
2. Generation of expected geochemical fractionation trend for volume of total gas extracted
3. Calculation of gas volume remaining in the reservoir and what percentage has been produced over a given production time period

4. Enhancement of the predicative capabilities of a shale gas reservoir production life

This will aid economic assessment of a shale gas field, namely, a measurable assessment of production time, volume of gas retained within the reservoir and the economic worth of restimulation of the well and it will no longer be economically viable to keep the well open.

Acknowledgments

Thank you to my two supervisors, Professor Mark Sephton and Dr Craig Smalley for their unwavering support, help and guidance throughout the past 3 (4…) years. It has been one long journey but we made it, thank you. Thanks must also be extended to Dr Jon Watson, Graham Nash, Dr Wren Montgomery and the soon to be Dr Jonathon Tan for their help in building and maintaining the equipment I relied on so heavily throughout the experimental process and general help, advise and song-singing that kept me sane. Jonny, you kept me sane and I know you go far. It was a privilege to share my lab bench with you.

Special thanks to my mum and dad who have picked me up when I've been in tears so many times throughout this long and difficult process, thank you for being there for me always. I am too grateful for words. Thanks to my brother for the promise of a break at the end to look forward to. Special thanks also to the incredible and wonderful women who I have had the honour and the pleasure to work with – you have been my cheerleaders throughout this process and I will repay you in likeness when it is your turn to write up. You make the scientific world a kinder, brighter and more hopeful place. Thank you to partners old and new who had to listen to me whine, moan and cry that the IRMS was broken yet again and especially to Rob for cheering me over the finish line. A final thankyou to my dogs who licked the tears of sadness from my face.

Dedication

I would like to dedicate this to my Pop Pop. He was a Dr of Hydrogeological Engineering but dementia took his mind before I was old enough to learn about his work. I hope he would be proud.

Contents

Acknowledgments 6
Dedication 7
1.0 Introduction 21
1.1 The Purpose of this research 21
1.2 Shale Gas: and overview 23
1.2.1 What is a shale? 23
1.2.2 Shales as hydrocarbon plays 24
1.2.3 What comprises shale gas? 25
1.2.4 How are hydrocarbon gases generated? 26
1.3 Commercial Production of shale gas extraction 27
1.3.1 How is shale gas extracted? 27
1.3.2 What makes a shale gas reservoir commercially viable? 28
1.4 What are the benefits of shale gas? 29
1.5 Shale Gas: storage and flow 31
1.5.1 Why do we want to calculate gas storage and why can't we accurately do so? 31
1.5.2 Why is gas storage hard to calculate? 33
1.5.3 Adsorption and storage capacity 35
1.5.4 What controls adsorption 36
1.5.5 Desorption and gas extraction 37
1.5.6 Gas flow regimes and diffusion 38
1.6. Why is adsorption-desorption and diffusion important? The potential for a geochemical index 39
1.7 Current methods for shale gas analysis: moving away from diffusion-desorption 40
1.7.1 Decline curve analysis 44
1.7.2 The need for a new method 44
1.7.3 Custom built sample cell – online measurements of adsorption, storage and change in gas geochemistry with volume of gas extracted. 45
1.8. Thesis Synopsis 46
2.0 Methodology 48
2.1 Custom-built sample cell 50
2.1.1 Cell Development 55
2.1.2 Sample cell design and components 56
2.2 GC-C-IRMS: Precision, accuracy and quality control 60

2.3 Method Development: GC-C-IRMS 64
2.3.1 Method development: GC-FID 71
2.4 Method: Sample Preparation 73
2.4.1 Laboratory Samples 73
2.4.2 Shale Samples 74
2.5 Experimental procedures 76
2.5.1 Rock-eval Pyrolysis 76
2.5.2 Fourier Transform Infrared Spectroscopy (FTIR) 77
2.5.3 Scanning Electron Microscopy (SEM) 78
2.5.4 X-Ray Diffraction (XRD) 78
2.5.5 Langmuir Isotherm Analysis 80
2.5.6 Brunauer-Emmett-Teller (BET) surface area 80
2.5.7 Barrett, Joyner and Halenda (BJH) Pore Size Distribution 82
2.5.8 Wet chemistry methods: 83
2.6 Data Analysis Methodology 88
2.6.1 GC-C-IRMS data and errors 88
2.6.2 GC-FID data and errors 88
3.0 Carbon Isotope Fractionation in Degassing Shale Constituents 90
3.1 Abstract 90
3.2. Introduction 92
3.2.1 What may cause the inherent stable carbon isotope fractionation? 94
3.2.2 Why is this question so difficult to answer? 95
3.2.3 Is there a more useful way to address the problem? 99
3.2.4 Questions to address 102
3.3. Experimental Methods 104
3.3.1 Samples 104
3.3.2 Sample Preparation 106
3.3.3 Characterisation of the samples: 107
3.3.4 Experimental Procedure 108
3.4 Results 112
3.4.1 Langmuir isotherm analysis 112
3.4.2 Langmuir volumes of the inert materials 112
3.4.3 Langmuir volumes for the clay samples 112
3.4.4 Langmuir volumes for Type II kerogen 113

3.4.5 BJH and BET Analysis 114
3.4.6 Characterising the samples: BET, BJH and Langmuir Isotherms 118
3.4.7 Direct Injection Data 123
3.4.8 Desorption Data: Time Steps 125
3.5 Discussion 131
3.5.1 Gas extraction data and volumetrics 131
3.5.2 Material Balance: plotting the tail of the isotopic fractionation curves 137
3.5.3 How might this data be applied as a geochemical index? 138
3.5.4 Material balance and predicting the end of the $\delta^{13}C$ curve 140
3.6 Conclusions 143
4.0 C_1-C_2 Fractionation in Degassing Shale Constituents 144
4.1 Abstract 144
4.2 Introduction 146
4.2.1 How do we access shale gas? 146
4.2.2 What happens to a shale gas well? 147
4.2.3 What can be done to improve recovery? 147
4.2.4 What do we need to understand? 148
4.2.5 Current methods for predicting the shale gas decline curve 151
4.2.6 Limitations of the current methods 152
4.2.7 The need for a new method 152
4.2.8 What causes this inherent gas fractionation? 153
4.2.9 A different approach to C_1-$C_{2\ as}$ a geochemical index 155
4.3 Methodology 158
4.3.1 Sample selection 158
4.3.2 Sample Preparation 159
4.3.3 Eagle Ford Shale Samples 160
4.3.4 Characterisation of the isolated shale components and whole shale samples: 163
4.3.5 Custom-built sample cell and GC-FID 165
4.4 Results 168
4.4.1 Isolated Mineral and Eagle Ford Shale BET, BJH and Langmuir analysis 168
4.4.2 Eagle Ford Shale Isotherms and BJH Analysis 169
4.4.3 Eagle Ford Shale XRD Data 171
4.4.4 Rock-eval Pyrolysis 172
4.4.5 FTIR: type II kerogen 172
4.4.6 Direct Injection Data 173

4.4.7 C_1-C_2 time steps: Minerals 174
4.5 Discussion 178
4.5.1 What was the aim of this setup? 178
4.5.2 Implications for a geochemical index 187
4.6 Conclusions 190
5.0 C_1-C_2 Fractionation in Degassing Shales: TOC and kerogen type 192
5.1 Abstract and Chapter Aims: 192
5.2 Introduction 193
5.2.1 Controls on gas storage capacity 195
5.2.2 The need for a new approach to understanding shale gas 197
5.2.3. Why focus on TOC and kerogen type? 199
5.3 Methodology 201
5.3.1. Samples 201
5.3.2 .Sample Preparation and Screening 202
5.3.3.Initial Sample Preparation 203
5.3.4 BET, BJH and Langmuir isotherm analysis 205
5.3.4 FTIR 206
5.3.5 Gas Chromatography - Flame-Ionization Detector (GC-FID) 207
5.4 Results 211
5.4.1. FTIR 211
5.4.2 Rock-eval data 213
5.4.3Langmuir Isotherm BET and BJH Analysis 214
5.4.5 Sample Cell – GC-FID 220
5.4.6. Summary of results 226
5.5 Discussion 227
5.5.1. Isotherm analysis: adsorption capacity of the materials 227
5.5.2. Observing the influence of kerogen type on material degassed from the custom-built sample cell 228
5.5.3. Literature hypothesis: TOC as a controlling factor on C_1-C_2 fractionation? 230
5.5.4. Other factors that could influence C_1-C_2 fractionation trends 235
5.5.5 Argument for Surface Area as the controlling factor on C_1-C_2 peak height 236
5.5.6 Surface area and adsorption capacity 239
5.5.7 Kerogen Type 241
5.5.8 Do porosity or pore volumes influence the C_1-C_2 fractionation trend? 241

5.5.9 Surface area of the organic material is the controlling factor on C_1-C_2 fractionation with degassing 242
5.5.10 What is the significance of these unique C_1-C_2 fractionation trends? 244
5.5.11Mass balance: predicting the gas tail 244
5.5.12 Summary of C_1-C_2 as a proxy for quantitative production decline 247
5.5.13 Volume-to-peak and $\Delta C_{1(0)} - C_{1(z}$ 248
6.0 C_1-C_2 Fractionation in degassing shales: artificial maturation 252
6.1. Introduction 252
6.1.1 Why consider artificial maturation? 253
6.1.2 Literature studies: thermal maturity influences gas storage, pore size and gas diffusion 256
6.1.3. Literature studies: thermal maturation has no influence on shale gas storage capacity 257
6.1.4 Aim of this chapter 258
6.2. Methodology 259
6.2.1 Samples 259
6.2.2. Experimental Parameters 259
6.3. Results 263
6.3.1. Langmuir Isotherm, BET and BJH Analysis 263
6.3.2 BJH and BET Comparison 269
6.3.3 GC-FID Time Plot 270
6.4. Discussion 272
6.4.1 Volumetric data 272
6.5. Conclusions 275
7.0 Discussion Applications to Industry 277
Adsorption and diffusion; δ^{13}CH degassing trends 277
How can δ^{13}CH trends be applied to industry 279
Sorption and diffusion processes; a combination controlling the C_1-C_2 fractionation trends 280
Using C_1-C_2 as a proxy for quantitative shale gas production decline 281
How realistic are these examples? 285
8.0 Conclusions 286
8.1 Future Work 287

Figure 1| Schematic representation of "conventional" and "unconventional" hydrocarbon reserves. Conventional reservoirs are comprised of macroporous grains where hydrocarbons are stored in the pores spaces (blue sections in the thin section). Unconventional shale gas reservoirs contain gas in several phases and are dominated by pores that are mesoscale < 50 nm) and smaller). Adapted from: (EIA, 2015), ... 25
Figure 2| An example ternary plot considering the properties of a shale that must be considered when looking at the geomechanical frackability of a shale (Sone and Zoback, 2013). 29
Figure 3| IAE global forecasting for natural gas consumption from is predicted to be continue to rise into 2040 with current states policies. Even with sustainable development and modelling accounting for the influx and growth of renewable energy, natural gas is still a global energy resource well into 2040. (IEA, 2019). 30
Figure 4| An example of the production-decline curves from 5 of the largest producing shale gas formations in the United States of America. All 5 fields are characterised by an initial gas pulse followed by a rapid decline and a long gas tail. The EUR curves do not accurately represent the real volumes of extractable gas. Adapted from EIA, 2013. 33
Figure 5| Different stages of gas storage and transport out of the various porescales within a shale. Adapted from (Xia and Tang, 2012b) 35
Figure 6 |Schematic flow chart showing the factors that may influence molecular weight and isotopic fractionation that can be used as a geochemical index for total gas in place and volume of total gas extracted (recovery factor). 42
Figure 7| Key questions to be asked, this thesis focusses predominantly on calculating the percentage of the total volume of gas extracted and this can relate to production timescales. The data also consider the free vs. adsorbed gas and area of shale drainage. Change seen in the stable carbon isotope and molecular weight ratios relating to specific, testable shale heterogeneities allow for a universal method for degassing profiles to be generated. 43
Figure 8 | Custom built sample cell in the oven, attached to the Gas chromatographer – combustion – isotope ratio mass spectrometer. Figure 8b| Schematic diagram of the sample cell set up. Part 1, the gas bottle in interchangeable, as are parts 15 and 16 which link the sample cell to the instrumentation. The corresponding component parts are outlined in Table 1. 52
Figure 9| Schematic diagram (10q) and photograph of the second-generation sample cell (9b). the cell has a much smaller dead volume using 1/16” instead of 1/8” tubing throughout, smaller valves with less associated dead volume, a secondary vacuum line and an inbuilt pressure transducer. 54
Figure 10 | Schematic diagram of a GC-C-IRMS Matt Finnigan operating system. The sample gas passes through the oxidation furnace, is separated out through the GC and then combusted into CO_2 in the combustion chamber. The CO_2 is then carried via He carrier gas into the IRMS where the isotopes are flung round a convex system causing separation into isotopic species which are captured in the Faraday cups. (Pancost and Bull, 2014) 60
Figure 11 | Reproducibility of the reference gas data measured by the GC-C-IRMS. Carbon dioxide is injected into the GC-C-IRMS at 40 second intervals. The instrument measures the ratio between ^{12}C and ^{13}C. This test is repeated twice daily, once prior to experimentation and once afterwards. The two sample runs lie almost directly on top of one another and both runs plot between -0.03 and 0.06 with 0 being the actual isotopic ratio of the gas. 63
Figure 12| Direct injection data collected for 25 gas injections with the maximum deviations above and below the average $\delta^{13}C$ measured shows a lower level of accuracy than the long on-off data. 64
Figure 13| an example of the IsoDat Workspace interface when displayed on a Windows computer. The upper peaks (green and red) show the measured peak ratios between mass 45 CO_2 and mass 44 CO_2. The lower graphic section shows the intensity of each peak (in blue). The lowermost section is a table of the data recorded for each peak, ... 70
Figure 14| FTIR data collected for the OC-325 sample. Each peak will relate to a different mineral or suite of minerals and can be used to give relative abundance of minerals present in a sample. 78

Figure 15| Example of the x-ray spectra collected from a shale sample. The peaks are identified from a pre-existing mineral spectra catalogue. 79
Figure 16 Example of an adsorption-desorption isotherm generated by the Quantachrome R ASiQwin Automated Gas Sorption Instrument, version 5.2. The sample shown here is West Lothian heated to 325°C. 80
Figure 17 BJH pore size distribution analysis for Kimmeridge Clay Type II kerogen, as an example of the raw data collected by the Quantachrome R ASiQwin Automated Gas Sorption Instrument, version 5.2. 83
Figure 18| image taken in the clean chemistry labs at Imperial College London, The beaker, which can contain 250ml of fluid, is shown sat on the hot plate. The hot plate was kept at 35°C to encourage the Hf to react with the sample whilst ensuring that the kerogen remained unaltered. 85
Figure 19| Hydrous pyrolysis schemtatc setup (Lewan, 2017) 87
Figure 20 Gas flow mechanisms within a shale gas reservoir. (B) shows desorption which will yield kinetic fractionation of carbon isotopes. (C) shows mass transport which may yield chromatographic fractionation. No fractionation is expected in (D) where Darcy flow is the dominant mechanism for gas movement (Dahaghi and others, 2010) 94
Figure 21 Controls on the initial isotopic and molecular weight composition of shale gas, adapted from (Xia et al., 2013) 95
Figure 22|Influences of maturity and bacterial imprint on the $\delta^{13}C$ value of a shale gas reservoir, originally from (Schoell, 1980). 97
Figure 23 Production Data over 10 years: Barnett Shale, Statoil 2011. Free gas is stored in any existing macropores or fractures thus is liberated first. The tail is often stated to be gas desorbing from the surfaces of organic material and/or clays (Rexer et al., 2013; Sandvik et al., 1992; Tang et al., 2017). Free gas would not generate isotopic fractionation as shown in figure 21 whilst desorption would produce some inherent fractionation between the lighter C^{12} and the heavier C^{13}. 100
Figure 24 | Simple schematic of the custom built online adsorption-desorption cell. 109
Figure 25| a. Langmuir isotherm analysis for quartz and b. Langmuir isotherm analysis for calcite . 113
Figure 26 | a. Langmuir isotherm curve for kaolinite clay and b. Langmuir isotherm curve for montmorillonite clay 113
Figure 27| Langmuir isotherm analysis for Type II Kerogen. 114
Figure 28| Calcite cumulative pore volume (a) and pore diameter to pore volume (b) for calculate. Most pores are greater than 100nm in size which can skew the data plots. 114
Figure 29| Quartz cumulative pore volume (a) and pore diameter to pore volume (b). Similar to calcite, most pores are greater than 100nm 115
Figure 30| Kaolinite cumulative pore volume (a) and pore diameter to pore area (b). There is a high volume of pores with diameters between 10 and 50nm. Pores of 2nm in diameter have the greatest pore area of the kaolinite sample. 115
Figure 31| Montmorillonite cumulative pore volume (a) and pore diameter to pore area (b). The largest pore area coincides with the smallest pore diameter at ~1nm. There is a distinct jump in the cumulative pore volume when considering the pores <2nm in diameter. 116
Figure 32| Type II kerogen cumulative pore volume (a) and pore diameter to pore area (b). The largest pore area coincides with the smallest pore diameter at ~1nm. Most pores fall between 10-5nm in size. 116
Figure 33| Volume of gas adsorbed (Langmuir volume) plotted against the measured BET surface area for the pure mineral 118
Figure 34 | A) The six types of isotherms that can be produced during adsorption-desorption experiments. Type I refers to adsorption limited to a few molecular layers and is considered true chemisorption. Type II is typical of a microporous adsorbent with unrestricted monolayer-multilayer adsorption. Type III is representative of weak adsorptive-adsorbent interactions. Type IV indicates complete pore-filling with monolayer-multilayer adsorption and capillary condensation. V refers to weak interactions between adsorbate and adsorbent with capillary condensation. VI isotherms reflect

step-wise multilayer adsorption on a non-uniform and nonporous surface (Sing, 1985). B. The four types of hysteresis loop associated with type IV and V isotherms. HI refers to a well-defined, cylindrical pore network. H2 is a heterogenous pore system with some pores blocked. Type H3 is typical of platy-clay minerals, especially in powdered form which produces slit-like pores. H4 creates narrow slit pores which a microporous in size. (Sing, 1985) 119
Figure 35| Langmuir volume measured on the Quantochrome Autosorb ® instrumentation plotted against measured BET surface area analysis. The bubble size represents the calculated volume of gas adsorbed in the online adsorption measurements during the experimental setup of the sample cell GC – C – IRMS. 121
Figure 36| Langmuir isotherm volume plotted against BJH pore volume shows a linear trend; as the pore volume increases, so does the measured Langmuir volume. Again, the size of the bubble represent the calculated molar volume adsorbed during experimental setup. 122
Figure 37 | Direct injection via gas syringe into the GC-C-IRMS. The standard deviation is 0.05‰ $\delta^{13}C_{CO2}$ with the average value for the bulk gas at -35.02 ‰ 124
Figure 38 | Raw data collected on degassing samples. Plotted as $\delta^{13}C$‰ against the retention time in seconds. 126
Figure 39| $\delta^{13}C$ of CH_4 fractionation trends for the 5 shale components tested plotted against the volume of gas extracted. 133
Figure 40| rough schematic of what a quartz, calcite and TOC rich shale would plot like (blue dashed), a 35%, quartz, 35% clay and 30% TOC shale would plot like (purple dahs) and a clay and TOC rich rock (red dashed line) 136
Figure 41| Material balance calculations for the 5 shale components tested 138
Figure 42| examples of canister desorption experiments from collected from depth which show the $\delta^{13}C$ trend for different degassing shales through time. A. (Liu et al., 2016b) and B. (Zhang et al., 2018) 139
Figure 43| Degassing trend lines with actual gas volume in psi from experimental setup. The psi is the total volume fo gas extracted with each extraction step and is the data in it's raw form As the fractionation of ^{12}C and ^{13}C occurs via desorption processes and not in mass movement of the free gas, this graph is showing the total amount of gas extracted and the associated fractionation but not the volume of gas in the adsorbed phase 141
Figure 44| Example of production decline curve plotted with billion cubic feet on the x-axis and time on the y-axis from Wood Mackenzie, Production Report 2011 150
Figure 45| Schematic diagram to show how methane and ethane would move through pore networks of different sizes. Methane has a smaller kinetic diameter than ethane and can navigate more readily through the tortuous, nanoporous network of a shale as demonstrated in this cartoon of a shale pore network. 155
Figure 46 | Location of the Eagle Ford Shale plays, transitioning from oil mature in the NW to gas mature in the SE. From (Mullen, 2010). The orange star is the location of the San Antonio Canyon, Texas, USA where these sample were collected. Full details on sample selection, refer to the thesis of Dr Miriam Wright (Wright, 2019). 162
Figure 47 | Stratagraphic column highlighting the age and lithological location of the Eagle Ford shale across south Tex (Mullen, 2010) 162
Figure 48| Custom-built sample cell coupled with the GC-FID. Chapter 2, Methodology explains the entire setup procedure. 166
Figure 49| Langmuir isotherms for EHO and ELO respectively. Both desorption curves exhibit mini hysteresis. EHO has a Langmuir volume of 19.347 cc/g whilst ELO has 8.04 cc/g. 169
Figure 50| BJH pore size distribution analysis for both EHO (top) and ELO (bottom). 170
Figure 51 | X-ray spectrum produced by XRD analysis of the EHO (upper) and ELO (lower). EHO has a broader spectrum of material present. 172
Figure 52| FTIR data showing the change in composition from the bulk rock, Kimmeridge Clay in blue, to the extracted kerogen in orange 173

Figure 53| Direct injection data from the sample bulk gas directly injected onto the GC-FID 174
Figure 54| C_1-C_1 molar mass of the gas mixture for a give extraction step. Montmorilonite directly almost undeliesthe trend of kaolinite showing that,even with different surface properties, the C_1-C_2 fractionation trend is the same. 177
Figure 55| time step and molar mass for the two Eagle Ford Shale Samples. 177
Figure 56| C_1-C_2 fractionation data collected for the pure mineral and Eagle Ford shale samples. These have been normalised to the respective bulk gases used for the mineral samples and the Eagle Ford Shale samples. Error bars were calculated as standard deviations between several experimental runs of the same sample. The error calculated was greatest in the type II kerogen but the trend is statistically significant. See Appendix Chapter 4: results for the multiple runs. 181
Figure 57|Fractionation factor and maximum adsorption capacity for all the tested samples. The fractionation factor is the average value that each measured data point deviates away from the bulk gas. 183
Figure 58| Fractionation factor ad BET surface area for all the tested samples. The fractionation factor is the average value that each measured data point deviates away from the bulk gas. 184
Figure 59| Material balance equations for the pure mineral samples. Even though the deviations from the bulk gas are relatively low in the case of kaolinite and montmorillonite, as after ~40% of the gas had been extracted plotted with an ethane value heavier than the bulk gas, some methane must be preferentially retained and the final few pulses of gas must be more methane enriched than the bulk. 185
Figure 60| Material balance equation for the ELO and EHO samples. 186
Figure 61| BET surface area in just the organic containing material compared to fractionation factor. 187
Figure 62| average C_1-C_2 data schematic for the three sample groups 188
Figure 63| Van Krevlen plot showing the hydrogen and oxygen indexes for the three shale samples tested. 202
Figure 64| Schematic diagram of the second generation cell. Instrumentation here is the GC-FID but could also be the GC-C-IRMS. Assignments as follows: (1) gas cylinder, (2) valve, (3) vacuum valve, (4) vacuum pump, (5) valve 1 – v1, (6) pressure transducer, (7)reference volume cell, (8) valve 2 – v2, (9) sample cell, (10) in-line filter, (11) valve 3 – v3, (12) injection needle valve, (13) 6-way injection valve, (14) vacuum pump valve 2, (16) Instrumentation – GC-FID. 208
Figure 65| FTIR data for the WL-N and WL-K samples. WL-N is depicted by the red line whilst WL-K is shown by the blue. Both samples are flattened to the background noise to increase the signal ratio and provides a direct comparison between the two samples. 211
Figure 66| FTIR data for the B-N and B-K samples. B-N is depicted by the blue line whilst B-K is shown by the red. Both samples are flattened to the background noise to increase the signal ratio and provides a direct comparison between the two samples. 212
Figure 67| FTIR data for the OC-N and OC-K samples. OC-N is depicted by the red line whilst OC-K is shown by the blue. Both samples are flattened to the background noise to increase the signal ratio and provides a direct comparison between the two samples. 212
Figure 68| Langmuir isotherm analysis carried out on the WL-N and WL-K samples. Langmuir Isotherm Analysis carried out by the iQ3 Quantachrome adsorption Instrument. P/P0 is the partial pressure of the N_2 adsorbate and the volume adsorbed is the calculated volume of N_2 adsorbed by each adsorbent. The measured Langmuir volume for the WL-N sample is 4.42cc/g whilst the WL-K is 82.92. 215
Figure 69| Langmuir isotherm analysis carried out on the B-N and B-K samples. Langmuir Isotherm Analysis carried out by the iQ3 Quantachrome adsorption Instrument. P/P0 is the partial pressure of the N_2 adsorbate and the volume adsorbed is the calculated volume of N_2 adsorbed by each adsorbent. A Langmuir volume of 42.016 cc/g is reached for B-N and 260.32 cc/g for B-K. Note the differences in shales between the two plots with B-K an order of magnitude greater than B-N. 215

Figure 70| Langmuir isotherm analysis for OC-N and OC-K Langmuir Isotherm Analysis carried out by the iQ3 Quantachrome adsorption Instrument. P/P0 is the partial pressure of the N_2 adsorbate and the volume adsorbed is the calculated volume of N_2 adsorbed by each adsorbent. The maximum adsorption capacity indicated by the Langmuir volume for OC-N is 55.75cc/g whilst OC-K has a Langmuir volume of 140.76cc/g. Note that the scales are different between OC-N and OC-K.....216
Figure 71| (A) BJH data for WL-N. The red line indicates the cumulative pore volume up to a maximum of 2000 Å. The blue line indicates the relative volume of pores for a given radius. The majority of pores are less than 50 Å in radius.(B) BJH data for WL-K. The red line indicates the cumulative pore volume up to a maximum of 2000 Å. The blue line indicates the relative volume of pores for a given radius. The majority of pores are less than 100 Å in radius. The overall pore volume is an order of magnitude greater than WL-N sample. 217
Figure 72|(A) BJH data for B-N. The red line indicates the cumulative pore volume up to a maximum of 2000 Å. The blue line indicates the relative volume of pores for a given radius. The majority of pores are less than 30 Å in radius.(B) BJH data for B-K. The red line indicates the cumulative pore volume up to a maximum of 2000 Å. The blue line indicates the relative volume of pores for a given radius. The majority of pores are less than 300 Å in radius. This kerogen has a high proportion of larger, mesoscale pores (10-30nm 217
Figure 73| (A) BJH data for OC-N. The red line indicates the cumulative pore volume up to a maximum of 2000 Å. The majority of pores are less than 60 Å. (B) BJH data for OC-K. The red line indicates the cumulative pore volume up to a maximum of 2000 Å. The majority of pores are less than 200 Å. This kerogen has a high proportion of larger, mesoscale pores (10-30nm 218
Figure 74| Time plots for the three natural samples. This is the raw data as extracted from the GC-FID. The ratio of C_1-C_2 measured at each extraction step is plotted against the extraction step. The time between each step is approximately 300 seconds. 221
Figure 75| Whole shale samples and isolated kerogens from the three shales: each show a distinctive C_1-C_2 with a given volume of gas extracted. 224
Figure 76| No. of moles adsorbed by each sample, calculated using the custom-built sample cell plotted against the N_2 calculated Langmuir volume shows a linear relationship except for the Oxford Clay isolated Kerogen sample, OC-K. There is no obvious correlation between either of the adsorption measurements and total organic carbon content. 225
Figure 77| TOC and Langmuir volume for the extracted kerogens and natural samples tested. There is no clear relationship between the volume of organic material and the amount the Langmuir volume measured. 232
Figure 78| TOC (%) plotted against the cumulative volume of gas extracted before the peak C_1-C_2 ratio was reached for each sample. There is no correlation between the amount of organic material and the amount of gas extracted before peak fractionation is met. The volume-to-peak can be a proxy for the volume of gas stored in the adsorbed phase as the desorption process would contribute to the increments of gas being extracted.....233
Figure 79| TOC (%) plotted against the C_1-C_2 ratio “peak height”. This refers to the point at which the C_1-C_2 ratio deviates the furthest away from the bulk gas was reached for each sample. There is no correlation between the amount of organic material and maximum change in C_1-C_2 ratio of the degassed material to the bulk gas. The magnitude of change in C_1-C_2 ratio compared to the bulk aas can be a proxy for the volume of gas stored in the adsorbed phase as the desorption process would contribute to the increments of gas being extracted or could be influenced by the diffusion processes in which case would be a proxy for distance travelled within the shale. 234
Figure 80| Molar adsorption calculated from the pressure measurements recorded from the sample cell during introduction of gas to the shale or kerogen, plotted against the cumulative volume of gas extracted before the peak C_1-C_2 ratio was reached for each sample. There is a weak correlation between the amount of moles adsorbed and the amount of gas extracted before peak fractionation is met. The volume-to-peak can be a proxy for the volume of gas stored in the adsorbed phase as the desorption process would contribute to the increments of gas being extracted.....235

Figure 81| cross plot of the C_1-C_2 peak height and the calculated BET surface area of the three shale samples and their respective extracted kerogens. The R^2 value relates to the proximity of each data point to the regression line, shown by the blue dashed line. 237
Figure 82| $\Delta C_{1(0)} - C_{1(z)}$ and BET surface area; how much does the extracted gas deviate away from the bulk, in total across the experimental procedure. 238
Figure 83| BET surface area (m^2/g) and Langmuir volume (cc/g) for each three samples and their isolated kerogens 240
Figure 84| Material balance for the OC-N sample. The sum total of methane molecules and ethane molecules for each extraction step relative to the initial molar volume of methane and ethane injected gives the remaining molar volume of methane and ethane in the cell. The material balance only gives the ratio of methane to ethane left in the cell, not the exact shape of the curve so this is only a prediction. The graph does however show that the final 25% of the gas still trapped in the sample has a higher proportion of ethane relative to ethane than the starting gas. 246
Figure 85| Mass balanced gas tail composition predictions for the three whole shale samples and the isolated kerogen samples. 247
Figure 86| Volume-to-peak height and $\Delta C_{1(0)} - C_{1(z}$ for the three shale samples and the kerogen samples 249
Figure 87| Hydrous Pyrolysis setup (Collard and Blin, 2014). The samples remain submerged in fluid thus are considered pyrolyzed in an aqueous setting. 261
Figure 88| Sample cell – GC-FID configuration. 262
Figure 89| OC-N, OC-250 and OC-325 Langmuir isotherm analysis. The blue line is the adsorption curve and the red lines the desorption curve. Note the scale variations between the plots. 265
Figure 90| OC-N, OC-250 and OC-325 pore size distributions, note the scale variations between plots. 267
Figure 91| Oxford artificial maturation suite; gas extraction steps plotted against the normalised C_1-C_2 gas fractionation trend 271
Figure 92|Volumetric data calculated for the OC-artificial maturation suite 273
Figure 93| Peak height and Langmuir volumes of the Oxford suite 275
Figure 94| Combined diffusion and desorption fractionation models from when D*/D=1 there is only desorptive fractionation through to α =1 (diffusion dominated) (Xia and Tang, 2012). 278
Figure 95| Effect of the sorption processes on the $\delta^{13}CH$. K refers to the desorption coefficient and increases from little effect when K=0 to sorption dominated when K=1 (Xia and Tang, 2012a) 279
Figure 96|Drainage area: a lot of gas from a large area or the same volume of gas from a much smaller area? A small area with a lot of gas would have minimal diffusion as the distance travelled would be less far. 280
Figure 97| Adsorption and diffusion curves plotted over the data collected in chapter 5 – Diffusion from Ray & Ramesh 2000- and Knudsen diffusivity modelling by Dr Craig Smalley. 281
Figure 98| Worked example where, after less than 3 months of production time, the peak C_1-C_2 has been achieved and 25% of the gas has been extracted. This will not be a long-lived well. 282
Figure 99| Worked example where, after 6 months of production, the peak to C_1-C_2 was met. The sum total of gas extracted up to this peak point accounts for 25% of the total extractable gas. This well has a long gas tail accounting for 150 billion cubic feet (b.c.f.) so will most likely be profitable to keep open. 283
Figure 100 Worked example where, after 12 months of production, the peak to C_1-C_2 ratio has been met. The sum total of gas extracted prior to this peak accounts for 25% of total gas in place. The sum total of gas up to this point is only 25 b.c.f. which suggests a low production rate compared to the previous two worked examples. 284

1.0 Introduction

1.1 The Purpose of this research

Shale gas can be considered a "stop-gap" resource, a fuel that will aid a managed transition from a high-carbon to low-carbon economy. Whilst the shale gas industry has achieved success in several plays in the USA such as the Bakken Shale in Montana-North Dakota, Eagle Ford and Barnett Shale shales in Texas, Monterey Shale in California (EIA, 2015), the success has yet to be replicated across the rest of the World. Even in the USA, shale gas project economics are fragile, and projects must be managed efficiently in order to remain economic.

Successful shale gas developments require the following key decisions, supported by high quality information and understanding:

Before development.

1. Develop or not? Before spending large amounts of money on developing a shale gas field, it is important to understand (a) the size of the potential resource, which includes the reservoir volume and richness (amount of gas per unit rock volume) and (b) the likely gas well production profile, as early gas is worth more than later gas. Connected with this is how effectively production could be stimulated using hydraulic fracturing.
2. How to develop. This involves predicting the likely drainage radius of a shale gas well so that well numbers and types, and hydraulic fracturing, can be optimised.

During production.

3. Infill drilling. Based on production performance from the initial well stock, are further wells required? This requires understanding of the actual effective drainage radius of the well based on an understanding of the shape of production decline curves.

4. Refracturing. Could more gas be produced, and production be accelerated by performing more fracturing on the wells? Again, this requires understanding of the actual effective drainage radius of the well, and thus how much gas remains within that drained volume.

The hypotheses being tested by the research outlined in this thesis is:

- Monitoring the compositional changes of gas degassed in the laboratory from shale reservoir samples gives information on how much gas is contained within the shale, and how this is situated (macropores, micropores, adsorbed) and thus the likely shape of a well production profile. This understanding could increase the quality of decisions (1) and (2).
- Monitoring the composition of gas produced from a shale reservoir sample in the laboratory, used as an analogue for compositional changes expected during shale gas well production in the field, can be applied to estimate instantaneous recovery factor in the drained volume, and thus remaining gas in the drained volume and drainage radius. This understanding would increase the quality of decisions (3) and (4).

This research develops the laboratory approach and data to test these hypotheses.

1.2 Shale Gas: and overview

1.2.1 What is a shale?

In the petroleum industry, shales are described as being fine-grained mud or clay rocks which contain particles less than 0.06 mm in size and at least 1% organic material (Freeman et al., 2012; Scanlon et al., 2014). They are typically dominated by clay minerals with the "average" shale comprising 59% clay (Yaalon, 1962). The most dominant clay mineral found in the average shale is illite, a non-swelling, layered phyllosilicate mineral formed from the breakdown of muscovite mica (Diamond, 1970). Other clays common in shales are kaolinite, montmorillonite, chlorite and smectite (Yaalon, 1962). Shales typically also contain some amount of quartz, feldspar and carbonates as well as accessory minerals such as iron oxides and cements. Shales with a higher percentage of siliclastic material are harder and less coherent whilst clay rich shales are softer and weaker (Sone and Zoback, 2013). The dominance of fine-grained, platy clay minerals in shales means that they have very low permeability and porosity, typically <1% with laboratory and regional studies suggesting porosities as low as 0.1% in a typical shale rock (Freeman et al., 2012; Neuzil, 1994).

Shales also contain organic material (Scanlon et al., 2014). To be considered a hydrocarbon source rock, they must contain >2% organic material (Jarvie et al., 2004). The total amount of organic material in a shale is often called total organic carbon and referred to as TOC (%). TOC (%) is either movable organic material, referred to as Extractable Organic Material (EOM) or immovable organic material, referred to as Kerogen Hosted Carbon (KHC) (Steiner et al., 2016). In conventional oil and gas reservoirs, the organic material is present due to migration out of the source rock and is thus only EOM. In unconventional shale gas reservoirs, the organic material is dominated by the KHC. For the purpose of this thesis, when referring to TOC (%), this considers solely the immovable KHC material and will be referred to as kerogen

throughout this thesis. Kerogen refers to the geo-polymer material formed after burial and diagenesis of bio-polymers (Dayal, 2017). This organic material can be lacustrine derived (type I kerogen), marine derived (type II kerogen) or terrestrially derived (type III kerogen) (Dayal, 2017).

1.2.2 Shales as hydrocarbon plays

In conventional oil and gas plays, several components are required to generate, store and trap hydrocarbons (Freeman et al., 2012). Firstly, a source rock, a shale with >1% TOC, is required. This source rock must be buried to a depth at which organic material breaks down into moveable hydrocarbons. The hydrocarbons must then migrate out of the matured shale and into a porous reservoir, often a sandstone or limestone. The reservoirs are composed of coarser grained material, with porosities typically ranging between 10-30% (Ehrenberg and Nadeau, 2005). Conventional reservoirs tend to have high permeability, resulting from good connectivity within the pore network which allows flow from reservoir to wellbore (Freeman et al., 2012; Holditch, 2013; Scanlon et al., 2014). Conventional reservoirs require a caprock seal, a tight lithology that will not allow flow through on a geological timescale. There must also be some mechanism for trapping - either structurally or stratigraphically - for a hydrocarbon accumulation to form, and a migration route from the source rock to the trap. An overview of such a petroleum system is shown in Figure 1. All these components together, occurring in the correct sequence are required to make a conventional play (Scotchman, 2016). The source rock must be buried to sufficient depth to become mature and release hydrocarbons but this must occur after the reservoir, trap and seal are in place. For shale gas reservoirs, this is not the case and exploration is much more simple, involving far fewer components than a conventional hydrocarbon reservoir.

In shale gas plays however, the play is self-sourcing and self-sealing (Binnion, 2012). The shale matures enough to produce hydrocarbons but not all of the oil and gas completely migrates out, retaining significant oil and gas trapped within the tight lithology (Dayal, 2017). The hydrocarbons reside in the low permeability pore network shown by the Scanning Electron Microscopy (SEM) image in Figure 1. The pore network is a combination of micropores (less than 2 nm in diameter), mesopores (2-50 nm in diameter) and macropores (>50 nm in diameter) (Kuila and Prasad, 2013) which are distributed across the organic material, between the platy layers and fibres of clays and between larger grains of silicates, carbonates and accessory minerals (Cao et al., 2015; Guo et al., 2017; Kuila and Prasad, 2013). Shale gas is thus defined as hydrocarbon gas trapped within a fine-grained sedimentary rock which, due to the low matrix permeability, requires mechanical stimulation such as hydraulic fracturing to be produced (McGlade et al., 2013).

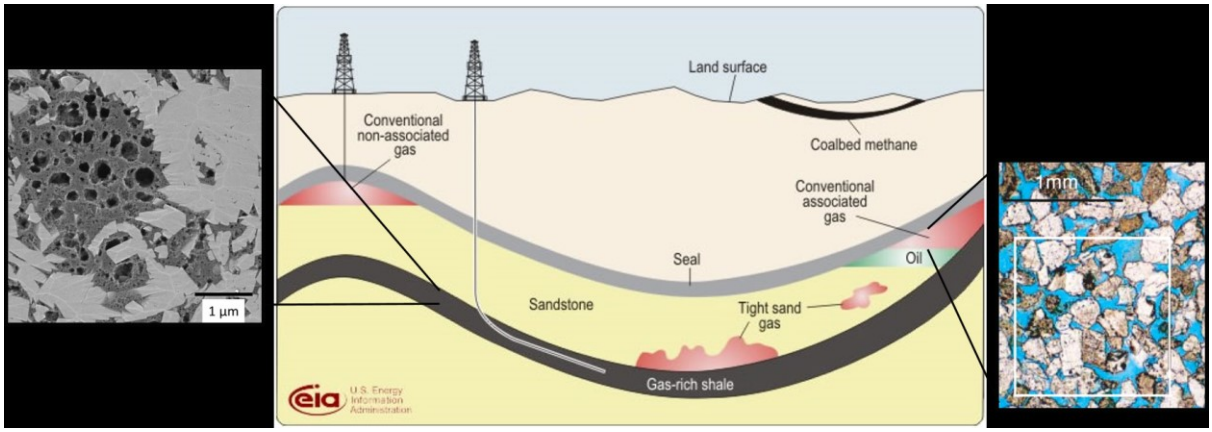


Figure 1| Schematic representation of "conventional" and "unconventional" hydrocarbon reserves. Conventional reservoirs are comprised of macroporous grains where hydrocarbons are stored in the pores spaces (blue sections in the thin section). Unconventional shale gas reservoirs contain gas in several phases and are dominated by pores that are mesoscale < 50 nm) and smaller). Adapted from: (EIA, 2015),

1.2.3 What comprises shale gas?

The hydrocarbon gas extracted from unconventional shale gas reservoirs is dominated by methane. Methane typically accounts for over 90% of the extractable gas (Ambrose et al.,

2011b; Dayal, 2017). Ethane and carbon dioxide are the next most common components with C_{3+} compounds being present in wetter gas reservoirs (Wang et al., 2015a).

1.2.4 How are hydrocarbon gases generated?

Shale gas reservoirs contain gas that is either thermogenically- or biogenically- derived (Curtis, 2002). Thermally derived gas comes from the burial and subsequent heating of shales (Curtis, 2002; Espitalie et al., 1988; Jarvie et al., 2007; Stolper et al., 2014). Kerogen, which makes up the original sedimentary organic material, is thermally cracked into bitumen which, with increased heating, decomposes further. The longer chain hydrocarbons are cracked into gas fractions, typically at temperatures exceeding 150ºC (Mango and Hightower, 1997). The volume of gas generated through thermal decomposition of organic matter is a function of time, temperature, organic matter content and organic matter composition (Curtis, 2002). The gaseous hydrocarbons formed through primary cracking, reactions which occur during the evolution of kerogen from organic material, are gaseous C_1 (methane), C_2 (ethane), C_3 (propane), C_4 (butane) and C_5 (pentane) and heavier $C_{6\text{-}15}$ fractions forming condensates (Espitalie et al., 1988). Secondary cracking occurs with further heating and burial of the shale formation and the longer chain hydrocarbons are broken down to shorter chain gases (Espitalie et al., 1988). The stable carbon isotope and molecular weight ratios of these gas accumulations is affected by the type of kerogen and the cracking process which is in itself a function of the burial history (Clayton, 1991).

Gas can also be generated biogenically as a result of methanogenic bacteria metabolising the organic material (Curtis, 2002). More than 20% of the World's gas reserves are from biogenically derived sources and its biogenic origin can be confirmed by isotopic and geochemical analysis (Rice and Claypool, 1981). Methane derived from biogenic sources are typically enriched in ^{12}C, as the reaction also involves generation of CO_2 that is conversely

depleted in ^{12}C. This is due to variations in isotopic fractionation by the methanogenic bacteria (Rice and Claypool, 1981). Biogenically derived shale gas occurs at significantly lower temperatures than thermogenically derived gas; <50ºC versus more than 157-221ºC respectively (Stolper et al., 2014).

1.3 Commercial Production of shale gas extraction

1.3.1 How is shale gas extracted?

Due to the low permeability of shale gas reservoirs, flow out of a shale gas well is not typical Darcy flow but transient flow which can take place over several years. This natural unstimulated, flow out of a shale gas well would be very slow and unlikely to be commercially attractive (Ambrose et al., 2011b). As such, porosity and permeability must be artificially introduced to the reservoir in order to allow the shale gas to flow to the well bore (Bello et al., 2010; Freeman et al., 2012). To access the gases trapped within the shale more effectively, wells drilled into shale gas reservoirs are generally stimulated using hydraulic fracturing, whereby fluids are pumped into well at pressures exceeding fracture pressure (Hubbert and Willis, 1972; Medlin, 1976). The artificial fractures generated are kept open by the subsequent injection of proppant, which forms a high permeability matrix within the fractures. A proppant is a solid material that is combined with the fracking fluid and is often grains of sand of manmade ceramic material (Mayerhofer et al., 1997). Hydraulic fracturing is by no means a new technology, but recent technological advances have made this an economically viable method of shale gas extraction. Gas now liberated from the shale matrix by fracturing can be extracted from the reservoir, flowing out of the shale into the fracture network and then into the wellbore.

As previously mentioned, whilst a shale gas reservoir must contain organic material to be considered a viable source rock, shales also contain various amounts of clays, quartz, feldspars,

carbonate and iron oxides (Yaalon, 1962). The proportions of rigid siliciclastic grains (quartz, feldspars) and carbonate material versus the more ductile clay minerals and organic matter will control the geomechanical properties of the shale. The more rigid the grains, the more brittle the shale and the more easily fracture stimulation will be achieved because fracturing will occur rather than ductile deformation (Scotchman, 2016; Sone and Zoback, 2013; D. Zhang et al., 2016). Modern shale gas wells in the US typically rely on multi-stage fracturing (i.e. multiple batches for fractures along the wellbore) and use directional drilling from multiple well pads to achieve full coverage of the reservoir (Bello et al., 2010; Gandossi and others, 2013). The most popular technique for extracting hydrocarbon gas from tight reservoir units is the multi-fractured horizontal well (MRHW) technique (Ambrose et al., 2011a; Britt et al., 2009).

1.3.2 What makes a shale gas reservoir commercially viable?

For a shale gas reservoir to be a viable shale gas resource, several parameters, some outlined in the paragraphs above, must be present. These parameters relate to composition, maturity, thickness and areal extent and large-scale geological architecture (Newsham et al., 2001). The shale must contain matured organic material to provide the hydrocarbons.

The shale must contain matured organic material to provide the hydrocarbons. The shale must also have geomechanical properties that enable effective hydraulic fracturing, with generally less than 40% clays. An example of a "frackability" ternary plot is show in Figure 2. The shale must be fairly isotropic with minimal laminations and a Young's modulus exceeding 3.5×10^6 psi (Newsham et al., 2001). The shale must be thick enough and covering a great enough aerial extent to contain enough gas volume to be economically material.

The precise thresholds for commerciality will vary depending on gas price and current market price of technology access. Whereas for conventional reservoirs, exploration requires

geological modelling and basin analysis to ascertain if all the required petroleum system components (Fig. 1) were present at the right time, shale gas exploration mainly involves finding a mature shale. Subsequent appraisal of whether the shale gas resource is potential commercial would involve successfully understanding the complex geological factors that dictate the amount of hydrocarbon gas that is stored within the shale, how much of this gas can be extracted and over what timescale. Understanding the controlling factors of these three components is the biggest challenge of shale gas exploration, exacerbated by the complex internal nanoporous and heterogeneous nature of shale lithologies.

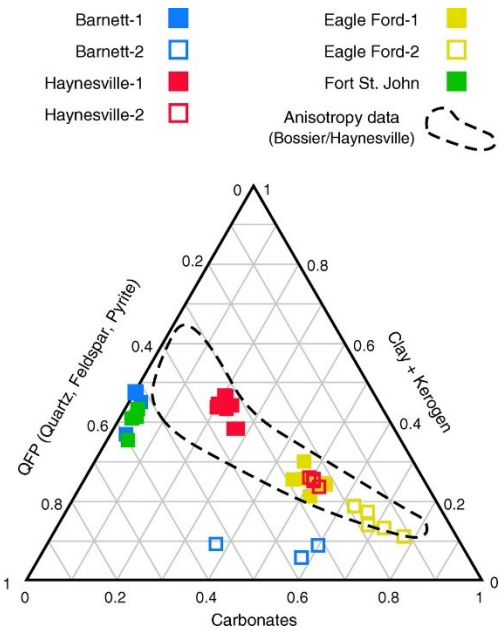


Figure 2| An example ternary plot considering the properties of a shale that must be considered when looking at the geomechanical frackability of a shale (Sone and Zoback, 2013).

1.4 What are the benefits of shale gas?

The term "shale gas revolution" reflects how shale gas as an energy source has grown prolifically in recent years and is now a major component of the global energy market (Blumsack, 2014). Benefits of shale gas include facilitating the move from away from coal-fired power generation in response to the increased supply of natural gas and a corresponding reduction in price (Arora and Cai, 2014). Natural gas generates half the carbon dioxide of coal

while achieving the same energy production. Increased natural gas use in the US has caused national emissions to fall (Heath et al., 2014) and a similar supplementation of coal by natural gas elsewhere in the world could lead to a comparable reduction in global carbon dioxide emissions. Power from natural gas can be varied in a controllable fashion unlike nuclear and renewables and this dispatchability supports the status of natural gas as an attractive bridge fuel to support the transition to a renewable energy-dominated low carbon future (Levi, 2013a; Mac Kinnon et al., 2018). With the clean energy transition required to meet EU climate targets, shale gas is the cleanest fossil fuel that would allow for the continued use of vast quantities of energy but with a lower carbon budget (Levi, 2013a; Weijermars et al., 2011; Zhang et al., 2016). The predicted growth of shale gas in the United States is shown by Figure 3 in which the volume of hydrocarbons derived from natural gas and shale gas reservoirs is expected to continue to play a significant role as a global energy resource into 2040 (IEA, 2019).

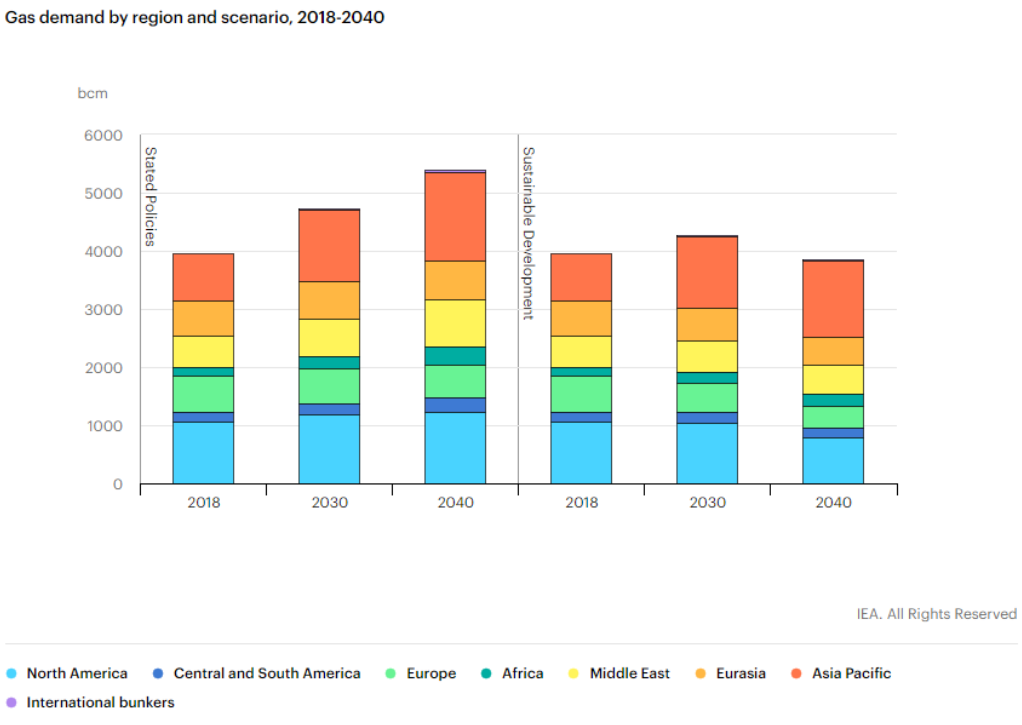


Figure 3| IAE global forecasting for natural gas consumption from is predicted to be continue to rise into 2040 with current states policies. Even with sustainable development and modelling accounting for the influx and growth of renewable energy, natural gas is still a global energy resource well into 2040. (IEA, 2019).

1.5 Shale Gas: storage and flow

1.5.1 Why do we want to calculate gas storage and why can't we accurately do so?

As outlined in Figure 1, shale gas reservoirs are compositionally different to their conventional counterparts. Shales are heterogenous not only in their mineralogy but also the size, shape, connectivity and tortuosity of the pore network, organic matter type, distribution and maturity as well as water saturation (Ambrose et al., 2010; Bernard et al., 2010; Bustin et al., 2008a; Chalmers and Bustin, 2007a; Guo et al., 2017; Hou et al., 2017; Ross and Bustin, 2009a). Over the past 40 years, the complexity of shale gas appraisal, development and production has become more apparent (King and others, 2010). Shales are heterogeneous both vertically and aereally in both composition and framework, no two shales are alike. This heterogeneity has implications for accurate calculation of the maximum gas capacity of a shale, the recovery factor (how much gas can ultimately be extracted), how long it will take to extract all the extractable gas and the shape of the production decline curve. The controlling factors on the volume of hydrocarbon gas that a shale gas reservoir can store is debated in the literature and no consensus exists (Akkutlu et al., 2012; Bustin and Clarkson, 1998a; Chen and Xiao, 2014; Chen et al., 2019; Cheng and Huang, 2004a; Fan et al., 2018; Gasparik et al., 2014; Hou et al., 2017; Li et al., 2019a; Wang et al., 2015a; Wang et al., 2019).

Over recent years, there has been an increase in the proportion of recoverable gas that has been extracted from US shale gas wells; recent increases in shale gas recovery factor from as low as 2% in the 1990s to as high as 50% in the mid 2000's is attributed to shale-specific horizontal well adaptations (King and others, 2010). Whilst technological advances mean that more of the gas in place may be extracted from producing wells, there is still a significant issue however with predicting the estimated ultimate recovery (EUR). EUR refers to the total volume of a shale gas resource that can be recovered based on the currently available technology. An

example of shale gas production profiles is shown in Figure 4. On these diagrams, EUR is the area under a rate vs time curve, or the end point of a cumulative production vs time curve (Figure 4). Accurately predicting the EUR is a major factor for hydrocarbon companies and investors as it predicts the profitability of a field development – and thus whether the field should be developed or not.

It is not just the recoverable volume of gas (EUR) that is important but the timescale over which this gas can be extracted. Shale gas operators may view the lifetime of a well as up to 50 years (King and others, 2010). Ultimately, accurate calculation of the recovery factor (RF) - the percentage of initial gas in place (GIP) that can be recovered - and the timescale over which this recovery occurs is an uncertainty for all shale gas wells across the world (McGlade et al., 2013). Figure 4 shows how shale gas reservoirs are characterised by an initial gas pulse followed by a rapid, exponential decline and long gas tail. In detail, production profiles are uncertain: the size of the initial pulse, the severity of decline and the length of the production tail; these relate to the way gas is stored in the shale – in macropores, micropores or adsorbed. Understanding the decline and tail is key to effective field management, affecting key decisions about infill drilling, refracturing (decisions 3 & 4 in Chapter 7) and eventual well shut-in. The main issue with these production decline curves is that production rate alone cannot differentiate between drainage and the recovery factor effects. If a large volume of gas has been extracted, does this relate to high recovery factor from a small drainage radius, or a low recovery factor from a large radius? This uncertainty has a massive impact on infill drilling and refracturing decisions. Production profiles alone cannot distinguish these two scenarios, hence the need for the geochemical surveillance tool outlined here.

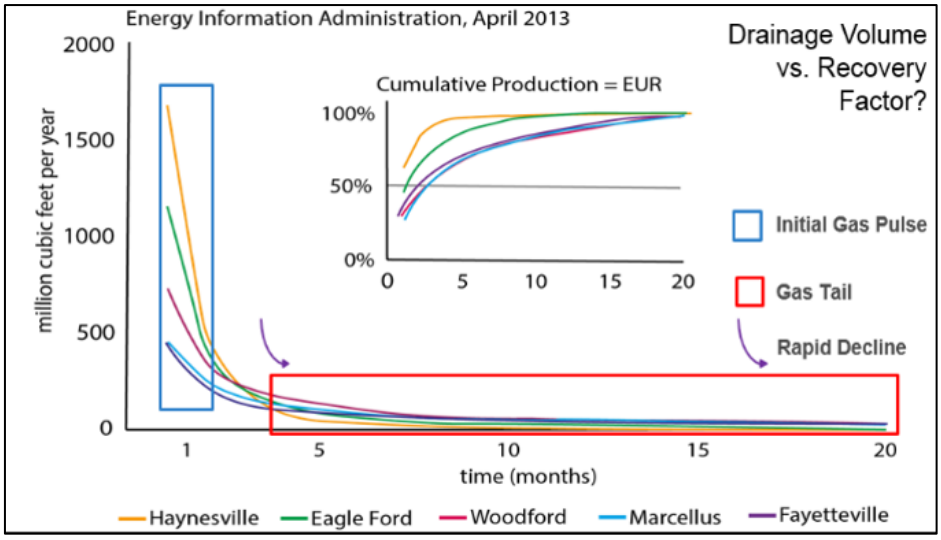


Figure 4| An example of the production-decline curves from 5 of the largest producing shale gas formations in the United States of America. All 5 fields are characterised by an initial gas pulse followed by a rapid decline and a long gas tail. The EUR curves do not accurately represent the real volumes of extractable gas. Adapted from EIA, 2013.

1.5.2 Why is gas storage hard to calculate?

Gas within a shale gas reservoir is stored in several possible sites. Gas can be stored as free gas within any pre-existing macropores, between coarser grains of quartz of calcite, or in pre-existing fractures or vugs. Once a well is drilled, the pressure gradient will induce flow; flow through macro scale pores is the same as that in a conventional reservoir and flow from these pores to the wellbore will be conventional Darcy flow (stage D in Figure 5) (Freeman et al., 2011). albeit slow due to the low matrix permeability.

Gas can also be stored as free gas in very small (micro- or nano-) pores. However, such gas would have to migrate through a very narrow and tortuous micropore network before emerging in the fracture network and moving to the well (stages B and C in Figure 5). Because the gas molecule sizes are a significant proportion of the diameter of the microporous network, the movement of the gas through the small pores is strongly affected by interaction with the pore walls. The process that best describes this gas movement is Knudsen diffusion (Freeman et al., 2011). Figure 5 shows a schematic of C^{12} and C^{13} isotopes with their relative sized exaggerated. Both carbon isotopes will desorb from the surface of minerals and travel through the tortuous

pore network to the fractures and on to the wellbore. The importance of C^{12} and C^{13} is that C^{12} will desorb more readily from a sorption site than C^{13} which is what causes the inherent fractionation during sample degassing (Berner et al., 1995; Lu et al., 2015).

Gas is also stored adsorbed onto the walls of shale constituents, most commonly cited as adsorbed onto the on the organic material but some authors also suggest the inorganic components (Cheng and Huang, 2004a; Dahaghi and others, 2010; Heller and Zoback, 2014a; Javadpour et al., 2007; Ross and Bustin, 2009a; Xiong et al., 2017a). Gas stored in the adsorbed phase cannot be measured using conventional petrophysical techniques and the controls and importance of gas storage in the adsorbed phase is contentious (Etminan et al., 2014a; Li et al., 2015b; Xia and Tang, 2012a). Gas can also be dissolved in the residual bitumen from kerogen cracking and in a diffused state within the nanoporous network (Ambrose et al., 2010; Cui et al., 2009; Fan et al., 2018; Hao et al., 2013; Hartman et al., 2011; Ross and Bustin, 2009a; Smith et al., 1984a; Zhang and Krooss, 2001a; Zou and Rezaee, 2019a).

The volume of gas stored as adsorbed, free in micropores, or free in macropores will vary between shales and even within a single shale due to its heterogeneous nature. The volume of gas stored in the adsorbed phase has been estimated to be anywhere between 20-80% of the total gas in place (Lancaster and Hill, 1993; Lane et al., 1989a).

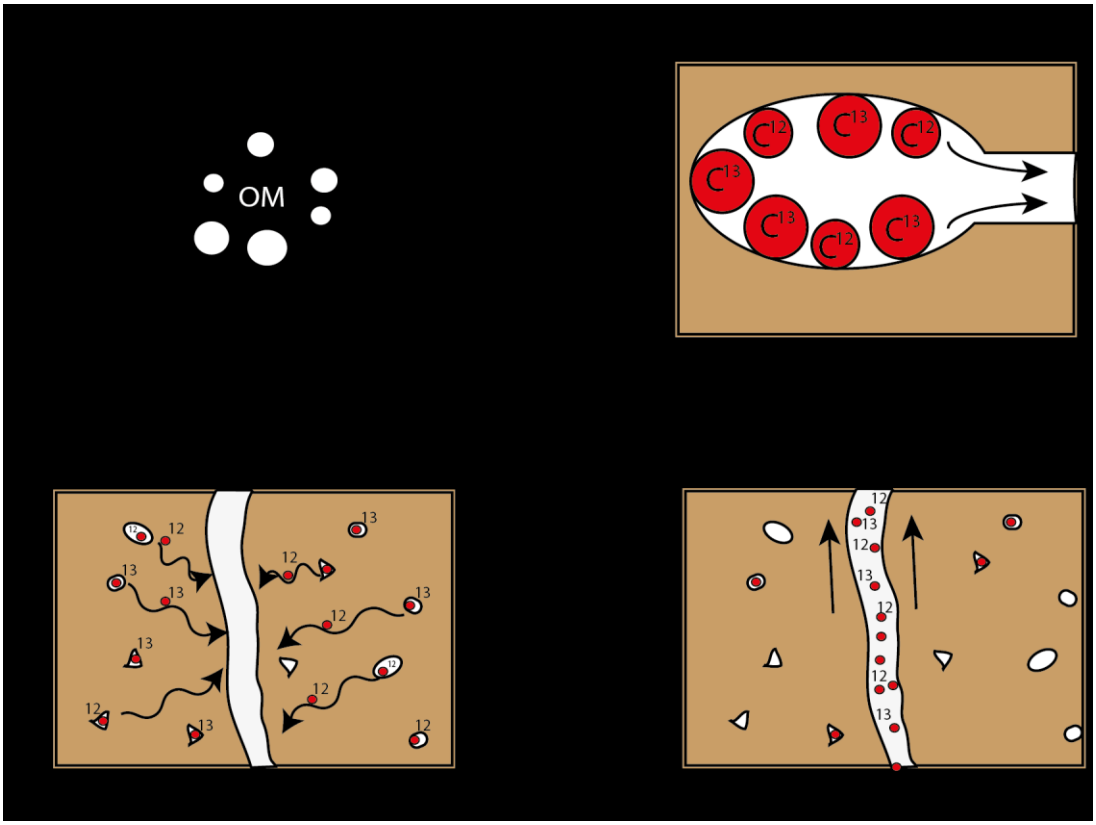


Figure 5| Different stages of gas storage and transport out of the various porescales within a shale. Adapted from (Xia and Tang, 2012b)

1.5.3 Adsorption and storage capacity

Adsorption refers to the adhesion of a fluid adsorbate to the surface of another material that can be a solid or a liquid, termed the adsorbent (Atkins, 2010; Langmuir, 1918). The bond between the adsorbate and the adsorbent can be physical, in which case it is reversible, or chemical which is irreversible. There are several assumptions when considering adsorption capacity of a material, the most widely cited being that adsorption occurs in a monolayer (Atkins, 2010). The modelling of adsorption using monolayer coverage as an assumption at a specific temperature was developed by Irving Langmuir (Langmuir, 1918) and is often used in shale gas adsorption numerical modelling. The Langmuir model assumes that, at equilibrium, the rate of adsorption is equal to the rate of desorption and this rate is dependent on the nature of the adsorbent and adsorbate.

The adsorption capacity is typically studied graphically and requires theoretical modelling. The adsorption process is modelled as a function of the adsorbate pressure and the concentration at a constant temperature. Langmuir isothermal adsorption assumes a monolayer coverage thus there are a fixed number of adsorption sites (Langmuir, 1918). As there are a fixed number of adsorption sites, there is also a maximum pressure at which the material is fully covered in a monolayer. This is referred to as the Langmuir pressure. The maximum storage volume is known as the Langmuir volume. Materials of different composition will have varying surface areas, pore size distributions, chemical surface properties etc. thus will have different Langmuir adsorption isotherms and Langmuir volumes.

As shales are a heterogeneous assemblage of mineral and organic constituents, the volume of gas adsorbed onto each constituent adsorbent surface will vary based on their surface chemical properties. Further, the volume of gas adsorbed depends on the properties of the adsorbate gas. For example, methane and ethane will have different propensities for adsorption, as will methane with a ^{13}C isotope compared to a ^{12}C isotope. The relative volume of gas stored as adsorbed gas versus free gas will also vary depending on the surface area to void volume of the material. This is important for the shale gas industry as the volume of gas adsorbed may contribute to the greatest portion of gas extracted but take a long time to produce.

1.5.4 What controls adsorption

Several literature studies have explored different aspects of gas adsorption capacity of shales. The changing nature of the adsorbent in terms of pore size, mineralogy, thermal maturity and kerogen type have been explored for gas adsorption capacity (Hao et al., 2013; Hou et al., 2017; Hu, 2014a; Jarvie et al., 2007, p. 20; Li et al., 2019a, 2015b; Rexer et al., 2013; Ross and Bustin, 2009a). It has been suggested that surface area plays a dominant role regardless of the composition of the material whereas other authors have argued that it is the

organic material specifically that contribute towards adsorption capacity (Lu et al., 1995), There is no definitive conclusions within the literature as to the dominant influencing factor of gas adsorption capacity of a shale or how these factors interplay.

Chemical surface affinity of different minerals

On a chemical level, adsorption requires an imperfect surface in order for a material to remain in contact with a surface upon collision (Atkins, 2010). On a perfect surface, a molecule will collide and bounce off as it will expend less energy taking this route. A surface that contains ridges, kinks, cleat or pits which create terraces allowing greater molecular interactions. If the influence of this intermolecular potential is great enough, the molecule or atom will "stick" to the surface. An imperfect surface, even at standard pressures and temperatures will quickly become covered in a monolayer of gas when exposed (Atkins, 2010). Physisorption, which dominates shale gas reservoirs, is dictated by Van der Waals bonds and requires similar levels of energy as condensation. Molecular adsorption onto an adsorbent is dictated by the surface chemistry and gas-surface interaction energy, the geometry of the absorbent, the pressure and temperature at which the adsorption is occurring and the presence of water, especially for hydrophyllic material (Chen and Xiao, 2014; Heller and Zoback, 2014a; Langmuir, 1918; Psarras et al., 2017; Soroush et al., 2014). The organic matter content of a shale (amount and type) could have a controlling influence on gas storage capacity; this will be investigated in the present study.

1.5.5 Desorption and gas extraction

Adsorption-desorption isotherms are often non-linear with a distinct hysteresis effect seen between the adsorption and desorption isotherms (Wang et al., 2016a). This is caused by adsorbate phase transitions and will depend on the adsorbate-adsorbent interactions. The rate of adsorption is modelled to be proportional to the volume of free gas whilst the desorption rate

is dependent on the volume of adsorbed gas (Langmuir, 1918; Y. Wang et al., 2016). The adsorption rate will be dependent on the adsorption affinity of different hydrocarbon gases and the adsorption capacity of the adsorbent. This selective adsorption-desorption process is a possible cause of the change in gas geochemistry with continuous gas extraction. Understanding the controlling factors of this fractionation between hydrocarbon gases during gas extraction can be used to better understand the storage mechanisms of gas in shales and whether the gas has been stored as free gas or in an adsorbed phase, with methane having a greater adsorption affinity than ethane and methane $^{12}CH_4$ having a greater adsorption affinity than methane $^{13}CH_4$ (Chareonsuppanimit et al., 2012a; Cheng and Huang, 2004a; Cui et al., 2009; Lu et al., 2015).

1.5.6 Gas flow regimes and diffusion

There are several different mechanisms proposed for how gases can flow out of a shale gas reservoir. Typical Darcy flow can occur when the pore size is large and pore connectivity is good. No fractionation of gas composition is expected during Darcy flow.

When the pores or pore throats are too small to allow this then Knudsen diffusion, where the mean path of the molecule is less than the pore length, can occur. There have also been models of slip flow (Freeman et al., 2011; Shabro et al., 2011) Slip flow refers to the Klinkenberg effect where gasses slipping across the pore walls produces an apparent dependence between permeability on the pressure; the permeability appears greater than if it were a liquid not a gas flowing through the low-permeability network. Diffusive fractionation occurs through Rayleigh distillation fractionation or the chromatographic effect where the smaller molecules are able to navigate the heterogeneous pore network and escape the shale reservoir more readily than larger molecules (Etminan et al., 2014; Wang et al., 2015a). This

diffusion controlled fractionation is driven by the concentration gradient across a shale reservoir.

1.6. Why is adsorption-desorption and diffusion important? The potential for a geochemical index

Adsorption-desorption processes are important for understanding gas storage in shales, and diffusion is important for understanding gas production mechanisms. Because gas desorption and gas Knudsen flow should both create a fractionation in methane/ethane ratio and methane $\delta^{13}C$, there is the potential for the development of a geochemical index which can be linked to volume of gas extracted and the processes involved. With adsorption, the lighter stable carbon isotope, carbon-12 preferentially adsorbs onto the surface of a material and will desorb more readily than the heavier carbon-13 (Atkins, 2010). As such there is expected to be a carbon isotopic fractionation trend that will relate to the degassing process, from 100% gas initially in place (GIP), changing with reservoir depressurisation.

Similarly, with adsorption, kinetically smaller methane molecules will adsorb onto a surface less readily than ethane but also diffuse through a tortuous, nanoporous network more readily than ethane. Thus there is also an inherent molecular weight fractionation expected with depressurisation of a reservoir dependent on the balance between desorption and diffusive flow. The idea behind the present work is that the molecular and isotopic composition of produced gas may have fractionations that are characteristic of the various gas storage sites in the shale: macropores (no fractionation), nanopores or adsorbed. Monitoring gas composition during progressive gas production could thus yield information about the gas storage and production mechanisms that could not be gleaned from production rates alone.

The controlling factors on fractionation between stable carbon isotopes and molecular weight fractionation has been discussed broadly in the literature but often in terms of either

adsorption and storage processes or degassing trends (Fuex, 1980; Li et al., 2015; Lu et al., 1995; Strąpoć et al., 2006a; Wang et al., 2015a; Xia and Tang, 2012b). Desorption experiments in the literature typically tend to be canister desorption experiments from coals or shale cores, collecting samples in situ and measuring the desorbed gas at intervals during the degassing process (Jing et al., 2016; Lane et al., 1989b; Schettler et al., 1989a; Schettler and Parmoly, 1990a; Strąpoć et al., 2006a; X. Wang et al., 2015). Whilst this provides a fractionation trend of the degassed material and indicates the potential for using $\delta^{13}C$ and C_1-C_2 as geochemical indices for volume of gas extracted, there are several fundamental problems with this technique.

The starting volume of gas in place cannot be accurately calculated and is using done so by back calculations from the time of degassing. Some, unquantifiable volume of gas is lost during the coring process. Furthermore, as this gas is lost, the starting molecular weight and isotopic composition of the sample is unknown. A further factor that is intrinsic to degassing a whole shale sample is that shales are heterogenous in composition, pore size, permeability and maturity. The molecular weight and isotopic fractionation trends vary depending on the shale degassed; various influencing factors have been suggested including clay composition, pore size, permeability, organic matter type, distribution and maturity and water saturation shown in the schematic Figure 6Figure 6 |Schematic flow chart showing the factors that may influence molecular weight and isotopic fractionation that can be used as a geochemical index for total gas in place and volume of total gas extracted (recovery factor) (Cheng and Huang, 2004b; Cui et al., 2009; Heller and Zoback, 2014; Hu, 2014b; Liu et al., 2016; Tang et al., 2019).

1.7 Current methods for shale gas analysis: moving away from diffusion-desorption

Literature studies which focus on adsorption tend to consider the storage capacity of a shale, be this for CO_2 sequestration of attempting to calculate the initial gas in place (Ji et al., 2012;

Ross and Bustin, 2009a; Strąpoć et al., 2006a; Wang et al., 2015b; Zhang and Krooss, 2001b). There are extensive literature studies on the adsorption capacity of coals which formed the basis of shale gas canister desorption studies (Bustin and Clarkson, 1998b; Diamond and Schatzel, 1998; Estep et al., 2008; Smith et al., 1984a; Strąpoć et al., 2006a). Previous desorption experiments on coals highlight the importance of organic matter as sorption sights as well as initial lithotype (Krooss et al., 2010; Zapušek and Marsel, 1998)(Zapusek & Marsel, 1998, Strapoc et al. 2006, Kroos et al. 2010). Several of these experiments consider both CO_2 and methane adsorption, showing that CO_2 has a greater affinity to sorb onto organic surfaces than methane (Charriere et al. 2010). Coals however are significantly different to shales; coals contain upwards of 80% TOC whilst shales tend to contain between 2-5% TOC (Krooss et al., 2010). Shales contain other materials such as clay, siliciclastics and carbonates. The cleat-like pore geometries in the organic macerals of coals are not diagnostic of the slit and spherical pores in shales (Chareonsuppanimit et al., 2012b; Diamond, 1970; Diamond and Schatzel, 1998; Li et al., 2019b). Coal experiments may thus have some relevance for high TOC shales, but are by no means direct analogues.

The role of adsorption on gas storage capacity in shales is debated in the literature, as is the effects that adsorption-desorption processes have on the overall fractionation trends seen in production data (Ambrose et al., 2011c; Jing et al., 2016; Lane et al., 1989b; Liu et al., 2016a; Soroush et al., 2014). Some authors argue that clay minerals have capacity to store gas in the adsorbed state (Busch et al., 2009; Heller and Zoback, 2014a; Ji et al., 2012a; Kuila et al., 2014a). Swelling clays such as smectite and illite have a greater affinity to adsorbing CO_2 than non-swelling kaolinite. These studies do suggest that clays can adsorb less methane than CO_2.

Other studies, using desorption experiments, suggest that the dominant mechanism of isotopic fractionation relates to mass transport in shales; the small amount of organic matter present in shales compared to coals and the weak adsorption of shale gas onto organic matter

cannot account for the fractionation trends seen (Fuex, 1980; Javadpour et al., 2007; Xia and Tang, 2012b; Zhang and Krooss, 2001b).

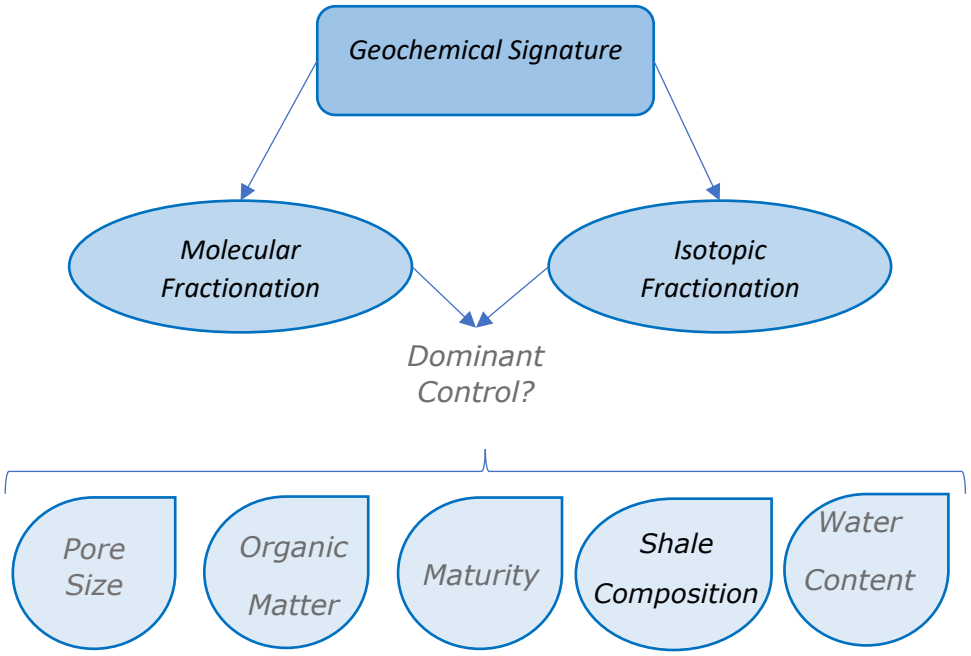


Figure 6 |Schematic flow chart showing the factors that may influence molecular weight and isotopic fractionation that can be used as a geochemical index for total gas in place and volume of total gas extracted (recovery factor).

In the flow chart in Figure 6, we aim to move away from directly relating the fractionation trends to desorption or diffusive processes but attempt to determine how different isolated components of a shale can influence the carbon isotope and molecular weight fractionation of a degassing shale and relate this directly back to the recovery factor (RF). Recovery factor relates to the proportion of gas that can be extracted from a shale relative to the total volume of gas stored. This will aid in decline curve analysis predications.

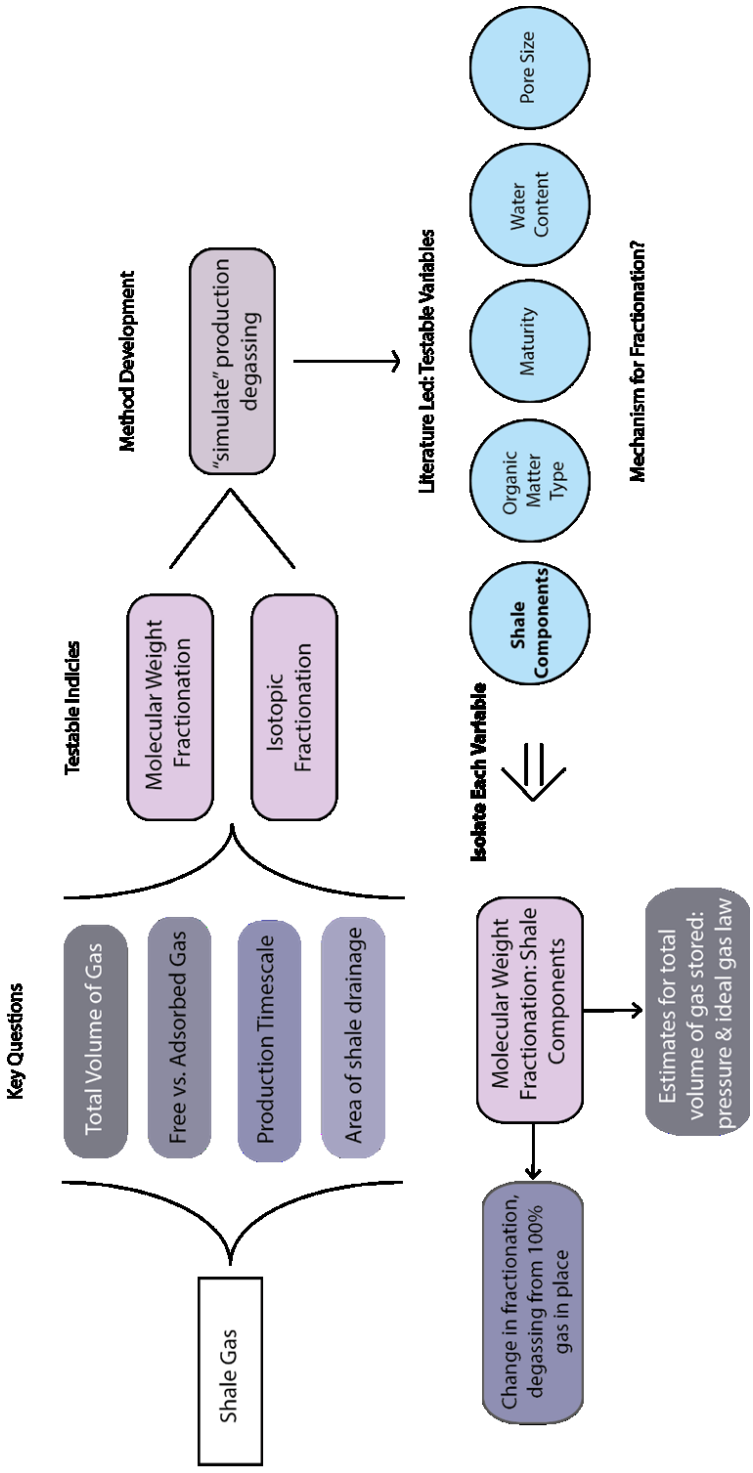


Figure 7| Key questions to be asked, this thesis focusses predominantly on calculating the percentage of the total volume of gas extracted and this can relate to production timescales. The data also consider the free vs. adsorbed gas and area of shale drainage. Change seen in the stable carbon isotope and molecular weight ratios relating to specific, testable shale heterogeneities allow for a universal method for degassing profiles to be generated.

1.7.1 Decline curve analysis

Decline curves refer to the time versus the volume of gas produced plots for shale wells or reservoirs. Accurate prediction of future production in shale gas wells, after the initial pulse of production, has proved difficult due to the complexities and uncertainties surrounding gas storage and transport mechanisms in unconventional reservoirs [Ambrose et al., 2011a]. Even with increased research into this area, empirical and numerical modelling methods remain the most popular for well production forecasting. The 1945 Arps analytical model uses a hyperbolic mathematical function based on existing production rate data to extrapolate future production (Arps and others, 1945). This resulting predicted decline curve is based on the assumption that the rate of production corresponds to a geometric curve shape.

In shales, initial production is dominated by a high flow of gas, typically attributed to free gas and gas residing in macropores and natural and induced fractures. Long term production however is generally at much lower gas rate but wells can continue flowing for decades. This long, low flow rate relates to how gas is stored within the shale itself and probably relates to the proportion of gas held in micro/nano pores that must diffuse to the well, and sorbed gas. Because of the number of parameters that may affect gas storage and flow coupled with the lack of understanding of the impact of each parameter (e.g mineralogy, maturity etc.), these decline curves are non-unique to specific shales and produce a generic forecast (Ambrose et al., 2011c). The fact that different gas storage and transport mechanisms dominate in the initial gas pulse and in the long production tail, it is very difficult to use an empirical decline curve fit to the early production data to predict later gas production behaviour.

1.7.2 The need for a new method

With the success of the shale gas revolution in the United States of America and the potential for energy security in the United Kingdom, there is real potential for shale gas to be the UK's

bridge between fossil fuels and carbon neutral energy (Levi, 2013b). For shale gas to be a success in the UK, there has to be a shift away from numerical and theoretical modelling to empirical, analytical observations that are based on the geochemical characteristics of a shale.

Whilst shales are characteristically complex, the gas stored within them is not, typically composed of over 90% methane, CO_2 and ethane making up the remaining fractions. The fact that there is inherent fractionation of the molecular components and isotopic components provides the foundations for a geochemical index. As the debate continues between the role of adsorption on gas storage capacity and the effects of desorption and diffusion on fractionation and rate of gas flow during the economically significant "tail-period" of the production decline curve, another, more simple and effective approach may yield information not only on the overall storage capacity of a shale but how the compositional characteristics of a shale control this inherent fractionation during degassing. The possibility of generating a geochemical index that can determine the recovery factor of a shale gas well during the first few months of production would influence how to make an economically successful well. Using the fundamental fractionation curves produced by isolated shale components, this method would be applied to shales of varying compositions.

1.7.3 Custom built sample cell – online measurements of adsorption, storage and change in gas geochemistry with volume of gas extracted.

To assess the utility of carbon isotope and molecular weight ratio measurements for understanding the life cycle of producing shale gas reservoirs, an online adsorption-desorption system was constructed. Unlike previous methods used in the literature, this custom-built cell allows for continuous, online measurement of the changing gas geochemistry measured from the extracted sample gas at set time intervals. Samples are degassed and cleaned prior to sampling and a gas of a known composition is introduced into the cell. This means that the

initial gas composition is known and deviations from the bulk gas reservoir geochemistry can be directly calculated with each gas extraction step. As the internal volumes of the sample are known, the volume of gas introduced to the sample can be calculated. The volume of gas at each extraction step can also be calculated. This means that a specific geochemical signature will relate to a percentage of the total gas extracted, ultimately generating a geochemical index related directly to the recovery factor of the component being tested.

Whilst the geochemical index is the primary tool, this method allows the exploration of the gas fractionation effects of mineralogy, pore size distribution and surface area. Would two clays of different compositions yet the same surface area produce the same fractionation curve? Does the Langmuir adsorption capacity of a material have a direct correlation with the magnitude in change of gas geochemistry from the bulk reservoir?

The main aim of this project is to understand how gas geochemistry changes with gas extraction, understanding how different variables of the shale reservoir unit can affect to resulting isotopic and molecular weight composition. The findings will provide insights into the shale gas decline curve and aid calculation of a shale's recovery factor in the initial stages of gas production.

1.8. Thesis Synopsis

This thesis will incorporate discuss the findings of isotopic fractionation of C^{12}-C^{13} and molecular weight fractionation of methane and ethane during sample degassing. The samples represent shale composition, organic matter content, organic matter type and artificial maturation of a type II kerogen shale. The aim of each chapter is to explore variables of a shale that may influence changing gas chemistry with depressurisation. Chapter 3 focuses on isotopic fractionation between C^{12}-C^{13} on isolated components that make up a shale; quartz and calcite, montmorillonite and kaolinite, and extracted kerogen. Chapter 4 focuses on the same isolated shale components but fractionation between C_1-C_2 with degassing. It became apparent that the organic material was by far the most influential variable on

changing gas geochemistry with sample depressurisation. This knowledge guided the direction of chapter 5 which focussed on C_1-C_2 fractionation during the depressurisation of shales with different kerogen types and volumes of organic material. Literature studies have pointed to maturation of organic matter as a key factor to consider in shale gas production as it may influence the shape, structure and pore volume of organic material (Chen and Xiao, 2014; Guo et al., 2017; Hu, 2014b; Tang et al., 2016). As the findings of the previous chapters suggested that organic matter has the greatest influence on changing gas geochemistry and literature studies suggested that maturation would influence gas storage, chapter 6 focusses on the artificial maturation of one kerogen type, type II kerogen, the most prolific shale gas source rock. Chapter 7 summarises the content of the preceding 4 data chapters and applies the results in context for a shale gas well.

2.0 Methodology

Interpretation of the geochemical signatures of hydrocarbon gases desorbed from shales can be used to understand important economic factors relating to shale gas extraction such as volume of gas initially in place, the percentage of total volume extracted and the remaining volume of gas. Several factors have been proposed to effect on gas storage and transport including;

- Composition of shale; amount and type of inorganic and organic constituents,
- Porosity, permeability and tortuosity of the matrix,
- Maturity of the organic matter,
- Surface area and pore volume,
- Water saturation.

Previous literature has reported on the isotopic and molecular weight characterisation of gases extracted from shales either through numerical modelling or the typical canister desorption experiments (Shabro et al., 2011; Strąpoć et al., 2006a; Xia and Tang, 2012b; Yin et al., 2017a; Zou and Rezaee, 2019b). Canister desorption experiments have relied on extracting shales from the subsurface and sealing them in an airtight canister with minimal dead volume. Aliquots of gas were extracted and sampled for changes in geochemical signatures with progressive degassing. Whilst the canister desorption method is useful, it is difficult to modify for different sample sizes and does not allow for on-line analysis of gases being desorbed. Furthermore, canister desorption experiments are expensive to conduct, requiring precise coring and extraction from the subsurface. The cores taken from the subsurface already contain hydrocarbon gases of unknown geochemical genesis and history. A number of questions are: has the gas undergone any microbial activity or post generational mixing, how has the kerogen type and maturity affected the initial gas geochemistry and if

there is water present in the core, how is this affecting the change in gas geochemistry with degassing. The uncertainties are numerous and the effects of shale composition on gas storage capacity and fractionation during desorption and pressure-driven gas flow cannot be accurately ascertained. To address these limitations, a custom-built sample cell was designed and built which allowed the injection of a gases of known isotopic or molecular weight values into a sorption chamber containing a sample of a known size and composition.

Whilst gas adsorption equilibria can be calculated using a number of methods, the cell built for these experiments used volumetric measurements to measure gas adsorption isotherms. The adsorption isotherms can be calculated by measuring the change in pressure in the cell during introduction of the sample gas to the sample material. The genesis of this type of experimental procedure began with studies on adsorption capacity of coal which looked at Langmuir isotherms generated from degassing coals (Bustin and Clarkson, 1998b; Clarkson and Bustin, 1999; Diamond and Schatzel, 1998). Experiments were derived to use isotopic and molecular weight fractionation from degassing highly organic rich and nanoporous coals to determine the original gas in place (Diamond and Schatzel, 1998). As the shale gas industry began to take off in the mid 2000s, these experimental procedures, thus far coal based, were transposed onto shale gas reservoirs.

The majority of these shale gas studies have focused on either solely gas desorption experiments or gas adsorption and storage. Those focused on gas desorption typically considered specific, whole shale samples from currently producing shale plays. This involved the costly process of extracting shale core in-situ from the subsurface and subsequently allowing the sample to naturally degas. Aliquots of gas extracted over time allowed the change in gas geochemistry to be measured. Those studies that focussed on adsorption experiments again tended to consider whole shale samples with a select few investigations which consider isolated components (Busch et al., 2009; Clarkson et al., 2013a; Heller and Zoback, 2014b; Xia

and Tang, 2012b; Zhang et al., 2012a; Zhang and Krooss, 2001b). There is yet to be a comprehensive study which isolates the online adsorption capacity of a shale based on individual variables such as mineralogy, TOC content, organic matter type, etc. which also considers desorption effects and gas transport mechanisms and how the change in gas geochemistry, based on these factors, can be used to predict the shale gas decline curve. Deconvolving the impact of isolated variables on both gas storage capacity (original volume of gas in place) and the speed and nature of shale degassing will aid greater economic assessment and shale gas well life cycle predictions and forecasting.

The experimental setup used in this work shares its foundations with the ubiquitous canister desorption experiments (Strąpoć et al., 2006a). Unlike the typical canister desorption experiments, the basis of my setup was to isolate individual shale parameters that might affect the geochemical signatures measured during degassing. As the same gas is injected into the sample material, the C_1-C_2(0) and the $^{13}C(0)$ is known. The only variable that is changed between experiments is the composition of the sample material and the effect of this on gas geochemistry can be isolated. The initial cell was designed and built as shown in Wright, 2019. This body of work is a combination of new method generation and development as well as active data collection.

2.1 Custom-built sample cell

The main purpose of the sample cell was to address the questions outlined above; i..e. how gas is stored and transported in shales and can change in the geochemical signatures of extracted gases be used to predict gas volumes. Once the limitations of existing methods outlined in literature were explored, examples of this include canister desorption experiments, the cell was designed, built and tested. As part of this body of work, a second iteration of the cell was developed, dramatically reducing the dead volume and increasing the signal to noise

ratio of the results. A comparative schematic of the two cells is shown in Figure 8b and 9a respectively.



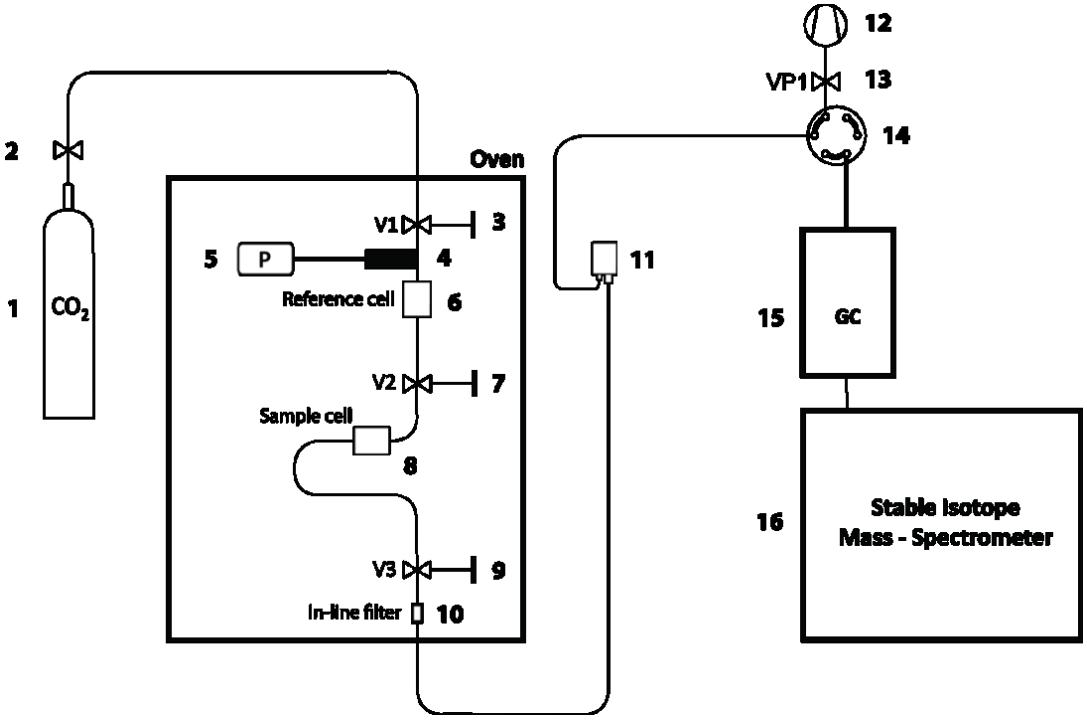
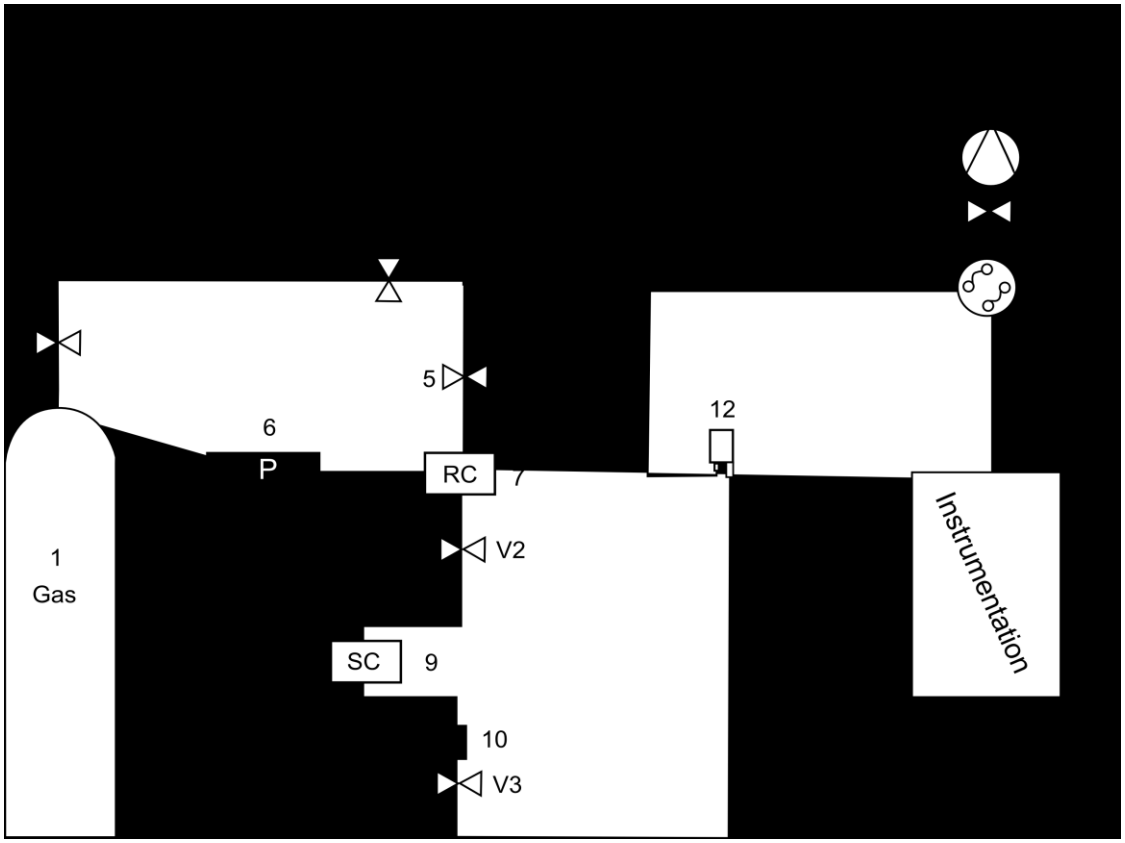


Figure 8 | Custom built sample cell in the oven, attached to the Gas chromatographer – combustion – isotope ratio mass spectrometer. Figure 8b| Schematic diagram of the sample cell set up. Part 1, the gas bottle in interchangeable, as are parts 15 and 16 which link the sample cell to the instrumentation. The corresponding component parts are outlined in Table 1.

Table 1 | Numbered components of the schematic sample cell in Figure 8 | Custom built sample cell in the oven, attached to the Gas chromatographer – combustion – isotope ratio mass spectrometer. Figure 8b| Schematic diagram of the sample cell set up. Part 1, the gas bottle in interchangeable, as are parts 15 and 16 which link the sample cell to the instrumentation. The corresponding component parts are outlined in Table 1.

Part Number	Name description
1	V-size gas cylinder (e.g. CH_4)
2	Cylinder regulator
3	On-Off valve
4	Pressure Transducer PDCR 5021
5	Digital Process Indicator, IDL-INT2-L
6	Stainless steel reference cell
7	On-off valve
8	Stainless steel sample cell
9	On-off valve
10	SS in-line filter, 2µm
11	On-off valve
12	Vacuum pump
13	Diaphragm-sealed valve
14	Valco Vici 6=way valve, 1/16” fitting
15	Gas Chromatograph
16	Isotope Ratio Mass Spectrometer (Finnigan MAT 252)



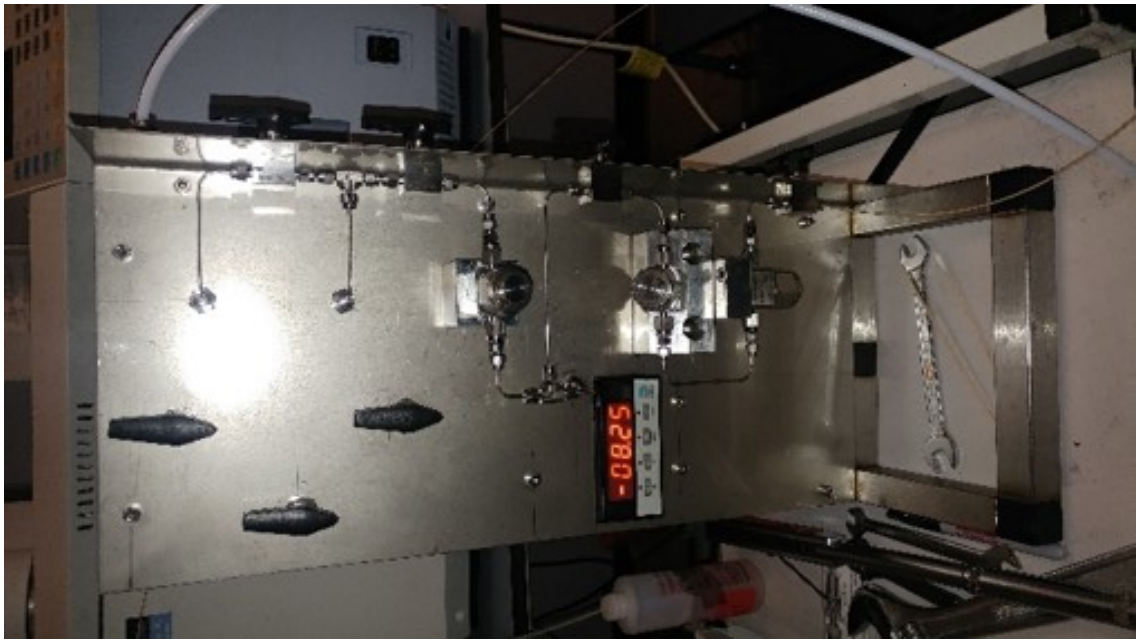


Figure 9| Schematic diagram (10q) and photograph of the second-generation sample cell (9b). the cell has a much smaller dead volume using 1/16" instead of 1/8" tubing throughout, smaller valves with less associated dead volume, a secondary vacuum line and an inbuilt pressure transducer.

Table 2| Key cell component volumes

Cell Component	Volume (cm^3)
Reference Cell (V1-V2)	8.52
Sample Container Cell	11.5
Cell Volume	20.02
Sample Cylinder	1.0

2.1.1 Cell Development

The initial phase of sample testing was carried out on the original cell Figure 8, the results of which are reported in chapters 3 and 4 and include results focusing on the pure minerals. The cell development was an iterative process; it became apparent after the initial testing phase that several key areas could be improved. The second generation of the sample cell setup in Figure 9 saw a significant reduction in the dead volume. Further adaptation included the addition of a more effective vacuum setup. To ensure that the cell was fully sealed prior to experimentation, the cell had to be taken to minimum vacuum capacity and calibrated at -14.75 psi. Only then were the valves sealed. Stable pressure at this point indicated the cell was sealed and the sample could be taken to vacuum for 12 hours.

Initially the vacuum was achieved by extracting air through the narrow 1/16" poly ether ether keyone (PEEK®) tubing, taking approximately 2 hours to fully evacuate the cell. By fitting an extra valve at the top of the cell in 1/8” tubing and attaching another vacuum line, the cell could be fully evacuated in less than a minute. Not only did this significantly reduce the experimental setup and preparation time but it also allowed for rapid assessment of any leaks in the system. By taking the cell to full vacuum in such a short time frame, V1-V3 could be sealed and the pressure stability measured. An increase in pressure towards 0 psi from -14.75 psi is indicative of a leak. If a leak was measured, the sample cell would be flooded with He

gas and tested with SNOOP©. SNOOP© produces bubbles when gas is escaping from a valve or fitting which would allow quick isolation of the faulty part of the setup.

The second issue addressed in the second generation of the cell was heating. Figure 8shows the cell residing in a large oven. The oven had to be sealed in order to heat up and reach 109°C however, the vacuum line could not be attached to the cell during heating. Whilst this meant that the cell could be heated up to evaporate any water, there was no vacuum ensuring that any residual water was removed. To address this issue in the second-generation cell, a Proheat ® Varitemp heat gun was purchased and the cell redesigned to sit outside the oven. This also allowed the pressure transducer to be built into the cell wall. Having the pressure transducer stable and in the same place throughout all experiments is preferable conditions over having to detach and re-attach after each heating cycle. Without the constraints of an oven, the metal cell components could be heated with 500°C heat whilst also under vacuum. The PEEK® components could be heated separately to 109°C to ensure that the tubes did not melt and distort. Being under vacuum whilst heated ensured removal of water and volatiles from the new cell.

A further change to the cell was switching from large stainless steel on-off valves, originally chosen to withstand high pressures and temperatures if the cell was taken to reservoir conditions to Valco Vici 0-10 ml combo needle valves which have a reduced dead volume.

2.1.2 Sample cell design and components

The original cell design was to provide quantitative analysis of the change in gas geochemistry with “reservoir” degassing. The total volume of injected, initial gas composition, change in gas composition and volume of gas extracted with each extraction step had to be calculable. A consequence of this setup was that online measurements of gas adsorption capacity of a material and desorption isotherms were also calculable. Design of the cell had to

facilitate quantification of the volume of gas introduced to the sample, volume of gas extracted with each extraction step and the molecular weight and isotopic composition of the sample gas. The ability to calculate adsorption capacity was a function of both the original and second generation cell.

The total volume of the two cells were calculated using water volumetric apparatus where water was injected from the base of the cell to the top valve. The whole volume of the initial cell was 32.08 cm^3 whilst the second iteration was 20.03 cm^3. This volume is between V1 and V3 in Figure 8.

The volume of the sample-containing section of the cell was calculated by dismantling the whole cell and injection water into the sample section only. In this way, the volume of the cell was calculated to be 8.52 cm^3. One of the benefits of this system is that it is modular and the reference and sample volumes can be easily modified in line with future testing. The total initial volume of gas injected into the cell could be calculated via gas injection into the reference cell which is connected to a pressure transducer. The internal volume of the reference cell was known, by rearranging the ideal gas law;

$$PV = nRT$$

Where P is pressure in pascals, V is volume in m^3, n is the number of moles, T is temperature in Kelvin and R is the ideal gas constant. R is defined as 8.314 J/(K/mol).

In the second-generation cell, Figure 9 , the reference cell, sample cell and filters were connected by 1/16" (i.d) stainless steel tubing. The whole cell unit was connected to the 6-way Valco injection valve by 1m of 1/16” (inside diameter, i.d.) PEEK® tubing. The cell contained a sample container which used the cylindrical the H600R T-Type filter to hold the sample. The sample holder had an internal volume of 10 cm^3 of material. Within this sample holder, a

custom-made stainless-steel dish of 3 mm depth could be inserted to cap the sample, stopping spillages and reducing the dead volume. The H600R T-Type filter was sealed with a silver O-ring. Valve 1 (part 5) connected the sample cell to the vacuum pump. Valves 2 and 3, (parts 8 and 11 respectively), allowed for controlled injection of gases. For carbon isotope fractionation tests conducted on the Gas Chromatography - Combustion - Isotope Ratio Mass Spectrometer (GC-C-IRMS), methane gas was connected to valve 2 (part 8). For molecular weight experiments, a small gas cylinder containing a mixture of methane and ethane (CH_4 and C_2H_6), made within the Imperial College laboratory was connected. Valve 3 (part 10) was connected to He gas. Experiments that were trialled but not included in this body of work used He gas to flush the cell and attempt to remove all residual sample gas. However, as the introduction of He gas altered the cell pressure and the molar volume of the sample gas is measured using pressure via the ideal gas law, these experiments were counterproductive to the ultimate aim of this work.

Valve 1, valve 2 and valve 3 - components 5, 8 and 11 respectively - were used to isolate sections of the cell. Between valves 1 and 2 is the pressure transducer and the reference cell. This set up meant that the molar volume of gas introduced into the reference cell could be calculated. When valve 2 was opened and valves 1 and 3 were closed, the sample gas was then exposed to the material sample in the sample cell. The H600R in-line filler, component 10, was situated between the sample cell and the instrumentation. The filter prevented particle greater than 2 μm reaching and possibly blocking the sample loop (component 13b) or damaging either the GC-C-IRMS or the GC-FID.

Fundamentally, creating a system that has no leaks is difficult, time-consuming and expensive. The experimental setup was designed so that experiments last for at most 6 hours. The cell had to be leak-proof only for this amount of time. Furthermore, the experiments were carried out at relatively low pressures, typically no more than 50 psi. Working at this lower

pressure also reduced the likelihood of leaks and inaccurate measurements. In order to leak-test the cell, 70 psi of He gas was injected into the sample cell between the 6-way valve (component 13a) and the first valve connected the vacuum to the cell (valve 1, component 5). During a leak test, measurements were taken every hour for 12 hours then left for a further 12 hours. Most leak tests showed that the cell was leak-proof at these moderate pressures for several hours longer than the required experimentation time. Leak tests were conducted after any alteration to the cell and after every 10th experiment. Between each sample run, as a quick and simple check to ensure the robustness of the seal, the cell was taken to full vacuum and then sealed off between component 3 and the sample loop, component 13b. If pressure remained at full vacuum after an hour, the seal was considered fully effective for the time scale required.

2.2 GC-C-IRMS: Precision, accuracy and quality control

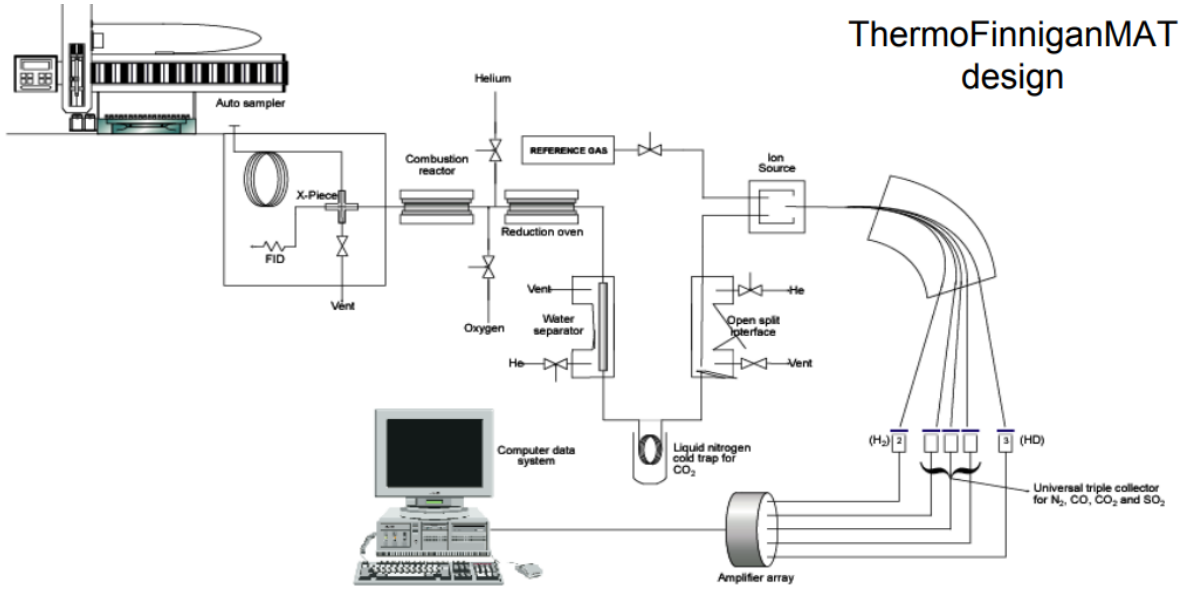


Figure 10 | Schematic diagram of a GC-C-IRMS Matt Finnigan operating system. The sample gas passes through the oxidation furnace, is separated out through the GC and then combusted into CO_2 in the combustion chamber. The CO_2 is then carried via He carrier gas into the IRMS where the isotopes are flung round a convex system causing separation into isotopic species which are captured in the Faraday cups. (Pancost and Bull, 2014)

GC-C-IRMS (Gas Chromatography-Combustion-Isotope Ratio Mass Spectrometer - shown in the Figure 10) is the world standard instrumental method used to for determining the relative ratio of the light stable isotopes of H/D, $^{12}C/\ ^{13}C$, $^{15}N/^{14}N$, $^{18}O/^{16}O$ for individual compounds (Carter and Barwick, 2011). The experimental procedure in this report focuses solely on carbon isotope fractionation between ^{13}C and ^{12}C. There is a substantial variation in the ratio between ^{13}C and ^{12}C in nature due to how the isotopes behave in various chemical and physical (and biological) processes. Because of this natural variation, isotopic ratios can be used to understand important processes both in the natural and human world. The simple equation outlining this is shown below:

$$\delta^{13}C(\text{h}) = [R_{sample} - R_{standard}]/R_{standard} * 10^3$$

$R_{standard}$ comes from VPDB (Vienna Peedee Belemnite) universal standard of 0.0112372 (Coplen, 1994). The GC component of the setup separates organic compounds which are then combusted into CO_2 and N_2. Whilst both C and O isotopes can be measured, the O isotopes are considered only as a means of testing the rigour of the oxidation furnace. The methane used in the IRMS experiments is combusted into CO_2 which is carried using He as a carried gas into the IRMS for isotopic analysis. This is shown in the schematic diagram (Figure 10).

The sample gas is introduced into the inlet via the autosampler. The gas flows through the gas chromatography column, carried by He. The GC column has a polimide coating, a fused silica wall and a stationary phase lining. The sample gas is separated into compounds based on how they interact with the stationary phase of the column; each compound elutes at a separate time.

Carbon eluting from the chromatography column is then combusted as it passes through a combustion reactor. It is important not to introduce too much carbon-containing gas into the combustion furnace as this can cause saturation and inhibit the oxidizing ability of the furnace. Prior to sampling, the combustion rector must be heated to 940° C, this oxidises the combustion furnace and maintains its oxidising capacity of the organic compounds passing through. Prior to use, the furnace is oxidised for half an hour. After this, a further two hours is given to allow the high volumes of thermally desorbed O_2 to be removed by flow of the He carrier gas. The combustion furnace converts organic compounds such as methane into CO_2 and H_2O and is composed of an aluminium housing case which contains 0.3 mm thick wires of copper, platinum and nickel.

The combusted gas will then travel through a Nafion membrane. This removes any residual water from the sample gas. This membrane is fine so must be kept clean. The membrane must be checked for signs of wear and replaced every year or so depending on volume of usage. Once water has been removed, the sample can be introduced to the ion source of the mass spectrometer by an open split interface. The carbon sample gas is then ionised using electron ionisation. Once ionised, the gas is fired through the ion source and flung at speed round a bend in the instrument setup. The different speeds at which the isotopes move cause them to separate and be detected individually by the array of Faraday cups. The signal is then amplified and calculated relative to the PDB standard and is reported by the IRMS software as "per mil", thus is dimensionless.

The mass range is between 1-150 dalton at 10 kb and the absolute sensitivity of the instrument between mass 44 and mass 45 (^{12}C and ^{13}C) is less than $2*10^{-6}$. To test the precision and accuracy of the instrument, test runs of the sample CO_2 gas were carried out twice daily, once prior to experimentation and once immediately following. It is shown in Figure 11 that the IRMS is capable of measuring the $\delta\ ^{13}C$ ratio of the reference gas with high accuracy and good reproducibility.

The GC-C-IRMS measures high precision stable isotope ratios. Modern day IRMS analysis using the Finnigan Mat 252 can measure isotopic ratio variations with an uncertainty of less than 0.02‰. In practice, the accuracy of the instrument used is shown in Figure 11. To test the accuracy and precision of the instrument, tests termed "long-on offs" are conducted. Long-on offs measures the sample gas directly injected from the reference gas into the GC-C-IRMS, not passing through the sample cell.

Figure 11 shows that data spread of a single run (either green or pink) deviates between -0.02 and +0.06 ‰ from the known baseline composition. The precision is shown between the

two runs, green and pink, which show that the data points overlie one another. Considering the interquartile ranges, the spread of data falls between -0.1 and +0.04 ‰ giving a working accuracy of -0.05 ‰.

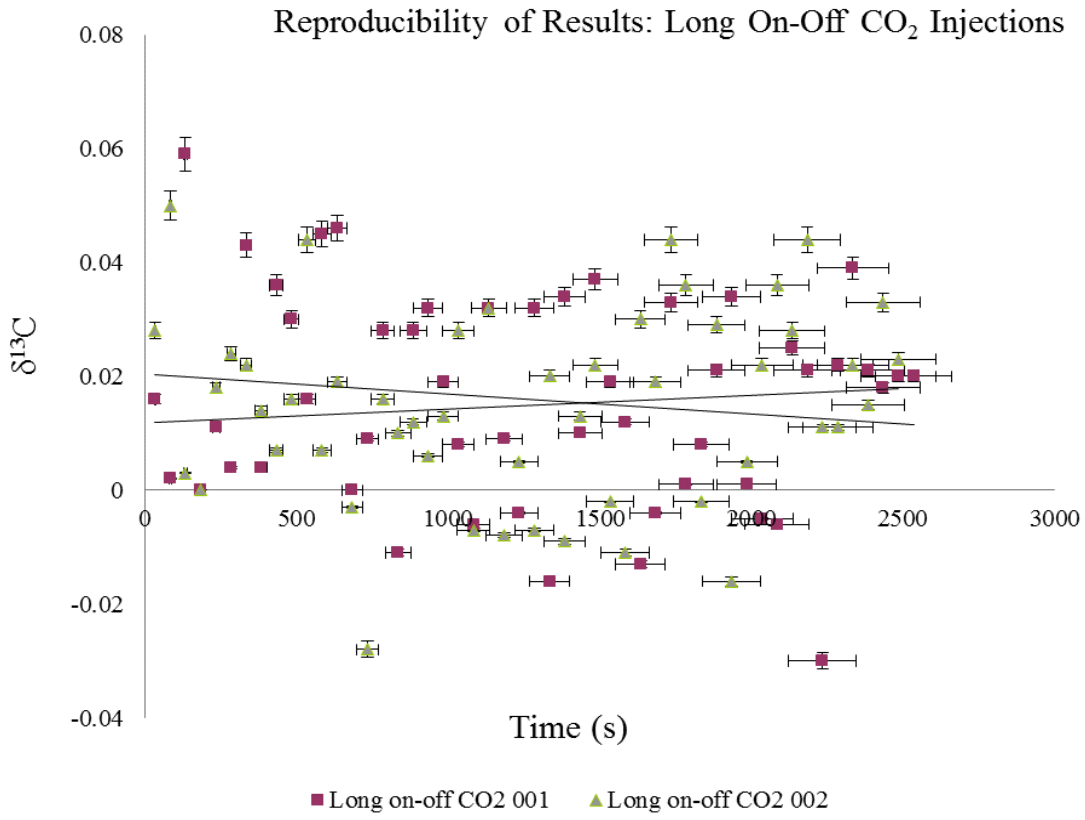


Figure 11 | Reproducibility of the reference gas data measured by the GC-C-IRMS. Carbon dioxide is injected into the GC-C-IRMS at 40 second intervals. The instrument measures the ratio between ^{12}C and ^{13}C. This test is repeated twice daily, once prior to experimentation and once afterwards. The two sample runs lie almost directly on top of one another and both runs plot between -0.03 and 0.06 with 0 being the actual isotopic ratio of the gas.

Considering the precision and accuracy of the isotope data through the 6-way valve (component 13 in Figure 8). Figure 12 shows the raw data for measurements of the sample gas CH_4. The spread of data is greater than that of the reference gas, falling +0.05 and -0.06‰, giving a working accuracy of 0.11‰.

By injecting the gas with a known composition, it is possible to test the ability of the instrument to provide the same isotopic ratio with each injection. Standard deviation calculations of all of the values measured give a range of accuracy for gas measurements in a

single run. Figure 11 shows the carbon isotope values measured for tow test runs. It is evident visually that the precision between runs is good. By comparing the standard deviation of the gas tested in a single run against several runs, it is possible to get a working accuracy of the instrument of 0.11‰.

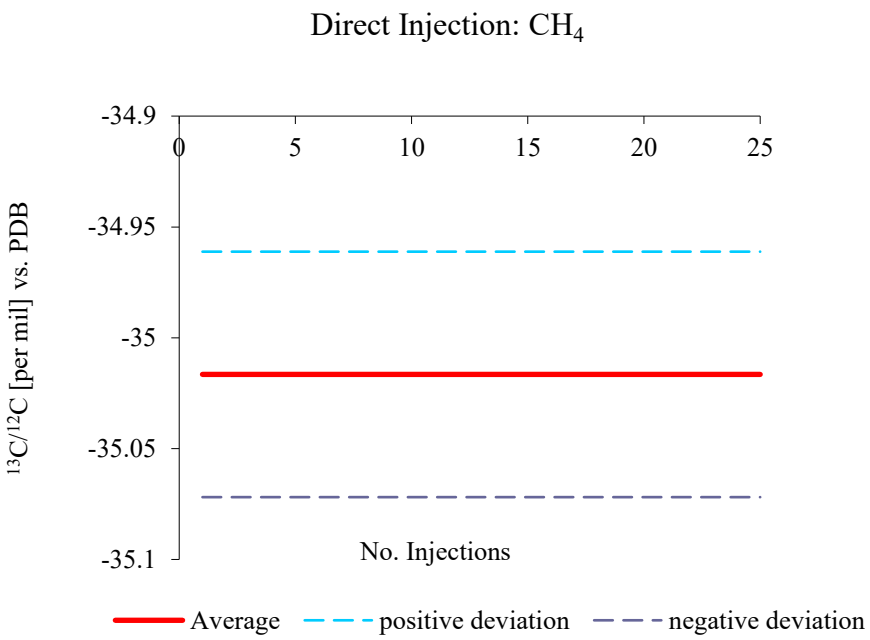


Figure 12| Direct injection data collected for 25 gas injections with the maximum deviations above and below the average $\delta^{13}C$ measured shows a lower level of accuracy than the long on-off data.

2.3 Method Development: GC-C-IRMS

The experimental procedure for this sample cell coupled with GC-C-IRMS had not been fully finalised or implemented prior to the start of this research. As such, the initial few months focused on developing a method that would allow as much gas to be extracted from the cell within the sensitivity range of the GC-C-IRMS. The initial experimental setup involved introduction of the sample gas into the reference chamber, expanding this known volume into the reference cell and allowing for equilibration. Once the sample gas had equilibrated with the solid sample material, the gas was expanded into the PEEK® tubing, there being a continuous connection of gas from V1 to the 6-way sample loop. Two major problems were associated

with the method. Firstly, the measured gas intensity would build up throughout the experiment and would typically cause an over-loading of the IRMS prior to the end of even the shorter, 3 hour long experiments. As the experiments would overload the instrument prior to the end of the experimental period, large volumes of gas would end up being retained within the sample cell, over 50% of the gas still being trapped within the cell. A further limitation of this method was that the gas was being continuously sampled at 3minute increments and could only be sampled once. There was no way to complete repeated samples on the same increment of gas extracted to test the reproducibility of the results during the experiment. To address these issues, a new method was developed and implemented which is as follows:

1. Cell evacuated to full vacuum, here calibrated to -14.75 psi
2. Heated the cell, whilst on the vacuum, through directed heat from Proheat R Varitemp heat gun 250ºC on stainless steel and 105ºC for PEEK® tubing to remove water
3. Whilst the cell was evacuating, cleaned sample container - the inner cylinder of the H600 T-type inline filter - with dichloromethane, methanol then water to remove any contaminants, particularly organic matter
4. Left sample container in oven at 109ºC for an hour to dry
5. Tested samples kept in either drying box if organic or contain bound water as part of its chemical structure or in oven at 109◦C to discourage background water adsorption
6. Once sample holder had been heated through and allowed to cool, the sample was loaded into the container using a clean stainless-steel spatula and weighed using a balance capable of measuring up to 0.0001 g
7. Inserted stainless steel lid at 3 mm depth to sample container and compress using a pellet maker to 0.2 tonnes

8. Loaded sample chamber into the cell and seal filter with a silver O-ring and torque wrench
9. Evacuated cell for ~15 minutes
10. Closed valves 1-2 and check for changes in pressure
11. Repeated for valves 1-3, after 15 minutes the cell should be under full vacuum and pressure should remain stable if no leak is present
12. Any change in pressure meant the sample must be unloaded, the O-ring replaced and the In-line filter cleaned
13. Once fully sealed, the sample was left under vacuum for 24 hours to ensure that all residual gas had been removed from the system
14. Injected gas, either pure methane for stable carbon isotope analysis or CH_4-C_2H_6 mixture into the reference cell
15. Recorded the pressure, as the volume of the reference cell is known, the volume and mass of gas in this chamber can thus be calculated
16. After 5 minutes equilibration time in the reference chamber, the gas was expanded into the sample chamber
17. Recorded the immediate drop in pressure at time 0 ($t_{(0)}$) then at 5 second intervals for the first 2 minutes, then every 30 seconds for 5 minutes and every minute up to 10 minutes
18. After 10 minutes, the sample was then left to fully equilibrate with the sample gas, typically this took around an hour however, the equilibration period was often increased 3-4 hours to ensure that the pressure had completely stabilised

19. During this equilibration period, maintenance and calibration of the IRMS was carried out

    a Three long on-off experiments were carried out, each lasting 45 minutes. The CO_2 reference gas was injected into the IRMS at 2-minute intervals. The data collected from this can be used to ensure that the instrument is taking accurate measurements

    b The oxidation furnace was engaged for ~30 minutes, this ensures rapid conversion of organic material to CO_2 and allows laminar flow into the GC-C-IRMS

    c Peak centres were run on mass 44, 46 and 45 whilst the reference gas was carried through the IRMS, checking for a narrow peak with no shoulders. A broad peak suggests inaccurate measurement on the masses whilst the presence of a shoulder indicates the presence of air (a leak) in the system

20. Gas was then expanded into the PEEK® tubing, between the sample container and valve 12 in Figure 8.

21. Valve 3 was then closed and the gas allowed to equilibrate in the PEEK® tubing for 2 minutes

22. The gas was then injected 5 times into the GC-C-IRMS or 3 times into the GC-FID using the 6-way valve

23. The 6-way valve was opened for 5 seconds to allow the gas to enter the sample loop (10 μm for the GC-FID and 2 μm for the GC-C-IRMS) and pass into the instrument

24. Once the gas has been tested either 5 or 3 times, valve labelled 14 in Figure 10 was opened and the PEEK® tubing is evacuated through the vacuum valve

25. This process was repeated over 3-6 hours depending on the sample and the instrumentation- some samples evacuate gas rapidly, others were able to continue degassing until the end of the experimental procedure

Once the experiment had ended, the sample container was removed, and the sample material returned to the oven or drying box. The container was cleaned as described in the steps above. The sample container fitting was also cleaned using a laboratory grade cotton bud to remove any material that had come loose from the sample container. This was done initially with a water-wet bud and then again with a DCM-wet bud. The O-ring seal was cleaned in a similar manner.

The data collected from this experimental procedure is shown on the IsoData Acquisition data interface and is shown in Figure 13. The first three peaks are measurements of the CO_2 reference gas. One of these peaks is chosen as the baseline "0" at which the other peaks are measured against. The deviation of the remaining CO_2 peaks can be used to determine if the instrument is running correctly. In the example shown in Figure 13, the reference peak to which all the other peaks are measured is the second of the three CO_2 peaks. The final CO_2 peak has a 0.06‰ variation between itself and the reference peak, indicating the working level of accuracy attained in this particular run. The 11 clusters of blue peaks indicate the 11 gas extraction steps associated with this experiment with each step being measured between 4 and 8 times. The 9th cluster has several peaks which saturated the detector (intensity over 7000 mV), This particular example coincides with the injection of helium into the sample cell in an attempt to flush out the remaining gas. The peak heights give the intensity in mV registered by the instrument but cannot be used to calculate the exact volume of gas injected at each step.

Ideally, the peaks should be at a similar height as there can be a shift in the linearity of the measurements between the lowest and highest working ranges of the instrument. Peaks that are >1000 mV higher than the others in a gas extraction step tend to produce a slightly different $\delta^{13}C$ value and are often discounted from further analysis.

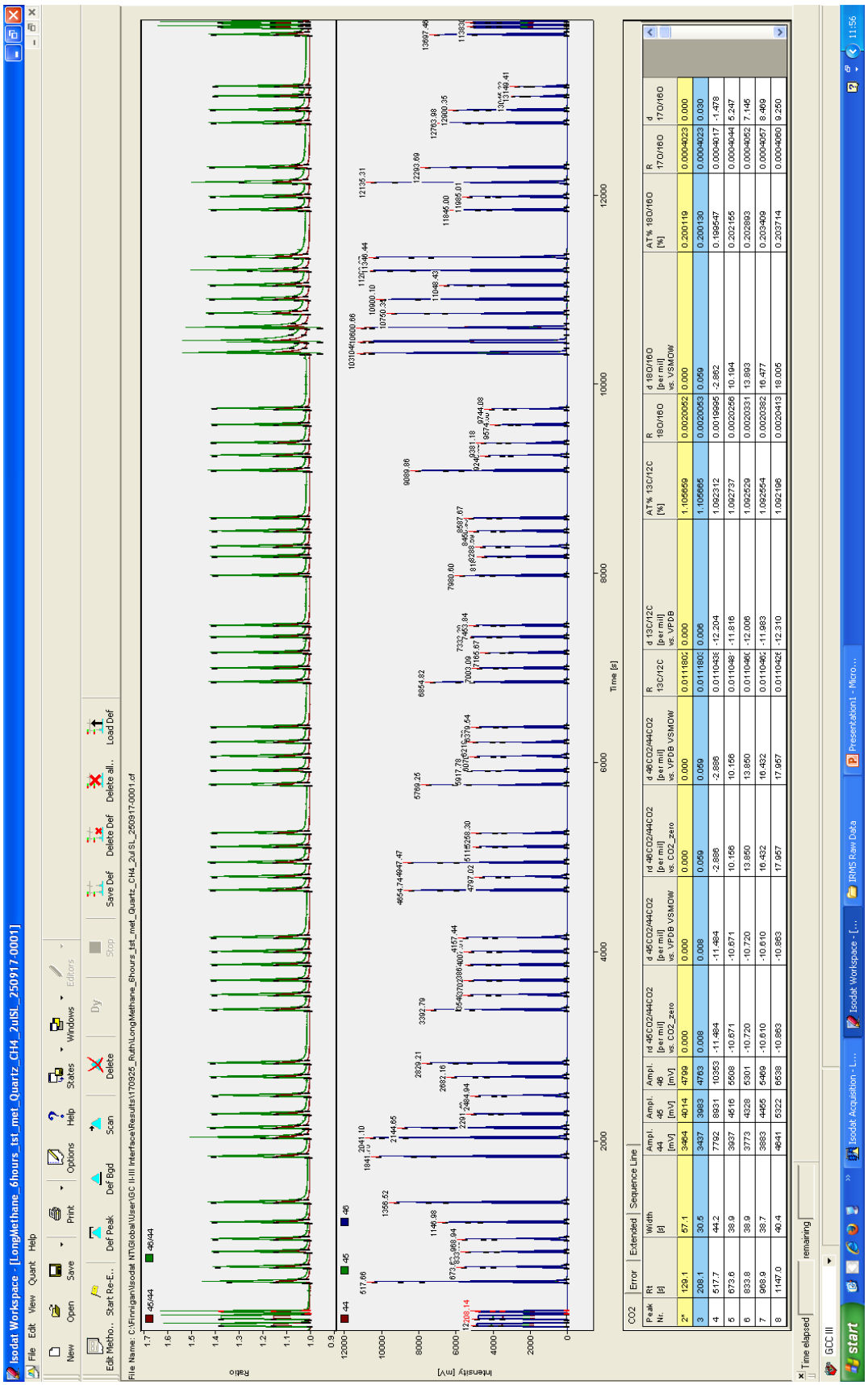


Figure 13| an example of the IsoDat Workspace interface when displayed on a Windows computer. The upper peaks (green and red) show the measured peak ratios between mass 45 CO_2 and mass 44 CO_2. The lower graphic section shows the intensity of each peak (in blue). The lowermost section is a table of the data recorded for each peak,

2.3.1 Method development: GC-FID

The GC-FID analysis gives a compositional overview of an organic compounds being analysed. Gas mixtures are separated out into different compounds whilst passing through the GC column. Individual gases within a gas mixture will elute out of the chromatography column at differing rates. Once the gas has travelled through the column and eluted out, they then pass through and are incinerated by a hydrogen flame. The hydrogen flame ionises these organic hydrocarbon gas molecules. This produces electrically charged particles which generate an electrical signal which is then measured by the instrument. The ionizing detector counts the number of ions that are generating during this incineration. The GC-FID system works on principle that hydrocarbons have molar response factors that are equal to the number of carbon atoms in their molecule; methane having only one carbon per four hydrogen molecules will produce a different electrical signature to ethane with two carbon molecules for every six hydrogen molecules (Sevcik, 2011). The FID method has a low efficiency, only 1 in 100,000 carbon ions will produce an ion that is measured. This is not a issue with this experimental setup - the relative proportion of each gas species tested is the variable being measured. The exact amount of gas that has been extracted is accounted for in the experimental setup of the sample cell.

The GC-FID instrument allows for calculation of the relative proportion of methane to ethane gas in each gas injection. The raw results show the intensity in mV of each gas species. The relative proportion of this cannot be used directly to calculate the exact volume of gas that has been injected into the instrument. Instead, as the sample cell in on-line i.e. connected to a pressure transducer, the change in pressure with each gas extraction step can be measured. As the initial molar volume of gas in the system is calculated at time 0, the incremental volumes of gas extracted can be calculated. The relative proportion of methane to ethane measured by

the GC-FID coupled with the exact molar volume of gas extracted at each step can be used to determine the molar volume of each species.

The main limitation of this technique comes from ensuring that the sample cell is entirely sealed and that there are no leaks. With several movable parts that require cleaning and replacing, the area of highest leak risk was associated with the sample container. Sealed with a silver O-ring and a torque wrench, the sample container had to be removed from the cell and cleaned prior to each experiment. Every experiment had potential for failure based on leaks. In order to reduce the likelihood of this, firstly a torque wrench was used to tightly seal the sample container. Secondly, to ensure that a leak was determined straight away, the method was altered to include helium injection. Helium gas was injected to 50 psi (20 psi greater than the typical working pressure of the instrument) and left to equilibrium in the cell. Any drop in pressure over the length of the experimental time span was indicative of a leak. SNOOP liquid was used to determine the location of any leaks.

Another limitation of this technique comes in the form of gas sampling. Testing the change in C_1-C_2 ratio in an empty cell allowed for calculation of any inherent fractionation within the cell. Measuring the change in gas composition with continued gas extraction was also simple. What could not be tested was the gas composition of the equilibrated gas reservoir. The initial composition of the gas was known through direct injection into the GC-FID and the composition of the first gas pulse extracted from the reservoir was measurable but this does not reflect the nature of the equilibrated gas reservoir unless the only material being extracted is free gas. It is not possible to use simple pressure gradients within the cell to extract all the gas and often ~20% of the gas is trapped as residual gas within the sample. As a result, the final composition of the gas in unknown. This means that material balance calculations are required to try and predict the starting and ending values of the gas reservoir. This is similar to issues

seem in standard off-line canister desorption experiments and there are several studies of back-calculation to the starting gas composition.

For future work, it would be useful to include a way of sampling the gas once it has equilibrated with the chosen sample. Not only would it allow for correct calculation of the change in gas composition through material balance equations but it would also show whether there is any gas fractionation attributed to the gas extracted in the initial gas pulse. Based on production data that is open-source, the initial gas pulse is often attributed purely to free gas. By including a step to measure the equilibrated gas in the sample chamber alongside the first gas pulse, this would determine whether only free gas was indeed being extracted in the initial phases.

As this thesis dealt initially with the first and second stages of the method development and building the new cell, this limitation must be addressed in future work.

2.4 Method: Sample Preparation

2.4.1 Laboratory Samples

The initial aim of this thesis, after method development and cell design, was to isolate and test individual shale components to measure the changes in gas geochemistry with isolated variables. In order to test the compositional changes, samples purchased from online laboratory retailers were used. This includes kaolinite, montmorillonite, calcite, quartz and anthracite. Isolated kerogens were also tested by these cannot be purchased and had to be extracted from whole shales - a procedure that will be outlined later in this body of work.

Laboratory Sample Sourcing

The clay samples collected were purchased from the Clay Minerals Society. The montmorillonite sample is referenced Srce_Clay_SWy-3 and is Na-rich Montmorillonite and

was sourced in Crook County, Wyoming, USA. The Kaolinite sample is referenced Srce_Clay_KGa-1b and was sourced from Warren County, Georgia, USA. The quartz beads (SiO_2) of <250 μm were purchased from Sigma Aldrich. These silica beads are uniform in size and represent inorganic grains of sand that are present in more siliceous shales. Calcium carbonate powder, representing grains of calcite were also purchased from Sigma Aldrich. The $CaCO_3$ has a purity value of 98-100%.

Laboratory Sample Preparation

The quartz, calcite and kaolinite contain no bound interstitial water and exposure to relatively low temperatures (<150ºC) will not cause irreversible, chemical changes to the samples. They can also be washed in water without changing their chemical compositions. As such, these three samples were cleaned using hydrogen peroxide diluted to 35% to remove any surface impurities. The samples were then baked at 110ºC to remove any surface water. Once dry, the samples were stored in a drying box, kept at 35ºC to inhibit surface water reabsorption. Montmorillonite contains interstitial water and thus baking the sample at temperatures exceeding 100ºC would alter the chemical composition of the sample.

2.4.2 Shale Samples

Some of the samples used in this thesis were collected by Dr Miriam Wright and Dr Alexandra Sarney in 2012 as part of two separate theses. These samples are the Eagle Ford Shale samples, collected from outcrops in the San Antonio Canyon, Texas, USA. Other samples came from sites across the United Kingdom including the West Lothian Shale (Edinburgh, Scotland), Kimmeridge Clay (Kimmeridge Bay, Dorset), Bowland Shale (Mam Tor, Derbyshire) and the Oxford Clay (Osmington Mills, Dorset, United Kingdom).

The samples were collected for a series of bodies of work and were gifted to this thesis. The samples were stored wrapped in tin foil, labelled and kept inside polypropylene bags. All of the samples were stored in clip boxes, in an air-conditioned lab and away from direct sunlight and extreme temperatures. As such, there was no change to the in-situ compositional or geochemical make-up of the samples.

The West Lothian Shales were taken from the Midland Valley in Scotland and are Carboniferous in age. An anoxic tropical lake in the large rift system between the Highland Boundary and the Southern Upland faults facilitated the deposition of anoxic lacustrine shales (Follows and Tyson, 1998). The Kimmeridge Clay is a prolific marine source rock which was deposited in the Upper Jurassic with significant bottom water anoxia and widespread deposition of organic rich marine mudstone (Fishman et al., 2012; Macquaker and Gawthorpe, 1993). The Oxford Clay is another prolific Upper Jurassic (Callovian) marine mudstone, deposited in periodically mildly oxygenated to entirely anoxic conditions (Morris, 1980). The Bowland Shale Formation is series of marine mudstone and near-shore turbidite facies. The turbidite facies typically have a low Hydrogen Index (HI) which correlates to type II-III and type III kerogen. Biomarker evidence from Bowland Shale samples indicate that at high stand systems tracts (HST) there is a distinct reduction in the levels of salinity as well as a dominant supply of land-plants and terrestrial organic material to the TOC content (Gross et al., 2015).

These samples were chosen as they represent three different kerogen types, type I lacustrine, type II marine algal and type III, terrestrial material (Hunt, 1995). They are also similar levels of maturity, plotting as marginally mature when looking at Rock-eval data. This will be discussed further in Chapter 5.

2.5 Experimental procedures

The main experimental procedures were conducted on the cell coupled with the GC-FID and GC-C-IRMS analysis. This will be discussed in the data analysis methodology. Several other commonly used geochemical instruments were used to categorise and analyse the samples. These include:

- Rock-eval pyrolysis: to determine the kerogen type of the sample as well as the total organic carbon content and maturity;
- Fourier Transform Infrared Spectroscopy: to determine the composition of the sample in terms of organic material, clays, silicates and carbonates;
- Scanning Electron Microscopy: to visualise the pore network, material present and the relationship of minerals to one another
- X-ray Diffraction: to determine the relative abundance of different materials present within the samples
- Lanmguir Isotherm Analysis: using the Quantachrome ® ASiQwin Automated Gas Sorption Instrument, version 5.2 to determine the N_2 adsorption capacity of a materiel
- Barret, Joyner and Halenda Analysis: using the Quantachrome R ASiQwin Automated Gas Sorption Instrument, version 5.2 to determine the pore size distribution of the sample
- Brunauer-Emmet-Teller Analysis: Quantachrome R ASiQwin Automated Gas Sorption Instrument, version 5.2 to determine the surface area of the sample

2.5.1 Rock-eval Pyrolysis

Rock-eval pyrolysis is a technique commonly used in the petroleum industry to screen potential source rocks for the volume of organic material within the sample, maturity of the material and quality of the material (Peters, 1998). The results of Roch-eval pyrolysis give the

Hydrogen Index (HI) and Oxygen Index (OI) for organic-rich samples which can be used to determine their kerogen "type". The HI indicated how much hydrogen is present in the organic material relative to the amount of organic carbon whereas the OI represents the amount of oxygen to organic carbon (Law, 1996). Type I kerogen refers to lacustrine material and has a high HI and a low OI (Law, 1996), Type II kerogen is typically marine algal and has moderate to high HI and a moderate OI. Type III kerogen has a low HI and a high OI. With increasing maturity, all samples will converge towards a low HI and OI (Law, 1996).

2.5.2 Fourier Transform Infrared Spectroscopy (FTIR)

The Fourier Transform Infrared Spectroscopy (FTIR) technique measures how well a sample absorbed light at each wavelength tested using a beam of light. The FTIR spectrometer collects data at high resolution and measures how much of the beam is absorbed by the sample for a given frequency. The wave frequencies are then altered and the process repeated to give many data points for a single sample. The results from this generates an IR spectrum of emissions using the Fourier Transform mathematical principle, converting the raw data into a spectrum. FTIR data works alongside X-Ray Diffraction (XRD) to interpret the mineralogy of rock samples (Chen et al., 2015c). FTIR analysis is one of the most versatile techniques for characterising both the organic and inorganic structure of a material (Chen et al., 2015c).

An example of the FTIR data is shown in Figure 14. The wave numbers correlate to different mineral species or material types such as organic carbon, water, silicate minerals and clay minerals. Each FTIR scan requires a background scan to remove any background noise. This becomes the baseline. Deviations away from the baseline when the sample is placed on the platform is shown by the red line in Figure 14. Each sample run took 120 seconds for optimum accuracy to time management.

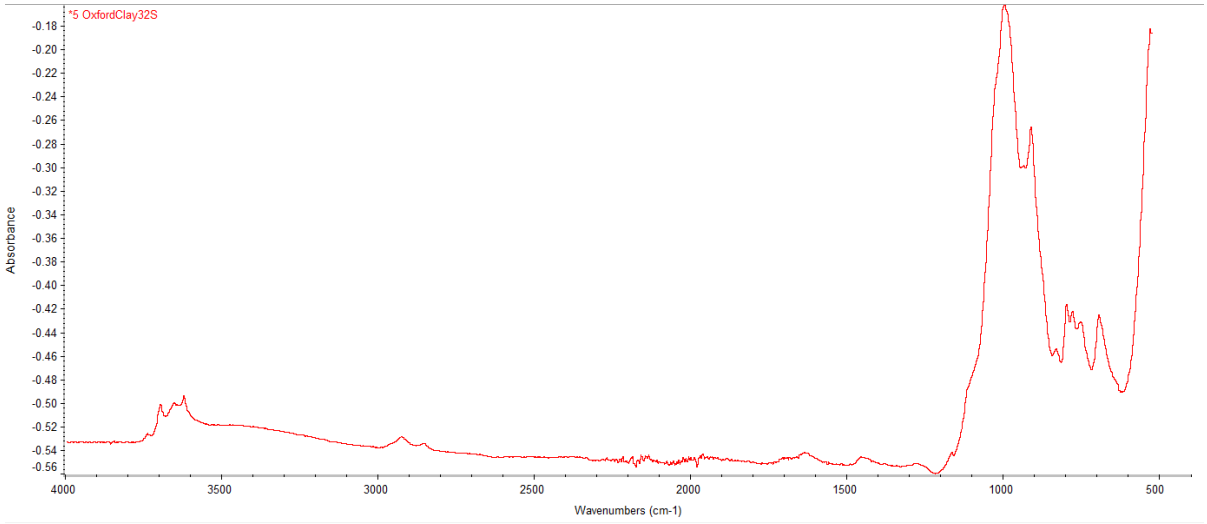


Figure 14| FTIR data collected for the OC-325 sample. Each peak will relate to a different mineral or suite of minerals and can be used to give relative abundance of minerals present in a sample.

2.5.3 Scanning Electron Microscopy (SEM)

A typical scanning electron microscope (SEM) has the capability to image samples down to 10 nm when imaging using topographic changes and 100 nm when considering composition, based on atomic number [Reed, 2005]. The instrument uses excited X-rays focused into an electron beam to generate an X-ray spectrum. The images produced can be used to identify minerals and void volumes as well as visualise pore geometries. The shape of the pores of a shale have been suggested to have an impact on shale storage capacity and diffusion processes during gas extraction. (Bustin et al., 2008b; Clarkson and Bustin, 1999; Trunschke, 2013a).

2.5.4 X-Ray Diffraction (XRD)

X-ray diffraction is a technique used to identify crystalline materials ((Dutrow, 1997). This technique can be used to identify inorganic materials such as clays, silicates and carbonates but does not measure the non-crystalline organic fraction. XRD is a rapid technique (<20 minutes a sample) and provides unambiguous inorganic composition of a material. X-ray

diffraction works as different minerals have specific wavelengths associated with them which generate an x-ray spectrum for a sample.

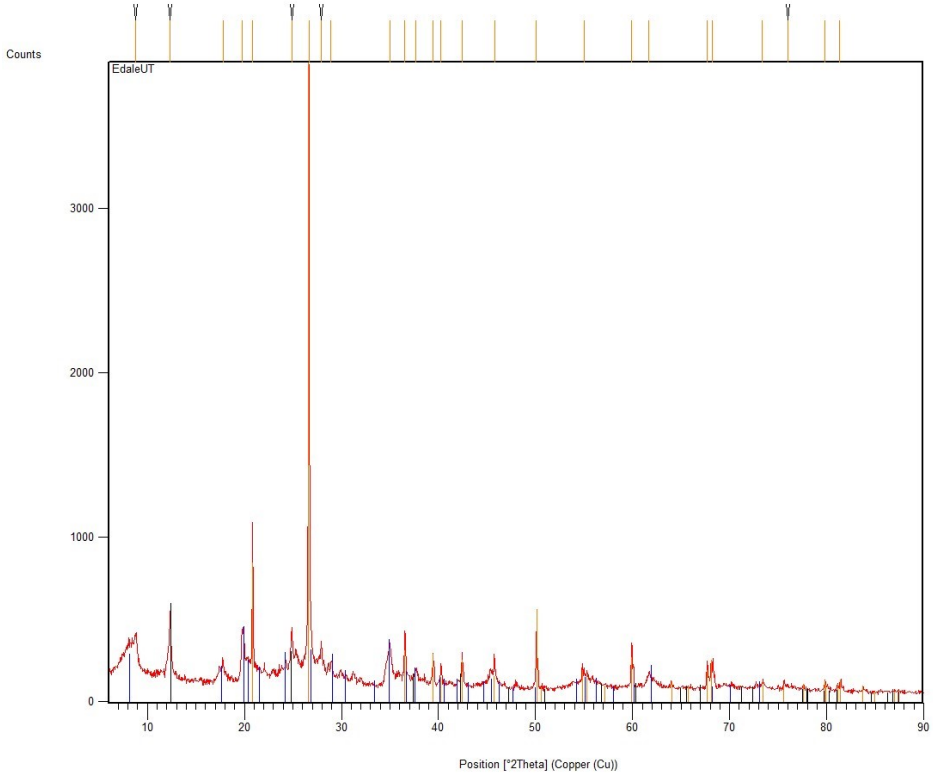


Figure 15| Example of the x-ray spectra collected from a shale sample. The peaks are identified from a pre-existing mineral spectra catalogue.

2.5.5 Langmuir Isotherm Analysis

The Langmuir isotherm data was collected using a Quantachrome ® ASiQwin Automated Gas Sorption Instrument, version 5.2. Nitrogen was used as the analysis gas and the experiments were conducted under standard pressure and temperature conditions. Full reports for the Langmuir Isotherm Analysis are available in the Appendix, Chapter 2, PDF and raw data formats. An example of the data report file is shown in Figure 16.

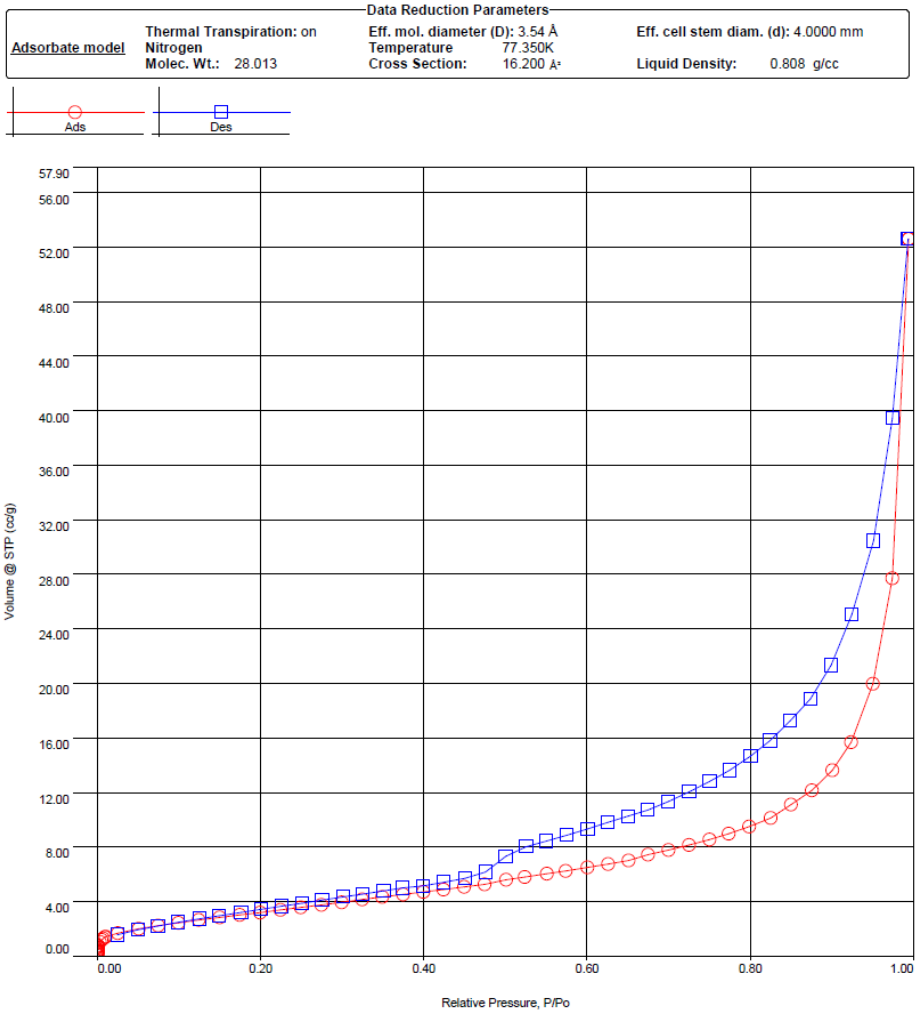


Figure 16 Example of an adsorption-desorption isotherm generated by the Quantachrome R ASiQwin Automated Gas Sorption Instrument, version 5.2. The sample shown here is West Lothian heated to 325°C.

2.5.6 Brunauer-Emmett-Teller (BET) surface area

BET surface area analysis was carried out by the Quantachrome ® AsiQwin automated gas sorption data instrument version 5.2. This software allows for comprehensive physisorption analysis of a sample. Nitrogen gas is used in BET analysis as it has a strong interaction with

most solids. Once the sample has fully adsorbed the N_2 gas and no further detectable gas adsorption is measured, the sample is degassed and the desorption process measured. BET differs from Langmuir isotherm analysis as it assumes multilayer adsorption. The analysis relies on several assumptions which allow for the surface area to be calculated. Primarily, that adsorption takes place on a uniform surface and all molecules in the monolayer cover the same area (J Rouquerol et al., 2007). The full reports are displayed in the following way:

Adsorbate model Nitrogen	Temperature 77.350K
Molec. Wt.: 28.013	Cross Section: 16.200 Å²
Liquid Density: 0.808 g/cc	
Relative Pressure P/Po	Volume @ STP cc/g	1 / [W((Po/P) - 1)] 1/g
1.00106e-02	1.4022	5.7701e+00
2.51012e-02	1.6722	1.2320e+01
5.07311e-02	1.9872	2.1518e+01
7.44206e-02	2.2195	2.8985e+01
9.92961e-02	2.4293	3.6309e+01
1.24190e-01	2.6319	4.3108e+01
1.49648e-01	2.8191	4.9948e+01
1.74273e-01	3.0035	5.6224e+01
1.99582e-01	3.1802	6.2733e+01
2.24335e-01	3.3795	6.8474e+01
2.49299e-01	3.5644	7.4545e+01
2.74501e-01	3.7458	8.0818e+01
2.99468e-01	3.9222	8.7205e+01

BET summary
Slope = 273.727 1/g
Intercept = 7.143e+00 1/g
Correlation coefficient, r = 0.997424
C constant= 39.320

Surface Area = 12.399 m²/g
Quantachrome® ASiQwin™- Automated Gas Sorption Data Acquisition and Reduction
© 1994-2017, Quantachrome Instruments
version 5.2

2.5.7 Barrett, Joyner and Halenda (BJH) Pore Size Distribution

The BJH data was also collected on a Quantachrome R ASiQwin Automated Gas Sorption Instrument, version 5.2. Nitrogen was used as the analysis gas with helium used in void volume mode to measure the pores. The analysis was carried out under standard pressure and temperature regimes. Full reports for these are available in the Appendix, chapter 2. BJH pore size distribution calculates a surface area, a pore volume and an average pore radius. Figure 17 shows the format for the data collected by the Quantachrome R ASiQwin Automated Gas Sorption Instrument. The cumulative pore volume is shown by the red line whilst the distribution of pores for a given pore radius is shown by the blue line. The pore radius is measured in angstroms, 15 angstroms is the equivalent of 1.5 nm which represents the smallest measurable pore volume.

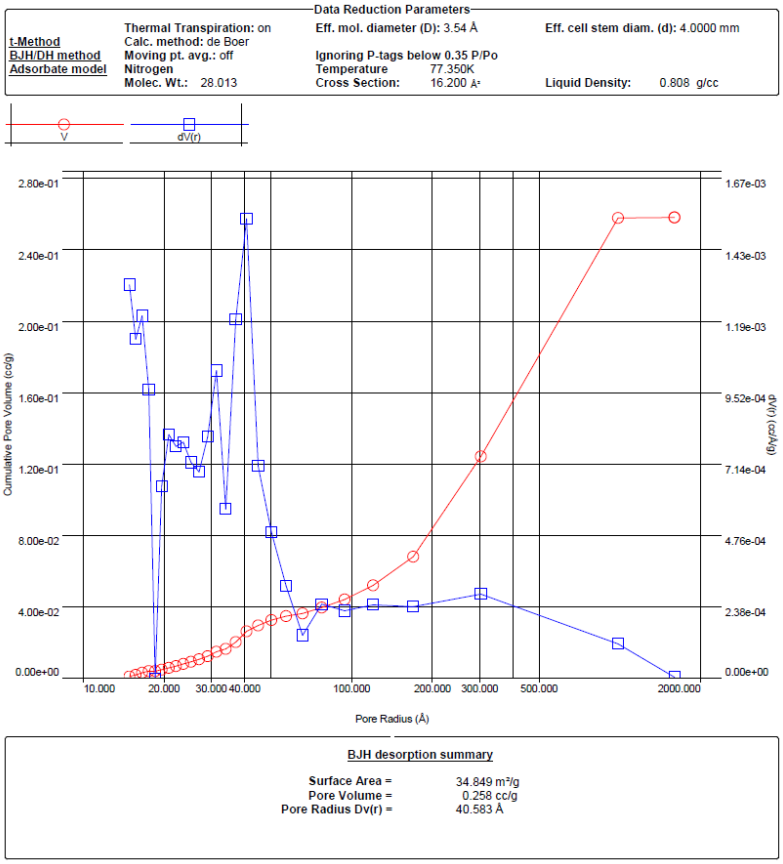


Figure 17 BJH pore size distribution analysis for Kimmeridge Clay Type II kerogen, as an example of the raw data collected by the Quantachrome R ASiQwin Automated Gas Sorption Instrument, version 5.2.

2.5.8 Wet chemistry methods:

Alongside the dry analytical techniques, several wet chemistry techniques were carried out on the samples. In order to isolate just the organic material from a shale, a kerogen extraction process had to be carried out. The procedures used in the kerogen extracted follow that outlined by the Australian Bureau of Mineral Resources (Horvath and Jackson, 1982).

Soxhlet Extraction: removal of free organics

Soxhlet extraction isolated any soluble organic matter which was juxtaposed with inorganic grains. The powdered samples were loaded into cellulose filters and placed within the extraction chamber. A round bottomed flask filled with a 60:40 benzene:methanol mix and several anti-breaking beads was placed on a hot plate and heated for 24 hours. The evaporated

benzene:methanol mixture condensed in the upper cooling section of the Soxhlet extractor and passed through the sample before returning to the round bottomed flask. The repetition of this process over 24 hours removed all free organic matter. The complete removal of free organic matter was confirmed by the appearance of a clear extraction fluid at the base of the extraction vessel.

Hydrochloric acid rinsing: carbonate removal

Hydrochloric acid (HCl) rinsing was a fast and efficient method for removing calcite from shale samples. HCl also removed any modern calcitic contamination such as calcrete which can form on surface samples. The soxhlet-washed samples were placed in Pyrex beakers and placed on a low temperature hot plate (35˚C) with a magnetic stirrer at the base. A low concentration of HCl was added for the initial step; 100 ml of 0.5N HCl, diluted further with water as required if the samples effervesced violently. Continuous stirring from the magnetic stirrer encouraged the complete removal of calcitic grains and coatings. After approximately 8-12 hours, the samples were covered with aluminium foil and left to separate into solid and liquid fractions. The supernatant fluid was then decanted. This process was repeated with increasingly stronger acid solutions until 200 ml of 1M HCl could be added without reaction. After the final acid bath, de-ionised water was used to rinse the sample to remove residual cations of Ca^{2+} then the samples were covered lightly and allowed to air dry.

Hydrofluoric acid rinsing: silicate removal

Once dried, the samples were halved and transferred to beakers resistant to HF. Due to the large nature of the samples and the dangers associated with HF, only half of the sample mass was extracted. Initially, a mixture of 1:4 parts HCl to HF was added to the samples in a fume cupboard. The acid-sample mix was sealed tightly and shaken to encourage dissolution. The suspension was then placed on a low temperature hot plate at 35˚C to encourage further

dissolution. Once settled, a process that took up to 6 hours due to the flocculating nature of the kerogen, the supernatant was removed and heavily diluted before disposal and an acid mix of 1:1 HF:de-ionised water was added. This process was repeated between 6-8 times depending on the nature of the sample. Once the acid no longer visibly reacted, seen in latter stages by the production of fine bubbles, and the supernatant remained clear after the allocated settling time, the sample was rinsed thoroughly and repeatedly with de-ionised water. When Litmus paper showed that the pH had of the supernatant had returned to pH 6-7, the sample was deemed safe to handle.

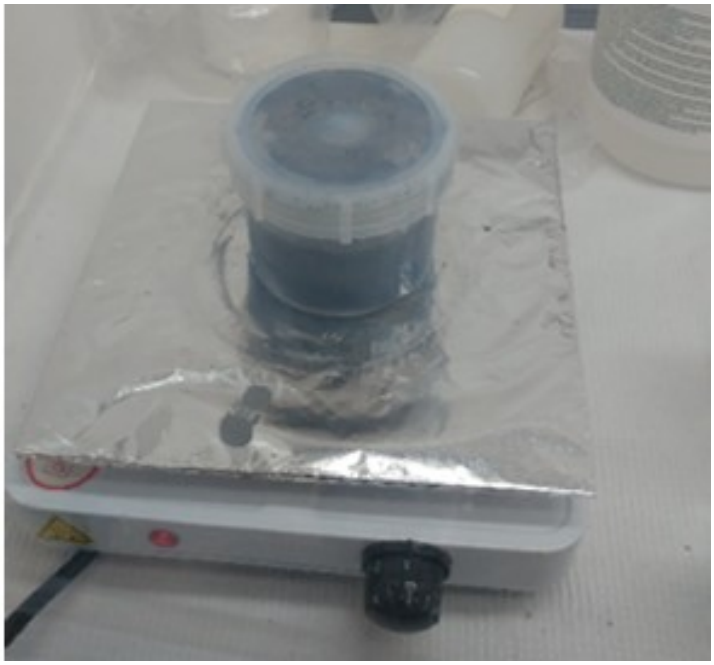


Figure 18| image taken in the clean chemistry labs at Imperial College London, The beaker, which can contain 250ml of fluid, is shown sat on the hot plate. The hot plate was kept at 35°c to encourage the Hf to react with the sample whilst ensuring that the kerogen remained unaltered.

Hydrous Pyrolysis

To artificially mature the samples, representing oil mature and gas mature, the powdered sample was split into three equally weighted sections. One was kept as the natural sample, representing a marginally mature type II kerogen rich source rock. The remaining two thirds were then prepared for artificial maturation via hydrous pyrolysis.

Hydrous pyrolysis is defined as a laboratory experimental procedure for stimulating the natural formation of hydrocarbons from organic rich material in an environment lacking oxygen but in the presence of liquid water [Lewan, 2017]. A stainless steel, 100ml volume reactor with a thermal source at the base and a sealed lid and pressure gauge at the head acts as the sample holder. As such, it is a closed reactor system and can generate oil from hydrocarbon bearing source rocks when heated to between 250-374˚C. The presence of liquid water is integral to the kerogen cracking procedure and is a more accurate representation of maturation through burial as liquid water is ubiquitous in sedimentary basins [Lewan, 2017]. The reactor limit is 374˚C, the critical point of distilled water.

In this experimental procedure, no more than 15g of sample was added at a time due to the size of the reactor. The sample must always remain submerged in liquid water throughout the experimental procedure. To maintain this submersion, around 35ml of water had to be added. Due to the small reactor size, the remaining volume of the reactor had to be left otherwise there was risk of explosion.

The hydrous pyrolysis bombs were cleaned with de-ionised water and cleaned with brushes to remove any material adhering to the inside. 30ml of de-ionised water was added to each bomb which was then sealed and heated to 320 degrees for 24 hours. After the heat cleaning cycle, the sample could safely be added without risk of contamination. The sample was added to the bomb and covered with 30ml of de-ionised water. The bomb was sealed and then flushed with He to remove air within the bomb. Prior to heating, the bomb contained only the sample, liquid water and He gas. The bomb was then heated to 250˚C for the oil-mature samples and 325˚C for the gas mature samples over the course of 24 hours. Once cooled, the contents of the bomb was placed in centrifuge tubes and separated into the solid sample and residue which was kept aside for GC-MS analysis. The samples were then transferred to silica glass beakers and loosely covered with aluminium foil to air dry.

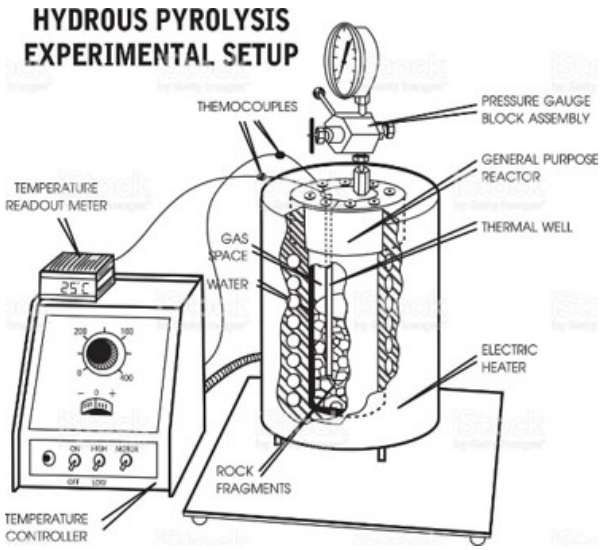


Figure 19| Hydrous pyrolysis schemtatc setup (Lewan, 2017)

2.6 Data Analysis Methodology

2.6.1 GC-C-IRMS data and errors

The raw data collected from the GC-C-IRMS is shown in Figure 13; the tabulated information can be extracted as an excel document. The $\delta^{13}C$ values for each peak are given directly. The peak intensity is noted for each injection which can be used to remove measurements that over or undersaturated the detector. From here, the average $\delta^{13}C$ for each pulse and the standard deviation can be calculated using the following equation:

$$SD = \sqrt{\frac{\sum|xi - \bar{x}|^2}{n-1}}$$

Where SD = standard deviation, xi is each number, $\bar{x}$ is the mean and n is the number of values. The standard deviation away from the average value was used to generate the working error associated with the experimental procedure. Due to the measuring capabilities of the GC-C-IRMS, it should be possible to measure the same gas sample 5 times and achieve a standard deviation of 0.1‰. Removing values from gas peaks which fell below 2800 mV and above 7500 mV significantly reduced the standard deviation associated with the gas pulse.

In order to test the precision of the experimental data collected, where possible each sample was run in triplicate. This will be discussed further in the relevant data chapters.

2.6.2 GC-FID data and errors

The raw data collected from the GC-FID is less immediately accessible. The data is shown in the USB digital appendix under GC-FID raw data. It is displayed as peak information in terms of intensity in mV for each peak. Methane is the first gas species to elute from the GC and generates the initial peak. Ethane elutes from the column more slowly and produces the second peak. The ratio between these two peaks alone gives the relative abundance of each

species but not the actual volume of each gas phase. Coupled with the custom built sample cell however, the online pressure measurements allows for the volume of gas being introduced to the GC to be measured. The C_1-C_2 ratio for a given volume of gas extracted can thus be determined.

Similar to the GC-C-IRMS error analysis, error bars are calculated using standard deviation of the several measurements made on one equilibrated aliquot of gas. Triplicate experiments are run of each sample where possible to measure the precision of the data.

3.0 Carbon Isotope Fractionation in Degassing Shale Constituents

3.1 Abstract

Fractionation between the stable isotopes of carbon is an inherent feature during depressurisation of a shale gas reservoir. Due to this inherent fractionation between stable carbon isotopes, this is one of the few geochemical indices applicable to shale gas exploration. However, variations in stable carbon isotope trends are not universal; shale gas produced from different fields produce unique stable carbon isotope fractionation trends Research into the characteristics of carbon isotope fractionation trends during reservoir degassing typically consider the degassing of shale cores; lithologies that are fundamentally heterogenous and complex, or focussing solely on storage capacity. The internal complexities within shales that affect carbon isotope fractionation include varying organic and inorganic matrix compositions and tortuous permeability pathways and pore size distribution. As such, degassing an intact shale core collected in-situ will produce a degassing fractionation signature that is unique to that shale and any generated data will provide limited transferability to other shales of different compositions, maturity, etc. Understanding how variables such as shale composition, maturity and tortuosity influence carbon isotope fractionation during shale gas production can help to o understand and monitor the lifecycle of a reservoir from genesis to residual gas.

In order to isolate the effects of individual components on the carbon isotope fractionation trends, we developed a custom-built sample cell coupled with a Gas Chromatography – Combustion – Isotope Ratio Mass Spectrometer (GC-C-IMRS) system which allows us to test individual shale components and their effects. In this study, isotope fractionation experiments were carried out in which $\delta\ ^{13}C$ values of CH_4 were monitored through time as the CH_4 was released from standard mineral samples which represent the key constituents of shales. This online GC-C-IRMS method simulates carbon isotope fractionation that should occur during

the degassing of a shale through its production life cycle over a short, 3-hour time period. As key variables such as total volume of shale, porosity, volume of initial gas in place (GIP) and the initial carbon isotope ratio of the bulk gas is known, a volume-specific fractionation curve can be generated indicating what the $\delta^{13}C$ trend looks like for a given volume of gas extracted. This volume-specific curve differs from typical production data that plots $\delta^{13}C$ in terms of production time and then obtains the volume of gas extracted as a percentage of total GIP by a numerical calculation.

Measurements were carried out on kaolinite ($AL_2Si_2O_5(OH)_4$, montmorillonite ($(Na,Ca)_{0.33}(Al,Mg)_2(Si_4O_{10})(OH)_2.nH_2O$,) calcite ($CaCO_3$), quartz ($SiO_2$ and type II kerogen extracted from the Kimmeridge Clay (C). Each isolated constituent produces its own distinct carbon isotope fractionation trend for CH_4. These preliminary findings highlighted the high-quality data (with error bars of $\delta^{13}C(‰) \pm < 0.5$) the new method is capable of generating, as well as providing a starting point for understanding, what causes changes in $\delta^{13}C$ of CH_4 through the life cycle of a shale gas reservoir. Hence, matrix composition was identified as a key variable that influences $\delta^{13}C$ trends during CH_4 extraction.

Using the custom-built sample cell - GC-C-IRMS apparatus, each component that may affect carbon isotope fractionation in a shale gas reservoir could be examined independently. The equipment allowed investigation of the intrinsic links between various shale parameters including shale composition, porosity-permeability, maturity and pressure-temperature variations. Our desorption method has the potential to be upscaled so that the change in gas geochemistry from core to reservoir scale and could be applied across all basins. Ideally, by measuring the change in gas isotope ratios through time, the lifecycle of a producing shale gas well can be calculated, based on shale composition. Understanding the position of the well in terms of production time and volume of gas would provide the information required to work

out a recovery factor. Knowledge of the recovery factor would allow the volume of rock drained to be calculated, which in turn would have great implications for future drilling locations.

3.2. Introduction

It is estimated that in 2018, shale gas accounted for 69% of the total gas production of the USA (U.S. Energy Information Administration, 2019). Even with the extensive research that has been conducted on shale gas throughout the shale gas boom from the early 2000's, the amount of gas that is stored within a shale and the state in which it is stored is difficult to quantify (Chen et al., 2019; Gasparik et al., 2014; Hu et al., 2015a; Javadpour et al., 2007; Song et al., 2019; Xia and Tang, 2012b; Zou and Rezaee, 2019b). The nature of unconventional shale reservoirs differs profoundly from conventional gas reservoirs because, in the former, gas is stored as both free gas within pores and adsorbed onto particle surfaces. The proportion of free gas to adsorbed gas cannot be calculated using conventional methods which rely on petrophysical analysis and Darcy flow in porous material (Mosher et al., 2013; Rexer et al., 2013). As such, predicting GIP using conventional gas methods is often inaccurate and unhelpful when estimating the production lifecycle of a shale gas field (Fathi and Akkutlu, 2009a).

The implications of a limited ability to estimate shale gas field lifecycles are two-fold. Firstly, the dominant mechanism for gas storage is unknown and thus gas volumetric calculations are often inaccurate. The primary storage site of gas in shales is debated heavily in the literature (Cheng and Huang, 2004a; Ji et al., 2012a; Song et al., 2019). Values for the volume of gas stored in the adsorbed state varies greatly in the literature from 80% (Ambrose et al., 2010) to 20% of the total gas volume (Jing et al., 2016; Rexer et al., 2013). Secondly, the factors which may influence the volume of gas stored in the adsorbed phase are also uncertain; surface area, pore size distribution TOC (%) and maturity have all been cited to have

an impact on gas adsorption capacity of a shale (Heller and Zoback, 2014a; Jarvie et al., 2007, p. 200; Song et al., 2019; Xiong et al., 2017a).

There is also the influence of fractionation during mass transport and flow; the flow regimes that dominate shale gas reservoirs are also debated, often with complex Knudsen diffusion, slip flow and convective flow models all being implemented (Freeman et al., 2011; Javadpour et al., 2007; Zhang and Krooss, 2001a). The influence of different flow regimes is shown in Figure 20.

Literature studies debate the influence of adsorption-desorption and diffusion on the δ^{13}CH trends (Fuex, 1980; Liu et al., 2016a; X. Wang et al., 2015; Xia and Tang, 2012b). This partly obscures the potential of using δ^{13}C as a geochemical index for (a) determining the initial GIP and (b) determining the recovery factor of a shale gas reservoir.

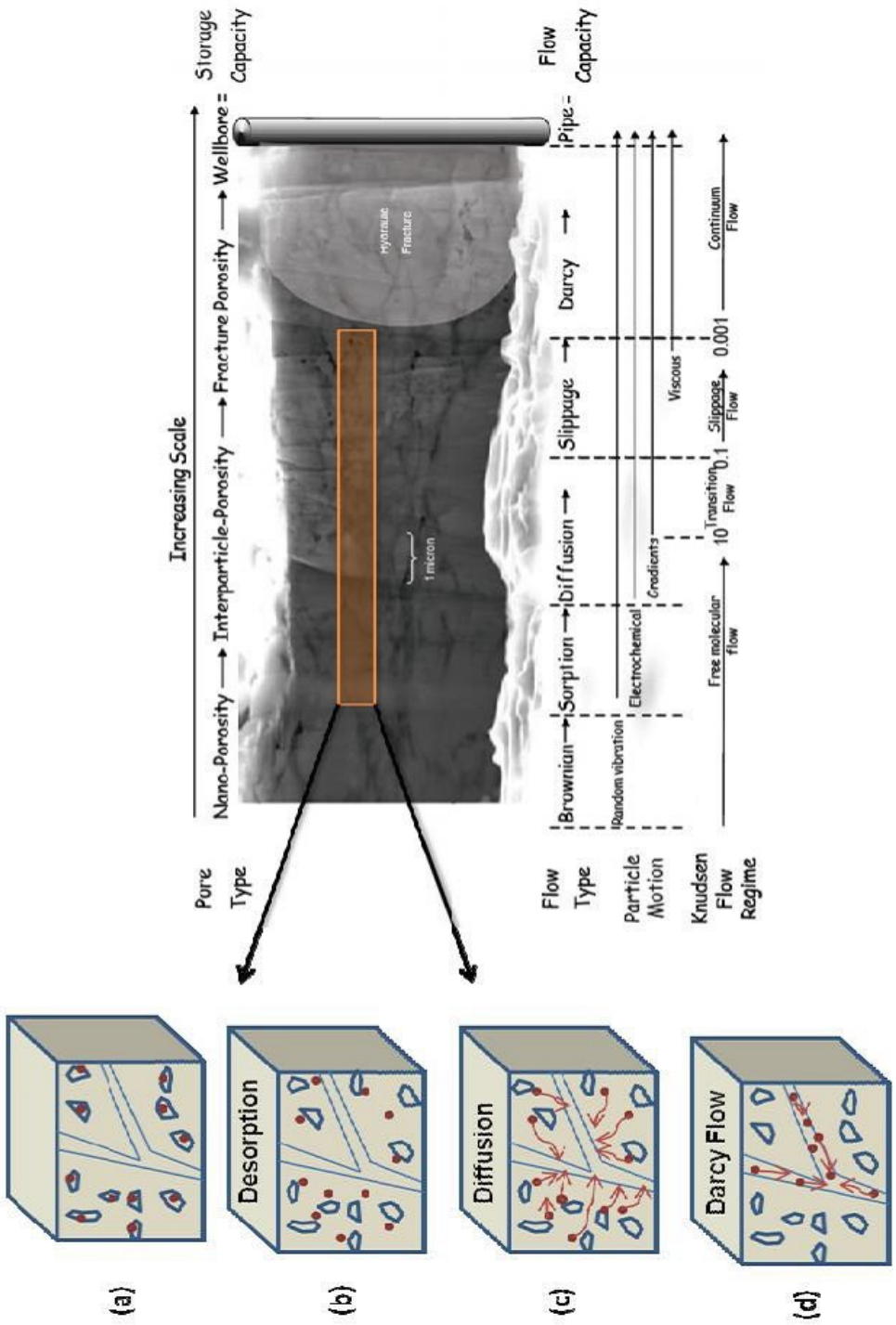


Figure 20 Gas flow mechanisms within a shale gas reservoir. (B) shows desorption which will yield kinetic fractionation of carbon isotopes. (C) shows mass transport which may yield chromatographic fractionation. No fractionation is expected in (D) where Darcy flow is the dominant mechanism for gas movement (Dahaghi and others, 2010)

3.2.1 What may cause the inherent stable carbon isotope fractionation?

Analysis of stable carbon isotope ratios of shale gases has been used in previous studies to provide an important fingerprint for defining the history of the gas, from genesis through

thermal maturation and to migration (Figure 21) (Berner et al., 1995; Clayton, 1991; Curiale and Curtis, 2016; Lorant et al., 1998; Prinzhofer and Pernaton, 1997). Stable carbon isotope analysis has also been suggested as a way of determining the volume of gas that a shale can store, the fractionation occurring through adsorption-desorption processes (Liu et al., 2016a; Schettler and Parmoly, 1990a; Tang et al., 2017; X. Wang et al., 2015; Xia and Tang, 2012b). A further focus of study is stable carbon isotopic fractionation driven by diffusive flow through the nanoporous shale matrix (Krooss et al., 2010; Prinzhofer and Pernaton, 1997; Schloemer and Krooss, 2004; Yin et al., 2017a; Zhang and Krooss, 2001a, 2001b).



Figure 21 Controls on the initial isotopic and molecular weight composition of shale gas, adapted from (Xia et al., 2013).

3.2.2 Why is this question so difficult to answer?

The cause of stable carbon isotopic fractionation with reservoir degassing is contentious and is likely to be an interplay of several factors. Isotopic fractionation can be considered in three phases:

1. Initial fractionation owing to the chemical transition from kerogen to free compounds (Clayton, 1991; Rooney et al., 1995),

2. Fractionation related to movement within the shale itself including adsorption and desorption, diffusive mass transport in both steady-state and non steady-state as shown in Figure 20 (Xia and Tang, 2012a; Zhang and Krooss, 2001a),

3. Post-generation migration, mixing and biodegradation (Fuex, 1980; Snowdon, 2001; Xia et al., 2013).

Phase 1, the initial fractionation and starting isotopic composition of a shale will be dependent on several factors; the thermal history of the shale, the initial kerogen composition and the generation and expulsion history are some examples of the factors related to the initial fractionation phase. Shales that have been cored and collected in situ and then degassed make up the bulk of studies considering changes in gas geochemistry with degassing. The initial isotopic composition cannot be predicted from the kerogen type alone. As such, this study aims to remove the initial generational fractionation effects by starting with a completely degassed sample and injecting gas of a known isotopic composition into the material.

Phase 2 considers fractionation through gas flow, in this case this links to depressurisation of the shale reservoir during gas extraction and can link to either (b) or (c) in Figure 20, B, desorption fractionation processes, will occur when there is a disruption to the equilibrium of the free gas and adsorbed gas, i.e. when the shale is fractured. C relates to gas flowing out of the tortuous nanoporous network into the hydraulically-induced fractures. These processes together are referred to as "degassing".

Phase 3 refers to the flow of gas from the hydraulically-induced fractures into the wellbore. The flow regime associated with this is Darcy flow and no fractionation is expected with this flow regime and is shown in Figure 20 by stage (d).

As many studies in the literature focus on the degassing of either intact or powdered core that has been collected in-situ, these factors overlie one another, producing a degassing trend that may be influenced by any combination of desorption, gas mixing or diffusion.

What controls the initial δ ^{13}C values in a shale gas reservoir?

Initial carbon isotope composition of a shale gas reservoir is dictated by several factors; kerogen type and primary cracking of kerogen, secondary hydrocarbon cracking and post generational gas mixing and microbial activity (Figure 21) (Prinzhofer and Huc, 1995; Rooney et al., 1995; Stolper et al., 2014). The degree of maturation will have an influence on the $\delta^{13}C$ values as shown in Figure 22.

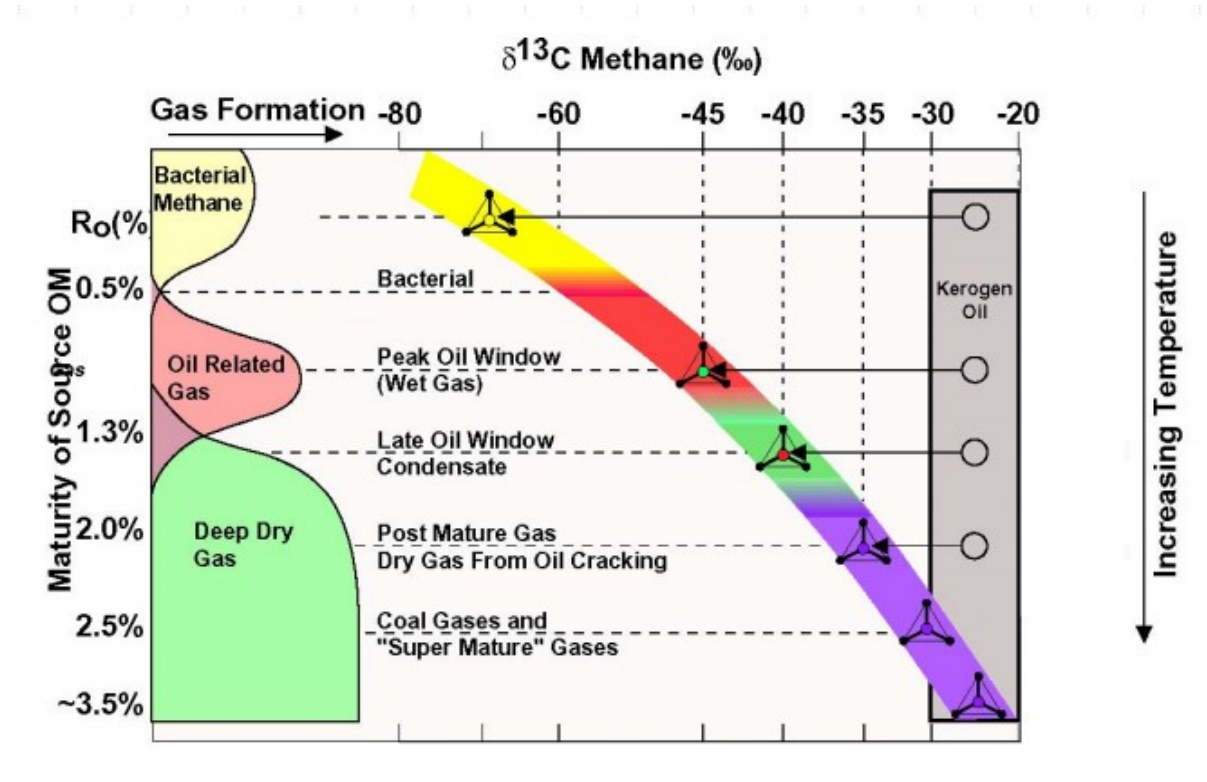


Figure 22|Influences of maturity and bacterial imprint on the $\delta^{13}C$ value of a shale gas reservoir, originally from (Schoell, 1980).

What may control change in the $\delta^{13}C$ value during adsorption-desorption?

In unconventional shale gas reservoirs, gas is held as both free gas in larger pores and fractures as well as adsorbed on the surface of organic matter and clays (Ambrose et al., 2010; Chareonsuppanimit et al., 2012a; Dahaghi and others, 2010; Jarvie et al., 2004; Rexer et al., 2013). This chapter focusses on the effects produced by inorganic, chemically inert material, inorganic clay material and organic material.

Sorption kinetics suggest that less energy is required to liberate ^{12}C from the surface of a mineral compared to ^{13}C (Xia et al., 2013)]. As such, gas produced from the sorbed material should, in theory, initially degas relatively more ^{12}C. With continued production, the degassed material is expected to degas relatively more ^{13}C throughout the lifecycle of the well (Li et al., 2017; Tang et al., 2017). However, data acquired from current shale gas wells often displays abnormal trends and does not relate to linear fractionation of $\delta^{13}C$ (Zumberge et al., 2012), suggesting the influence of multiple and/or complex mechanisms.

Potential causes for these uncertainties include the following:

- It is unknown how much fractionation is driven by adsorption-desorption. As such, $\delta^{13}C$ of CH_4 cannot be used as a direct proxy for volume of gas stored in the adsorbed phase,
- It is still uncertain how to accurately calculate storage capacity of a shale, i.e. how do composition, maturity, water saturation etc effect the adsorption capacity,
- It is uncertain what effect diffusion has on isotopic fraction with gas extraction,
- It is incompletely understood how different diffusive flow regimes might influence the $\delta^{13}C$ of CH_4 during degassing

3.2.3 Is there a more useful way to address the problem?

Instead of working backwards from a whole shale, attempting to unravel a complex mosaic of effects, we isolated different minerals, and examined how they affected isotopic fractionation. In this way, we developed a geochemical index that does not directly rely on adsorption-desorption/diffusion but one that is based on compositional effects. The implications of this are twofold. Initially, many studies in the literature focus primarily on the organic content for gas storage capacity, the desorption from which is suggested as the dominant cause of change in $\delta^{13}C$ for CH_4 (Hao et al., 2013; Li et al., 2017; Prinzhofer and Huc, 1995). This chapter isolates the individual components of a shale to show that in fact clays have a significant effect on the $\delta^{13}C$ of CH_4 with degassing, suggesting that an interpretation of $\delta^{13}C$ of CH_4 production data is related purely to TOC content and desorption then it will not yield an accurate geochemical index that will predict the $\delta^{13}C$ of CH_4 with degassing. Furthermore, it is necessary to understand which components influence the $\delta^{13}C$ of CH_4 in order to predict the tail of the production decline curve, an example of which is shown in Figure 23. Whilst the initial gas pulse is predicted to be free gas, the tail is very much dominated by either desorbing gas or gas diffusing out of the nanoporous network or some combination of the two.

If the $\delta^{13}C$ of CH_4 can be related to composition and each component produces its own unique $\delta^{13}C$ of CH_4 degassing curve from 100% GIP to 100% gas extracted then the expected $\delta^{13}C$ curve from a shale of given compisition can be attributed to a volume of total gas extracted rather than purely time as shown in Figure 23.

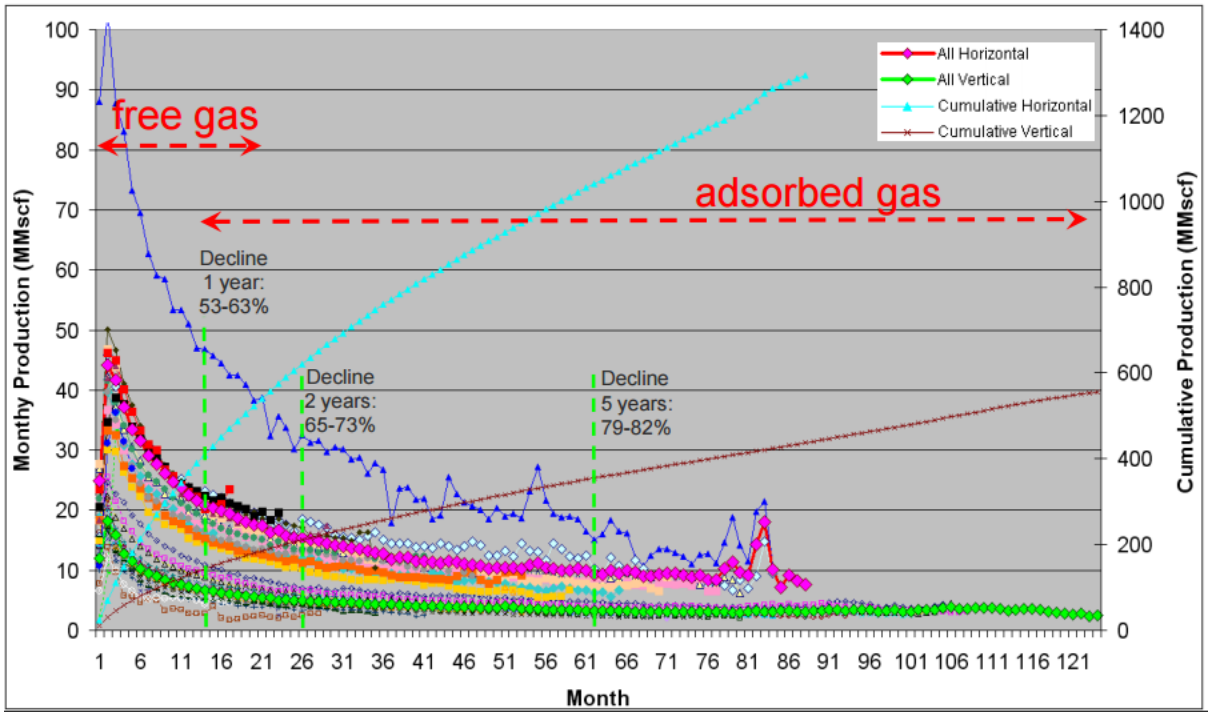


Figure 23 Production Data over 10 years: Barnett Shale, Statoil 2011. Free gas is stored in any existing macropores or fractures thus is liberated first. The tail is often stated to be gas desorbing from the surfaces of organic material and/or clays *(Rexer et al., 2013; Sandvik et al., 1992; Tang et al., 2017)*. Free gas would not generate isotopic fractionation as shown in figure 21 whilst desorption would produce some inherent fractionation between the lighter C^{12} and the heavier C^{13}.

The objective of this study is to use the change in gas geochemistry as a proxy for recovery factor and total gas in place – regardless of adsorption/desorption and diffusion process, and to identify which individual factors influence fractionation trends and "build" the geochemical features of a shale up from its foundations. As part of the characterisation of the testable parameters, BET surface area, Langmuir isotherm volumes and BJH pore size distributions will be measured. Whilst these will be discussed in this chapter, full interpretation of how these data may be used to consider adsorption-desorption and diffusive $\delta^{13}C$ will be discussed in chapter 7.

Testable Parameters

In the literature, there are several key parameters that effect the capacity of a shale reservoir to store gas volumes. Table 3 summarises these parameters. Each of these variables can be directly tested under laboratory conditions by varying each parameter (e.g. amount of organic matter or

clay type, or varying the temperature or pressure during an experiment) and thereby performing a sensitivity analysis.

Table 3| from literature studies, this table outlines the various factors that have been suggested as controlling factors in $\delta^{13}C$ of CH_4 with shale reservoir degassing.

Influencing Factor	Reasoning	Reference
Total Organic Carbon (TOC)	1. Provides site for adsorption to occur 2. Has greater internal porosity than shale matrix, providing more sorption sites	Bernard et al., (2010) Xia & Tang, (2012) Zhang et al. (2012)
Clay Type	1. Different clays have varying sorption capacity, typically smectite>>kaolinite>chlorite>illite 2. Clays also have different degrees of hydrophobia which inhibit methane adsorption	Bernard et al, (2010) Heller & Zoback, (2014) Ji et al. 2016
Porosity	1. Nano-porosity: sorption site 2. Meso-porosity: free gas and some adsorption with permeability potential 3. Macro-porosity: free gas in large pores and fractures: no sorptive fractionation	Saghafi, (2016) Bernard et al., (2010) Ambrose et al. (2010) Zhang & Krooss, (2001)
Maturity	1. Required for gas generation and conversion of kerogen 2. Believed to increase pore volume and size within organic matter 3. Increase surface area of sorption sites	Stahl & Carey, (1975) Xia et al., (2013) Clayton, (1990) Tilley & Muehlenbachs, (2013) Alexandra Sarney, pers. Comm. (Eagle Ford samples)

Temperature	1. Links to maturity and Vitrinite reflectance; higher temperature history results in greater maturity 2. Reservoir temperature has an effect on adsorption capacity *and* adsorption rate	Lafortune et al., (2014)
Pressure	1. Pressure (P) driven diffusive fractionation – greater ΔP results in greater volume of gas desorbed initially	Cheng et al., (1997)
Water Saturation	1. Solubility factor of shale gases in water 2. Wettability of reservoir 3. Hydrophilic clays reduce sorption sites when water is present	Charriere et al., (2010) Xia and Tang, (2012) Zhang and Krooss, (2001)

3.2.4 Questions to address

There are several facets to the use of carbon isotopes as a proxy for gas storage and extraction in a shale gas reservoir that must be considered. Initially, there is the uncertainty around the dominant mechanism behind the fractionation between ^{12}C and ^{13}C seen during the extraction process. As outlined, the influence between adsorption-desorption versus diffusive fractionation is contentious within the literature and our current understanding is unhelpful when trying to attribute the change in geochemistry to *either* gas storage *or* gas flow.

In order to fully utilise the inherent change in gas geochemistry with reservoir degassing, a new setup must be considered. The experimental setup in this chapter focusses on the use of $\delta^{13}C$ of CH_4 as a geochemical index to produce a recovery factor and seeks to determine what components of a shale influence the $\delta^{13}C$ of CH_4. As such, instead of following the well-beaten narrative of desorption versus diffusion, we address the question "what factors influence $\delta^{13}C$

of CH_4 in a shale" by determining the changing gas geochemistry relating to isolated shale variables.

The composition of the Eagle Ford Shale was used as a guideline. The object of this chapter was to determine isothermal carbon isotope fractionation trends in of CH_4 injected into standard samples which make up the key constituents of the Eagle Ford shale: quartz, kaolinite, montmorillonite, illite, calcite and type II kerogen. Collected on a custom-built sample cell - gas chromatography - combustion - isotope ratio mass spectrometer (GC-C-IRMS), our data shows that each individual component generates a unique carbon isotope fractionation trend. To assist the understanding in the underlying causes of the distinct $\delta^{13}C$ of CH_4 trends with composition, other analytical techniques such as Langmuir isotherm, Brauner-Emmett-Teller (BET) and Barrett-Joyner-Halenda (BJH) analysis were carried out.

The initial experimentation addresses the question – how does shale composition influence the $\delta^{13}C$ of CH_4 with reservoir degassing? Whilst the focus of this thesis is isolating and determining which parameters of a shale influence changes in gas geochemistry, the possible effects of adsorptive fractionation versus diffusive fractionation will be explored in Chapter 7. Development of this new method facilitates the future work highlighted in Table 3. isolating effects such as matrix tortuosity, maturity and organic matter type on carbon isotope fractionation

3.3. Experimental Methods

3.3.1 Samples

Table 4 shows the five representative components of shales used in this experimental procedure. These samples were chosen as representative components for shales based on the known composition of the Eagle Ford Shale (Driskill et al., 2013a; Psarras et al., 2017). Full descriptions of these samples are presented in the section below.

Table 4| Table of standard minerals studied.

Sample Name	**Chemical Formula**	**Distinguishing Characteristics**
Kaolinite	$Al_2Si_2O_5(OH)_4$	Non-swelling phyllosilicate clay
Montmorillonite	$(Al_{2-y}Mg_y)(SiO_4O_{10}(OH)_2$	Hydrous swelling clay from the smectite group
Calcite	$CaCO_3$	Non-swelling pure carbonate mineral
Quartz	SiO_2	Non-swelling pure silicate mineral
Type II Kerogen	C	Marine, mixed algal and plant derived immobile organic material

Kaolinite

Kaolinite ($Al_2Si_2O_5(OH)_4$) is a layered phyllosilicate clay mineral and is the weathering product of aluminosilicate minerals (e.g. feldspar). As such, it is a major clay mineral component of many shales. It has a low cation exchange capacity and is composed of sheets held together by H-bonds. As a result, kaolinite is a non-swelling clay suggesting only moderate adsorption capacity (Heller and Zoback, 2014a; Ji et al., 2012b; Zhong et al., 2016). The kaolinite is a laboratory standard, purchased from the Clay Mineralogical Society. It was cleaned using hydrogen peroxide diluted to 35% and baked at 110ºC to remove any surface water.

Montmorillonite

Montmorillonite ($(Al_2\text{-}yMgy)(SiO_4O_{10}(OH)_2$) is a phyllosilicate mineral and is a member of the smectite clay group. The individual montmorillonite clay particles are not tightly bound together. As such, this is one of the most swelling clays with a high water retention capacity. Cleaning in the typical manner (dilute hydrogen peroxide) was not possible due to the swelling nature of this clay. Heating to over 100°C was also not possible as this would remove structural water and change the composition of the clay.

Calcite

Calcite ($CaCO_3$) was purchased from Sigma Aldrich as a lab standard chemical. It was cleaned using hydrogen peroxide diluted to 35% and baked at 110°C to remove any surface water. Because of the marly nature of the Eagle Ford Shale, this was considered a vital standard to test (Driskill et al., 2013a). Minimal adsorption is expected in calcite, less than that of the clays.

Quartz

Pure quartz (SiO_2) of <250 μm (Sigma Aldrich). The adsorptive capacity of quartz is ~0.02 mmol/g rock at atmospheric pressure and 34.5ºC (Ji et al., 2012b). As such, good quality data for carbon isotope fractionation involving quartz is required to give a reasonable baseline for almost pure diffusive related fractionation for a given grainsize (S. Wang et al., 2016).

Type II Kerogen

Type II kerogen was extracted from a sample of the Kimmeridge Clay, a classic petroleum source rock in the United Kingdom. This particular sample was collected from a surface outcrop at the type locality, Kimmeridge Bay in Dorset, southern England. Type II kerogen contains organic matter that was deposited in a marine shelf environment, containing

inputs from both marine algae and land plants (Wignall, 1989). The kerogen was extracted through a series of acid extraction steps that are described in full in Chapter 2.

3.3.2 Sample Preparation

Outlined in detail in Method: Sample Preparation, to ensure that the materials were cleaned and removed of any adsorbed gases, water or free organics, most samples were washed in a 35% dilution hydrogen peroxide solution on a hot plate heated to 50ºC. Once the cleaning process was complete, the supernatant was decanted off and rinsed 5 times with de-ionised water, removing the hydrogen peroxide solution. After the final rinse, the remaining slurry was then baked at 110 ºC to remove any residual water and the solid residue stored in a drying cupboard (35 ºC) between tests.

Neither montmorillonite clay nor type II kerogen could undergo all steps of this cleaning procedure. Montmorillonite is a swelling clay, containing bound water. As such, addition of water or excessive heating would alter the composition of the clay. The montmorillonite was purchased from the Clay Mineral Society ® and a reasonable level of purity was expressed on the container (>99%). Montmorillonite was thus kept in the drying box at 35 ºC with no further cleaning.

Type II kerogen was extracted from a Kimmeridge Clay shale using a series of kerogen extraction techniques outlined in the Australian Bureau of Mines report 1982 (Horvath and Jackson, 1982). Both before and after the kerogen had been extracted, Fourier Transform Infrared Spectroscopy (FTIR) was carried out on the sample to compare the relative abundance of organic to inorganic fractions. The FTIR procedure is outlined in Chapter 2, Methodology: 2.5.2 Fourier Transform Infrared Spectroscopy (FTIR).

3.3.3 Characterisation of the samples:

Langmuir isotherm analytical procedure

A full description of this procedure can be found in Chapter 2, Methods: 2.5.5 Langmuir Isotherm Analysis but a brief description will follow.

Langmuir isotherms were measured using N_2 adsorption with the Quantachrome ® ASiQwin Automated Gas Sorption Instrument, version 5.2. The Langmuir volume refers to the maximum volume of gas that can be stored on the surface of a sample through monolayer adsorption and is often used for the basis of shale adsorption numerical modelling. Isotherms with varying hysteresis loops between adsorption-desorption volumes can be used to indicate the pore types found within the material and suggest the type of adsorption occurring e.g. mono-layer, multilayer etc. (Sing, 1985; Sing and Williams, 2004).

BET surface area analysis procedure

A full description of this procedure is found in Chapter 2, Methods: 2.5.6 Brunauer-Emmett-Teller (BET) surface area., but a brief description follows.

BET surface area analysis was carried out using a Quantachrome ® ASiQwin Automated Gas Sorption Instrument, version 5.2. BET surface area calculates the total area of a sample onto which gas can be adsorbed, the results of which are reported in m^3/g.

BJH pore size distribution procedure

A full description of this procedure is found in Chapter 2. Methods: 2.5.7 Barrett, Joyner and Halenda (BJH) Pore Size Distribution but a brief description will follow.

The BJH data was collected on a Quantachrome ® ASiQwin Automated Gas Sorption Instrument, version 5.2. BJH pore size distribution given measurements of several key

parameters; surface area, a pore volume and an average pore radius. Pore radius is reported in Å.

3.3.4 Experimental Procedure

To assess the utility of carbon isotope ratio measurements for understanding the life cycle of producing shale gas reservoirs, an unprecedented online desorption GC-C-IRMS system was constructed. Unlike previous methods used in the literature, this custom-built cell allowed for continuous, online measurement of carbon isotopes measured from the extracted sample gas at set time intervals. Figure 24 is a schematic diagram showing the instrument configuration. Methane gas was injected from the gas cylinder (1) into the reference volume (V1-V2). This was then expanded into V1-V3 which contained the sample cell.

A pressure transducer measured the pressure drop between the reference volume and the sample and reference volume which allowed the volume of gas injected into the sample to be calculated. Time was then given to allow the gas to fully penetrate the sample material. Depending on the sample, this took between 2-6 hours and was dictated by the stabilisation of the pressure within the cell. Previous studies have shown that grain size has the greatest influence on time taken to reach sorption equilibria with large grained samples (125 μm) taking up to 6 hours to become equilibrated (Busch et al., 2004). Gas was then extracted at given time intervals and passed into the Gas Chromatography - Combustion - Isotope Ratio Mass Spectrometer (GC-C-IRMS) instrument. The data collected by the instrument provided $\delta^{13}C$ values plotted against the intensity (mV) of each gas injection. The IRMS has a working intensity range between ~2000 - 7000 mV which limited the number of gas injections, especially towards the end of the experimental period where the residual gas volume was small. Within this working range, the IRMS had a sensitivity of <0.08 $\delta^{13}C$ (‰) when measuring the isotope ratio of the reference gas. How this was calculated is outlined in detail in 2.2 GC-C-

IRMS: Precision, accuracy and quality control section. As such, this instrument is capable of monitoring very small changes in carbon isotope ratios with reservoir degassing.

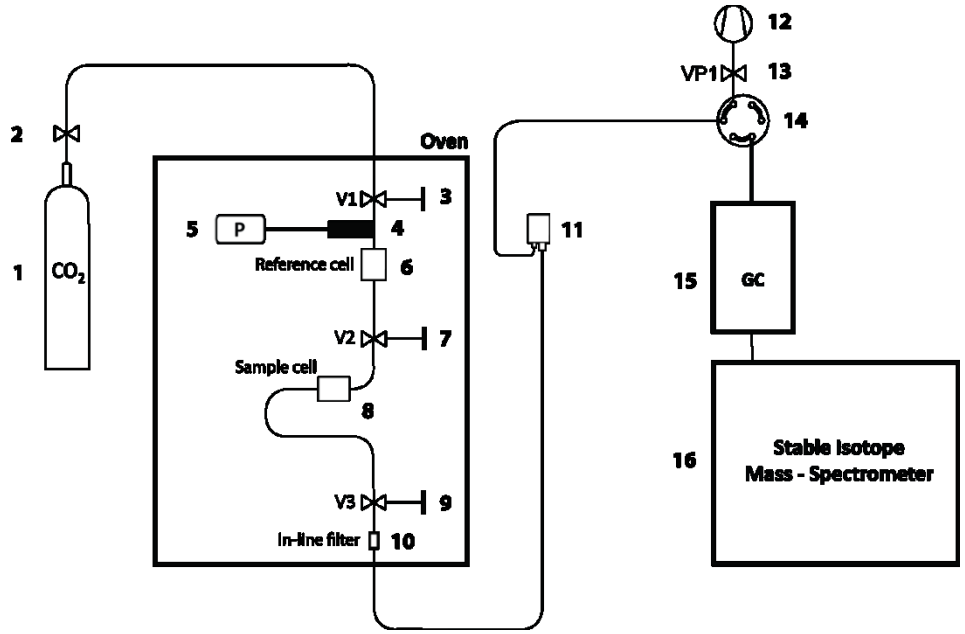


Figure 24 | Simple schematic of the custom built online adsorption-desorption cell.

Table 5| components relating to the schematic diagram in Figure 24.

Part Number	Name description
1	V-size gas cylinder (e.g. CH_4)
2	Cylinder regulator
3	On-Off valve
4	Pressure Transducer PDCR 5021
5	Digital Process Indicator, IDL-INT2-L
6	Stainless steel reference cell
7	On-off valve
8	Stainless steel sample cell
9	On-off valve
10	SS in-line filter, 2µm

11	On-off valve
12	Vacuum pump
13	Diaphragm-sealed valve
14	Valco Vici 6=way valve, 1/16” fitting
15	Gas Chromatograph
16	Isotope Ratio Mass Spectrometer (Finnigan Mat 252)

Operational Procedure

The operational procedure for the methane desorption experiment is described in detail in the methods section.

Error Calculation

Error bars displayed were produced using standard deviations with the mean obtained from five measurements of the same gas sample. Often, the first two measurements of the first desorption step were unreliable as they typically plotted outside the sensitivity of the IRMS. As such, the error bar for the first data point was significantly greater than the other data points. Equation 1 shows the calculation for obtaining δ^{13}C of CH_4. The universal standard used was Pee Dee Belemnite (Vienna), a Cretaceous marine belemnite found in the Pee Dee Formation, South Carolina.

$$\delta^{13}C = \left(\frac{\frac{^{13}C}{^{12}C}(sample)}{\frac{^{13}C}{^{12}C}(standard} - 1 \right) * 100‰ \qquad \text{(eqn 1)}$$

In Chapter 2, Methodology, section: 2.6.1 GC-C-IRMS data and errors there is a full explanation of how the errors were calculated both for the IRMS reference gas as well as direct injections and sample runs. The error calculations for sample runs will be reiterated here for clarity.

As outlined in the method above, the gas sample, once expanded into the PEEK® tubing, could be sampled several times in order to test the precision of the instrument during an experimental run. Peaks which fell out of the detectable range of the IRMS could be discounted. Once those data points were removed, the standard deviation from the mean value could be calculated using the simple equation below:

$$SD = \sqrt{\frac{\sum|xi - \bar{x}|^2}{n-1}} \qquad \textit{Eqn. 2}$$

Where SD = standard deviation, xi is each number, $\bar{x}$ is the mean and n is the number of values. Ideally, 5 gas samples were taken so that, if one or two were above the working range of the instrument, there were enough data points to have statistical significance and to generate the working error associated with the experimental procedure. As previously outlined, the GC-C-IRMS had the capability to measure the reference gas with a standard deviation of 0.1 ‰.

In order to test the precision of the experimental data samples were run in triplicate or at least duplicate where possible.

3.4 Results

In this section, the physical and chemical characteristics of the samples will be outlined first namely; the Langmuir isotherm volume, BET surface area, BJH pore size distribution and the FTIR where applicable. Once the characteristics of the samples have been commented on, the results of the custom-built sample cell GC-C-IRMS will be discussed.

3.4.1 Langmuir isotherm analysis

Langmuir isotherm analysis is the process by which the maximum volume of adsorbate adhering so the surface of an adsorbent can be calculated (Langmuir, 1918). This isotherm analysis is carried out at a static temperature and assuming monolayer coverage. The results below show the isothermal analysis of the five standard samples.

3.4.2 Langmuir volumes of the inert materials

Figure 25a and b show the adsorption capacity of quartz and calcite. It is evident that both materials have surface chemistry that does not encourage adsorption of the adsorbate. Calcite can adsorb less than 3 cc/g of N_2 whilst quartz can adsorb less than 1 cc/g of N_2.

3.4.3 Langmuir volumes for the clay samples

Figure 26a and b show the adsorption capacity of kaolinite and montmorillonite. Both clays have a similar desorption capacity but very differently shaped isotherms. The maximum adsorption capacity for the two samples is similar with kaolinite capable of adsorbing 42.9 cm^3/g compared to montmorillonite which has a maximum Langmuir volume of 48.01 cm^3.

3.4.4 Langmuir volumes for Type II kerogen

Figure 27 shows the Langmuir isotherm analysis and the BJH pore size distribution analysis for the type II isolated kerogen sample. The extracted kerogen has a maximum adsorption capacity of 51.42 cc/g and a minor hysteric effect.

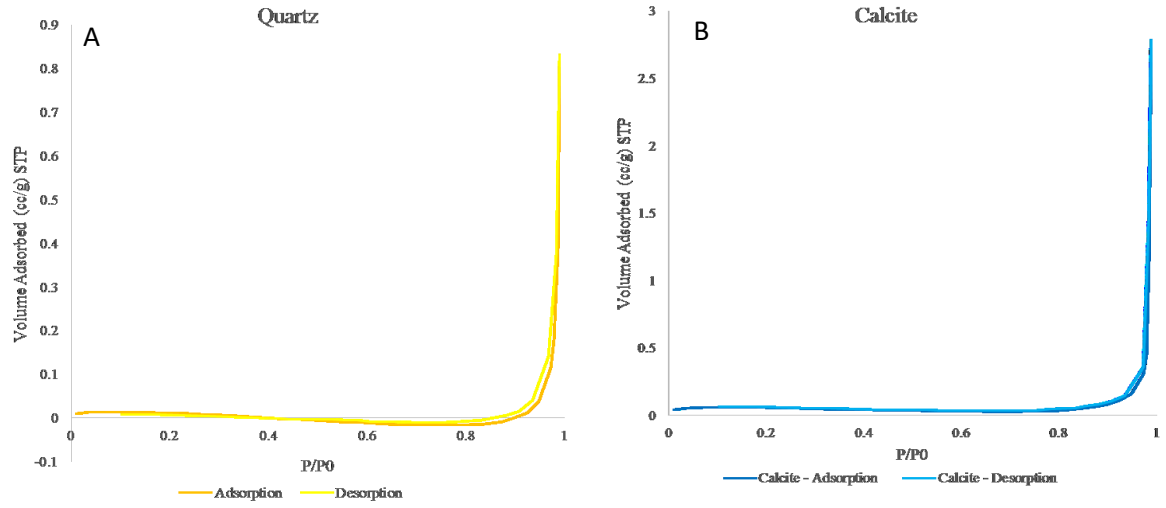


Figure 25| a. Langmuir isotherm analysis for quartz and b. Langmuir isotherm analysis for calcite

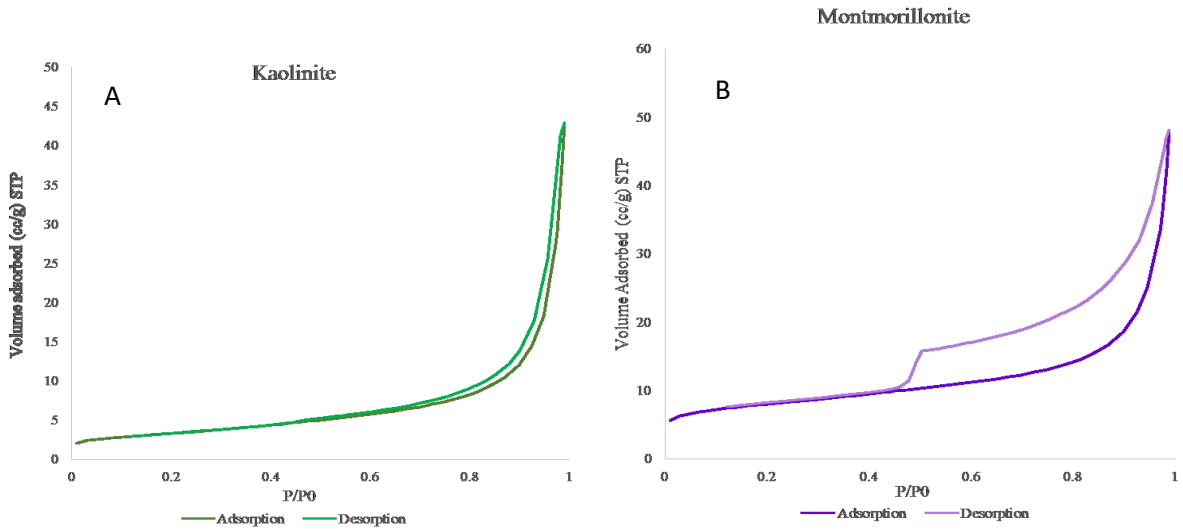


Figure 26 | a. Langmuir isotherm curve for kaolinite clay and b. Langmuir isotherm curve for montmorillonite clay

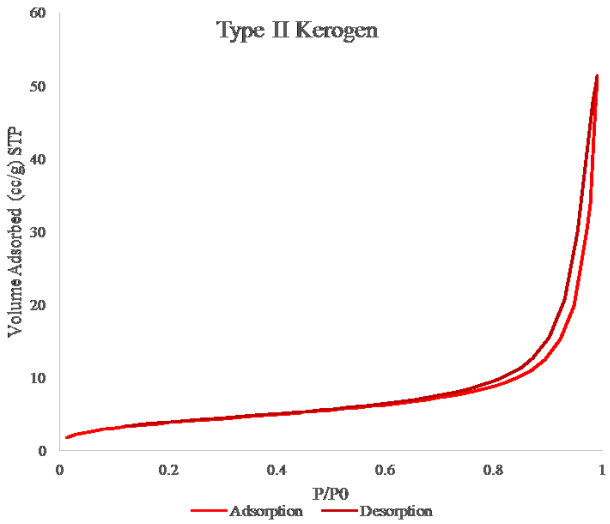


Figure 27| Langmuir isotherm analysis for Type II Kerogen.

3.4.5 BJH and BET Analysis

Collected on the Quantachrome Autosorb ® version 5, the BET surface area data details the specific surface area of each sample. The BJH indicated the pore size distribution. Pore size distribution was expected to be uniform in the mineral fractions whilst the organic material was expected to have more variation. Figures 28-32 indicate the BET and BJH data collected for the inorganic and organic materials tested.

BJH: Calcite and Quartz

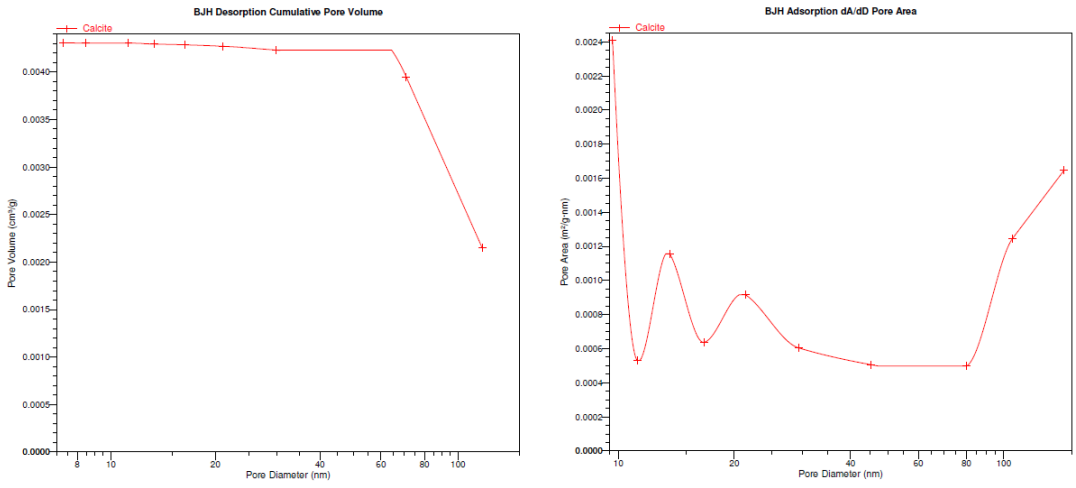


Figure 28| Calcite cumulative pore volume (a) and pore diameter to pore volume (b) for calculate. Most pores are greater than 100nm in size which can skew the data plots.

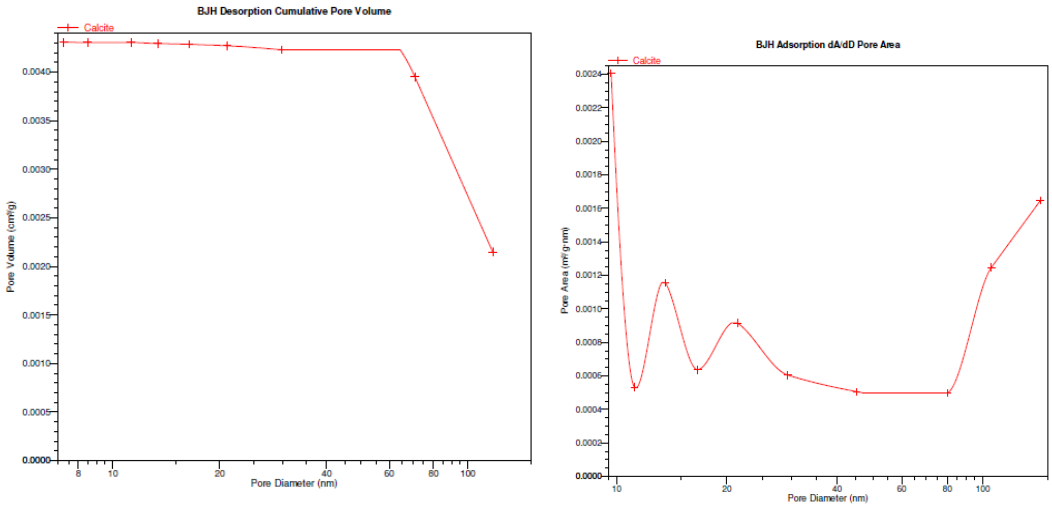


Figure 29| Quartz cumulative pore volume (a) and pore diameter to pore volume (b). Similar to calcite, most pores are greater than 100nm

BJH: kaolinite and Montmorillonite

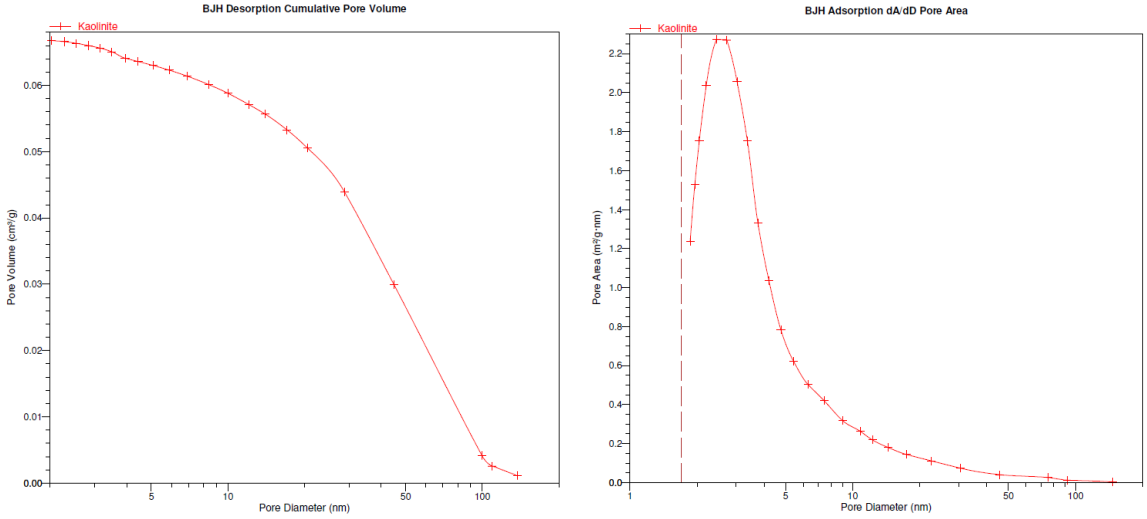


Figure 30| Kaolinite cumulative pore volume (a) and pore diameter to pore area (b). There is a high volume of pores with diameters between 10 and 50nm. Pores of 2nm in diameter have the greatest pore area of the kaolinite sample.

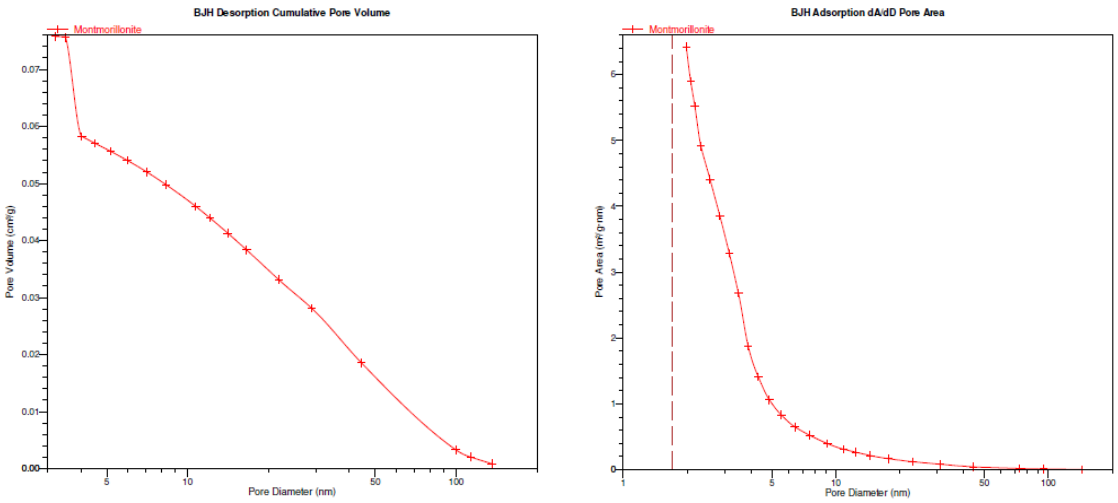


Figure 31| Montmorillonite cumulative pore volume (a) and pore diameter to pore area (b). The largest pore area coincides with the smallest pore diameter at ~1nm. There is a distinct jump in the cumulative pore volume when considering the pores <2nm in diameter.

BJH: Type II Kerogen

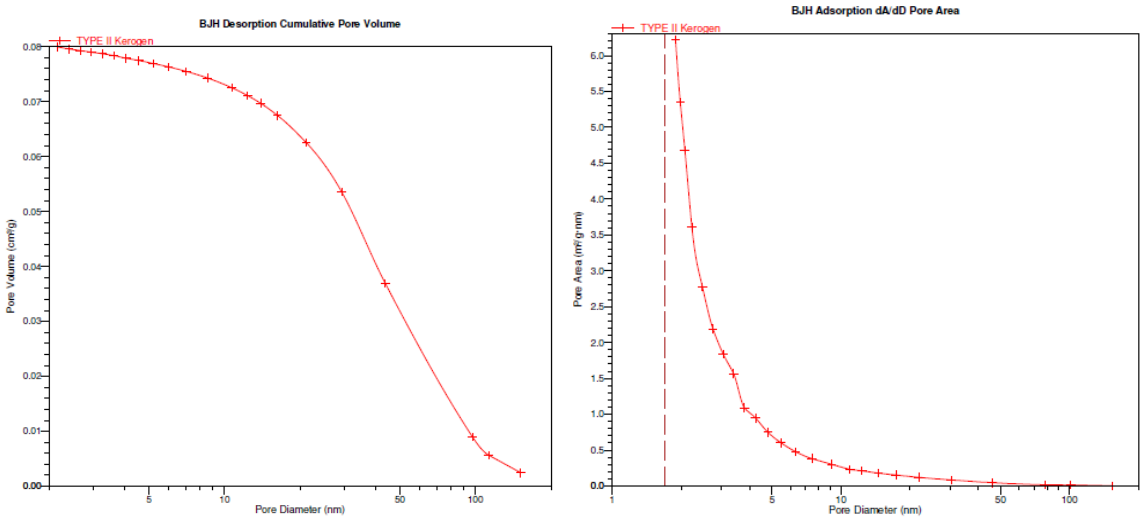


Figure 32| Type II kerogen cumulative pore volume (a) and pore diameter to pore area (b). The largest pore area coincides with the smallest pore diameter at ~1nm. Most pores fall between 10-5nm in size.

The data combined from the analysis above is displayed in the table below.

Table 6| Table of combined BET surface area, Langmuir volume and BJH pore distribution analysis for the standard samples.

Sample	Adsorbed Quantity (N_2) Cm^3/g	BET Surface Area cm^3/g	BJH pore vol. cm^3/g	BJH pore volume <72nm cm^3/g
Kaolinite	42.9	11.80	0.0668	0.042
Montmorillonite	48.01	28.12	0.076	0.052
Calcite	2.78	0.189	0.004	0.0005
Quartz	0.83	0.04	0.001	0.0001
Type II Kerogen	51.42	14.40	0.08	0.047

It is evident from the data displayed in table Table 6 that there is a significant difference in properties between the relatively inert quartz and calcite materials and the kaolinite, montmorillonite clay minerals and type II kerogen. Calcite and quartz have very low adsorption capacity with their Langmuir volumes calculated at less than 3 cm^3/g. Type II kerogen has the greatest adsorption capacity at 51.42 cm^3/g with montmorillonite achieving the second highest Langmuir volume at 48.01 cm^3/g. Kaolinite has a lower adsorption capacity than both montmorillonite and type II kerogen with a Langmuir volume of 42.9 cm^3/g.

Similarly, quartz and calcite both have significantly lower measured surface areas and pore volumes than the clay and kerogen samples. Kerogen has a moderate BET surface area measurement, similar to kaolinite (14.4 and 11.8 cm^3/g respectively). Montmorillonite has the greatest surface area and volume of pores than plot <72 nm whilst type II kerogen has the greatest overall pore volume measured. BET surface area plotted against Langmuir volume is shown in Figure 33. There appears to be an exponential increase in the volume of gas that can be adsorbed by a sample irrespective of material type.

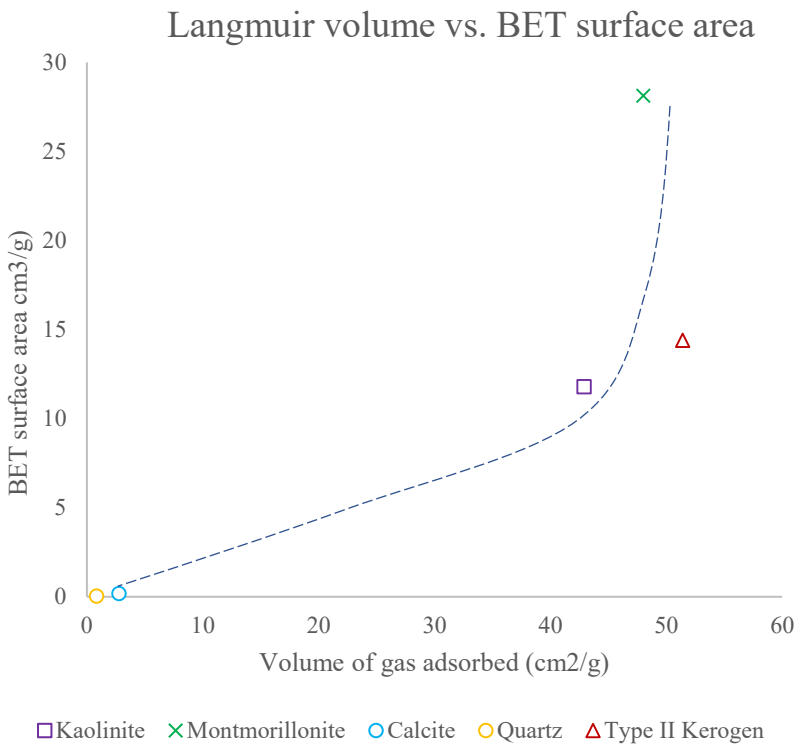


Figure 33| Volume of gas adsorbed (Langmuir volume) plotted against the measured BET surface area for the pure mineral

3.4.6 Characterising the samples: BET, BJH and Langmuir Isotherms

Table 6 shows the BET, BJH and Langmuir isotherm summary for the shale components tested in this chapter. From literature studies, it was expected that the extracted kerogen would have the greatest Langmuir volume (Gasparik et al., 2014; Tang et al., 2017). The data collected and displayed here confirmed that expectation. The clays however, also had a significant adsorption capacity, montmorillonite was almost as adsorptive as the type II kerogen. Literature studies have tended to focus on just the organic material as a site for gas storage with few studies considering the roles of clays in this process (Cheng and Huang, 2004b; Heller and Zoback, 2014a; Ji et al., 2012a).

As expected, the chemically inert material, quartz and calcite have little adsorptive capacity low surface area and overall small pore volume. Both quartz and calcite have negligible adsorptive capacities and can thus be used as a proxy for diffusive fractionation

through the pore network. The measurable pore volume for calcite and quartz is 0.004 and 0.001 cm^3/g respectively. This may not be a true reflection of the grains as macropores may be too large to be measured by the instrument (>500 $m\mu$). The overall surface area is small, 0.04 cm^3/g and 0.189 cm^3/g for quartz and calcite grains respectively.

Montmorillonite has the greatest surface area and the greatest number of pores in the micropore size range. Kaolinite has the lowest adsorption capacity, surface area and pore volume of the three adsorptive samples. It was expected that type II kerogen would have the greatest surface area but it is evident that, whilst the organic material has the greatest measurable pore volume, the number of pores <73 nm is less than that of montmorillonite. This suggests that type II kerogen has a more diverse range of pore sizes which result in an overall lower surface area.

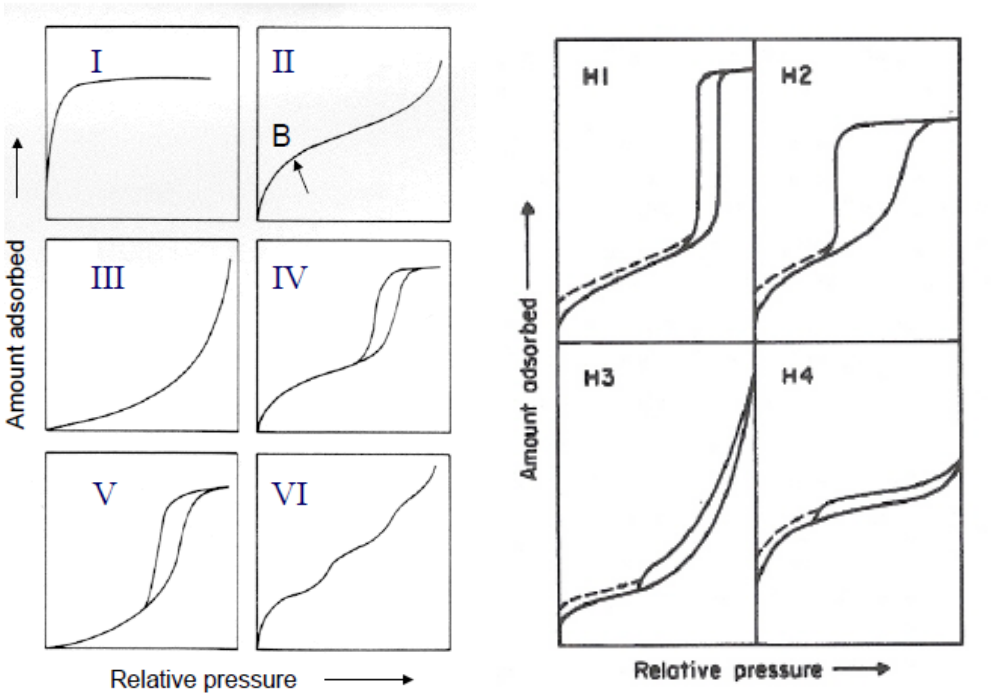


Figure 34 | A) The six types of isotherms that can be produced during adsorption-desorption experiments. Type I refers to adsorption limited to a few molecular layers and is considered true chemisorption. Type II is typical of a microporous adsorbent with unrestricted monolayer-multilayer adsorption. Type III is representative of weak adsorptive-adsorbent interactions. Type IV indicates complete pore-filling with monolayer-multilayer adsorption and capillary condensation. V refers to weak interactions between adsorbate and adsorbent with capillary condensation. VI isotherms reflect step-wise multilayer adsorption on a non-uniform and nonporous surface (Sing, 1985). B. The four types of hysteresis loop associated with type IV and V isotherms. HI refers to a well-defined, cylindrical pore network. H2 is a heterogenous pore system with

some pores blocked. Type H3 is typical of platy-clay minerals, especially in powdered form which produces slit-like pores. H4 creates narrow slit pores which a microporous in size. (Sing, 1985)

Figure 34a shows the 6 categories of isotherm whilst Figure 34b shows the sub-categories for interpreting the hysteresis loop. Calcite and quartz exhibit no hysteresis and, due to their large and uniform pore size, they produce an extreme version of a type II, non-adsorbent microporous material. Type II kerogen and kaolinite produce a mainly type III isotherm with some IV influence and minor hysteresis loop between adsorption and desorption processes. Using Figure 34b, the hysteresis loop is most like type H1, referring to a cylindrical pore network. It was not expected that type II kerogen and kaolinite would have similar adsorption-desorption isotherms due to their differing pore networks and chemical surface properties. Montmorillonite on the other hand has a type IV isotherm that suggests monolayer adsorption and capillary condensation. Further analysis suggests an H3 type IV isotherm, indicative of slit-shaped pores and platy minerals (Trunschke, 2013b). The maximum adsorption capacity of montmorillonite is 48.07 cc/g with a strong hysteresis loop between the adsorption-desorption process.

The process for calculating the molar volume of and gas volumes will be discussed in the section below.

Figure 35 shows the Langmuir volume measured by the Quantachrome Autsorb ® instrumentation plotted against the BET surface area where the size of the bubble represents the relative number of moles adsorbed per sample, calculated during the experimental setup when gas is first introduced into the sample. There is a discrepancy between the adsorbed volume of N_2 and the volume of CH_4 adsorbed by each material. Type II kerogen has the greatest Langmuir volume but a lower overall calculated adsorption capacity. Kaolinite has the greatest adsorption measured but a lower Langmuir volume from the N_2.

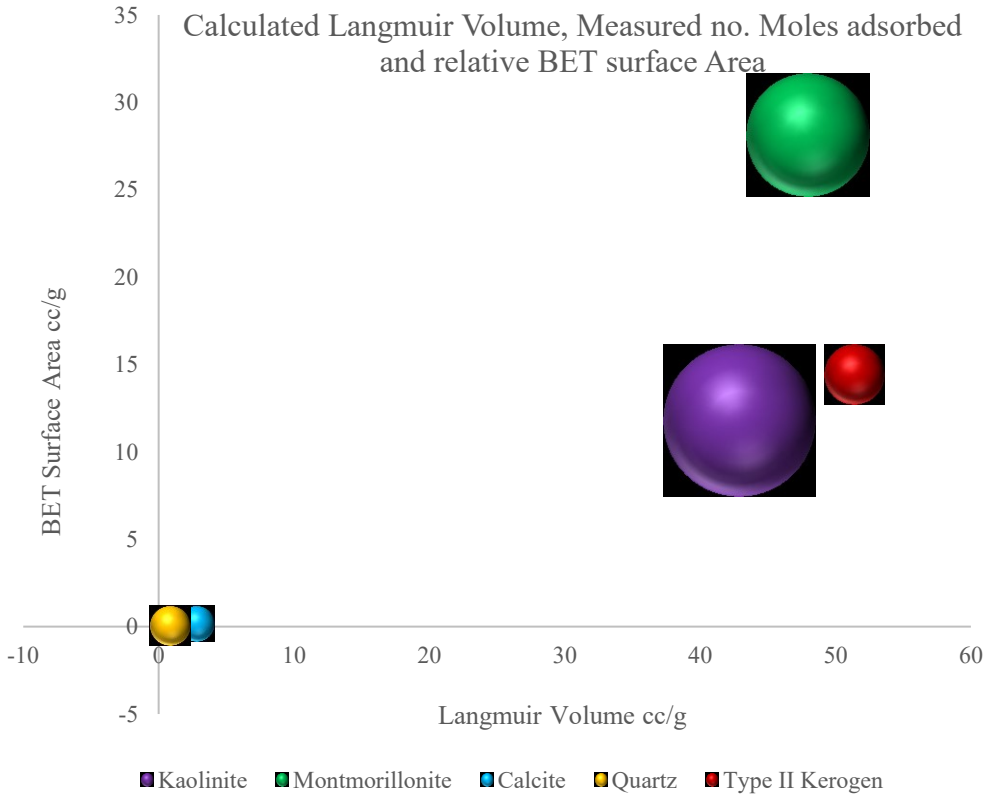


Figure 35| Langmuir volume measured on the Quantochrome Autosorb ® instrumentation plotted against measured BET surface area analysis. The bubble size represents the calculated volume of gas adsorbed in the online adsorption measurements during the experimental setup of the sample cell GC – C – IRMS.

Figure 36 shows the BJH pore volume plotted against the measured Langmuir volume for each sample. There appears to be a linear correlation between the Langmuir volume and the total pore volume. Again, there is the discrepancy between the Langmuir volume from the Quantachrome Autosorb ® N_2 analysis and the online CH_4 adsorption. The low BET but high

adsorption has been shown in previous work with suggestions of some additional retention capacity of organic material that is not related to the surface area but perhaps the surface chemistry (Cheng and Huang, 2004b; Ross and Bustin, 2009a).

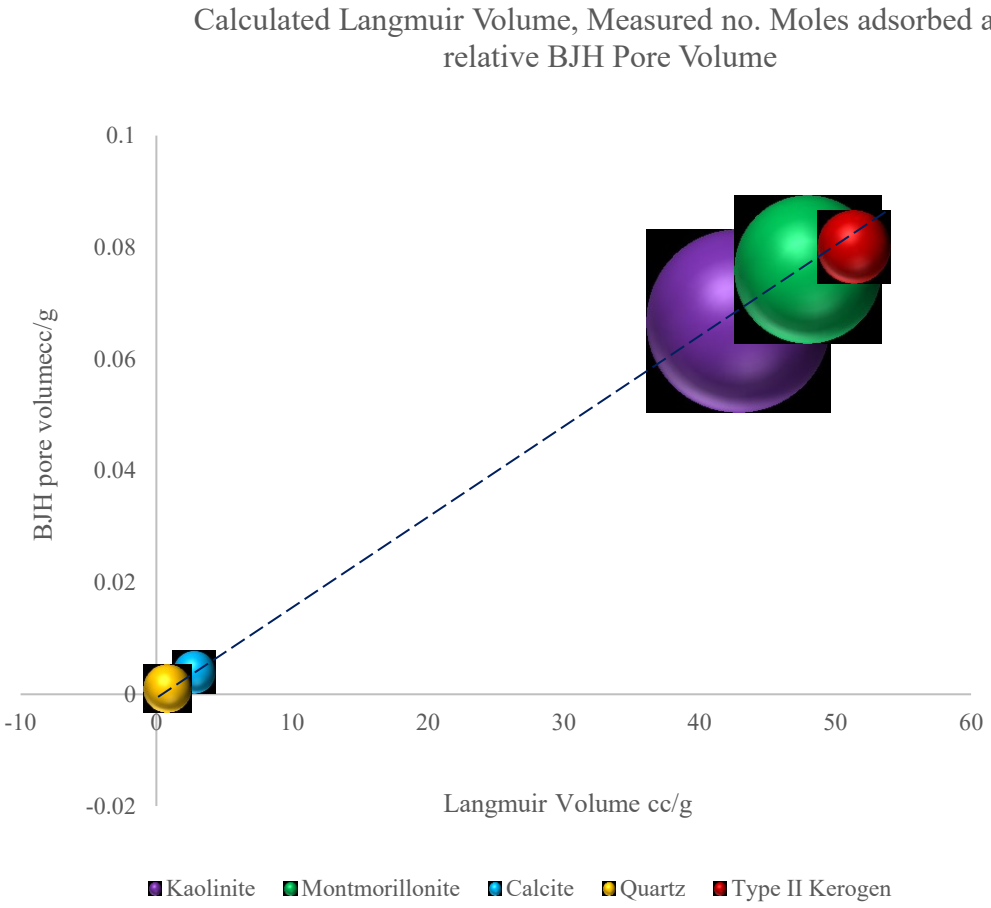


Figure 36| Langmuir isotherm volume plotted against BJH pore volume shows a linear trend; as the pore volume increases, so does the measured Langmuir volume. Again, the size of the bubble represent the calculated molar volume adsorbed during experimental setup.

The Langmuir isotherm, BET and BJH analysis allow for characterisation of the samples beyond their simple chemical composition. The data obtained from this will be used to help understand the nature of the δ^{13}C‰ degassing trend dictated by shale composition. Chapter 7 will consider how these fractionation curves may be used to infer the mechanism of fractionation based on the calculated adsorption capacity. The remainder of the discussion here

will focus on the prospect of relating δ^{13}C‰ fractionation trends in terms of volumetrics as a method of predicting the shale gas decline curve based on composition; the viability of δ^{13}C‰ as a geochemical index for volume of total GIP extracted.

3.4.7 Direct Injection Data

To test the accuracy and reproducibility of data on the IRMS, carbon dioxide of a known isotopic value ($\delta^{13}C_{CO2}$ = -41.98 ‰) was directly injected into the GC-C-IRMS. The values given for each direct injection show the accuracy of each individual gas injection to the known $\delta^{13}C_{CO2}$ value as well as the overall precision of the instrument. Figure 37 displays direct injection data for $\delta^{13}C_{CO2}$. The average value from 25 direct injections is -41.98 $\delta^{13}C_{CO2}$ with a standard deviation of +/-0.05‰ has shown in Figure 37. Not only is the average measured value <0.1‰ $\delta^{13}C_{CO2}$ away from the true $\delta^{13}C_{CO2}$ of the gas, data plotting with a standard deviation <0.1‰ $\delta^{13}C_{CO2}$ is considered high quality. These data are highly promising and indicates that the instrument itself is capable of performing high quality measurements.

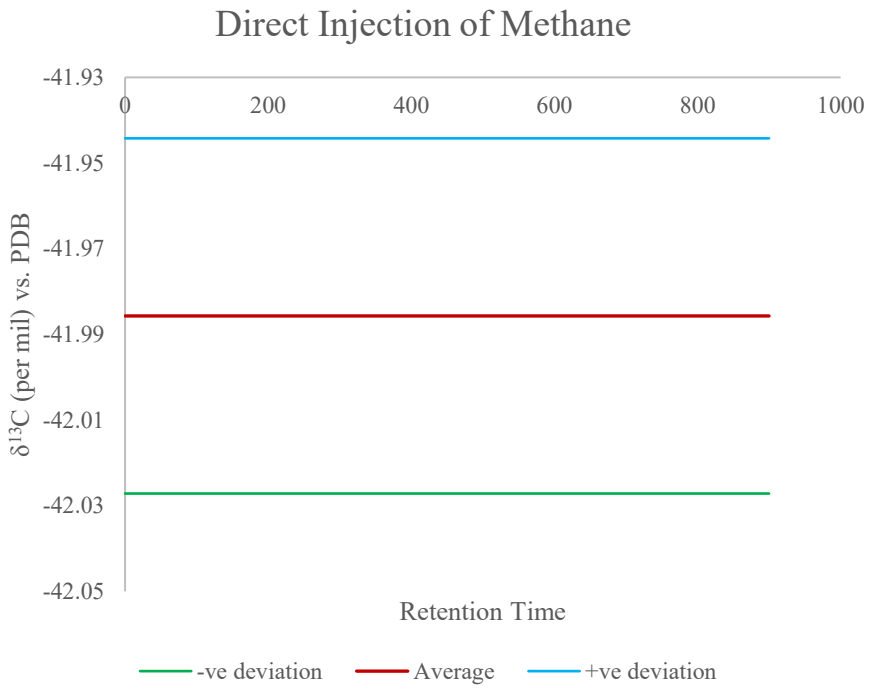


Figure 37 | Direct injection via gas syringe into the GC-C-IRMS. The standard deviation is 0.05‰ $\delta^{13}C_{CO2}$ with the average value for the bulk gas at -35.02 ‰

3.4.8 Desorption Data: Time Steps

When the data are first collected from the IRMS IsoDat ® interface, the raw results were generated as a comma separated values (CSV) file. This provided information about the intensity of each peak, centred on mass 44, 45 and 46. Intensities that fell outside the 2000-7000 mV range were immediately identified and removed. The $\delta^{18}O‰$ values were presented alongside the $\delta^{13}C‰$ values. Whilst the oxygen values were not used in the interpretation of results, they were used to identify if the oxidation furnace was effective in each experiment, providing a reassuring quality-control. Deviations in the $\delta^{18}O‰$ values suggested that the furnace was not effectively oxidising the gas and the data may have been inaccurate. Once these checks were carried out, the CSV file was converted to an Excel spreadsheet (see Appendix Chapter 3 Results for full details). The average $\delta^{13}C‰$ value for the 5 gas injections was calculated and the average retention time used as the time step point to plot up the data. This is shown in Figure 38. The data obtained from this is akin to production data. Note that, after around 70% of total gas extracted, the volume of gas being removed from the sample was too small to produce a signal within the working range of the GC-C-IRMS.

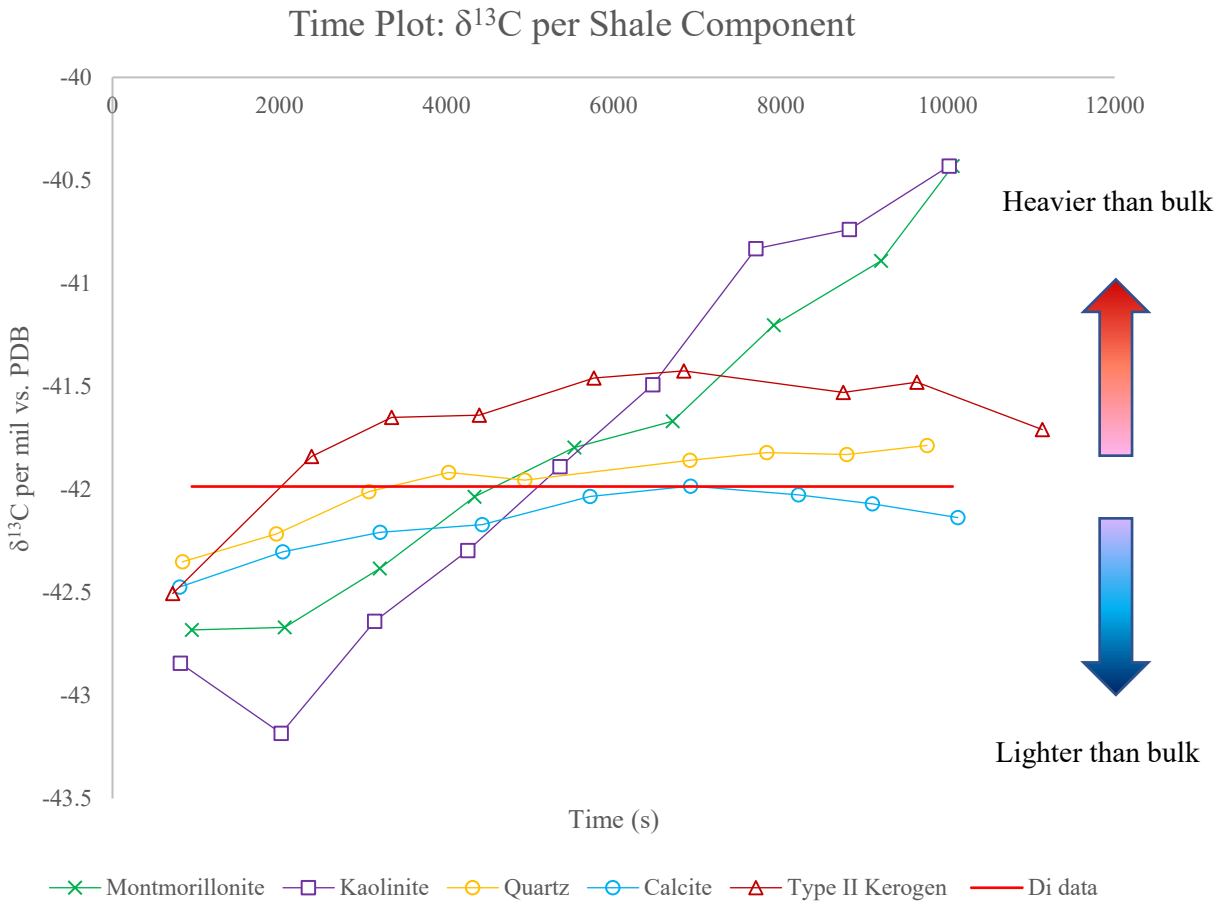


Figure 38 | Raw data collected on degassing samples. Plotted as $\delta^{13}C$‰ against the retention time in seconds.

Calcite

Figure 38 and Table 7 show the carbon isotope fractionation ratios for seven desorption steps of methane gas from calcite. For the initial 7000 seconds of the experiment, the degassed methane became increasingly positive, isotopically heavier than the first gas measurement but still isotopically more negative than the bulk gas. With time, the degassed gas trended towards the bulk gas. After 7000 seconds, the $\delta^{13}C$ values began to get slightly isotopically lighter and begin to deviate away slightly from the bulk gas. The $\delta^{13}C$ trend was fairly linear.

Table 7| Table showing the time step in seconds and the $\delta^{13}C$ value for a given step.

Time Step	$\delta^{13}C$ ‰
806.5	-42.47
2040.6	-42.30
3206	-42.21
4427.5	-42.17
5719.4	-42.03
6922.7	-41.98
8215.9	-42.03
9101	-42.07
10123	-42.14

Quartz

Figure 38 and Table 8 show the overall degassing trend of quartz over the 10,000-second-long experiment. The $\delta^{13}C$ ‰ for methane gas extracted from quartz does not deviate far from the bulk reservoir gas. The initial 400 seconds degassed material with a composition slightly isotopically more negative than the bulk gas. After 5000 seconds, the remaining gas extraction steps were progressively heavier with $\delta^{13}C$ ‰ more positive than the bulk reservoir. The $\delta^{13}C$ ‰ trend was linear.

Table 8| Table showing the $\delta^{13}C$ of the degassing methane from the quartz sample plotted against the time step in seconds.

Time Step	$\delta^{13}C$‰
837.8	-42.35
1961.9	-42.22
3069.3	-42.01
4024.3	-41.92
4935.7	-41.95
6915.3	-41.86

7836	-41.82
8792	-41.83
9755	-41.79

Montmorillonite

Figure 38 and Table 9 show the δ^{13}C ‰ values measured for each given time step throughout the 10,000-second-long experiment. The initial time steps plotted with δ^{13}C ‰ values significantly isotopically more negative than the bulk reservoir gas and became progressively isotopically more positive throughout the course of the experiment. After ~4300 seconds, the δ^{13}C ‰ compositions became isotopically more positive than the bulk gas. The δ^{13}C ‰ trend was linear but has a much steeper gradient than the linear δ^{13}C ‰ trends of calcite and quartz.

Table 9| Degassing steps through time and δ^{13}C value for the methane gas extracted at each time step for montmorillonite.

Time Step	δ^{13}C ‰
949	-42.68
2062.8	-42.67
3202	-42.38
4336.8	-42.04
5531.1	-41.80
6709.3	-41.67
7919	-41.20
9202.5	-40.89
10062.5	-40.43

Kaolinite

Figure 38 and Table 10 show the δ^{13}C ‰ values measured for each given time step throughout the 10,000-second-long experiment for methane-degassing kaolinite. Kaolinite had the most negative δ^{13}C ‰ values of all the samples tested and the second measured time-step was more negative still. After this point, however the δ^{13}C ‰ trend showed a linear trend

toward an isotopically more positive composition, finishing at a similar $\delta^{13}C$ ‰ to montmorillonite. The gradient of the trend line was similar to that of montmorillonite and much steeper than calcite and quartz.

Table 10| Degassing steps through time and the $\delta^{13}C$ values measured for methane at each gas extraction step for kaolinite.

Time Step	$\delta^{13}C$ ‰
811.8	-42.84
2018.5	-43.18
3139	-42.64
4253.8	-42.30
5359.2	-41.89
6471.6	-41.49
7704.7	-40.83
8825.5	-40.74
10019.5	-40.43

Type II Kerogen

Figure 38 and Table 11 show the $\delta^{13}C$ ‰ values measured for methane-degassed from the type II kerogen through time throughout the duration of the 10,000-second-long experiment. Starting at a $\delta^{13}C$ ‰ value that was isotopically more positive than the bulk reservoir and similar to quartz and calcite, after only 2000 seconds the $\delta^{13}C$ ‰ value measured was isotopically less negative than the bulk gas. Unlike the inorganic material samples, type II kerogen did not plot a linear $\delta^{13}C$ trend but rather a gentle curve. After ~6000 seconds, the $\delta^{13}C$ values became isotopically more negative again.

Table 11| The degassing steps for Type II Kerogen and the $\delta^{13}C$ measured for each methane-degassing step.

Time Step	$\delta^{13}C‰$
722	-42.84
2382.6	-43.18
3341.6	-42.64
4393.8	-42.30
5763.8	-41.89
6840.8	-41.49
8750.5	-40.83
9631.8	-41.48
11134.7	-41.71

3.5 Discussion

The raw data collected in the sample cell - GC-IRMS experiment will now be discussed. It is evident from the results and Figure 38 that the individual components produced a unique $\delta^{13}C$ degassing curve. The utility of this for determining the following will be discussed:

A. A geochemical index to help determine original GIP and volume of total gas extracted,
B. The composition of the shale that a gas has been extracted from,
C. How these two factors can help determine the drainage of a shale gas well and the recovery factor of a given shale gas well.

3.5.1 Gas extraction data and volumetrics

The setup of the custom-built sample cell allows for calculation of several key parameters;

1. Isotopic composition of the bulk gas injected
2. Volume of gas initially injected into the reference cell and thus introduced onto the sample
3. Adsorption onto the sample
4. Volume of gas extracted at each extraction step
5. $\delta^{13}C‰$ value of each extraction step
6. Volume of residual gas that cannot be extracted
7. Material balance to calculate the isotopic ratio of the residual gas

Canister desorption experiments do not know the starting isotopic composition of the gas, how much gas was originally in the sample, accurate calculation of residual gas or the

material balance required to ensure a closed system. To recover the residual gas, the shales must be pulverised and degassed but there is high potential for gas to be lost in this process.

The full details of how the gas volumes are calculated are outlined in chapter 2: Methodology bur some details are reiterated here Table 12. The cell is attached to a pressure transducer. By rearranging the ideal gas law, the volume of gas in the reference cell and introduced into the sample can be calculated. The full volumetric calculations for each sample are in Appendix: Chapter 3 Results.

Table 12| Volume of sample cell and reference cell total cell volume and the sample cylinder measured using water injection techniques.

Cell Component	Volume (cm^3)
Reference Cell (V1-V2)	12.85
Sample Container Cell	11.5
Cell Volume	32.08
Sample Cylinder	1.0

Figure 39 shows the $\delta^{13}C$ fractionation trends for each of the 5 samples tested, plotted against volume of gas extracted. Initially, this looks similar to the time plot but with a few noticeable differences. The Type II kerogen, which was the longest running experiment retained more gas than calcite and quartz which ran for a shorter time period. The kerogen $\delta^{13}C$ of CH_4 plot is also significantly compressed in the latter half of the curve when compared to the time data. Kaolinite and montmorillonite also have a more compressed curve after 50% gas extraction when compared to 5000 seconds (half the time plot). This generates a steeper $\delta^{13}C$ of CH_4 profile in the latter half of the fractionation trend. Quartz on the other hand has a more compressed first half, the 4th extraction step at ~4000 seconds occurring at over 55% of the gas extracted. Note that the gas volumes measured are for the total gas extracted from the cell, the

free gas and any desorbed gas. This is to reflect a shale gas well which would be a mixture of gas absorbed onto surfaces but also free gas within the pore spaces.

How can these degassing curves be used to understand the lifecycle of a shale gas well?

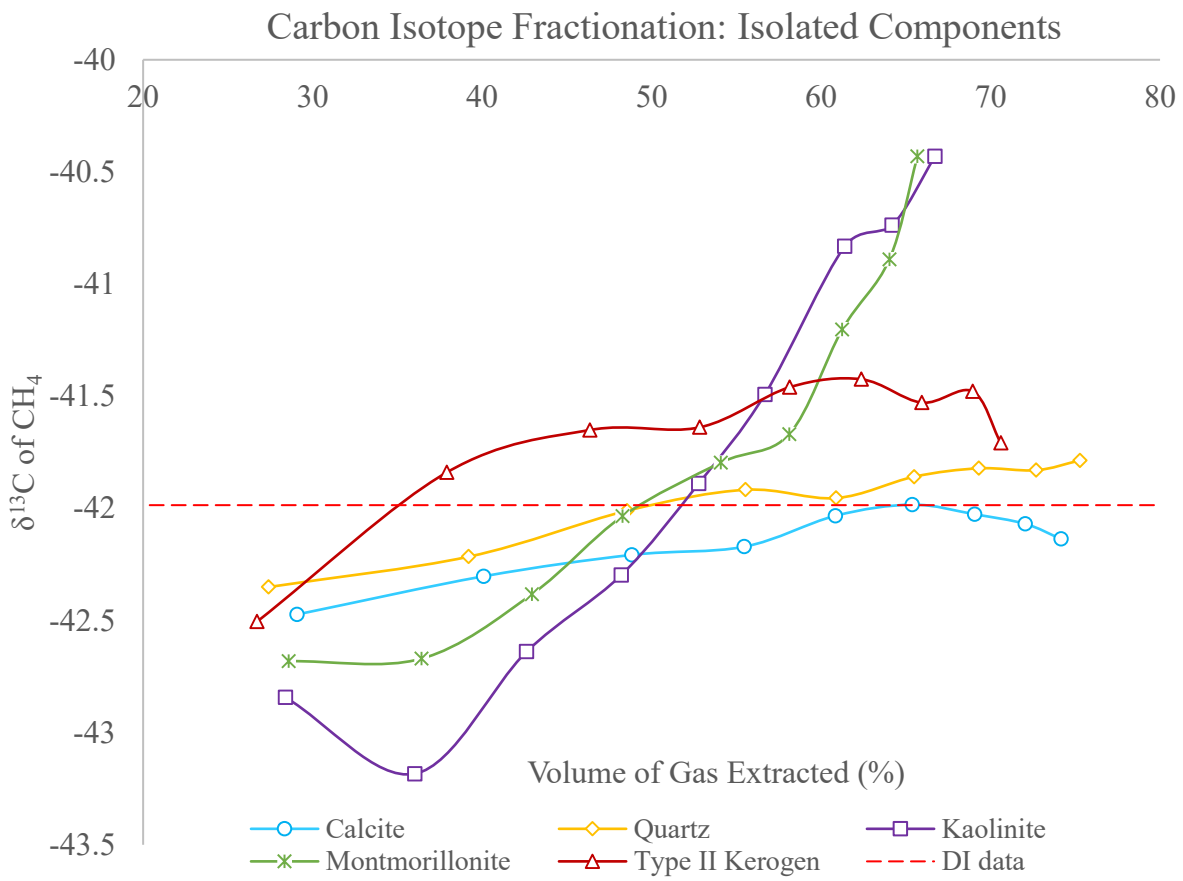


Figure 39| $\delta^{13}C$ of CH_4 fractionation trends for the 5 shale components tested plotted against the volume of gas extracted.

The significance of this data is that the individual shale components yield their own unique effect on isotopic fractionation with gas extraction which, in this experimental set up, can be correlated with a specific volume of gas extracted. Unlike the commonly sited trope that $\delta^{13}C$ of CH_4 is dominated purely by the TOC content, this data suggests that clays also have a significant impact on the $\delta^{13}C$ of CH_4. This has implications for papers which suggest that the $\delta^{13}C$ of CH_4 relates purely to desorption of gases from organic surfaces and using this proxy for gas storage capacity of a shale (Liu et al., 2016a; Ross and Bustin, 2009a; Strąpoć et al., 2006b; Tang and Xia, 2011). The change in stable carbon isotope composition with degassing

is strongly influenced by the clay minerals. The Langmuir isotherm analysis suggests that the clays were contributing to the overall storage capacity of the shale and cannot be ignored when considering a stable carbon isotope geochemical index for determining the percentage of total available gas extracted from a shale gas well. This is also shown in table 13 which show the calculated excess soption for the kerogen and clays. This was not possible for calcite and quartz due to the inaccuracy of the pore size analysis and presence of too-large pores for accurate BJH pore size distribution and total porosities.

Table 13| Excess sorption for Kerogen and clay samples

SAMPLE TYPE	$\Delta^{13}C$	EXCESS SORPTION (G/L)
TYPE II KEROGEN	-42.29	9.342E-04
	-41.90	9.396E-04
	-41.78	6.870E-04
	-41.75	5.812E-04
	-41.80	5.014E-04
	-41.71	4.401E-04
	-41.76	3.899E-04
	-41.82	3.500E-04
	-41.60	3.163E-04
MONTMORILLONITE	-42.20	1.006E-03
	-42.19	9.738E-04
	-41.90	6.861E-04
	-41.55	6.072E-04
	-41.32	5.417E-04
	-41.19	4.878E-04
	-40.72	4.295E-04
	-40.41	3.889E-04
	-39.95	3.574E-04
KAOLINITE	-42.36	1.027E-03
	-42.70	9.750E-04
	-42.16	6.903E-04
	-41.82	6.139E-04
	-41.41	5.478E-04
	-41.01	4.917E-04
	-40.35	4.460E-04
	-40.26	4.068E-04
	-39.95	3.596E-04

If the $\delta^{13}C$ of CH_4 is influenced by clay components which this data shows is the case then $\delta^{13}C$ of CH_4 is not a proxy for gas desorbing from TOC but could be a combination of

desorption-diffusion through clay and TOC pore networks or desorption from organic or clay surfaces. As shales are dominated mainly by clays, siliciclastics and carbonates with typically less than 5% TOC, by not attributing $\delta^{13}C$ of CH_4 to clays, current theories for interpreting $\delta^{13}C$ of CH_4 values are likely to be misleading. This potential importance of clays has been suggested in previous bodies of work but is often overlooked in favour of TOC (Bustin et al., 2008b; Cheng and Huang, 2004b).

Each mineral contributed to the $\delta^{13}C$ ‰ to varying degrees in order to produce distinct isotopic fractionation curves from 100% gas in place to ~70% gas extracted. This suggests that, if the composition of a shale is known then the expected isotopic fractionation degassing trend can be predicted. Figure 40 shows a rough schematic of what this could look like for three shales of three different compositions:

1. Blue dashed would represent a s shale with moderate TOC and a high quartz and calcite content
2. Purple-dashed line would represent a shale with fairly equal proportions of clays, inert material and organic material
3. Dark-red dashed line would represent a shale with a high clay and moderate TOC (%)

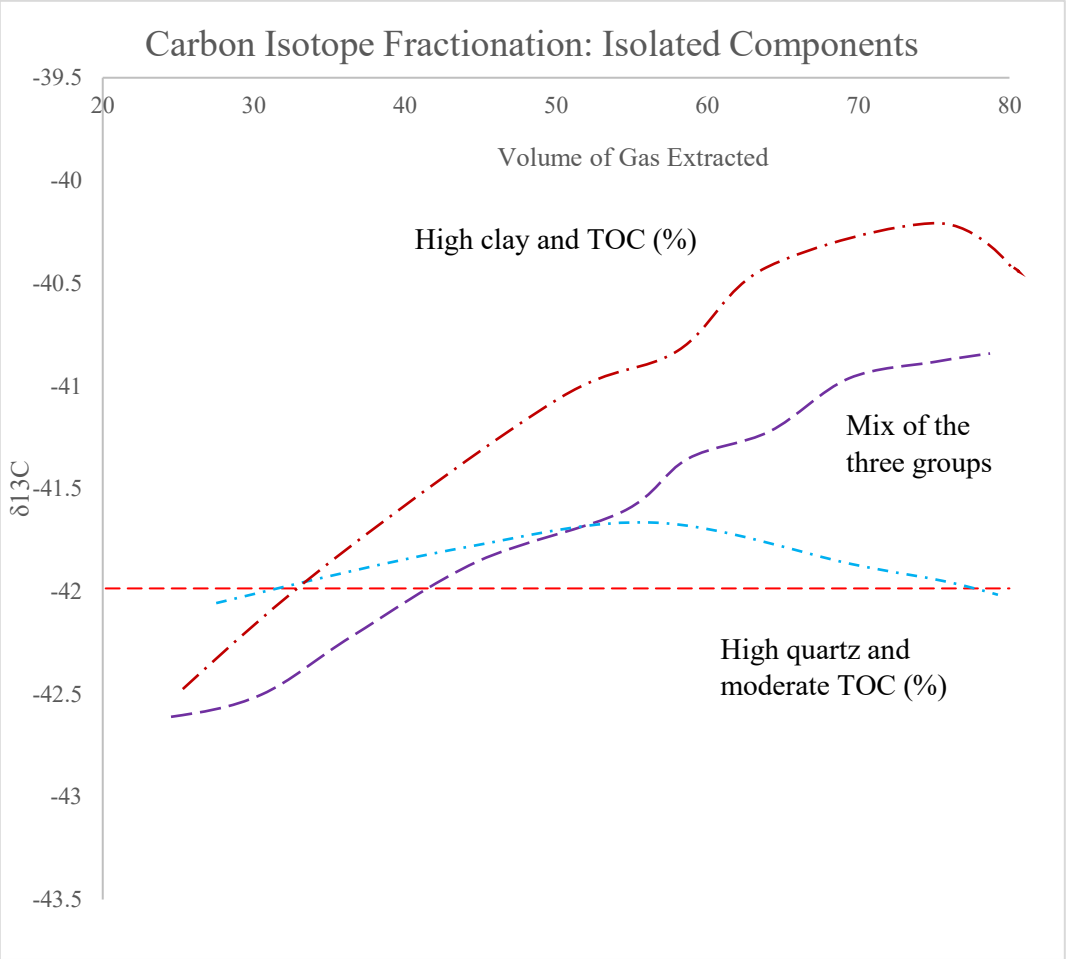


Figure 40| rough schematic of what a quartz, calcite and TOC rich shale would plot like (blue dashed), a 35%, quartz, 35% clay and 30% TOC shale would plot like (purple dahs) and a clay and TOC rich rock (red dashed line)

Understanding how the $\delta^{13}C$ ‰ changes with shale composition with regards to the total volume of gas in place can inform how to manage the well. If the $\delta^{13}C$ ‰ plots towards the end of the curves produced in Figure 40 then a large proportion of the original GIP has been produced and it would not be viable to refracture the well. If only a small volume of the total GIP, based on the composition of the shale, has been extracted after several months of production but the production rate has declined it would be viable to refracture the well as it is likely there is gas remaining. However, to best inform this decision, the tail of these compositional curves must be considered.

3.5.2 Material Balance: plotting the tail of the isotopic fractionation curves

Figure 41 shows the material balance plot for the five isolated shale components. Full calculations of this are shown in Appendix: Chapter 3 results. The simple equation used for this calculation is as follows;

$$M_{(z)}F_{(z)} = m_{(1)}f_{(2)} + m_{(2)}f_{(2)} \dots m_{(x)}f_{(x)}$$

Where M(z) = initial δ^{13}C of CH_4, $F_{(Z)}$ = total gas fraction, $m_{(x)}$ = δ^{13}C of CH_4 for each step, $f_{(x)}$ = volume extracted for a given step.

Figure 41 shows that the inert materials continue to become isotopically heavier with progressive gas extraction. The clay minerals must be retaining gas that is isotopically lighter than the final measured gas extraction step. This is not expected in a typical isotope fractionation system in which the isotopically more negative gas is degassed first (Tang and Xia, 2011). It may mean that some gas is irretrievably trapped in pores and will not degas unless there is further stimulation. Similar to the clay materials, the organic material is retaining gas that is isotopically lighter than the last measured pulse of gas.

Plotting the tail of the isotopic fractionation curve against total volume of gas is a useful indicator for forecasting the future of a shale gas well. Whilst laboratory experimental conditions are different to those of a producing reservoir and upscaling between the two is unlikely to be straightforward, the data collected here suggests that the clays and organic material would produce a roll-over of the δ^{13}C ‰ value after ~70% of the total GIP has been extracted. Whilst that value is too when considering the recovery factor for real shale reservoirs, the fact that there is a reversal in the isotope trend when a large volume of the total extractable volume of gas has been removed when clays and organics are degassed may still be applicable to shale gas reservoirs with much lower recovery factors. If a shale gas well

which has been producing for several months begins to degas gas which is becoming progressively isotopically more negative, changing from a progressively more positive trend, and is degassing from a clay-rich shale, it may be an indication that well is has tapped most of the extractable gas and is plotting towards the end of the production curve.

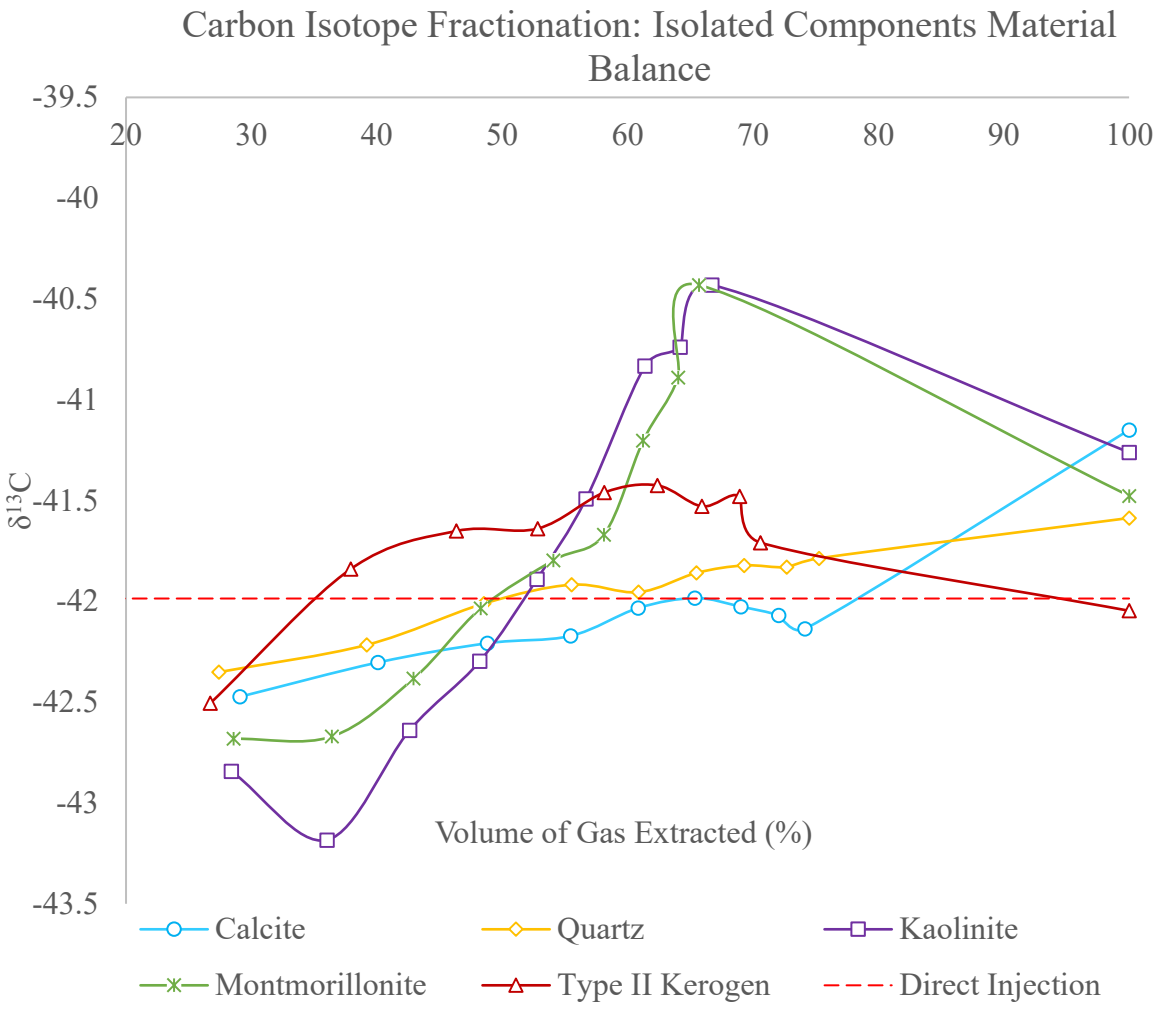


Figure 41| Material balance calculations for the 5 shale components tested

3.5.3 How might this data be applied as a geochemical index?

This data is promising for the generation of a $\delta^{13}C$ of CH_4 geochemical index for degassing shales. Comparing the data seen here to data in (Liu et al., 2016a) where XRD analysis is carried out on the Lower Permian Shale of southern North China shows that degassing illite

and quartz rich shales produces a $\delta^{13}C$ of CH_4 trend similar to the degassing clays and quartz shown in this body of work, however the trends in the paper are related to the total organic carbon content of the shale.

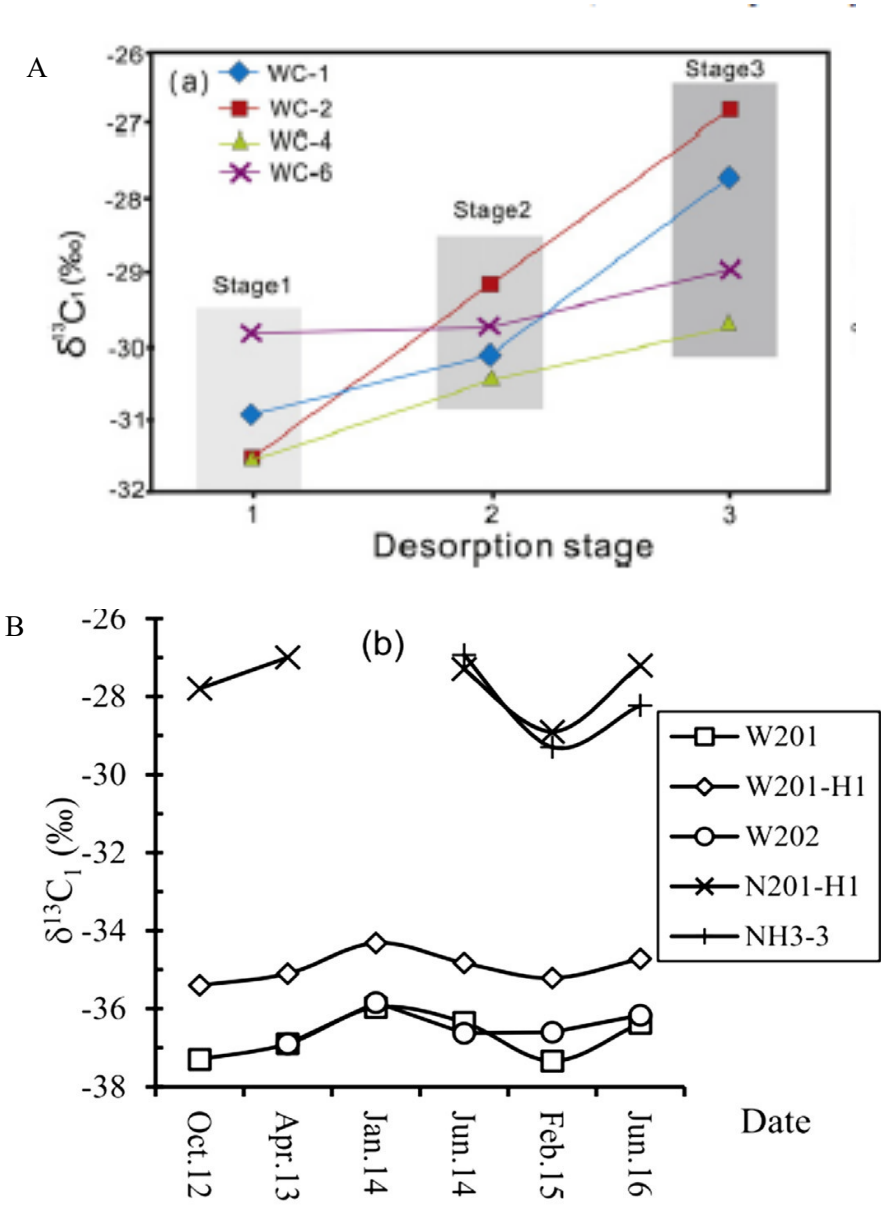


Figure 42| examples of canister desorption experiments from collected from depth which show the $\delta^{13}C$ trend for different degassing shales through time. A. (Liu et al., 2016b) and B. (Zhang et al., 2018)

Similarly, in other bodies of work, carbon isotope fraction trends are mapped and broadly related to mineralogy and TOC (%) by suggestion and theory as opposed to laboratory measurements (Zhang et al., 2018). Figure 42a shows four shales with varying TOC. WC-4 with the highest and WC-6 with the lowest and the magnitude $\delta^{13}C$ of CH_4 does not correlate

with TOC (%). Using the data collected in this thesis, the implication would be that WC-1 and 2 are dominated by clays and the $\delta^{13}C$ of CH_4 trend seen is related to the clay content. In order to use this method as a geochemical index, the petrographic composition of the shale would have to be identified. The relative proportions of each material would be multiplied by the $\delta^{13}C$ of CH_4 points of the standard curve to create an expected $\delta^{13}C$ of CH_4 trend with volume of shale degassed. This would then be compared to the measured, desorbed through time data. This would allow the time plots to be plotted in terms of volumetric data and the total volume of gas in place calculated. The data shown Figure 42b shows data collected from the Longmaxi Formation in China and would undergo a similar interpretation. The trends shown here are more similar to the type II kerogen plots, unfortunately no mineralogy data is available from this study but the authors suggest that the $\delta^{13}C$ of CH_4 seen relates to both TOC and mineralogy without further clarification.

These examples of $\delta^{13}C$ of CH_4 from degassed shales show time steps, not volumetrics and cannot provide any further information about the volume of gas extracted from the total gas in place. Many studies attempt to use complex models to predict how much gas is stored in the adsorbed phase vs free gas using isotopic variations however this typically discounts any effect from diffusion which some authors believe is the dominant cause of $\delta^{13}C$ of CH_4 (Xia and Tang, 2012a). By focusing primarily on the composition of the shale, the $\delta^{13}C$ of CH_4 can be attributed to a mineral component rather than diffusion/desorption which allows for a simple geochemical index to predict the total GIP of a shale.

3.5.4 Material balance and predicting the end of the $\delta^{13}C$ curve

The volumetric data shows two key points. Firstly, that individual mineral samples yield their own unique $\delta^{13}C$ of CH_4 trend with volume of gas extracted. Clays have a steep, linear gradient from isotopically negative to isotopically more positive. Inert calcite and quartz have

a shallow, linear gradient from isotopically negative to isotopically more positive. Type II kerogen however has an unusual trend, initially degassing and becoming isotopically more positive, then rolling over and becoming isotopically more negative again. Figure 41 shows how this data can also be used not only to identify which components of a shale influence the $\delta^{13}C$ of CH_4 of CH_4 but also how mass balancing the curve can be used to show what the final stage of the curves must look like. As the custom-built sample cell allows for full volumetric calculation, the entire $\delta^{13}C$ of CH_4 curve for each mineral has been predicted.

What can the degassing trend inform about the drainage area?

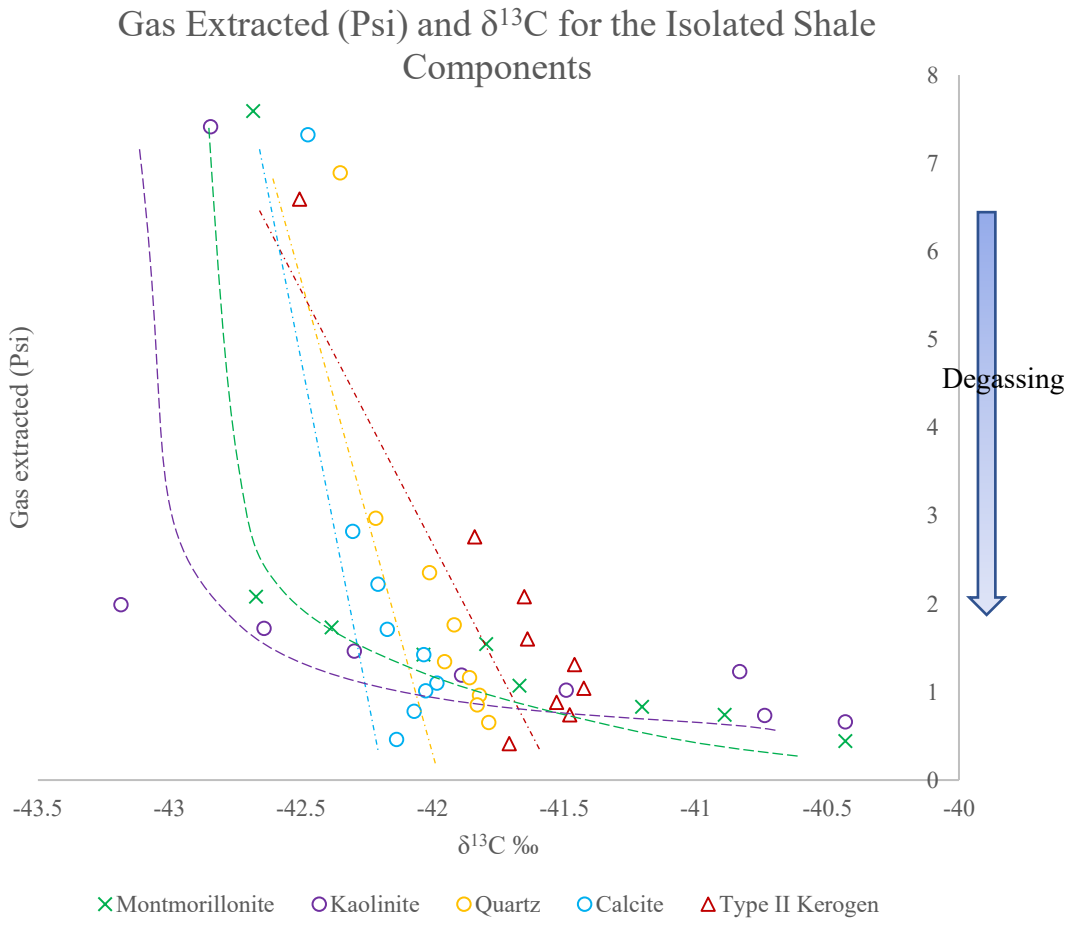


Figure 43| Degassing trend lines with actual gas volume in psi from experimental setup. The psi is the total volume fo gas extracted with each extraction step and is the data in it's raw form As the fractionation of ^{12}C and ^{13}C occurs via desorption

processes and not in mass movement of the free gas, this graph is showing the total amount of gas extracted and the associated fractionation but not the volume of gas in the adsorbed phase.

Figure 43 shows the stable carbon isotope degassing trend for each shale component plotted against the actual psi volume of gas for each experiment. The psi scale on the y-axis is the total pressure change with each gas extraction step which is proprotional to the total volume of gas extracted. As isotopic fractionation does not occur in blank cell runs, isotopic fractionation is not an inherent effect of Darcy flow. The fractionation seen in figure 43 relates to just desorption processes whilst the psi refers to the total gas removeed, both free gas and adsorbed gas.

Each constituent produces a distinct trend. Quartz, calcite and type II kerogen produce a linear trend whislt the clays produce a curved trend with changes in the $\delta^{13}C$ of CH_4 seen only in the later stages of degassing. The implications of these observations are that monitoring the $\delta^{13}C$ value of CH_4 with gas extraction from a shale gas well can inform the presence of shale constituents. Specific curves can be predicted from shale composition and deviations away from this may be an indication that the gas being extracted is in fact coming from a large drainage area, tapping into CH_4 that is degassing from a shale of a different composition. If several wells have been drilled in the area and the compositions of the target shale in each well is known, it may be possible to predict the drainage area based on overlap of the $\delta^{13}C$ of CH_4 signatures. This will be explored further in chapter 7, Applications to industry and final discussion.

3.6 Conclusions

The new, online combined sample cell - GC-C-IRMS method has the potential to yield high quality data with errors 1-2 orders of magnitude smaller than the overall trend of the data. The main conclusion from the preliminary data is that individual minerals do yield their own isotopic fractionation signature isothermally with volume of gas extracted – the fundamental basics of building a geochemical index for shale gas production data. The principals of this data suggest that, if the composition of the shale is known then expected $\delta^{13}C$ curves can be predicted with volume of gas extracted. Comparing this to production data would allow back calculation of the initial gas in place. Whilst the step from isolated shale components measured under laboratory conditions is a significant step away from unravelling the $\delta^{13}C$ trends seen in production data, it indicates that:

a. $\delta^{13}C$ of CH_4 is not solely a function of the organic material as is often stated in the literature
b. Presence of clay has a significant impact on the $\delta^{13}C$ of CH_4 even more so than the type II kerogen
c. Clay types, regardless of surface area tend to give a similar $\delta^{13}C$ of CH_4 trend
d. The link between the Langmuir volume and the gradient of the $\delta^{13}C$ is unusual with the inert and clay materials plotting on a linear axis but the Type II kerogen plotting separately

Furthermore, the isotherms for each constituent plot as expected based on literature; through simulated production time, the isotopic signature becomes more positive which is expected with both diffusive and adsorptive fractionation (Ji et al., 2012a; Jing et al., 2016; Strąpoć et al., 2006a). This will be considered further in Chapter 7.

4.0 C_1-C_2 Fractionation in Degassing Shale Constituents

4.1 Abstract

Assessments of both potential and producing shale gas reservoirs require several key pieces of information: i) how gas is stored within the shale, ii) total gas in place (GIP) and iii) location on the decline curve allowing calculation of estimated ultimate recovery (EUR). In shale gas plays, gas is stored within a heterogeneous, organic and inorganic matrix and with tortuous networks of macro to nanoscale pores. Gas can be stored free within pore spaces or absorbed onto the matrix of solid shale components. Total GIP of a shale reservoir requires prediction of gas stored freely in macro pores and adsorbed onto mineral surfaces however there is not currently a consensus on how to accurately calculate the free gas to adsorbed gas ratio. A suggested proxy for gas stored in the adsorbed phase has been using isotopic or molecular weight fractionation driven by sorption kinetics however other factors may influence geochemical gas fractionation during depressurisation such as diffusive fractionation and surface chemistry of shale components.

Considering this question in another way; how do components of a shale contribute to change in gas geochemistry and how can this information guide calculations of the recovery factor for a shale? Measuring change in gas geochemistry during the entire depressurization procedure gives a fractionation trend related directly to the isolated shale component and recovery factor (overall proportion of gas extractable from a reservoir), regardless of whether the change in geochemistry relates to desorption or diffusive processes. Identification of the position on a decline curve early in well production history and proportion of total gas extracted after a given amount of production time informs well spacing, use of infill drilling and timing of refracking. Current decline curve methods apply a best fit mathematical model to production data and may be unconnected to the physical and chemical reality of the reservoir. By linking

the empirical geochemical characteristics of a shale to production decline, more shale-specific analysis of decline curves can be carried out.

Chapter Aims

- to isolate individual shale components and test how they influence change in C_1-C_2 ratio with gas extraction,
- to generate a molecular weight fractionation curve for each isolated shale component for a given volume of gas extracted thus creating a volume-based production decline curve related to shale geochemistry,
- consider the influence of organic material on C_1-C_2 fractionation by degassing two shales from the same formation but with differing amounts of organic carbon and inorganic constituents,
- make inferences about how C_1-C_2 fractionation trends can be used when considering volume of total gas extracted from a shale reservoir

4.2 Introduction

Shale gas is natural gas trapped within mature and low permeability shale beds. Unlike conventional gas reservoirs, which are dominated by free gas in a porous, inorganic matrix, shale gas reservoirs are more complex and contain gas stored in multiple forms, namely free in fractures and pores, sorbed onto the surfaces of kerogen and clay minerals, or dissolved in bitumen and kerogen (Curtis, 2002). Sorbed gas can make up 20 to 80% of the total gas present (Jing et al., 2016). As gas is stored in several phases, the contributions of each phase to total gas in place (GIP) must be known in order to predict the total volume of gas in place. Calculating the volume of shale gas in place however, is an ongoing area of dissention in the literature (Chalmers and Bustin, 2007a; Gensterblum et al., 2015a; Jarvie et al., 2004; Ross and Bustin, 2009a; Schettler et al., 1989b).

4.2.1 How do we access shale gas?

Shale gas is accessed by technologies such as hydraulic fracturing and horizontal drilling (Yuan et al., 2014a). Hydraulic fracturing induces new fractures, which ideally join with existing natural fractures, to transform the low permeability matrix into a more permeable horizon. Proppants delivered by the fracturing fluid maintain connectivity of the new fracture network. Horizontal drilling enables a number of wells to be drilled from a single pad. Economically, it is more cost effective to drill fewer wells that target “sweet spots” in the shale reservoir which have large volumes of extractable gas associated with them. Ideally, the drainage area of a shale gas well, volume of total gas extracted after a given length of production time and residual gas would be known to maximise the productivity of a well.

4.2.2 What happens to a shale gas well?

Shale gas well production is characterised by a reduction in extracted gas volumes over time to form a decline curve with a steep initial phase and a subsequent gentle tail. The first short-term phase occurs mainly in the first 12 months and represents around 25% of the recovered gas. The second long-term phase lasts for one or two decades and represents 75% or more of well production. This is shown in the production data in

Figure 7 (Middleton et al., 2017). Predicting the nature of the production decline curve has implications for the economic forecasting of a well; if a large volume of gas was being extracted from a small area then infill drilling is a viable option whereas the same volume of gas over a larger area would reduce viable options to refracturing the well and would help to dictate the concentration of well spacing.

4.2.3 What can be done to improve recovery?

Following hydraulic fracturing of a shale the average recovery of the total gas in place is only around 13% (Sandrea and Sandrea, 2014). Refracturing of a shale, therefore, can access some of the remaining gas in place and the initial production levels of the virgin well can be reproduced or exceeded (Middleton et al., 2017). Refracturing of existing wells has obvious financial and environmental benefits owing to the reduced impacts related to the reuse of existing infrastructure. Refracturing will only provide economic benefit however if there is enough gas retained within the rock that has yet to be extracted. This requires realistic approximations of the recovery factor of a shale gas well, or expressed alternatively, the volume of gas extraction as a proportion of the gas reserves.

4.2.4 What do we need to understand?

Knowledge of the expected gas likely to be extracted from a hydraulically fractured shale allows informed estimates of the likely return from the initial financial investment. The initial pulse of shale gas, which experiences an exponential decline, is a relatively smaller fraction of the total. Managing the tail, which reflects a gradual long-term decline in produced gas volumes, represents most of the gas from the well (King and others, 2010). Understanding of the expected rate of decline allows informed estimates of when the financial return will be delivered, when the well will be closed and whether any further stimulation should be considered (King and others, 2010). An example of a production decline curve is shown in Figure 44, a well drilled into the Barnett Shale, US. The original predicted production decline curve is shown in green with the actual production data plotted in red. After 12 months the well was re-stimulated. The refractured gas curve is plotted as three predicted phases, blue is high, grey is median and yellow is low. The actual produced data plots initially higher than the highest phase then drops rapidly to the median. There is uncertainty as to what the following months and years of production will produce. Managing this tail effectively is integral to the well economics.

Understanding the decline curve relates to the proportion of gas extracted from the well relative to the remaining extractable abundance i.e. the recovery factor. Current methods to predict the recovery factor attempt to either numerically model the volume of gas stored as free gas vs. adsorbed gas or by using decline curve analysis to predict the tail based on the initial production (Arps and others, 1945). Modelling or laboratory testing yields varying results on what components dictate gas storage. Questions related to gas storage include: whether gas dominantly stored adsorbed onto the surface of organic material or the surface of clays; what proportion of the gas is in the adsorbed phase, and does this vary between different shales; what causes the variation. The storage capacity of a shale and the controls on gas adsorbed are not

fully understood due to the complex, heterogenous nature of shale rocks (Etminan et al., 2014; Hao et al., 2013; Schettler et al., 1989b; Song et al., 2019; Tang et al., 2016, Sandvik et al., 1992).

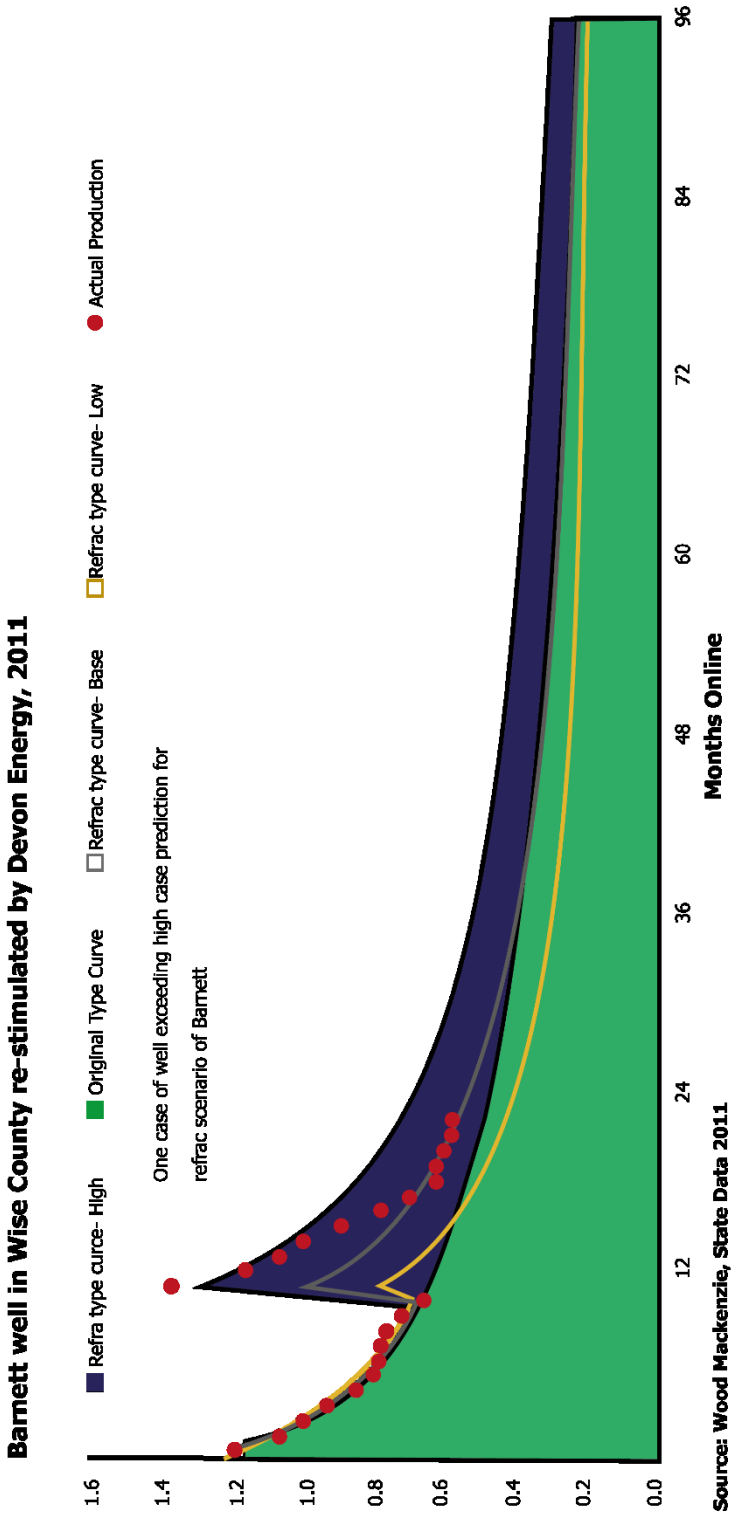


Figure 44| Example of production decline curve plotted with billion cubic feet on the x-axis and time on the y-axis from Wood Mackenzie, Production Report 2011.

4.2.5 Current methods for predicting the shale gas decline curve

Three modes of operation are used to estimate the recoverable gas from a shale gas target:

i) Analogue approaches use pre-existing resource estimates made for similar producing shale horizons can be applied and where data is available for a number of producing shales that data can be used to determine a range of expected values (Guo et al., 2015.; Jarvie et al., 2007; Romero-Sarmiento et al., 2013a). The Barnett Shale has been studied in detail since the early 1980's and has been suggested to be a good analogue for British Shales, especially the Bowland Shale (Department or Energy and Climate Change, 2013).

ii) Volumetric calculations using geological fundamentals such as estimated porosity and interconnectivity of nano-, meso- and macro- pores can be used to predict the recoverable shale gas contents and these are especially applicable to shale gas targets that have no existing production data (Ambrose et al., 2010). Estimates of Gas in Place (GIP) are obtained by application of a recovery factor to arrive at a value for estimated ultimate recovery (EUR), (Dahaghi and others, 2010; Smith et al., 1984a; Zou and Rezaee, 2019b).

iii) Decline curve analysis relies on existing data from producing wells that can be extrapolated forward (Arps 1945). A cut-off can be defined based on daily amounts of gas extracted(Ambrose et al., 2011a; Tan et al., 2018). See section 1.7.1 for a more detailed explaination

An example of the decline curve would be: economic limits of 215 Mcf/d for the total gas stream (including condensate) and 50 Mcf/d for dry gas only produced an average cut-off production rate at 133 Mcf/d for the Barnett shale (Guo et al., 2013). The EUR is then calculated by integrating the area of the decline curve up to the cut off.

4.2.6 Limitations of the current methods

Analogue approaches, useful in conventional reservoir analysis, are less applicable to shale gas reservoirs (Shabro et al., 2011). Shales are heterogenous. The heterogeneity in a shale is unparalleled in conventional reservoirs. The volume of shale gas that can be stored will be influenced by the sorption capacity of the surfaces of shale continents thus the compositional heterogeneity will have a profound influence on storage which is not a consideration in conventional reservoirs. The total pore volume and pore size distribution will also influence the total volume of gas that can be stored as well as influence the rate at which the gas can escape the shale gas reservoir (Etminan et al., 2014a; Fathi and Akkutlu, 2009a; Schloemer and Krooss, 2004; Soroush et al., 2014; Tang et al., 2017). Volumetric calculations are typically based on conventional reservoirs and thus do not provide an accurate measurement of the gas stored as this does not directly account for gas stored in the adsorbed phase.

Decline curve analysis most commonly involves the fitting of a production data from single or aggregated wells to a mathematical function. Originally, decline curve analysis found that hyperbolic models provided the best fit for production data from conventional reservoirs and future performance was predicted by extrapolation of curve function (Höök et al., 2014). In unconventional reservoirs, the characteristically low permeability of the shale makes hyperbolic models less applicable and overestimations of recoverable gas are generated (Tan et al., 2018)]. The main issue with decline curves is that they may not be directly related to the physical properties of the reservoir (Höök et al., 2014; Tan et al., 2018).

4.2.7 The need for a new method

Next generation methods that enhance or replace conventional decline curves are an attractive proposition. Methods that are directly connected to the shale reservoir by diagnostic chemical data, rather than just a best fit mathematical approach to existing production data,

could provide a more accurate prediction of future production. One chemical characteristic that appears to have diagnostic potential is the change in molecular weight of gas components. Typically, in dry gas reservoirs, methane (C_1) , ethane (C_2) and carbon dioxide (CO_2) account for 99% of the total gas volume of a shale play (Ambrose et al., 2010). Thermogravimetric studies have revealed deviations in the adsorption/desorption isotherms of methane and ethane on the Marcellus Shale suggesting the possibility of a molecular weight-based geochemical index that is diagnostic of reservoir depletion levels (Wang et al., 2015b). Understanding what influences this inherent fractionation and relating it to proportional volume of gas extracted from the initial total gas in place would provide another way to predict the recovery factor of a shale gas well.

4.2.8 What causes this inherent gas fractionation?

According to literature studies, causes of the change in gas geochemistry with reservoir depressurisation is driven by sorption processes and/or diffusive flow (Etminan et al., 2014a; Li et al., 2017; Lorant et al., 1998; Romero-Sarmiento et al., 2013a; Schloemer and Krooss, 2004; Zhang et al., 2018). These studies are typically carried out by degassing, whole heterogenous shales (Etminan et al., 2014a; Psarras et al., 2017). The issues with this method are two-fold. Primarily, assumptions must be made about the proportion of lost gas from the initial coring procedure and lost gas when powdering the sample to measure any residual gas which means that gas in place measurements are uncertain. Change in gas geochemistry cannot be attributed to a specific volume of gas extracted which nullifies C_1-C_2 fractionation as a proxy for recovery factor.

The second issue is that the molecular weight composition of shale gas can be dictated by a number of factors which may influence the C_1-C_2. The initial composition of the gas relates to the origin of the gas depending on biogenic or thermogenic origin (Rice and Claypool, 1981;

Stolper et al., 2014). Initial kerogen cracking generates a specific C_1-C_5 distribution based on kerogen type, maceral content and maturity (Rexer et al., 2013; Xia et al., 2013).

Secondary fractionation through gas movement out of the kerogen into the shale matrix generates further fractionation as well secondary in-situ kerogen cracking [(Snowdon, 2001)]. Partial loss through migration will further alter this signature. Bacterial contamination can also have an effect on the molecular weight composition of the gas (Civan et al., 2011; Prinzhofer and Pernaton, 1997) This level of complexity involved in understanding the causes of molecular weight fractionation through time is exacerbated by further complicating factors such as water saturation, porosity, permeability and composition (Bustin et al., 2008b; Gensterblum et al., 2015a; Ross and Bustin, 2009b). As such methods which look at the change in C_1-C_2 with shale degassing cannot unravel these effects. Often however, fractionation is used purely as a proxy for desorption effects.

Using C_1-C_2 purely for desorption and thus a proxy for gas stored in the adsorbed phase does not account for any change in gas geochemistry with diffusion through the nanoporous network. The case for both of these factors to influence the C_1-C_2 ratio is as follows; less energy is required to desorb methane from mineral surfaces and it follows that smaller methane molecules will be preferentially liberated during desorption. Once desorbed, methane is almost twice as small as ethane (Figure 45) and navigates the nanoporous, tortuous matrix more readily than its higher molecular weight counterparts. The magnitude of C_1-C_2 fractionation is hypothesised to vary based on mineralogy as the components of a shale have differing surface chemistries and surface area which may influence sorption processes as well as exhibiting different pore network geometries which will influence diffusional fractionation (Javadpour et al., 2007; Loucks et al., 2009a; Zhang and Krooss, 2001b).

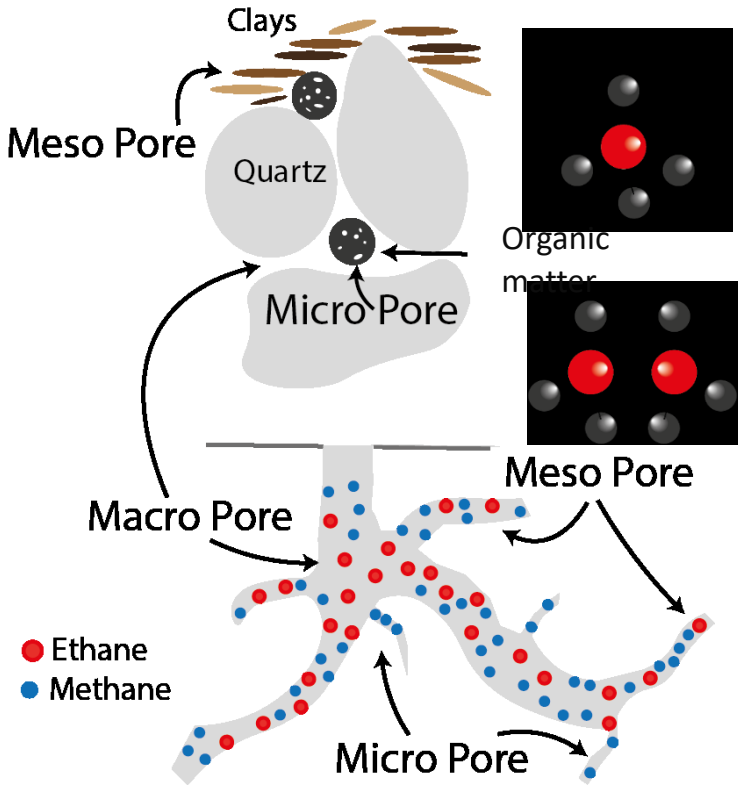


Figure 45| Schematic diagram to show how methane and ethane would move through pore networks of different sizes. Methane has a smaller kinetic diameter than ethane and can navigate more readily through the tortuous, nanoporous network of a shale as demonstrated in this cartoon of a shale pore network.

4.2.9 A different approach to C_1-C_2 as a geochemical index

Instead of using C_1-C_2 fractionation as a proxy purely for desorption *or* diffusion processes, this study aims to develop a geochemical index based on testable parameters of shales, injecting samples of a known composition with a known volume and molecular composition of gas. This allows measurements of the change in gas geochemistry through time, de-tangling the mechanisms that influence the C_1-C_2 ratio with degassing. By isolating individual shale parameters, the influence of mineraology specifically can be studied. Characterisation of the minerals in this study also show which factors may or may not have an effect on the C_1-C_2 ratio such as the influence of surface area, Langmuir volume and pore size.

In this study, we have developed a dedicated online adsorption/desorption-gas chromatography-flame ionization detector system that can detect and quantify the relative abundances of methane and ethane liberated from powders or plugs of whole rock shales or isolated shale components or standards. Understanding quantitatively the role that shale constitution plays in changing gas geochemistry with depressurization which will further our understanding of shale gas fundamentals and ultimately allow greater certainty when estimating GIP and volumes of gas extracted.

Why consider isolated components?

Many studies focus on the role of organic material in terms of gas storage capacity a shale, sorption processes and diffusion (Guo et al., 2017; Kim et al., 2017; Romero-Sarmiento et al., 2013a; Sandvik et al., 1992; Zhang et al., 2012a). There is less research into the gas storage capacity of shale minerals that may also influence the overall gas storage capacity. Some authors argue that clays play a significant role in the adsorption capacity of a shale, with illite and/or smectite displaying strong adsorption capacities (Boruah et al., 2019; Cao et al., 2015; Schettler Jr et al., 1991; Schettler et al., 1989b).

Some authors consider only the effects of the increase of surface area resulting from the clay nano pores to have significant effects on shale gas storage (Kim et al., 2017; Kuila et al., 2014b; Ross and Bustin, 2009a). Others suggest that the methane adsorption affinity varies by clay type (Heller and Zoback, 2014a; Kuila and Prasad, 2013). It has been suggested that the inorganic fraction can account for half of the adsorbed gas within a shale (Rexer et al., 2014) and that mudstone porosity is dominated by inorganic inter- and intra-particle porosity (Fishman et al., 2012). The technique of using the fundamental difference in sorption capacity of solid materials in the separation of hydrocarbon components for conventional natural gas is well known (Yang et al., 2017). The kinetics of adsorption is particularly important when

considering methane and ethane which have similar kinetic diameters (4.0 Å vs. 4.4 Å respectively). Clay minerals have electronically charged surfaces which make them ideal for separating gas mixtures (Yang et al., 2017).

Conversely, some authors argue that it is entirely dependent on the shale as to whether a positive correlation between kerogen volume, porosity and surface area is observed (Chen et al., 2019; Mastalerz et al., 2017). It has been suggested that the role of organic material pores on gas storage become more important than clay hosted porosity above a threshold of 2% TOC (Chen et al., 2018; Hao et al., 2013; Hou et al., 2017). Other authors suggest no correlation between adsorption capacity and clay volume or indeed, a negative correlation (Gasparik et al., 2014; Y. Wang et al., 2016).

An extensive study of the New Albany Shale, containing type II kerogen, showed no relationship between TOC and porosity (Mastalerz et al., 2013a) . Some authors have argued that in fact no definitive correlation exists between TOC and gas storage capacity (Zhang et al., 2012b; Zhong et al., 2016).

As such, the influence on individual minerals and components that make up a shale on gas storage capacity are uncertain. C_1-C_2 fractionation will not occur in flow of free gas but will be caused by molecular sieving via diffusion or through adsorption/desorption processes (Li et al., 2017; Zapušek and Marsel, 1998). If the fractionation of C_1-C_2 is driven solely by desorption then the fractionation may be quantitively relatable to volume of gas stored in the sorbed phase. Clays are fine grained and typically platy, they can generate very tight matrixes with a molecular sieving effect. The samples used in these experimental suites however, are powdered, the influence of diffusive fractionation is thought to be negligible (Etminan et al., 2014a).

4.3 Methodology

In order to test the change in C_1-C_2 gas ratios with depressurisation, from 100% gas in place to 100% gas extracted, a custom-built sample cell coupled with Gas Chromatographer Flame Ionising Detector (GC-FID) was developed. The sample storage container allowed for easy exchanging of samples between experiments and calculation of the volume of each sample. In order to test the influence of difference shale components on C_1-C_2 ratios in shale gas reservoirs, 5 key components were tested. Two clay samples, kaolinite and montmorillonite, two mineral samples, calcite and quartz and finally type II isolated kerogen.

The results of our experiments showed that, unlike the isotope geochemistry results discussed in chapter 3 where clays, kerogens and inert material all exert some level of influence on the changing gas geochemistry with depressurisation, molecular weight is almost solely dictated by the presence of organic material.

4.3.1 Sample selection

In this study, we have developed a dedicated online adsorption/desorption-gas chromatography-flame ionization detector system that can detect and quantify the relative abundances of methane and ethane liberated from powders or plugs of whole rock shales or isolated shale components or standards. Understanding quantitatively the role that shale constitution plays in gas storage and release will allow greater certainty when predicting GIP and volumes of gas extracted

In order to compare the results of the data collected in the isolated samples, two samples from the prolific Eagle Ford Shale reservoir were collected and sampled. Eagle Ford low organic with 0.06% TOC and a c composition dominated by calcite and quartz –

essentially a marl – and Eagle Ford high organic with quartz, calcite and kaolinite as the dominant material and a TOC of 5.35%, shown in Table 14

Table 14| Distinguishing features of the samples selected for degassing. The Eagle Ford samples were chosen to represent the end members for the mineralogies tested; clay and organic rich compared to clay and organic poor.

Sample Name	Chemical Formula	Distinguishing Characteristics
Kaolinite	$Al_2Si_2O_5(OH)_4$	Non-swelling phyllosilicate clay
Montmorillonite	$(Al_2\text{-}yMgy)(SiO_4O_{10}(OH)_2$	Hydrous swelling clay from the smectite group
Calcite	$CaCO_3$	Non-swelling pure carbonate mineral
Quartz	SiO_2	Non-swelling pure silicate mineral
Type II Kerogen	C	Marine algal-derived immobile organic material
Eagle Ford High Organic (EHO)	XRD: Quartz (40%), calcite (25%) clays (35%)	TOC: 5.35%
Eagle Ford Low Organic (ELO)	XRD: Calcite (82%) and quartz (18%)	TOC: 0.06%

4.3.2 Sample Preparation

Quartz, calcite and kaolinite were cleaned using heated 35% hydrogen peroxide for 8 hours then heated in air to 110˚C prior to experimentation. Montmorillonite is a type 2:1 clay mineral with anhydrous-Al layer between two Si-O layers. As it contains water loosely bound in its structural form, heating causes a transition to illite (Emmerich, 2013). Montmorillonite, therefore, was placed in a moderate temperature (35˚C) drying box for 72 hours prior to experimentation

The Kimmeridge Clay sample chosen to represent the type II kerogen underwent isolation of its solid organic matter content using acid extraction techniques (Horvath and Jackson, 1982). These techniques are described in detail in chapter 2: Methodology. A brief overview is given here.

The relatively high Kimmeridge Clay TOC (15%) also allowed manageable volumes of rock to be collected and acid digested, removing inorganic material whilst leaving a large enough volume of material to be experimented on. Type II kerogen was extracted initially by washing powdered Kimmeridge Clay shale with dichloromethane (DCM) to remove any free organic matter coating the calcite and silica grains. The sample was then rinsed and washed with 0.5M HCl (x3) and left overnight in 1M HCl. Finally, HF digestion required rinsing of the sample in 1:4 HCl/HF solution and heating on a hot plate at 40˚C. This process was repeated until there was no evidence of reactions occurring. The samples were then freeze-dried to remove any excess water, leaving a dry sample that had not been subjected to heat which could cause artificial maturation of the kerogen.

4.3.3 Eagle Ford Shale Samples

For examples of shales involved in shale gas production, two samples were selected from a suite of Eagle Ford shale samples collected at outcrop from the San Antonio Canyon, Texas, USA. These two samples were chosen after RockEval data to represent a low organic matter horizon and a high organic matter horizon. The Eagle Ford shale is a prolific source rock for shale oil and shale gas across the southern Texas border with Mexico. Cretaceous in age, this shale is really more of a marl of carbonaceous limestone. Table 15 indicates the diagnostic features of the Eagle Ford Shale as a shale gas play.

The location of the Eagle Ford Shale play is shown in Figure 46 which is complemented by a schematic stratigraphic column in Figure 47. An overview of the Eagle Ford Shale is summarised in Figure 47. The two samples were collected from the San Antonio Canyon on the 24th March, 2013. To characterise the samples, they were analysed using XRD, Rock-Eval and Brunauer–Emmett–Teller (BET) surface analysis to determine the internal features (e.g. pore size, shale composition, organic matter type and maturity). The techniques for this

analysis and the results will be discussed in the Methodology and Results section of this chapter.

Eagle Ford Shale sample preparation

Initially, the samples were cored into 1 cm^3 core plugs to test however it became apparent that in the coring procedure there was significant interference with the structure and composition of the shales. Large volumes of water were introduced to the shale whilst coring which caused swelling and breakages of the Eagle Ford High Organic (EHO). When attempting to core without water, the heat from coring the procedure also caused the shale plugs to crack. Coring without water to reduce the friction also increases the likelihood of alteration of the organic material from the high temperatures induced by fiction.

In order to prepare the samples with minimal alteration to the chemistry of the shale but also reducing the sample down to a testable size, the samples were powdered. Several studies have used powdered samples in their research at varying sieve mesh sizes (Cao et al., 2015; Chen et al., 2015a; P. Li et al., 2016; Mastalerz et al., 2017; Rexer et al., 2014, p. 20; Wright et al., 2015). In this study a range of 250-125 µm was used. Large grains would leave a greater than ideal dead volume in the sample container between these large grans. Grains less than 125 µm would be so fine and powdered that they would not retain any of the internal pore network and tortuous pathways.

The shale samples were powdered crushed with a hammer wrapped in aluminium foil to avoid sample contamination. They were then crushed further with a ceramic pestle and mortar. Finally, they were sieved to the 250-125 µm range, weighed and stored in the drying box.

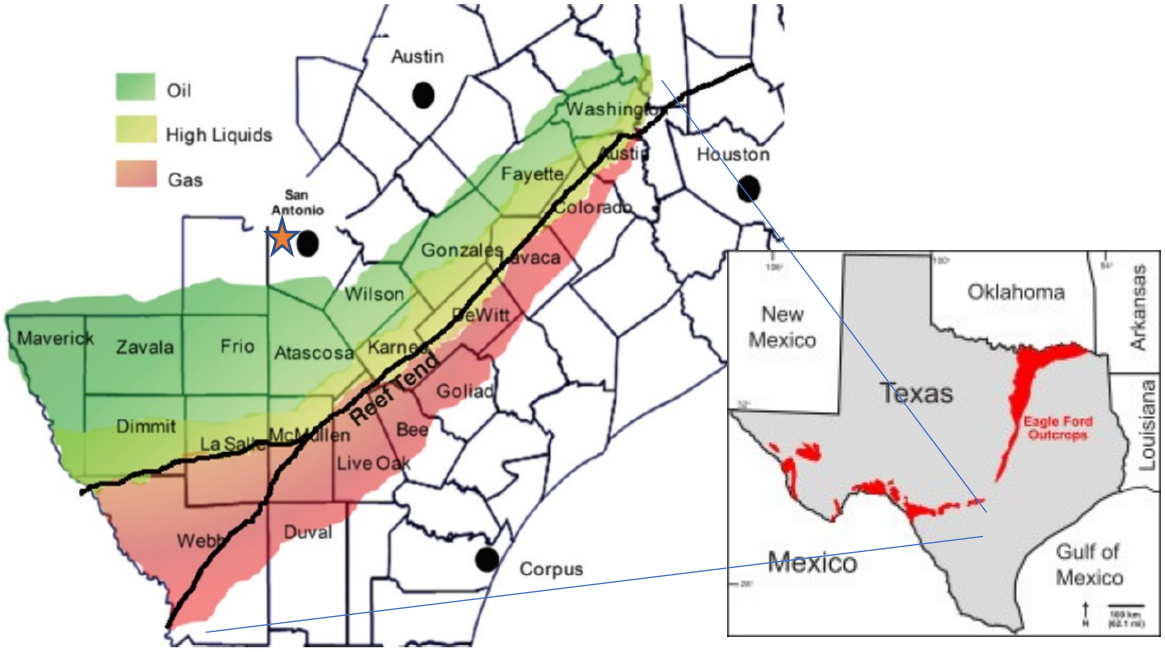


Figure 46 | Location of the Eagle Ford Shale plays, transitioning from oil mature in the NW to gas mature in the SE. From (Mullen, 2010). The orange star is the location of the San Antonio Canyon, Texas, USA where these sample were collected. Full details on sample selection, refer to the thesis of Dr Miriam Wright (Wright, 2019).

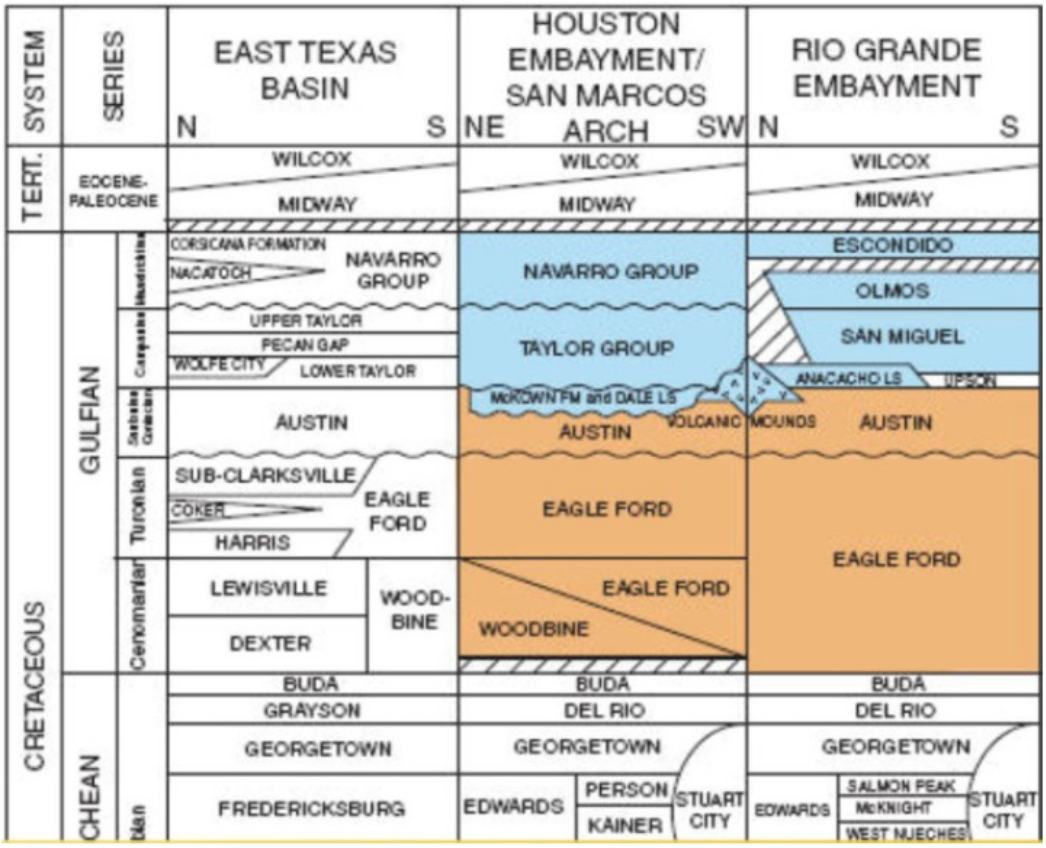


Figure 47 | Stratagraphic column highlighting the age and lithological location of the Eagle Ford shale across south Tex (Mullen, 2010)

Table 15| Table summarising a basic overview of the Eagle Ford Shale. (Dawson and Almon, 2010; Driskill et al., 2013a; Guo et al., 2012; Hsu and Nelson, 2002; Mullen, 2010)

Feature	Eagle Ford Shale
Age	Late Cretaceous: Cenomanian-Turonian
Location/Play Extent	West: Rio Grande River at the Mexican South: bounded by the Sligo Reef Margin (Fig. 2) North East: Thermal maturity and tapering into East Texas Basin
Thickness	Max 400ft thick with 250ft average thickness
Environment of Deposition	Marine-continental shelf, lateral and vertical variations in reservoir facilitated by marine transgressions depositing shales and marls
Producing Burial Depth	2,000 – 15,000ft with the eastern margin of the play seeing the deepest burial depths
General Composition	Highly variable, m-scale changes in % of carbonate, swelling vs. non-swelling clays and organic matter

4.3.4 Characterisation of the isolated shale components and whole shale samples:

Langmuir isotherm analytical procedure

A full description of the Langmuir isotherm analysis procedure can be found in Methods: 2.5.5 Langmuir Isotherm Analysis

To measure the monolayer adsorption capacity of each sample, Langmuir isotherms were measured using N_2 adsorption with the Quantachrome ® ASiQwin Automated Gas Sorption Instrument, version 5.2. The maximum volume of N_2 gas that can be adsorbed onto a sample is termed the Langmuir volume and is often used as a proxy for total adsorption capacity of a shale. Both adsorption and desorption is measured, generating an isotherm loop which can provide information about the pore geometry and capillary pressures of the pores. (Sing, 1985).

BET surface area analysis procedure

A full description of the BET surface area analysis procedure is found in Methods: 2.5.6 Brunauer-Emmett-Teller (BET) surface area. BET with be summarised briefly below.

BET surface area analysis measures the specific surfacea area of a material. This analysis was conducted using the Quantachrome ® ASiQwin Automated Gas Sorption Instrument, version 5.2. An extension of the Langmuir theory, BET surface area considers multilayer adsorption.

BJH pore size distribution procedure

A full description of this procedure is found in Methods: 2.5.7 Barrett, Joyner and Halenda (BJH) Pore Size Distribution but will be summarised briefly below

BJH analysis is employed to define the area of the pores and pore size disruption of materials with a range of pore size, from macro-pore to nano-pore was also collected on a Quantachrome R ASiQwin Automated Gas Sorption Instrument, version 5.2. BJH pore size distribution provides information of several key material characteristics including surface area, a pore volume and an average pore radius.

X-Ray Diffraction procedure

A full outline of the XRD procedure is available in the Chapter 2: Methodology section but will be summarised briefly below.

The two powdered shale samples were testing using an X-Ray Diffractometer, producing an x-ray spectrum of the crystalline minerals present in each sample. The peaks of these spectra were analysed and assigned to different mineral fractions based on the available mineral peak catalogue.

4.3.5 Custom-built sample cell and GC-FID

A custom-built desorption cell was built and connected to a Gas Chromatograph coupled to a Flame Ionization Detector (GC-FID) to measure molecular weight fractionation continuous degassing of samples. The online desorption cell-GC-FID instrument allowed for continuous measurement of hydrocarbon abundances within the extracted sample gas at set time-intervals; similar protocols have been followed for coal using off-line experiments using desorption canisters for the collection of gas (Institute, 1995) and stand-alone analytical instruments for GC-based analyses (Strąpoć et al., 2006). Figure 48 is a schematic diagram showing our instrument configuration.

Experiments utilised a 30:70 C_1-C_2 gas mixture, the initial molar composition of which was confirmed by direct injection onto the GC-FID. During operation of the online desorption cell-GC-FID instrument, the gas mixture was injected from the gas cylinder (1) into the reference volume (V1-V2) and then expanded into V1-V3 which contained the sample cell. A pressure transducer measured the reduction in pressure between the reference volume alone and the reference volume combined with the sample cell, allowing the volume of gas injected into the sample to be calculated. As such, the initial volume of gas in place could be determined. The equivalent of 55 psi of gas mixture was injected into each sample at the start of each experiment. As the pressure transducer was calibrated to -14.75psi as full vacuum, a value of 40.00 psi was aimed for within the reference cell.

Time was then given was then given to allow the gas to fully penetrate the sample material; normally the time required was between 2-5 hours and was dictated by the stabilisation of the pressure within the cell.

Gas was then extracted at given time intervals and introduced into the GC-FID. The data collected by the instrument generated intensity peaks of methane and ethane (measured in mV)

for each gas injection. The GC-FID had a working intensity range between 50 to 10,000 mV, allowing almost all the sample gas to be extracted and measured. He gas was used to flush out the remaining sample gas to ensure full extraction, allow very small volumes of gas to be measured and enable comprehensive monitoring of the beginning to end of reservoir gas depletion.

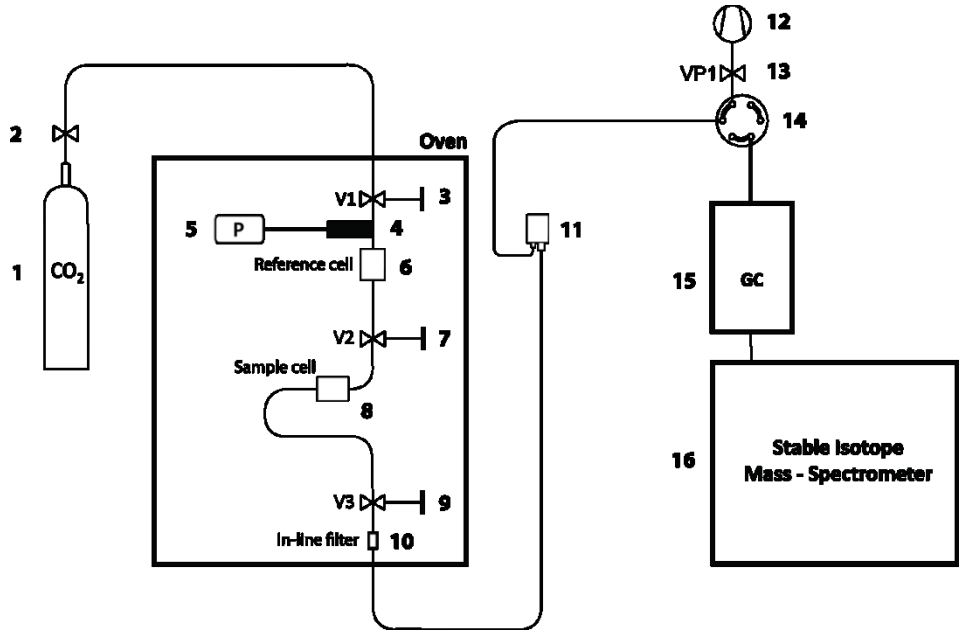


Figure 48| Custom-built sample cell coupled with the GC-FID. Chapter 2, Methodology explains the entire setup procedure.

Operational Design

A series of experiments were designed to assess molecular fractionation during progressive reservoir depletion. A 30:70 mixture of methane and ethane were adsorbed onto and then desorbed from isolated shale components. The isolated shale components provided the ability to assess the magnitudes of fractionations related to individual or isolated shale components and whole rock shales. Specifically, the online desorption cell-GC-FID instrument allowed calculation of: i) volume of sample, ii) sample composition, iii) initial gas starting composition, iv) molar volume starting gas mixture, v) number of moles extracted at each step, vi) number

of moles remaining at each step. These data enabled the calculation of the volume of gas extracted relative to the total volume of gas in place for each sample and its associated gas contents.

4.4 Results

The results of the Langmuir, BJH and BET analysis on the pure minerals have been discussed in chapter 3, Section: results. Here, the pure minerals will be reiterated only in table form whilst the full details of the Eagle Ford Shale samples will be discussed.

4.4.1 Isolated Mineral and Eagle Ford Shale BET, BJH and Langmuir analysis

Table 16 indicates the results of the BET, BJH and Langmuir isotherm conducted on the isolated shale components and the Eagle Ford Shale samples. EHO has a greater surface area, total pore volume and greater adsorption capacity than ELO. Both EHO and ELO have a lower surface area, Langmuir volume and total pore volume than the two clay minerals and Type II kerogen but greater than the calcite and quartz.

Figure 49 show the two Langmuir isotherms for EHO and ELO. EHO has a greater adsorption capacity than ELO, 19.347 and 8.047 cc/g respectively. Both isotherms exhibit a hysteresis loop between the adsorption and desorption process. Figure 50 shows the results of the pore size distribution BJH analysis with cumulative pore volume, pore radius and volume of pores plotted. Both samples have a similar median pore radius of 20.4 Å for ELO and 19.6 Å for EHO.

Table 16| BET, BJH and Langmuir isotherm analysis of the mineral fractions.

Sample	Adsorbed Quantity (N_2) Cm^3/g	BET Surface Area cm^3/g	BJH pore vol. cm^3/g	BJH pore volume <72nm cm^3/g
Kaolinite	42.9	11.80	0.0668	0.042
Montmorillonite	48.01	28.12	0.076	0.052
Calcite	2.78	0.189	0.004	0.0005
Quartz	0.83	0.04	0.001	0.0001
Type II Kerogen	51.42	14.40	0.08	0.047

Eagle Ford Low Organic (ELO	8.047	2.348	0.012
Eagle Ford High Organic (EHO)	19.347	7.303	0.029

4.4.2 Eagle Ford Shale Isotherms and BJH Analysis

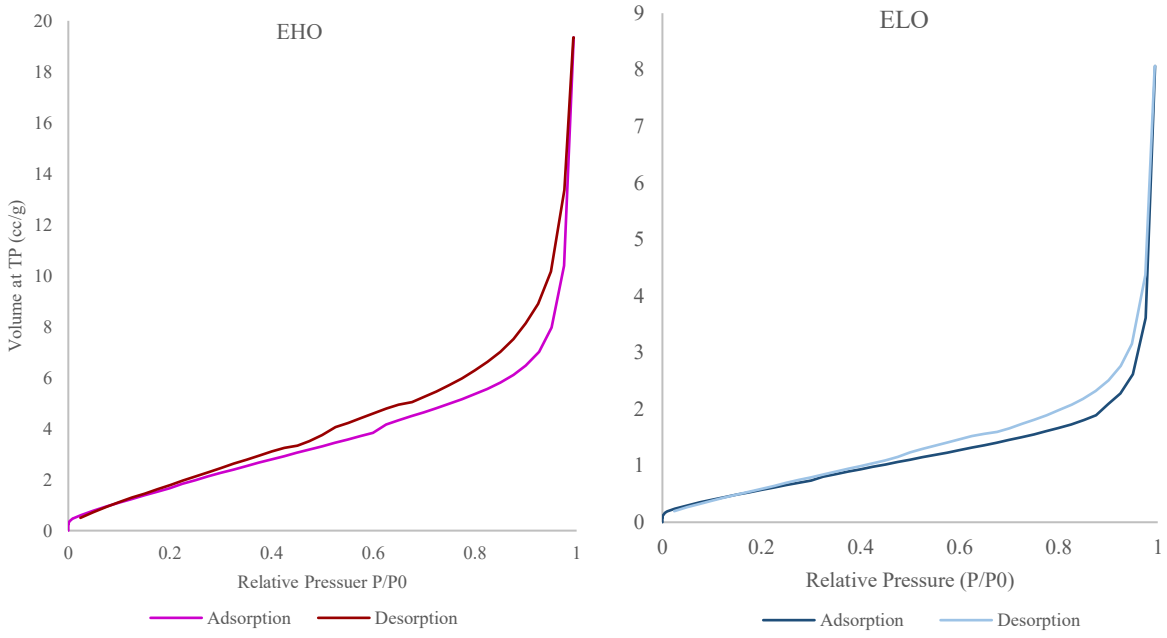


Figure 49| Langmuir isotherms for EHO and ELO respectively. Both desorption curves exhibit mini hysteresis. EHO has a Langmuir volume of 19.347 cc/g whilst ELO has 8.04 cc/g.

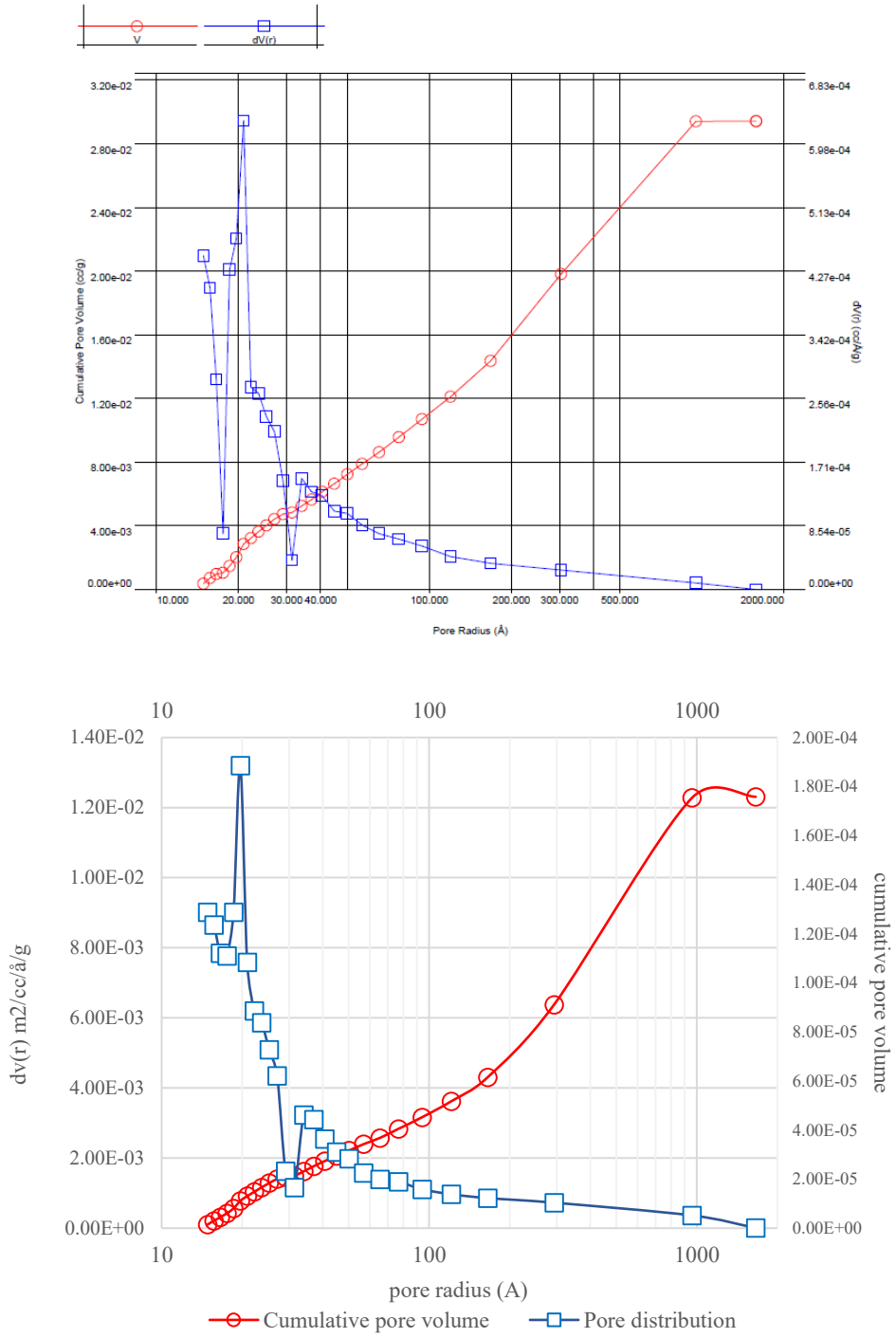
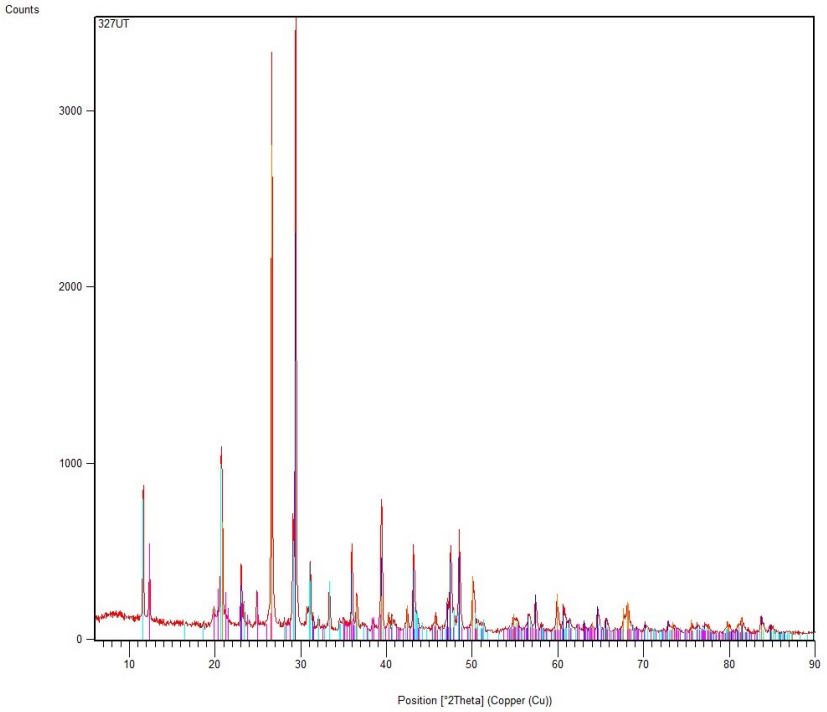


Figure 50| BJH pore size distribution analysis for both EHO (top) and ELO (bottom).

4.4.3 Eagle Ford Shale XRD Data

The two Eagle Ford samples were analysed by XRD to determine their crystalline composition, the peaks of this are shown in *Figure 51*.



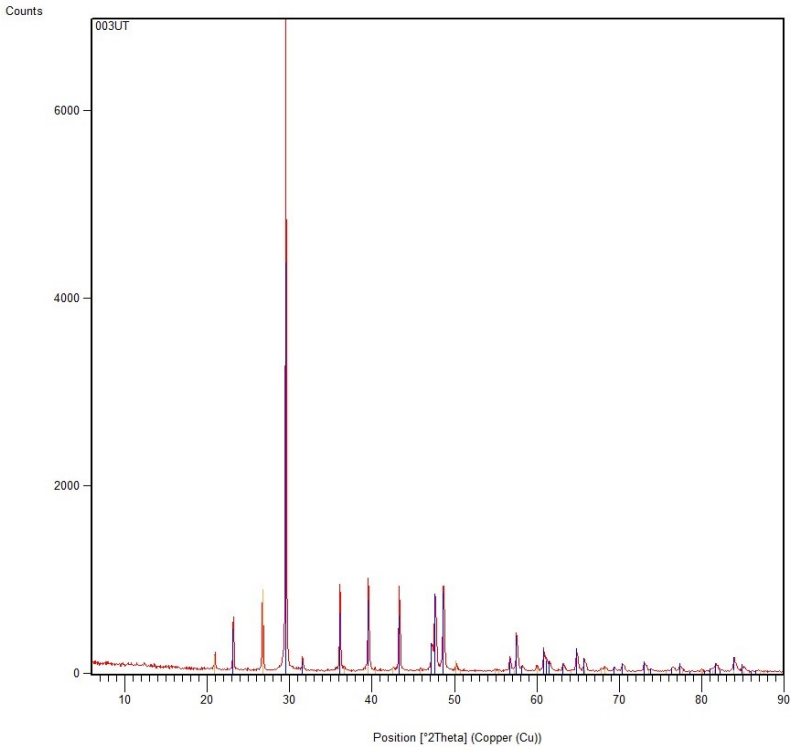


Figure 51 | X-ray spectrum produced by XRD analysis of the EHO (upper) and ELO (lower). EHO has a broader spectrum of material present.

ELO had a simple composition dominated by calcite (82%) and quartz (18%). There was a small number of clays present but the peaks were uncertain in the analysis. EHO contained 40% quartz and 25% calcite with 18% kaolinite and the remining 17% clay minerals with rough peak fits.

4.4.4 Rock-eval Pyrolysis

Table 17 shows the Rock-eval Pyrolysis data obtained. For the full procedure on the Rock-eval technique, refer to the methods section. Both sample were collected from surface outcrops and are marginally mature. ELO contains a very low amount of organic material whilst EHO is a relatively rich source rock.

Table 17| Rock-eval pyrolysis data for the EHO and ELO samples

Sample	Lithology	TOC	HI	OI
EHO	Clay and Organic rich	5.35	473	17
ELO	Carbonate rich - marl	0.06	154	909

4.4.5 FTIR: type II kerogen

Figure 52 shows the FTIR spectra collected for the bulk Kimmeridge Clay rock and the extracted Kimmeridge Clay kerogen, a type II kerogen. It is evident that not all of the inorganic fraction was completely removed in the HF and HCl digestion process outlined in Chapter two: Methodology, Organic sample preparation. However, it is evident that the relative proportion of the organic material has significantly increased compared to the inorganic fraction.

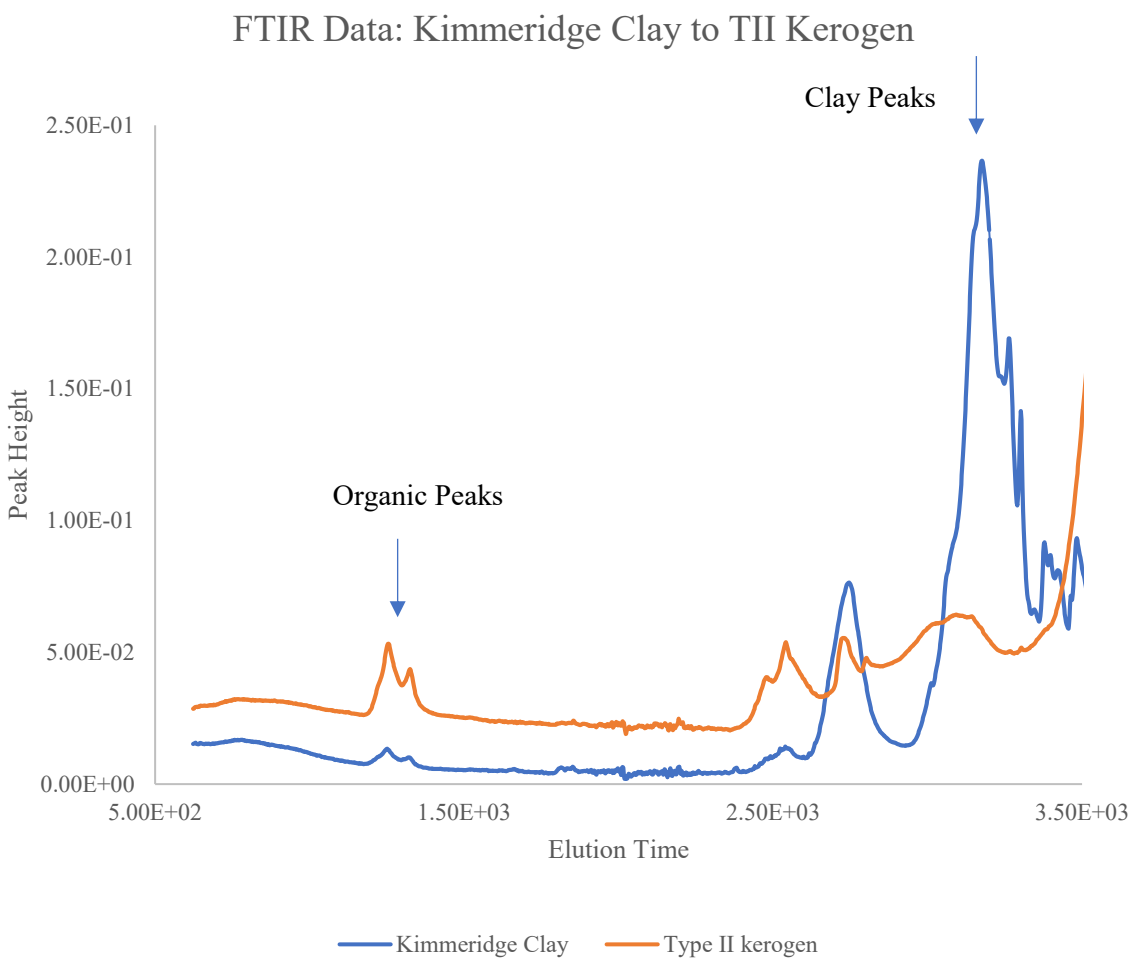


Figure 52| FTIR data showing the change in composition from the bulk rock, Kimmeridge Clay in blue, to the extracted kerogen in orange

4.4.6 Direct Injection Data

To ascertain both the composition of the bulk gas and to test the precision and accuracy of the GC-FID instrumentation, the C_1-C_2 mixture was directly injected into the GC-FID. Figure 53| Direct injection data from the sample bulk gas directly injected onto the GC-FIDshows the data collected from numerous direct injections. The average value of 0.298 was determined for the proportion of methane. The standard deviation associated with this was 0.000855.

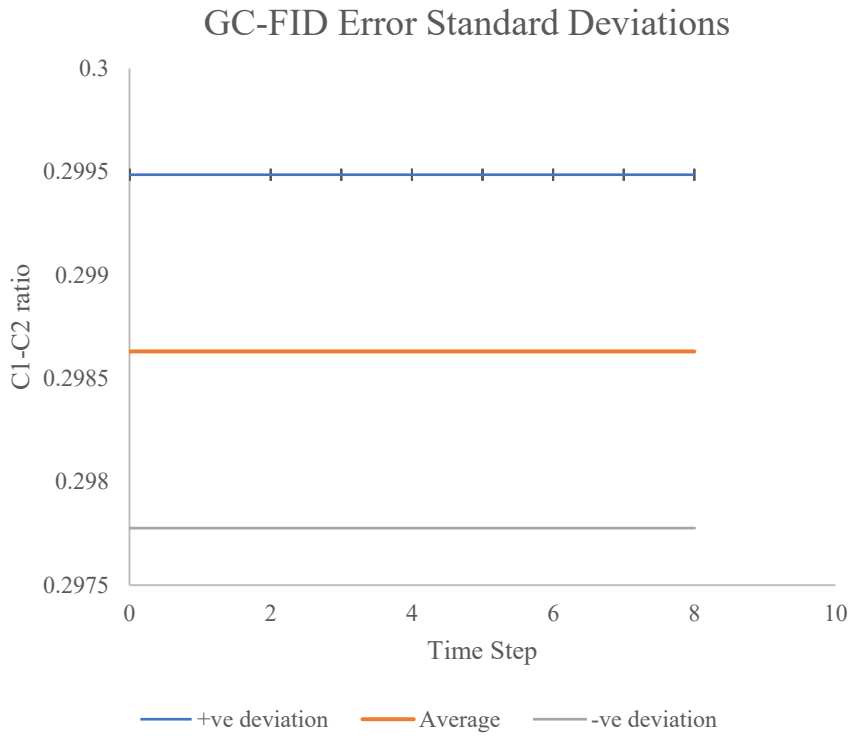


Figure 53| Direct injection data from the sample bulk gas directly injected onto the GC-FID

4.4.7 C_1-C_2 time steps: Minerals

Figure 54 shows the C_1-C_2 collected with progressive gas extraction from the sample cell. The bulk gas is shown by the red dashed line. It is evident from the graph that the organic material has a significant impact on the C_1-C_2 ratio.

Quartz and calcite begin with a slightly lower molar mass than the bulk gas so more C_1 relative to C_2. Whilst remaining fairly close to the bulk gas, both calcite and quartz degas material that is slightly more ethane enriched than the bulk gas. Towards the final stages of the experiment, both samples degas gas that is close to the baseline C_1-C_2 molar mass. Both montmorillonite and kaolinite have a more significant deviation away from the bulk gas and continue to degas more ethane rich material in the final degassing stages. Type II kerogen begins by degassing material that is more methane rich than the bulk gas but rapidly becomes more ethane rich than the bulk.

Table 18 indicates the data collected at each time step for these samples. It was possible to degas the kerogen sample for a prolonged period before reaching the intensity limit of the GC-FID. Both quartz and calcite remain at a molar mass between 25.85 and 25.96, close to the molar mass of the bulk gas (25.87).

Table 18| time step data and related molar mass of sample measured.

	Molar Mass						
Time Step	Quartz	Calcite	Kaolinite	Montmori-llonite	Type II Kerogen	ELO	EHO
1	25.85	25.85	25.85	25.83	25.67	23.95	23.88
2	25.87	25.86	25.87	25.86	25.75	23.93	23.86
3	25.88	25.87	25.89	25.90	25.87	23.94	23.89
4	25.89	25.87	25.90	25.92	25.98	23.95	23.92
5	25.91	25.89	25.91	25.94	26.07	23.96	23.95
6	25.92	25.91	25.93	25.95	26.15	23.97	23.97
7	25.90	25.93	25.95	25.97	26.24	23.98	23.99
8	25.89	25.96	25.973	25.99	26.37	23.98	24.01
9	25.91	25.96	25.99	26.00	26.33	23.99	24.02
10	25.89	25.95	26.02	26.02	26.40	23.99	24.04
11	25.87	25.88	26.12	26.04	26.48	24.00	24.05
12					26.55	24.01	24.06
13					26.62	24.02	24.07
14					26.68	24.02	24.09
15					26.76	24.023	24.11
16						24.06	24.10
17						24.04	24.10
18						24.03	24.14
19						24.02	24.13

ELO and EHO were tested on a second gas mixture after the first was fully used. As the gas mixtures were made in house using the pressure gauges, it was not possible to make a gas of the exact same methane – ethane composition so the total molar mass is different. In the discussion when the data are directly compared, the results will be displayed normalised to the

bulk gas. The results here are in their raw form. The bulk gas for the ELO and EHO samples had a molar mass of 24.00 with 43% of that being methane and 57% being ethane.

Table 19| the relative proportion of methane gas extracted from each gas pulse for all the samples.

Proportion of Methane per gas pulse							
Time Step	Quartz	Calcite	Kaolinite	Montmori-llonite	Type II Kerogen	ELO	EHO
1	0.300	0.300	0.300	0.302	0.313	0.436	0.441
2	0.299	0.299	0.299	0.299	0.307	0.437	0.442
3	0.298	0.299	0.297	0.297	0.299	0.437	0.440
4	0.297	0.299	0.296	0.295	0.291	0.436	0.437
5	0.296	0.297	0.296	0.294	0.285	0.435	0.436
6	0.295	0.296	0.295	0.293	0.279	0.434	0.434
7	0.296	0.295	0.293	0.292	0.272	0.434	0.433
8	0.297	0.293	0.292	0.290	0.263	0.433	0.431
9	0.296	0.292	0.290	0.289	0.266	0.432	0.431
10	0.298	0.293	0.288	0.288	0.261	0.433	0.429
11	0.299	0.298	0.286	0.287	0.256	0.432	0.429
12					0.250	0.432	0.428
13					0.245	0.431	0.427
14					0.241	0.431	0.426
15					0.235	0.430	0.424
17						0.428	0.425
18						0.429	0.425
19						0.430	0.422

Table 19 displays the raw proportion of methane extracted from each gas pulse. The bulk gas for the minerals samples had a C_1-C_2 ratio of 30% whilst the Eagle Ford samples had a C_1-C_2 ratio of 43% methane.

Figure 54 and Figure 55 show the time data for the pure minerals and the Eagle Ford Shale samples respectively. EHO has a composition that is a combination of quartz, clays, calcite and

organic material whilst ELO has a composition that is dominated by calcite with quartz and very minor organics. Both ELO and EHO begin with more methane outgassing that the bulk gas. ELO remains fairly similar to the bulk gas whilst EHO deviates away, releasing more ethane rich gas relative to the bulk towards the end of the experiment.

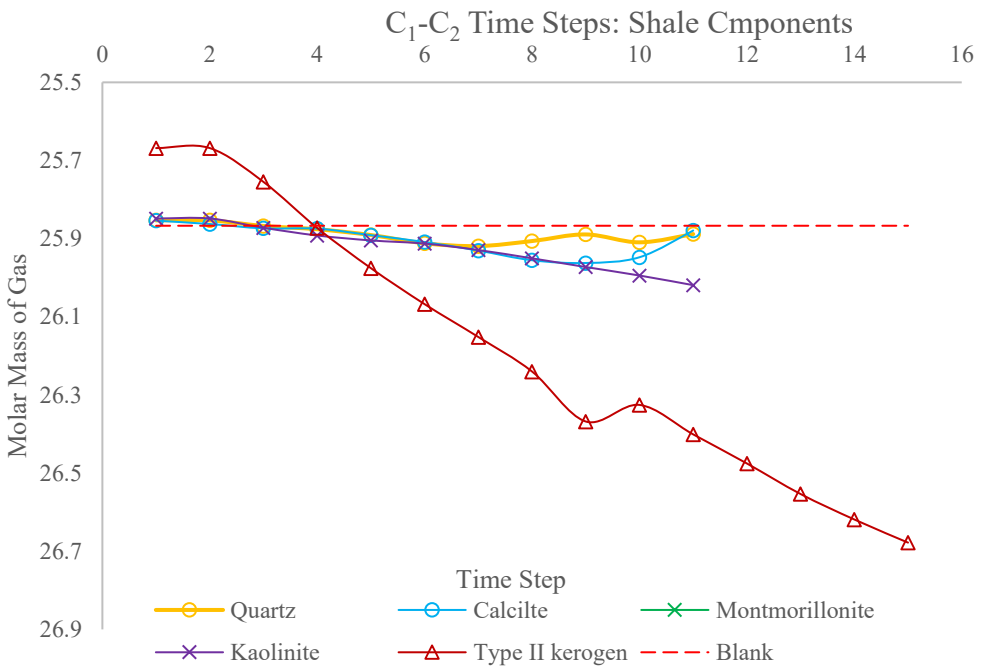


Figure 54| C_1-C_1 molar mass of the gas mixture for a give extraction step. Montmorilonite directly almost undeliesthe trend of kaolinite showing that,even with different surface properties, the C_1-C_2 fractionation trend is the same.

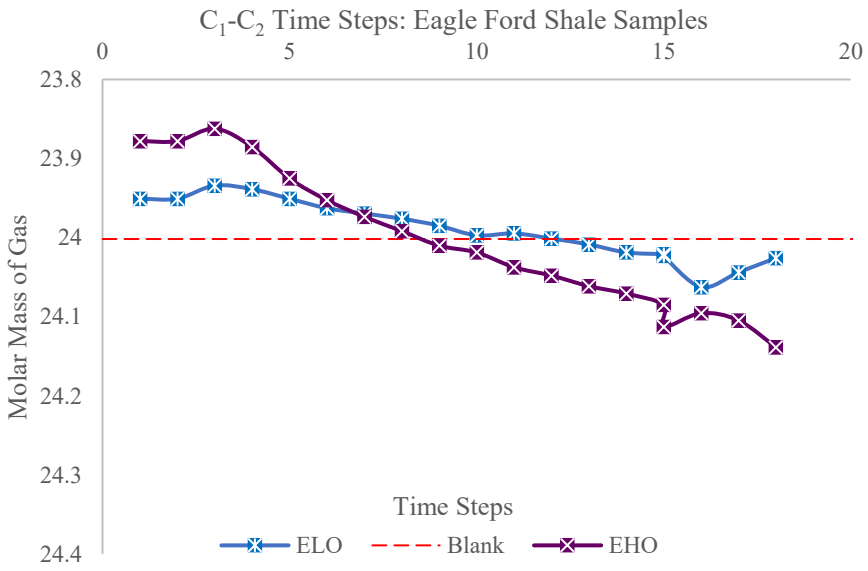


Figure 55| time step and molar mass for the two Eagle Ford Shale Samples.

4.5 Discussion

Whilst the raw time and C_1-C_2 data provides a general idea of the effects of mineraology on degassing C_1-C_2 gas composition, this experimental setup was specifically designed with the intention to allow volumetric calculation of the initial, extracted and residual gas.

4.5.1 What was the aim of this setup?

The setup of the custom-built sample cell is outlined in Chapter 2, Methodology and reiterated in Chapter 3, Carbon Isotope Fractionation from Degassing Shale Constituents. As a reminder, the cell is set up for calculation of several key parameters;

1. Molecular weight and relative proportion of C_1 and C_2 of the bulk gas injected
2. Volume of gas initially injected into the reference cell and thus introduced onto the sample
3. Adsorption of gas mixture onto the sample
4. Volume of gas mixture extracted at each extraction step
5. Relative proportion of C_1 and C_2 value of each extraction step
6. Volume of residual gas that cannot be extracted
7. Material balance to calculate the isotopic ratio of the residual gas

Table 20 reiterates the volume details of the sample cell.

Table 20| Volume of sample cell and reference cell total cell volume and the sample cylinder measured using water injection techniques.

Cell Component	Volume (cm^3)
Reference Cell (V1-V2)	12.85
Sample Container Cell	11.5
Cell Volume	32.08
Sample Cylinder	1.0

The volumetric data was calculable as the volume of gas injected and removed as each stage could be calculated using the cell volume and ideal gas law. See Appendix: Chapter 4 Results for full details on how these calculations were carried out. As stated in the introduction, the aim of this experimental series was to re-examine the typical way of degassing a shale reservoir, isolating the key mineral and organic constituents and examining how they influence the C_1-C_2 degassing trend. By beginning the experiment with a known volume of gas which has a known molecular weight composition, the change in gas geochemistry could be assessed from 100% gas in to place to maximum gas extracted. The final gas composition could be predicted through material balance plots. Table 21 indicates the standard deviation calculated for each gas extraction point for each component from the bulk gas. Type II kerogen has the greatest whilst the two clays have values almost indistinct from one another and certainly in error of one another. Calcite has a greater overall standard deviation away from the bulk reservoir gas whilst quartz has the smallest standard deviation away from the bulk reservoir. The sum total of the standard deviation of the measured C_1-C-$_2$ values from the bulk gas value is similar to a "fractionation factor" but is termed $\Sigma\Delta C_{1(0)} - C_{1(z)}$. $C_{1(0)}$ refers to the bulk gas. $C_{1(z)}$ refers to the measured C_1 fraction with each step. The deviation of each measured value from the bulk is summed to give a numerical approximation of the level of C_1-C_2 fractionation associated with each component.

Table 21| Standard deviation of the extracted gas from the bulk gas reservoir for the isolated minerals and the whole shale samples.

Sample	$\Sigma\Delta C_{1(0)} - C_{1(z)}$ (Standard Deviation from Bulk)
Quartz	0.0244
Calcite	0.0403
Montmorillonite	0.0732
Kaolinite	0.0736

Type II kerogen	0.3908
EHO	0.0974
ELO	0.0403

Volumetric data

Figure 56 plots the calculated volumetric data obtained for each sample. As the bulk gas was slightly different in composition between the pure mineral samples and the Eagle Ford Shale samples, they have been normalised to the respective bulk gas compositions in order to plot on the same graph.

Quartz and calcite: inert material

Quartz, the yellow circles, and calcite, the blue circles, in Figure 56 show that, with continuous degassing from 100% gas in place to ~95% gas extracted, there is little deviation in C_1-C_2 ratio away from the bulk gas (normalised in Figure 56). Both calcite and quartz degasses gas with a C_1-C_2 ratio that is similar to the bulk gas throughout the entirely of the experiment. Quartz has a slightly more C_2 enriched mixture than the bulk gas compared to calcite between 50 and 80% of the gas volume extracted. Calcite then has a more C_2-enriched signature than quartz between 80 and 90%. The final values for both minerals are approximately that of the bulk gas.

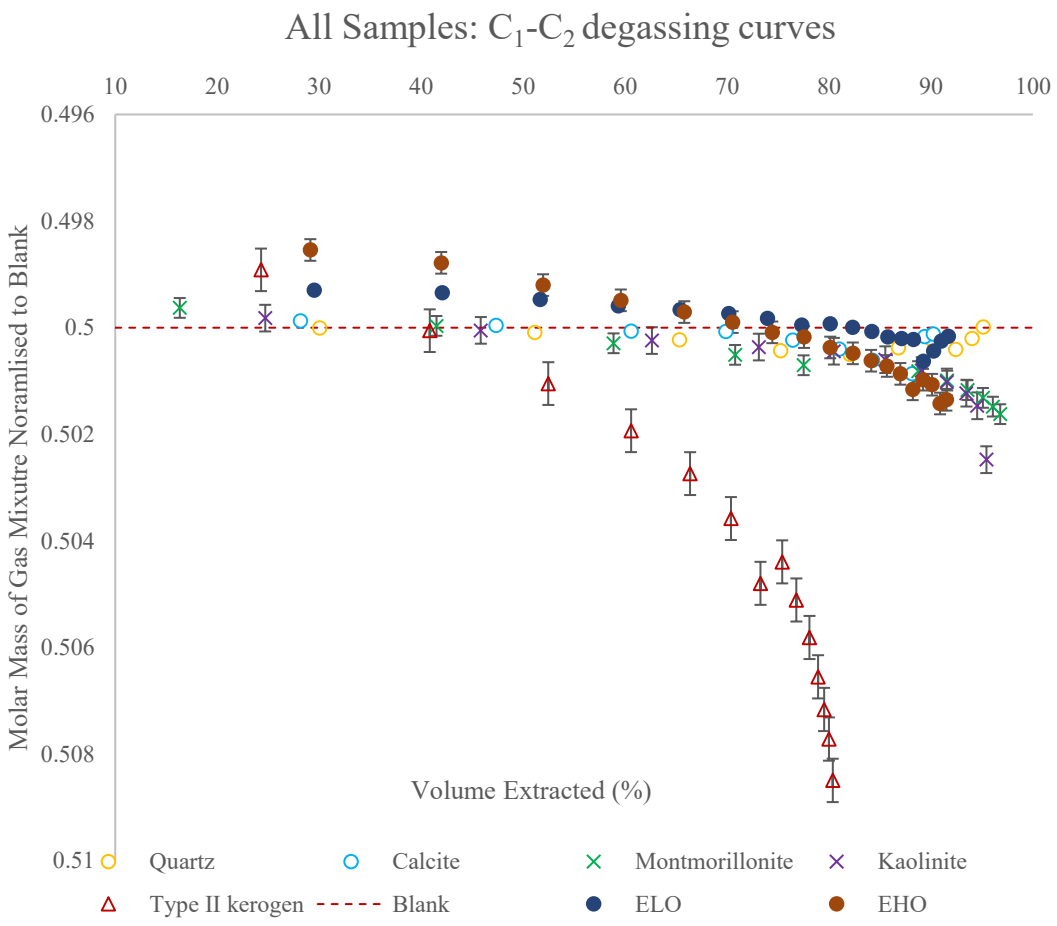


Figure 56| C_1-C_2 fractionation data collected for the pure mineral and Eagle Ford shale samples. These have been normalised to the respective bulk gases used for the mineral samples and the Eagle Ford Shale samples. Error bars were calculated as standard deviations between several experimental runs of the same sample. The error calculated was greatest in the type II kerogen but the trend is statistically significant. See Appendix Chapter 4: results for the multiple runs.

Clays: Montmorillonite and kaolinite

Many authors focus solely on the influence of organic material on adsorption capacity of a shale, some authors have studied the effects of clays on gas adsorption and microporosity which influences diffusive fractionation (Romero-Sarmiento et al., 2013a; Schloemer and Krooss, 2004; Tang et al., 2016; Yuan et al., 2014a). Studies have shown that clay minerals have different adsorption capacities with smectite having the greatest and illite the least which would also influence the C_1-C_2 fractionation trend seen from the degassing clay minerals(Cheng and Huang, 2004b; Heller and Zoback, 2014a; Ji et al., 2012b; Liang et al., 2016). Others however, have suggested that illite has a strong adsorption capacity whilst

kaolinite has little(Busch et al., 2009; Kuila and Prasad, 2013; Schettler and Parmoly, 1990a). Both adsorption capacity of a material and diffusion through a nanoporous network are controlling factors that will influence the C_1-C_2 ratio (Schloemer and Krooss, 2004). The data collected here however indicates that the clays, regardless of their BET surface area (11.8 and 28.12 cm^3/g for kaolinite and montmorillonite respectively) and their significant pore volume (0.067 and 0.076 cm^3/g), there is relatively little fractionation caused by these minerals. This is reiterated in Table 21 which shows the calculated standard deviation of each data point from the bulk reservoir for each mineral. Montmorillonite and kaolinite produce almost identical curves with very similar standard deviation from the bulk gas regardless of their different surface chemistries and pore distributions.

Both clays begin degassing material with a higher C_1-C_2 ratio than that of the bulk gas, becoming more C_2 enriched than the bulk gas after ~45% of the gas has been extracted. Between 70 and 95% of the gas extracted, the C_1-C_2 ratio becomes more C_2 enriched than the bulk gas. The final kaolinite value deviates the greatest amount away from the bulk gas. Both kaolinite and montmorillonite produce a similar shaped degassing C_1-C_2 curve which appears distinct from the inert materials but only in the final 20% of gas extracted. The curves are not statistically significantly different and tend to plot within error of each other up to this point.

Organic material: Type II kerogen

It is evident from Figure 56 that the organic material has by far the greatest influence on the C_1-C_2 ratio of the extracted gas. Initially, the degassed material has a greater C_1-C_2 ratio than that of the bulk gas. After ~40% of gas extraction, the C_1-C_2 ratio of the extracted gas drops below that of the bulk, releasing gas than is more enriched in C_2 relative to the bulk gas. The shape of the degassing curve trends towards exponential, getting increasingly enriched in C_2 relative to the bulk gas. Approximately 20% of the gas however, is retained within the sample

and could not be degassed within the time frame and at high enough volumes to be accurately measured by the GC-FID. The data displayed in Table 21 shows numerically rather than graphically that the type II kerogen degasses material that is distinctly different to the bulk gas and does so an order of magnitude greater than the inorganic minerals.

The BET data suggests that type II kerogen has a smaller surface area than montmorillonite and a greater one than kaolinite. Type II kerogen also only has a slightly greater N_2 adsorption capacity (51.42 cm^3/g) than either kaolinite (42.9 cm^3/g) or montmorillonite (48.01 cm^3/g). Likewise, the pore volume is similar between the three samples; 0.067, 0.076 and 0.08 cm^3/g for kaolinite, montmorillonite and type II kerogen respectively. This suggests that the influencing factor on the C_1-C_2 ratio is not a function of the overall sorption capacity of the rock or the over surface area but is directly related to the organic material. This is shown graphically in Figure 59 and Figure 60.

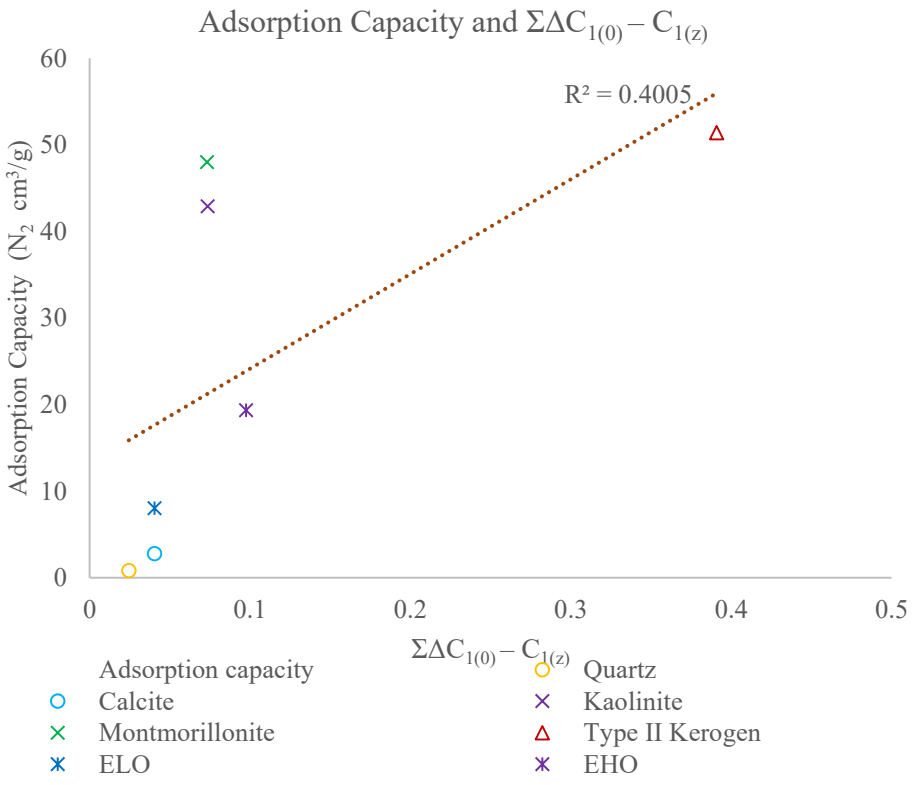


Figure 57|Fractionation factor and maximum adsorption capacity for all the tested samples. The fractionation factor is the average value that each measured data point deviates away from the bulk gas.

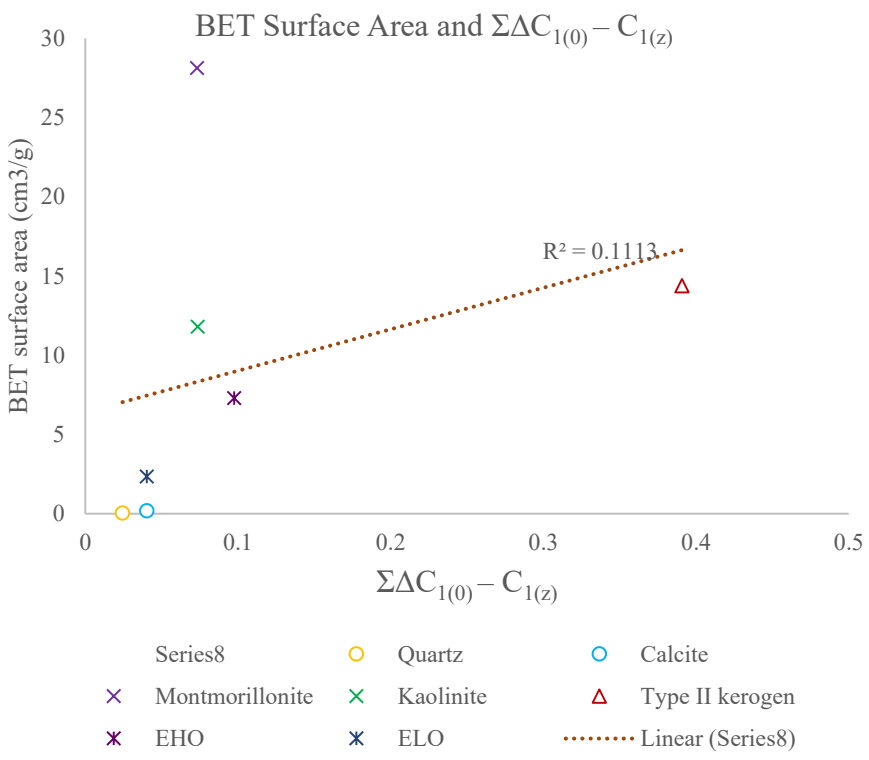


Figure 58| Fractionation factor ad BET surface area for all the tested samples. The fractionation factor is the average value that each measured data point deviates away from the bulk gas.

EHO and ELO

The EHO shale has a greater $\Sigma\Delta C_{1(0)} - C_{1(z)}$ than the ELO, plotting with a similar starting composition to the pure organic material. ELO plots with a similar trend to the inert materials although with a slightly higher C_1-C_2 enriched initial gas pulse. The EHO initially plots a C_1-C_2 fractionation curve more similar to the organic material with the initial gas pulse more C_1 rich than the bulk before plotting on a similar trend to the clay materials in the final third of the experiment. In this final 30%, the C_1-C_2 fractionation curve shows a trend of degassed gas that is more ethane enriched that the bulk gas.

It is apparent that methane is being retained within all non-inert samples with the degassing material trending to a composition more ethane rich than the sample gas. In the case of the organic material this is exponentially so. For material balance purposes, this of course cannot be the case. The remaining 20% of the gas within the organic material, which could not

be extracted from the cell as the sensitivity range of the instrument was too low to measure the small volumes of extractable gas accurately, must be more enriched in methane than the bulk. To determine the residual gas, mass balance calculations were conducted (see Appendix: Chapter 4 results). The results of this are displayed in Figure 59 for the isolated shale constituents and Figure 60 for the EHO and ELO samples.

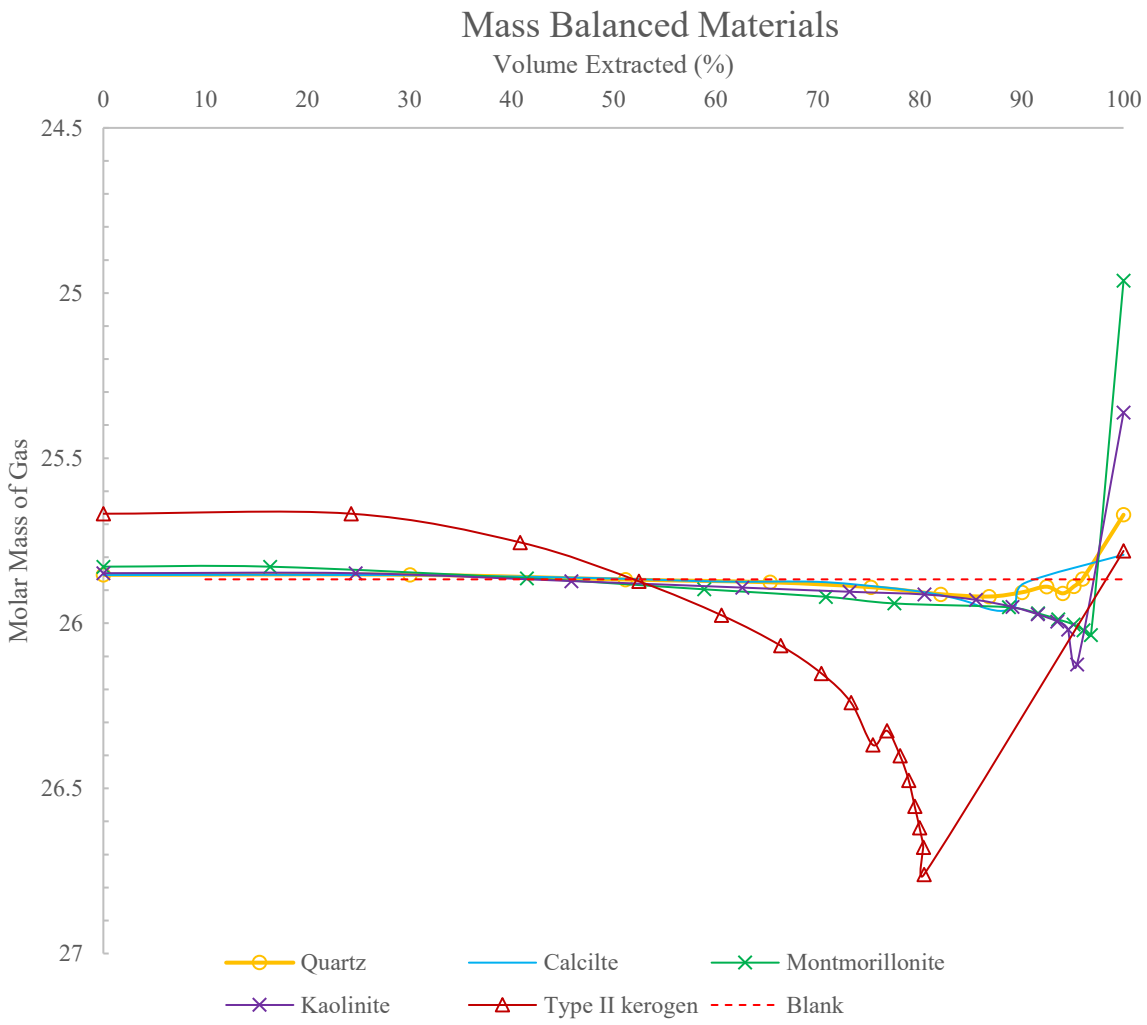


Figure 59| Material balance equations for the pure mineral samples. Even though the deviations from the bulk gas are relatively low in the case of kaolinite and montmorillonite, as after ~40% of the gas had been extracted plotted with an ethane value heavier than the bulk gas, some methane must be preferentially retained and the final few pulses of gas must be more methane enriched than the bulk.

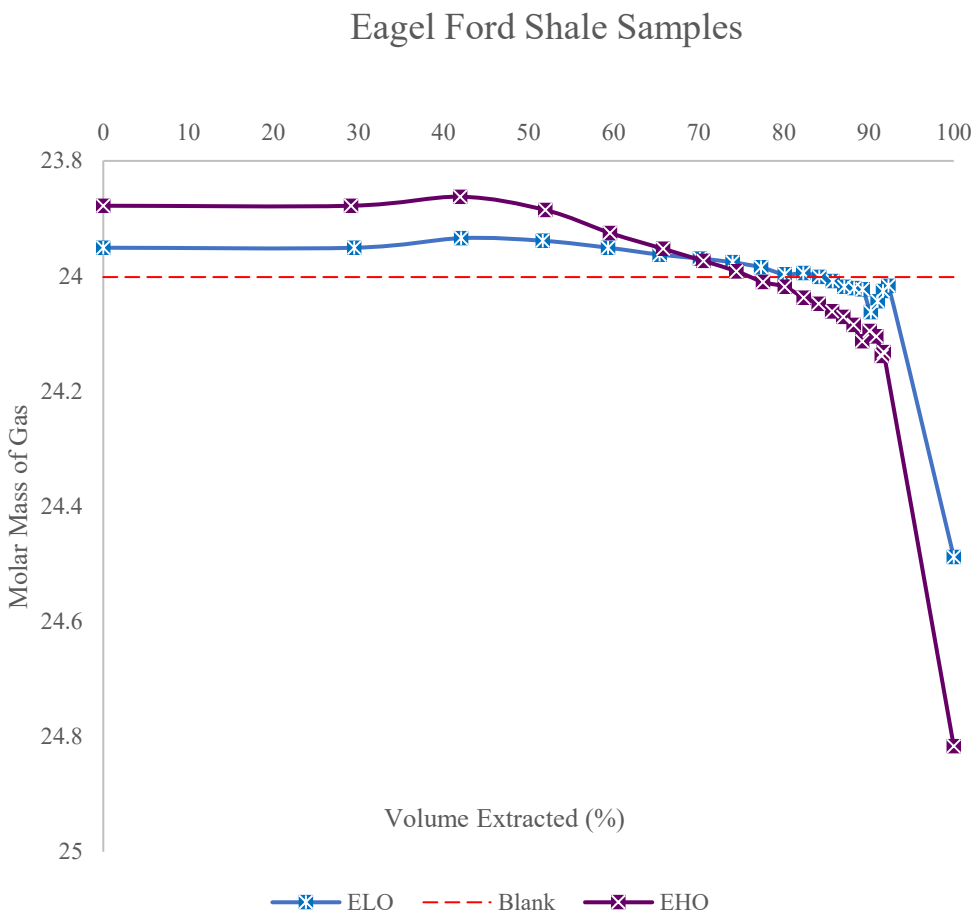


Figure 60| Material balance equation for the ELO and EHO samples.

It is evident from Figure 56 that the organic material has by far the greatest influence on the C_1-C_2 ratio of the extracted gas. Unlike the carbon isotopes tested in chapter 3, the clays have a much-reduced impact on the C_1-C_2 fractionation during gas extraction. The inert material, calcite and quartz exhibit less significant deviations away from the baseline. The data collected here indicates that, for C_1-C_2 fractionation to be a viable geochemical index when determining the volume of gas extracted in a given volume of shale, the role of TOC is vital. Whilst clays have a minor influence, the change in C_1-C_2 ratio with gas extraction is an order of magnitude greater in the organic material than the inorganics.

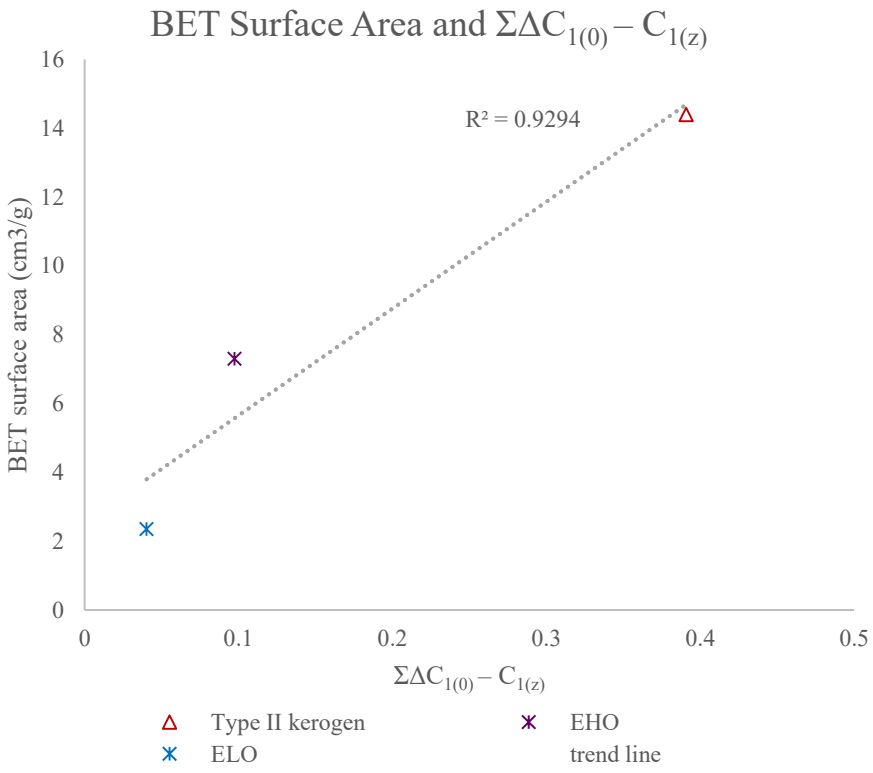


Figure 61| BET surface area in just the organic containing material compared to fractionation factor.

Considering the BET surface area data for all the samples tested, there is no correlation between the change in C_1-C_2 ratio and the BET surface area, this is represented in Figure 58. Isolating just the organic-containing samples however, there is a linear correlation between the BET surface area and the fractionation factor. Increasing the relative proportion of organic material increases the organic material surface area and increases the overall C_1-C_2 fractionation factor. This is further evidence that the inorganic components of a material have little impact on the C_1-C_2 fractionation curve produced during degassing. The overall influencing feature is the organic material within the shale.

4.5.2 Implications for a geochemical index

The data collected show that there is a potential to use C_1-C_2 fractionation trends in degassing shales to predict the volume of gas extracted. Shales of different mineral

compositions and kerogen volumes will produce unique C_1-C_2 fractionation curves dominated mainly by the TOC content. This TOC content appears to relate to the surface area of the sample. Surface area only appears to be a factor however when considering the organic fraction, not the mineral fraction. The composition of EHO is dominated by quartz, clays and calcite with 5.35% TOC. The fractionation factor reflects the influence of the organic material by producing a higher factor than the inorganic materials (Figure 61).

Ultimately, the data indicates that C_1-C_2 fractionation with shale degassing is a viable geochemical index and is influenced predominantly by the organic fraction of a shale. Quartz rich shales with a 5% TOC and clay rich shales with 5% TOC would be expected to produce marginally different C_1-C_2 fractionation trends with degassing due to the minor influence of clays. A shale with 10% TOC compared to 2% TOC would produce a much greater C_1-C_2 fractionation trend. This is shown by the schematic curves Figure 67.

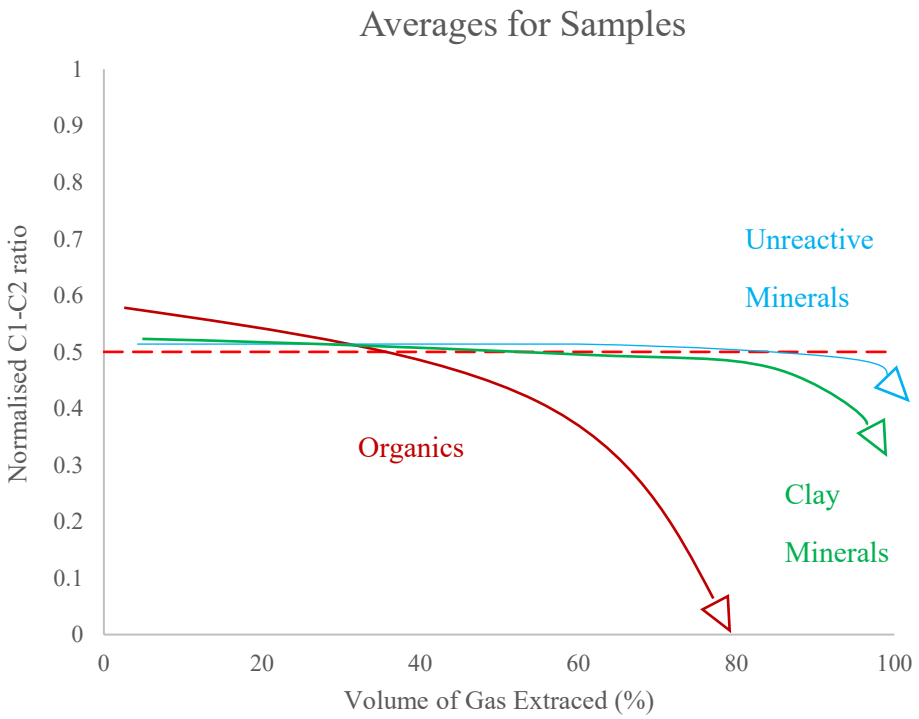


Figure 62| average C_1-C_2 data schematic for the three sample groups

There are similarities in the way that the carbon isotopic fractionation trends and the C_1-C_2 fractionation trends could be applied to a degassing shale reservoir. C_1-C_2 fractionation is strongly influenced by the organic fraction but with minor influences from the clays and inert material. A shale with a known composition, that is where the mineral fraction and organic material have been analysed, the expected C_1-C_2 fractionation trend can be predicted, from 100% GIP to 100% gas extracted. By collected and measuring production data, the actual C_1-C_2 ratio can be measured and compared to the predicted curve. Comparison of the two curves in time can then be transposed onto the volumetric plots. This will provide information on the proportion of the total volume of gas that has been extracted which will, in turn, command the future operation of the well.

4.6 Conclusions

Our isolated and individual sample data reveal that clay minerals have a moderate influence on C_1-C_2 fractionation and so clay rich shales are expected to display a C_1-C_2 fractionation trend with significant deviation from baseline. Our isolated and individual sample data reveal that organic matter has a major influence on C_1-C_2 fractionation and imply that shales with a greater TOC% should display a C_1-C_2 fractionation trend with substantial deviation from the initial gas reservoir C_1-C_2 bulk.

Our whole rock shale data confirm that organic matter content induced a strong effect on C_1-C_2 fractionation trends. The two shale samples and isolated kerogen sample showed an increase in C_1-C_2 fractionation with increasing TOC%. The low TOC% ELO displayed a C_1-C_2 fractionation trend closest to baseline, whist the higher TOC% EHO displayed a C_1-C_2 fractionation trend with a greater fractionation factor (overall deviation away from the bulk gas). By increasing the organic content further to a sample representing pure kerogen, the fractionation factor was greatest and the greatest change in C_1-C_2 from the bulk reservoir was measured.

Clay mineral content, is significantly less influential than organic matter content but does have a small fractionation factor which, considering many shales contain high volumes of clay, must be taken into consideration, having a minor influence on the C_1-C_2 fractionation degassing curve. This is most evident in the final stages of degassing.

Clay minerals and organic matter are hydrodynamic equivalents and are often deposited together. High TOC% samples that display C_1-C_2 fractionation trends that deviate strongly away from baseline will, therefore, be commonly enhanced by the minor additional fractionation introduced by clay minerals. Inert material exerts almost no influence on the C_1-C_2 ratio with quartz having the smallest fractionation factor and calcite the next smallest.

Ultimately, the data indicates that C_1-C_2 fractionation with shale degassing is a viable geochemical index and is influenced predominantly by the organic fraction of a shale. Quartz rich shales with a 5% TOC and clay rich shales with 5% TOC would be expected to produce marginally different C_1-C_2 fractionation trends with degassing due to the minor influence of clays. A shale with 10% TOC compared to 2% TOC would produce a much greater C_1-C_2 fractionation trend. This is shown by the schematic curves in Figure 62

The data suggests that, if the composition of a shale gas reservoir is known, then a specific C_1-C_2 fractionation curve could be predicted and related to total GIP thus helping to obtain a recovery factor. Evidently, it is a leap from laboratory experiments at standard pressure and temperature regimes but this experimental procedure provides the experimental building blocks for future work.

5.0 C_1-C_2 Fractionation in Degassing Shales: TOC and kerogen type

5.1 Abstract and Chapter Aims:

To understand the interplay of shale composition and gas adsorption capacity of a shale, the influence of organic matter and kerogen type must be considered. Organic matter has been shown in previous chapters to be the dominant sorption site for methane and ethane and is almost solely responsible for C_1-C_2 fractionation during shale degassing. Knowing the sorption mechanics and role of kerogen in shale gas adsorption will allow targeting of sweet spots which will inform drilling decisions. The role of type I, type II and type III kerogen is explored and indicates that kerogen type has a greater influence in gas storage capacity and C_1-C_2 fractionation than TOC %.

- To explore the influence of varying amounts of TOC on C_1-C_2 fractionation with shale reservoir degassing,
- To investigate the effects of organic matter type on the C_1-C_2 fractionation trends in each degassed shale,
- To characterise the organic matter through BET surface area analysis, Langmuir isotherm analysis and BJH pore size distribution in order to explore the effects on C_1-C_2 fractionation during degassing of shale gas reservoirs,
- To isolate the organic material through acid extraction to determine how volume of TOC and type of TOC together influence C_1-C_2 fractionation trends with reservoir degassing,
- To measure the change in C_1-C_2 ratio from 100% as in place to generate unique fractionation curves associated with volume of total gas extracted, the basis of a shale gas geochemical degassing index.

5.2 Introduction

Conventional gas reservoirs are characterized by an inorganic framework with a macroscale pore network and permeability that permits Darcy Flow (Gensterblum et al., 2015b). Conversely, shale gas reservoirs are tight lithologies composed of both inorganic and organic framework with a multiscale network of poorly connected pores with heterogeneous geometries (Akkutlu et al., 2012; Amann-Hildenbrand et al., 2012; Bustin and Bustin, 2012; Clarkson et al., 2013b; Kuila et al., 2014b; Schettler et al., 1989b; Y. Wang et al., 2015b; Wei et al., 2012a; Yin et al., 2017a; Yuan et al., 2014a).

Gas is stored as free gas in any pre-existing fractures or macro pores within the shale, adsorbed gas on the surfaces of organic material and minerals and diffused gas within the nanoporous network(Akkutlu et al., 2012; Amann-Hildenbrand et al., 2012; Bustin and Bustin, 2012; Hao et al., 2013). Conventional techniques for predicting the gas capacity of a reservoir, such as numerical Darcy flow models, do not adequately represent shale gas storage and flow regimes (Javadpour et al., 2007; Smith et al., 1984a). Shale gas production from reservoirs is characterised by rapid peaks in initial production followed by a long tail-off period (Gensterblum et al., 2015b). Shale gas reservoirs cannot use the existing conventional reservoir numerical modelling prediction methods because of the differences in the two reservoir types. Shale gas reservoirs are distinct from their more conventional counterparts and show local variations in shale gas production between adjacent wells indicating the impact of shale heterogeneity on gas extraction (Bustin and Bustin, 2012; Gensterblum et al., 2015b). To achieve economic success during the exploitation of a shale gas reservoir, an understanding of the original volume of gas in place (GIP), volume of total gas extracted and recoverable gas volumes is required. As conventional petrophysical techniques and numerical modelling methods fail to accurately predict these three key parameters, another method is required. This is particularly pertinent when considering shale gas exploration in the UK. Unlike the large

shale gas basins of the USA such as the Eagle Ford Shale, Barnett Shale or Monterray shales which are relatively unfaulted, the UK basins containing possible shale gas reserves tend to be more structurally complex. As such targeting sweet spots and fully utilising each well is more economically significant in the UK.

Much of the existing literature focuses on either storage capacity of a shale via adsorption experiments or volume of extractable gas through degassing experiments (Bustin et al., 2008b; Chalmers and Bustin, 2007b; Chareonsuppanimit et al., 2012b; Gensterblum et al., 2015a; Strąpoć et al., 2006a; Zou and Rezaee, 2019b). Whilst the existing literature provides an insight into shale reservoirs it is restricted to particular shales with specific compositional and historical characteristics and, consequently, the data cannot be accurately applied to other basins or even other parts of the same shale reservoir that displays different conditions. In order to successfully analyse the storage capacity of shale, we must move away from empirical observations that relate to specific shales under specific conditions. Individual parameters that affect the adsorptive storage capacity and the desorptive gas extraction process must be explored. A new technique, explored in Chapters 4 uses the inherent fractionation of hydrocarbons of different molecular weights (C_1-C_2) as proxies for gas storage and transport. The inherent fractionation of gases of different molecular constitution occurs through the adsorption/desorption processes on the surface of a material and by molecular sieving with mass transport through a tortuous, meso to nano- porous network (Etminan et al., 2014b; Smith et al., 1984b; Xia and Tang, 2012b; Yuan et al., 2014b).

Changes in the methane-ethane (C_1-C_2) ratio with gas extraction from isolated shale components are recognisable using our dedicated degassing cell-gas chromatography-flame ionisation detector. The experimental setup has been described in detail in chapter 2 and facilitates calculation of the following parameters:

1. The amount of gas that can be sorbed onto a material
2. The amount of gas that is recoverable within the experimental time frame
3. Deviation of the C_1-C_2 ratio from the bulk gas for a given material and specific extracted gas volume

Chapter 4 shows that isolated shale components, especially the organic carbon, have distinct impacts on the shape of the molecular weight fractionation trend observed during shale reservoir gas extraction.

5.2.1 Controls on gas storage capacity

The role of organic material on gas storage has been extensively documented in the literature. Previous research suggests that gas storage sites within shales are strongly influenced by the presence of organic material, conventionally expressed using total organic carbon (TOC) values (Chalmers and Bustin, 2008; Cheng and Huang, 2004a; Etminan et al., 2014a; Gasparik et al., 2014; Hao et al., 2013; Ji et al., 2017; Kuila et al., 2014b; Li et al., 2015a; Loucks et al., 2009a; Ross and Bustin, 2009a; Strąpoć et al., 2006a; Wei et al., 2012a; Yin et al., 2017b; Zhang et al., 2012b). The positive influence of TOC on increased gas storage capacity is now generally accepted based on the literature. Looking at the published work as a whole, however, indicates that this relationship is not so straightforward. There are several theories that have explained why there is often a positive trend between shale storage capacity and proportion of TOC. The key theories are:

1. TOC Porosity and Pore Distribution,
    - Increasing the amount of organic material present will increase porosity and create adsorption sites onto which shale gas can sorb (Chareonsuppanimit et al., 2012a; Ji et al., 2017; Wang et al., 2013; Zhang et al., 2012b),

- An increase in TOC relates to an increase in adsorption capacity but that adsorption does not necessarily correlate with a shale's overall porosity (Wei et al., 2012a). The size and shape of the pores is more important than the overall porosity thus the surface area is only a factor when a high surface area reflects nanoscale porosity (Chalmers et al., 2012a; Sigal and others, 2015).

2. TOC and Surface Area

- Organic material contains pores and it follows that increasing the TOC (%) would thus increase the overall surface area of a shale (Heller and Zoback, 2014a; Ji et al., 2017; Li et al., 2015b; Song et al., 2019; Y. Wang et al., 2016),

- Higher TOC increases surface area but also enhances adsorption owing to the its relatively high adsorption capacity for hydrocarbon gases(Ambrose et al., 2011c; Gasparik et al., 2014),

- Increasing the clay content has a negative impact on the specific surface area and reduces pore volume. This is because clay minerals compact and recrystallise during diagenesis and further burial leads to very low porosities (Song et al., 2019).

3. TOC and Kerogen Type

- TOC is dominated by kerogen but not all kerogens are chemically-identical. The type of kerogen may play a role in gas storage with lacustrine type I kerogen exhibiting the lowest adsorption and terrestrially-influenced type III kerogen having the greatest (Chalmers and Bustin, 2007a; Hao et al., 2013; Zhang et al., 2012b),

- Variation in absorption between kerogen types may be a result of different pore size distributions and physical adsorption capacities of the different kerogens or variations in surface area (Li et al., 2019c),

- Different pore structures are associated with the three kerogen types and organic matter porosity from lacustrine sources has a lower contribution to overall porosity and shale storage capacity (Chen et al., 2019).

5.2.2 The need for a new approach to understanding shale gas

Understanding how gas is stored within a shale is only part of the question. In terms of application to a shale gas reservoir, it is just as useful to be able to calculate how much of the total volume of gas has been extracted over a certain production period. The geochemistry of shale gas is simple, often containing >90% methane with the remaining components being carbon dioxide and C_2-C_5 gases. Previous studies have focused on shales cored and collected in-situ. These cores are brought to the surface and degassed (Chareonsuppanimit et al., 2012a; Li et al., 2019c; Yuan et al., 2014a). Whilst this data is important for understanding the fluid dynamics within that specific shale, other contributing factors such as water saturation, original kerogen cracking and post diagenetic gas mixing may mask the effects of organic material on fractionation trends (Gensterblum et al., 2015b; Mastalerz et al., 2013a).

Chapter 4 considered isolating the effects of individual shale components on the storage and transport of gas and to allow calculation of changes to gas geochemistry using a new method, developed for this research. Outlined fully in chapter 2, a custom-built sample cell coupled with a Gas Chromatography - Flame Ionization Detector (GC-FID) allowed the isolation of mechanisms that have been suggested to impact shale gas storage and transport. Measuring the change in gas geochemistry when the initial volume of gas in place and C_1-C_2 ratio is known the effects of shale composition on gas extraction was studied and the organic

material was shown to have by far the greatest influence on the C_1-C_2 fractionation with sample degassing.

5.2.3. Why focus on TOC and kerogen type?

This chapter builds on the groundwork of chapter 4 which highlighted the significant effect of organic material on controlling the C_1-C_2 fractionation trend when kerogen and shale samples were degassed.

Chapter 4 and the work outlined above suggest that increasing the amount of TOC should thus result in a positive relationship between fractionation of C_1-C_2 with degassing and proportion of TOC (%). Chapter 4 compared the C_1-C_2 fractionation trends between pure mineral components of a shale and 2 Eagle Ford Shale samples with varying TOC content. The results suggest that increasing the TOC in a shale correlates to a greater degree of fractionation.

The fractionation between C_1-C_2 could be used as a proxy for gas storage as methane will desorb more readily from the surface of organic material than ethane. However, as methane also has a smaller molecular diameter than ethane and can navigate out of the nanoporous network more readily, there is also diffusive fractionation through molecular sieving as the gas exits the sample.

In this chapter, the role of kerogen type and TOC content on change in C_1-C_2 ratio with sample degassing are explored with the aim to build up a picture of the influencing factors on C_1-C_2 fractionation and if this is a viable geochemical index for GIP and RF. To do test the hypothesis generated in chapter 4 that the amount of organic material controls the change in C_1-C_2 composition of a degassing shale, three shales of different TOC (%) and kerogen type were tested. Through acid extraction, the kerogens of each shale were isolated and tested as isolated organic fractions.

As TOC is believed to be the dominant control on sorption capacity, it was hypothesised that shales with higher TOC would have greater molecular weight fractionation trends driven

by the assumption that organic material has greater adsorption capacity. The diverse nanoporous network related to organic material may also facilitate greater molecular sieving. These factors can be observed by considering BET surface area, BJH pore distributions, SEM imagery and Langmuir isotherm analysis. Increasing the TOC proportion can be tested to the extreme by isolating the kerogen and increasing the relative proportion of organic material. Based on the literature studies outlined and the preliminary data collected in chapter 4, a greater change in the C_1-C_2 ratio was expected by simply increasing the volume of organic material in this shale.

5.3 Methodology

5.3.1. Samples

5.3.1.1. Oxford Clay

The Oxford Clay shale is Callovian to Oxfordian aged and was collected from Chickerell, Crook Hill Nature Reserve near Weymouth, south of England. Containing 11.09% TOC, this shale is considered to be a prime shale gas source rock in the UK. Described by the British Geological Society Lexicon, the Oxford Clay is a siliceous mudstone with beds of variable organic richness. The Weymouth Member of the Oxford Clay, from which this sample was taken has minor silt beds with pyritised ammonite fossils and sideritic nodules suggesting a reducing environment of desorption. The Oxford Clay is a typical type II marine kerogen as shown in Figure 63. This sample is immature with a Tmax values of < 435°C.

5.3.1.2 Bowland Shale

The Bowland Shale is of Carboniferous age and was collected from Mam Tor in Derbyshire, Midlands of England. Described by the British Geological Society as a weakly calcareous fissile and organic-rich mudstone, this sample has 2.9% TOC and is also considered to be a prime shale gas source rock in the UK. Although deposited in a basin-floor submarine fan, the Van Krevlen plot in Figure 63 indicates a type III kerogen, traditionally considered to contain terrestrial material.

5.3.1.3 West Lothian Shale

The West Lothian Shale was also deposited in the Carboniferous and was collected from Port Edgar, West of Craigs in Scotland. Described by the British Geological Society as a pale sandstone with numerous bands of organic-rich mudstones, this sample has 15.4 %TOC. The

depositional environment for this unit is lacustrine, indicated by the type I kerogen represented in the Van Krevlen plot, Figure 63. Table 22 has the Tmax data for these samples showing that they fall within immature (Oxford Clay) to marginal maturity, at the onset of the oil window (Bowland Shale and West Lothian).

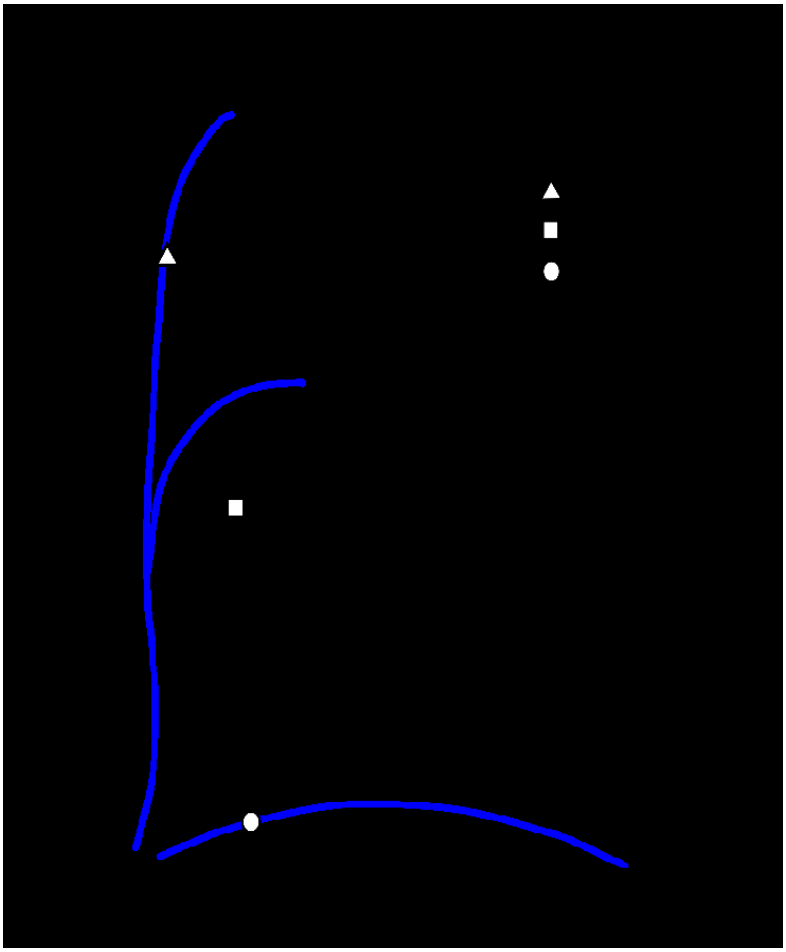


Figure 63| Van Krevlen plot showing the hydrogen and oxygen indexes for the three shale samples tested.

5.3.2 .Sample Preparation and Screening

The three shale samples were collected from the locations outlined above. Once collected, the shale samples were wrapped in aluminium foil and stored in polythene bags. Prior to experimentation, the shale samples were crushed with pestle and mortar and sieved to 125-250 μm grain fractions. Grains less than 125 μm were not used as this fine, powdery material would not retain any of the original pore structure of the shale sample. Grains coarser than 250 μm

would retain the internal pore structure but would pack less tightly within the sample container. Samples between 250–125 μm have been shown in literature to be the ideal grain size to test; intact shale cores are difficult to core without causing brittle failure and extracting residual gas takes considerable time (Chalmers et al., 2012b; Chen et al., 2015b; Han et al., 2016; Ross and Bustin, 2009b). By crushing the samples, residual gas can be removed with less than 12 hours of vacuum time. Once crushed and sieved, the samples were kept in a drying box, set to 35˚C. The drying box reduced exposure of the shales to moisture whilst retaining a low enough temperature to not alter the remaining kerogen fraction. This encouraged loss of any surface water and activated the mineral surfaces to increase adsorption capacity during experimentation. Unlike the isolated shale components in chapter 4 (clays, quartz and calcite), the shale samples were not washed or cleaned with chemicals such as HCl, DCM or water. Contact with these fluids would have altered the composition of the sample. Ideally, there would be no change to the mineral components or any addition of water to the clays or organic components prior to experimental analysis. This limited the amount of pre-experimental cleaning that had to be carried out.

5.3.3.Initial Sample Preparation

The OC-N, B-N and WL-N samples were each crushed individually, primarily with a hammer covered with aluminium foil into workable chunks and then pounded in a pestle and mortar before being sieved to 125 μm. To ensure no contamination, the sieves were cleaned with DCM and methanol then heated in an oven at 105˚C prior to use. The pestle and mortars were cleaned with 200 μm silicate grains and de-ionised water before being rinsed with DCM and heated in a furnace to 600˚C.

5.3.3.1. Soxhlet Extraction

Soxhlet extraction isolated any soluble organic matter which was juxtaposed with inorganic grains. The powdered samples were loaded into cellulose filters and placed within the extraction chamber. A round bottomed flask filled with a 60:40 benzene:methanol mix and several anti-breaking beads was placed on a hot plate and heated for 24 hours. The evaporated benzene:methanol mixture condensed in the upper cooling section of the Soxhlet extractor and passed through the sample before returning to the round bottomed flask. The repetition of this process over 24 hours removed all free organic matter. The complete removal of free organic matter was confirmed by the appearance of a clear extraction fluid at the base of the extraction vessel.

5.3.3.2. Hydrochloric Acid Rinsing: Carbonate Removal

Hydrochloric acid (HCl) rinsing was a fast and efficient method for removing calcite from shale samples. HCl also removed any modern calcitic contamination such as calcrete which can form on surface samples. The soxhlet-washed samples were placed in Pyrex beakers and placed on a low temperature hot plate (35˚C) with a magnetic stirrer at the base. A low concentration of HCl was added for the initial step; 100 ml of 0.5N HCl, diluted further with water as required if the samples effervesced violently. Continuous stirring from the magnetic stirrer encouraged the complete removal of calcitic grains and coatings. After approximately 8-12 hours, the samples were covered with aluminium foil and left to separate into solid and liquid fractions. The supernatant fluid was then decanted. This process was repeated with increasingly stronger acid solutions until 200 ml of 1M HCl could be added without reaction. After the final acid bath, de-ionised water was used to rinse the sample to remove residual cations of Ca^{2+} then the samples were covered lightly and allowed to air dry.

5.3.3.3. Hydrofluoric Acid Rinsing: Silicate Removal

Once dried, the samples were halved and transferred to beakers resistant to HF. Due to the large nature of the samples and the dangers associated with HF, only half of the sample mass was extracted. Initially, a mixture of 1:4 parts HCl to HF was added to the samples in a fume cupboard. The acid-sample mix was sealed tightly and shaken to encourage dissolution. The suspension was then placed on a low temperature hot plate at 35˚C to encourage further dissolution. Once settled, a process that took up to 6 hours due to the flocculating nature of the kerogen, the supernatant was removed and heavily diluted before disposal and an acid mix of 1:1 HF:de-ionised water was added. This process was repeated between 6-8 times depending on the nature of the sample. Once the acid no longer visibly reacted, seen in latter stages by the production of fine bubbles, and the supernatant remained clear after the allocated settling time, the sample was rinsed thoroughly and repeatedly with de-ionised water. When Litmus paper showed that the pH had of the supernatant had returned to pH 6-7, the sample was deemed safe to handle.

5.3.3.4. Freeze Drying

The final stage of kerogen extraction involved freeze-drying the samples to remove any remaining water without heating the sample and altering the original nature of thee kerogen. This was done using a Labconco freeze-drying unit. Once the whole shale samples and kerogen samples were prepared and stored in the drying box, preparation for the experiment could begin.

5.3.4 BET, BJH and Langmuir isotherm analysis

The Langmuir isotherm data was collected using a Quantachrome R ASiQwin Automated Gas Sorption Instrument, version 5.2. Nitrogen was used as the analysis gas and the

experiments were conducted under standard pressure and temperature conditions. Full reports for the Langmuir Isotherm analysis are available in the Appendix: Chapter 5 results, PDF and raw data formats.

BET surface area analysis was carried out by the Quantachrome R AsiQwin automated gas sorption data instrument version 5.2. This software allows for comprehensive physisorption analysis of a sample. Nitrogen gas is used in BET analysis as it has a strong interaction with most solids. Full reports for these are available in the Appendix: chapter 5 results

The BJH data was also collected on a Quantachrome R ASiQwin Automated Gas Sorption Instrument, version 5.2. The pore radius is measured in angstroms, 15 angstroms is the equivalent of 1.5 nm which represents the smallest measurable pore volume. Full reports for these are available in the Appendix: chapter 5 results.

5.3.4 FTIR

FTIR was used to measure the molecular structure of the three natural shale samples and their extracted kerogens. FTIR is capable of charactering both the inorganic and organic components of a rock sample (Chen et al., 2015c). A full description of the FTIR process is in chapter 2, methodology.

5.3.5 Gas Chromatography - Flame-Ionization Detector (GC-FID)

The main instrumentation for this experimental procedure was the custom-built sample cell (section 3.3.4) coupled with a Gas Chromatograph-Flame-Ionisation-Detector (GC-FID). The GC-FID can measure gas responses between 50 mV and 10,000 mV. The GC-FID can only be used to measure hydrocarbon gases and will not report values for CO_2 or other non-hydrocarbon gases. Raw GC-FID data was collected using a fit-for purpose interface and converted into Excel files which allowed for further processing.

5.3.5.1 Custom-Built Sample Cell

A full description of the construction and operation of the cell is presented in chapter 2. A schematic of the cell is shown in Figure 64. The volumes of the reference cell (v1-v2) and the sample cell (v2-v3), the initial C1-C2 ratio and the molar volume of gas injected were all known parameters. The key volumes associated with the reference cell are shown in Table 22. The reference cell was 8.52 cm^3 and the sample container cell's volume was 11.5 cm^3. The reference gas used in this experiment has a C1-C2 ratio of 75:25. The gas mixture was made in a 1 L gas canister and the composition tested by running a blank cell. The molar volume of the gas mixture could be calculated using the ideal gas law, with pressure measured by an online pressure transducer.

Table 22| Volumetric data, calculated using water injection, of the key components of the custom-built cell setup

Cell Component	Volume (cm^3)
Reference Cell (V1-V2)	8.52
Sample Container Cell	11.5
Cell Volume	20.02
Sample Cylinder	1.0

5.3.5.2Principles of Operation

Similar to previous chapters, the premise of this experiment is to remove extraneous variables from a shale and test individual factors which may influence the volume of gas stored within a shale. Shales with a known surface area, mineralogy and organic matter content are loaded into the sample cell of a known volume. The sample gas contains a known molar volume of C_1 and C_2. The volume of C_1 and C_2 extracted from the cell with each gas pulse is indicated by the GC-FID responses and the ratio calculated.

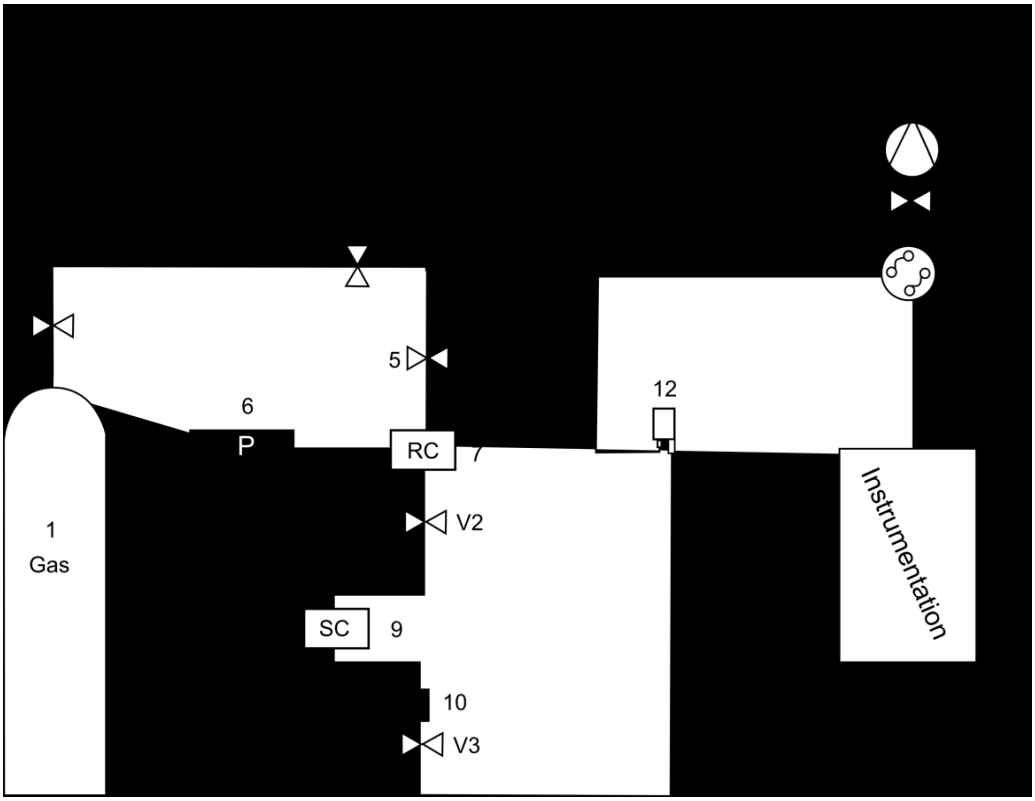


Figure 64| Schematic diagram of the second generation cell. Instrumentation here is the GC-FID but could also be the GC-C-IRMS. Assignments as follows: (1) gas cylinder, (2) valve, (3) vacuum valve, (4) vacuum pump, (5) valve 1 – v1, (6) pressure transducer, (7)reference volume cell, (8) valve 2 – v2, (9) sample cell, (10) in-line filter, (11) valve 3 – v3, (12) injection needle valve, (13) 6-way injection valve, (14) vacuum pump valve 2, (16) Instrumentation – GC-FID.

A molar volume of C_1 and C_2 could thus be calculated for each individual gas extraction step. This allowed calculation of the volume of each gas extracted not just through time but as a percentage of the initial gas volume injected. From this, residual gas in place could be calculated. As the samples tested were crushed to 125–250 μm, tortuosity of the matrix in these

grains was retained. The crushed samples were more easily evacuated than the corresponding whole shale samples, removing any residual gas that may have been adsorbed onto the sample prior to testing. The shale samples were assigned the abbreviations: OC-N (Oxford Clay, natural), OC-K (Oxford Clay kerogen), B-N (Bowland Shale, natural), B-K (Bowland Shale kerogen), WL-N (West Lothian, natural) and WL-K (West Lothian kerogen.

5.3.5.32 Experimental Setup

The cell was first attached up to a vacuum and heated with a ProVac Varitemp heat gun at 200◦C for 30 minutes. Any residual water within the cell would thus be removed. The cell was then left for 2 hours to reach full vacuum, calibrated to -14.75 psi. The sample container, in the meantime, had been washed with DCM followed by de-ionised water and left in an oven at 109°C. This container was removed and allowed to cool. Once cool, the container was weighed. The sample was then inserted into the container using a round ended spatula. The container and sample were then weighed to measure the sample mass accurate to 4 decimal places. A lid was then fitted to the sample container to stop any spillages. The lid was compressed in a pellet maker to 0.2 tonnes to ensure the same level of compaction between all the samples. The sample container was then loaded into the sample chamber sealed with a torque wrench. Once sealed, the cell was put under vacuum for 2 hours to ensure any gas still within the sample was removed and that the cell was empty.

After 24 hours, the sample gas was injected into the reference cell (V1-V2, Figure 64) Using the pressure transducer, it was possible to ascertain the number of moles injected into the reference cell and thus the initial gas volume was known. The gas was allowed to sit in the reference cell for 5 minutes to ensure that 1) there was no leak and 2) that the pressure was stable and could reliably be read. After 5 minutes, V2 was opened and the gas allowed to flow into the reference cell, time = 0. After the initial drop in pressure by volume expansion, further

change in pressure was recorded along with the time taken from t=0. Change in pressure at this point relates to gas moving from the free gas state to the adsorbed state. Once the pressure remained stable, gas equilibrium was obtained between the free gas and adsorbed gas states. Due to the small sample size, this usually only took between 2 and 3 hours. Once equilibrated, aliquots of gas were continuously extracted and analysed by the GC-FID. Change in pressure at each stage was calculated to determine number of moles extracted at each stage and number of moles remaining.

5.4 Results

5.4.1. FTIR

Figure 65 shows the FTIR analysis for the WL-N (red) and WL-K (blue) samples. The silicate peak (black oval) is significantly reduced and the realtive proportion of organic material (green oval) increased in the WL-K compared to the WL-N. This cannot be used to give quantative volumes of the organic material bit indates the successful removal of silicate and clay minerals. Wavelengths between 2800-3000 cm^{-1} refer to aliphatic CH, CH_2 and CH_3. 1075 cm^{-1} and 790 cm^{-1} peaks refer to quartz, present in WL-N and significantly reduced in WL-K. Peaks 1431, 869 cm^{-1} and 307 cm^{-1} refer to calcite, significantly reduced in WL-K compared to WL-N. There is a peak of clay minerals – likely to be smecitite, at 1052 seen in WL-N which has been significantly removed in WL-K. There is still evidence of O-H phyllosilicates present betenn 3500 and 4000 cm^{-1} in the WL-K indicating that the kerogen is not completely 100% organic material. (Chen et al., 2015c; Estep et al., 2008; Kershaw, 1989; Solomon and Carangelo, 1988).

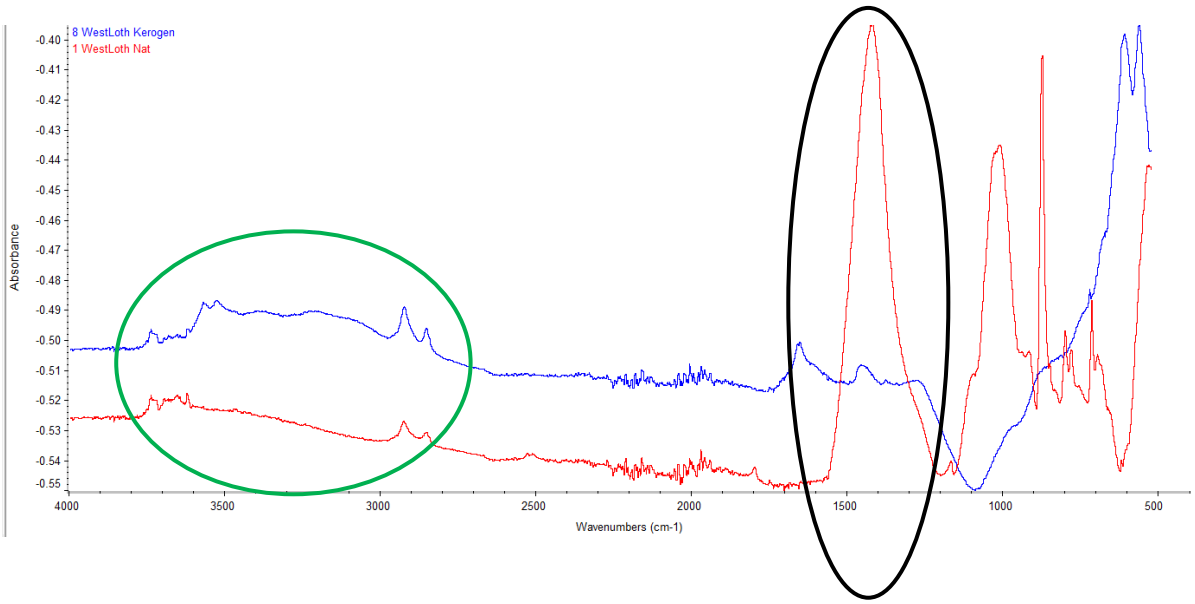


Figure 65| FTIR data for the WL-N and WL-K samples. WL-N is depicted by the red line whilst WL-K is shown by the blue. Both samples are flattened to the background noise to increase the signal ratio and provides a direct comparison between the two samples.

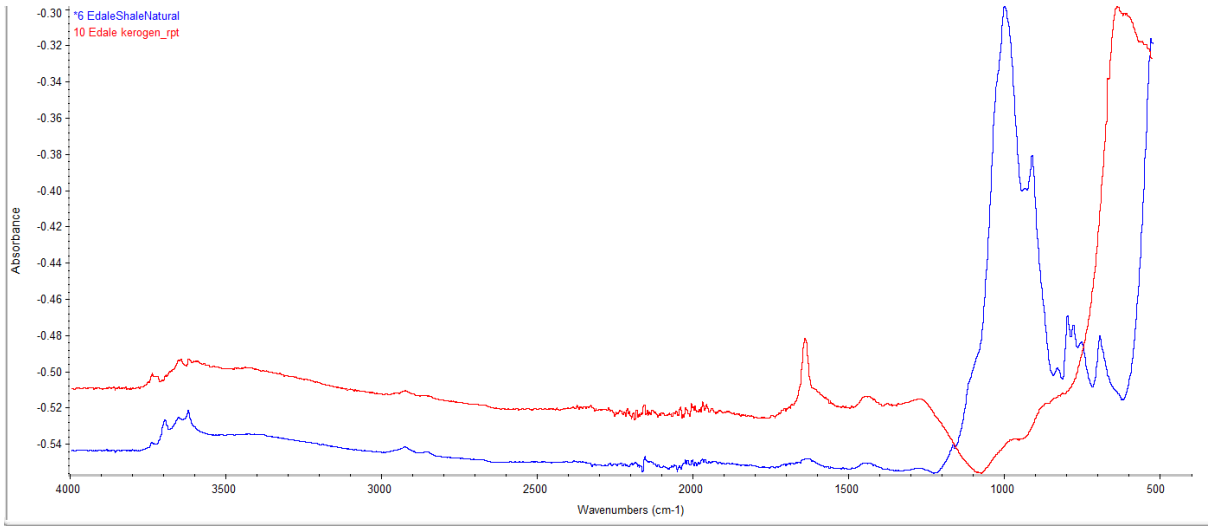


Figure 66| FTIR data for the B-N and B-K samples. B-N is depicted by the blue line whilst B-K is shown by the red. Both samples are flattened to the background noise to increase the signal ratio and provides a direct comparison between the two samples.

Figure 66 shows the FTIR data gathered for B-N and B-K. The large silicate peak at ~1075 and the smectite peak at ~1052 cm^{-1} is significantly reduced between B-N to B-K. There are some residual clays still seen between 3500 and 4000 cm^{-1} but the overall relative abundance of organic material has significantly increased between B-N to B-K.

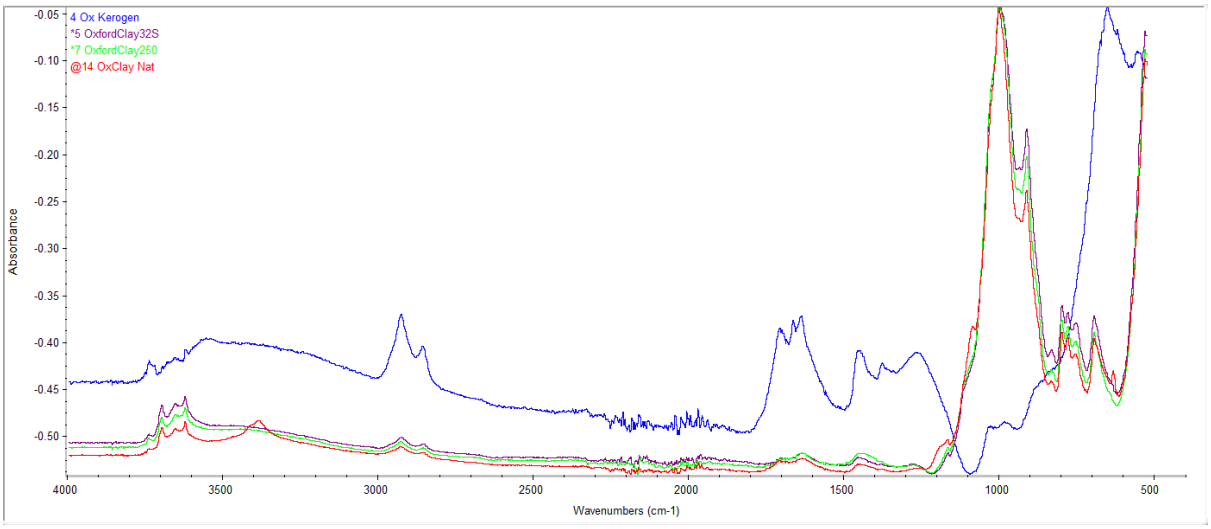


Figure 67| FTIR data for the OC-N and OC-K samples. OC-N is depicted by the red line whilst OC-K is shown by the blue. Both samples are flattened to the background noise to increase the signal ratio and provides a direct comparison between the two samples.

Figure 67 shows the FTIR data comparison between OC-N and OC-K. Similar to WL and B series, the silicate and smectite peaks are significantly reduced relative to the organic peaks.

OC-K has a significant aliphatic peak at 2950 cm^{-1}. There may be residual calcite and some phyllosilicate minerals still present.

5.4.2 Rock-eval data

The three shale samples were subjected RockEVAL analysis. A brief summary of this is shown in Table 23. Figure 63 shows the Van Krevelen plot generated for these three samples. The three shales represent the three kerogen types with hydrocarbon potential as well as a varying abundance of TOC. The WL-N sample has the highest abundance of TOC at 15.4 % whilst the B-N sample has the lowest at 2.9 %. The Tmax range suggests that each sample is at the lower threshold for the onset of oil, often termed marginal maturity (McCarthy et al., 2011).

Table 23| RockEVAL pyrolysis data for the three shale samples tested in this thesis. The Tmax indicates the thermal maturity of each sample. For Type I kerogen, the onset of oil is typically at ~445°C, for type II kerogen it is 435°C and for type III kerogen it is ~440°C.

Sample Name	Locality	HI	OI	Tmax	TOC	Van Krevlen Plot
Oxford Clay	Chickerell, Dorset, UK	421	46.28	421	11	Type II
Bowland Shale	Mam Tor, Derbyshire, UK	43	17	448	2.9	Type III
West Lothian	Port Edgar Scotland, UK	733	4	450	15.4	Type I

5.4.3Langmuir Isotherm BET and BJH Analysis

Langmuir Isotherm Analysis

Full reports on the isotherm analysis is documented in Appendix: Chapter 5.

It is evident from the Rock-eval data and Figure 68 that, whilst the WL-N has the greatest volume of organic material at 15.4%, it has the lowest adsorption capacity measured by the Autosorb Quantachrome instrumentation. Sample OC-N, shown Figure 70, has the highest sorption capacity at 55.75 cc/g yet a lower TOC than WL-N at 11%. B-N has the lowest volume of organic material at 2.9 % yet a relatively high adsorption capacity, measured at 42.0 cc/g. Figure 68 indicates that WL-N has little in the way of hysteresis between the adsorption and desorption whilst B-N exhibits a strong hysteresis effect between the volume of gas adsorbed and desorbed at a given pressure.

The hysteresis effect relates to differing adsorption processes within the samples. Isotherms are characterised into different type from type I to type VI with unique adsorption-desorption properties (Trunschke, 2013a). WL-N is a type III isotherm, with weak adsorptive-adsorbent interactions. Both B-N and OC-N are a hybrid type, a combination of type IV termed H3 which indicated adsorption in non-rigid aggregates dominated by slit-shapes pore geometries (Trunschke, 2013a).

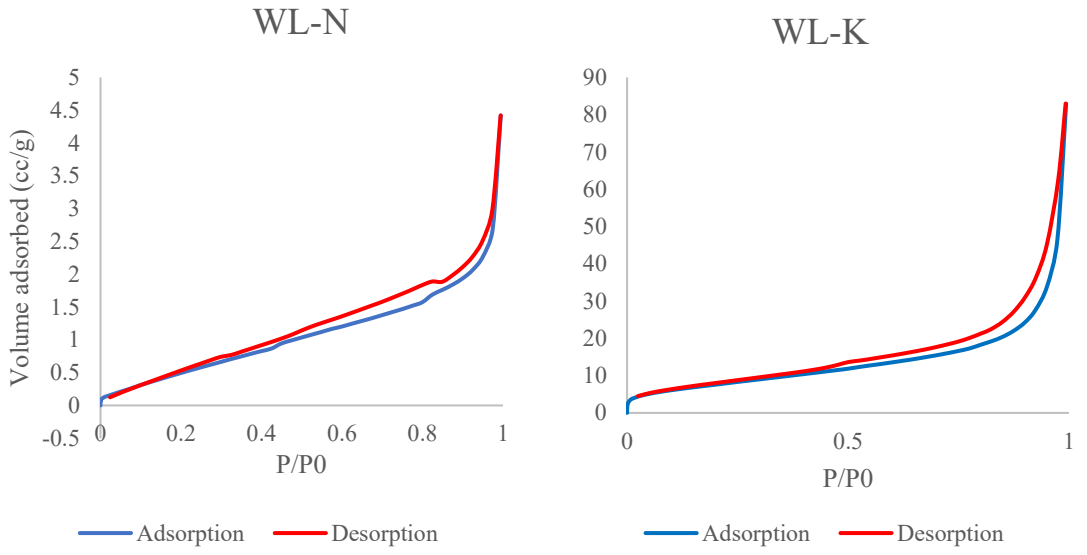


Figure 68| Langmuir isotherm analysis carried out on the WL-N and WL-K samples. Langmuir Isotherm Analysis carried out by the iQ3 Quantachrome adsorption Instrument. P/P0 is the partial pressure of the N_2 adsorbate and the volume adsorbed is the calculated volume of N_2 adsorbed by each adsorbent. The measured Langmuir volume for the WL-N sample is 4.42cc/g whilst the WL-K is 82.92.

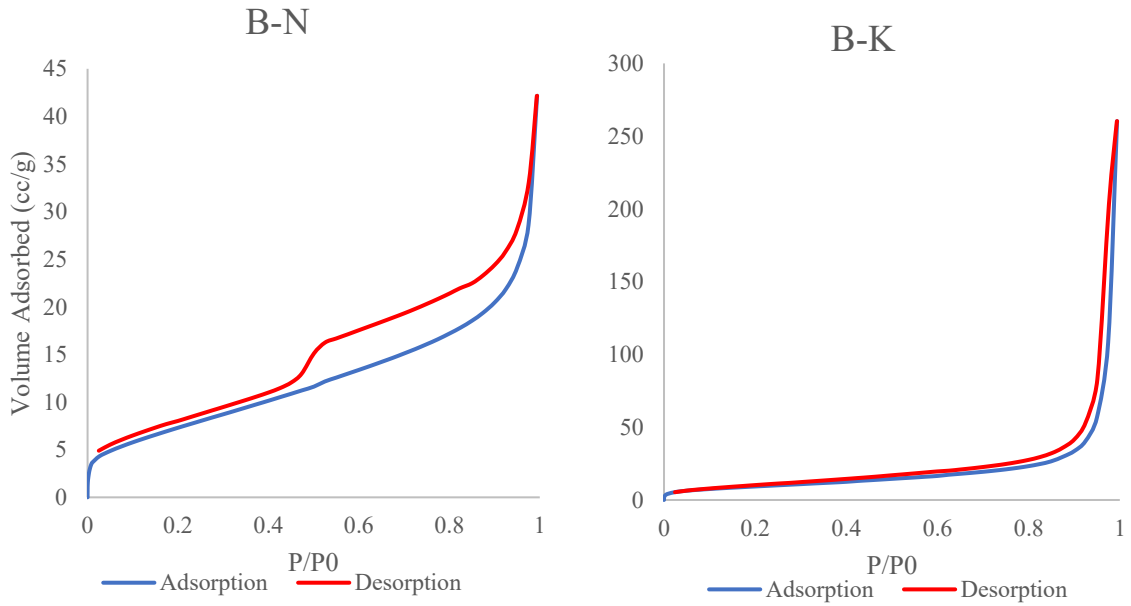


Figure 69| Langmuir isotherm analysis carried out on the B-N and B-K samples. Langmuir Isotherm Analysis carried out by the iQ3 Quantachrome adsorption Instrument. P/P0 is the partial pressure of the N_2 adsorbate and the volume adsorbed is the calculated volume of N_2 adsorbed by each adsorbent. A Langmuir volume of 42.016 cc/g is reached for B-N and 260.32 cc/g for B-K. Note the differences in shales between the two plots with B-K an order of magnitude greater than B-N.

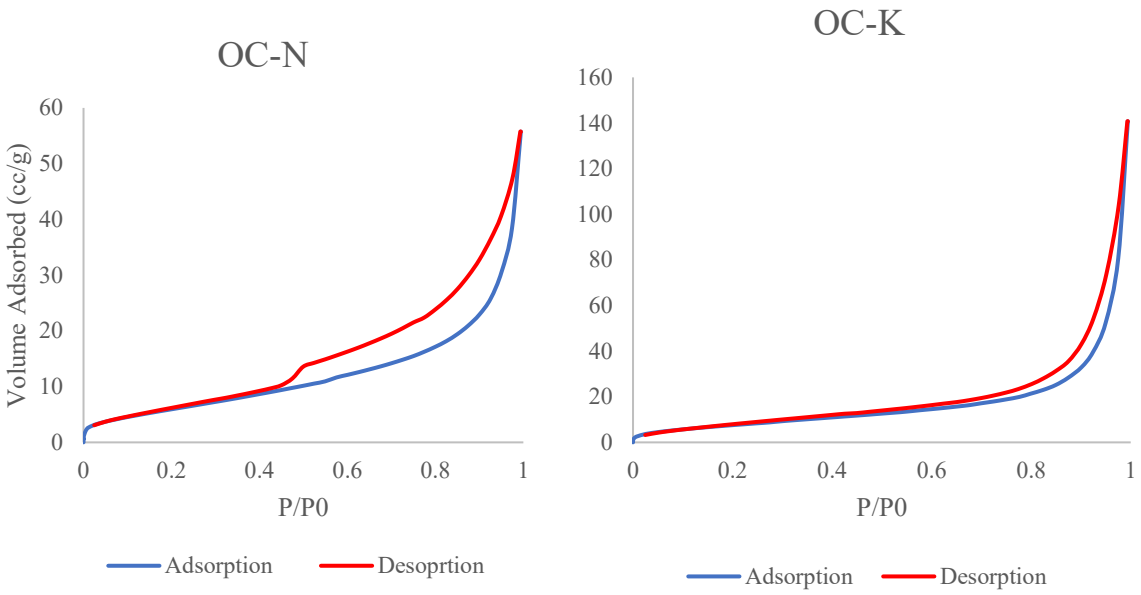


Figure 70| Langmuir isotherm analysis for OC-N and OC-K Langmuir Isotherm Analysis carried out by the iQ3 Quantachrome adsorption Instrument. P/P0 is the partial pressure of the N_2 adsorbate and the volume adsorbed is the calculated volume of N_2 adsorbed by each adsorbent. The maximum adsorption capacity indicated by the Langmuir volume for OC-N is 55.75cc/g whilst OC-K has a Langmuir volume of 140.76cc/g. Note that the scales are different between OC-N and OC-K

BJH Pore Size Distribution

The BJH data was also collected on a Quantachrome ASiQwin Automated Gas Sorption Instrument, version 5.2. Nitrogen was used as the analysis gas with He used in void volume mode to measure the pores. The analysis was carried out under standard pressure and temperature regimes. Figures 74 to 77 display the BJH pore size distribution data for the three whole shale samples (image A) and their isolated kerogens (image B). It is evident when comparing part A in both Figure 72 and Figure 73 that B-N and OC-N have a similar pore size distribution with a peak pore size at 18-20 nm. WL-N on the other hand has a unique distribution with more pores present at <20nm and broad-shouldered peak between 20 and 60nm, shown in Figure 71.

Comparing part B in both Figure 72 and Figure 73, it is evident that the OC-K and B-K have a similar profile for the pore size distribution. WL-K has a unique plot, in comparison to

the other two extracted kerogen samples. Similar to WL-N. WL-K has a broad shoulder region after a spike of pores at 20 nm in size.

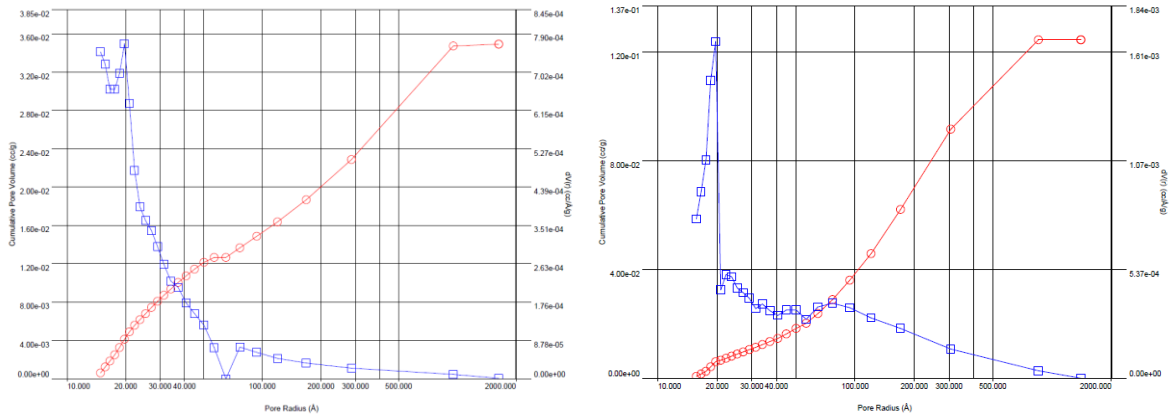


Figure 71| (A) BJH data for WL-N. The red line indicates the cumulative pore volume up to a maximum of 2000 Å. The blue line indicates the relative volume of pores for a given radius. The majority of pores are less than 50 Å in radius.(B) BJH data for WL-K. The red line indicates the cumulative pore volume up to a maximum of 2000 Å. The blue line indicates the relative volume of pores for a given radius. The majority of pores are less than 100 Å in radius. The overall pore volume is an order of magnitude greater than WL-N sample.

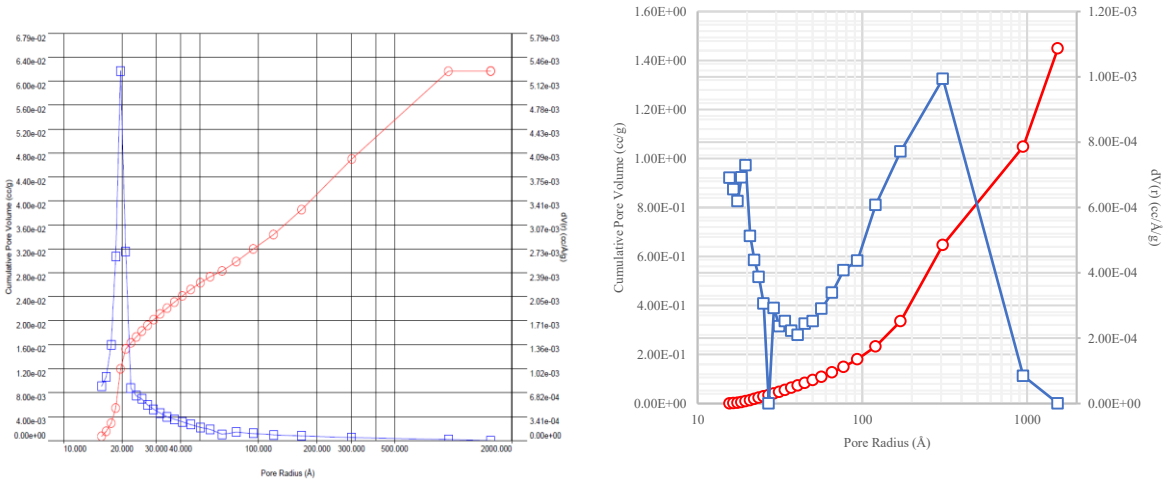


Figure 72|(A) BJH data for B-N. The red line indicates the cumulative pore volume up to a maximum of 2000 Å. The blue line indicates the relative volume of pores for a given radius. The majority of pores are less than 30 Å in radius.(B) BJH data for B-K. The red line indicates the cumulative pore volume up to a maximum of 2000 Å. The blue line indicates the relative volume of pores for a given radius. The majority of pores are less than 300 Å in radius. This kerogen has a high proportion of larger, mesoscale pores (10-30nm

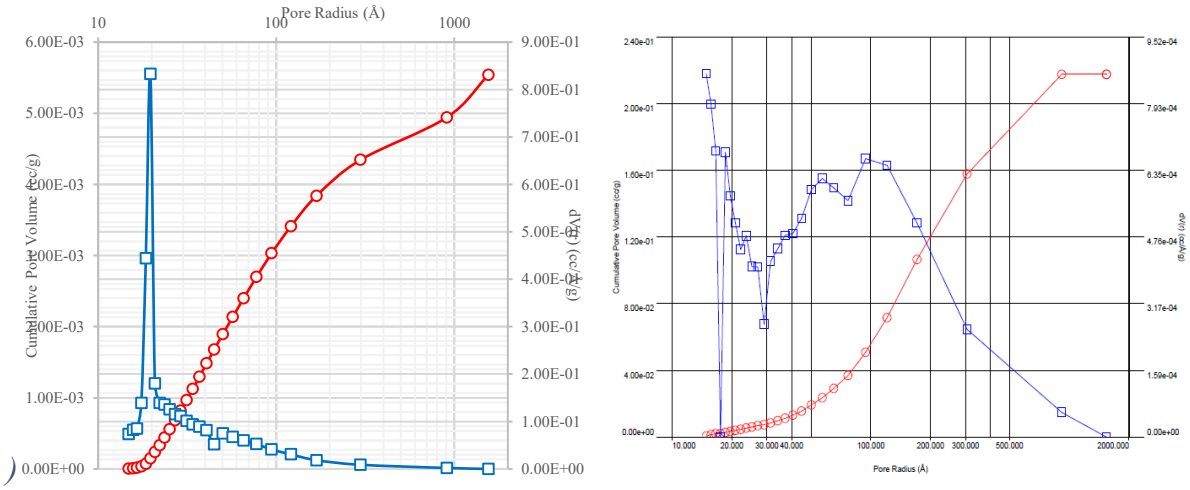


Figure 73| (A) BJH data for OC-N. The red line indicates the cumulative pore volume up to a maximum of 2000 Å. The majority of pores are less than 60 Å. (B) BJH data for OC-K. The red line indicates the cumulative pore volume up to a maximum of 2000 Å. The majority of pores are less than 200 Å. This kerogen has a high proportion of larger, mesoscale pores (10-30nm

A summary of the BJH, BET and Langmuir Isotherm analysis data is shown in Table 24 Extracting the kerogens from their parent shale significantly increased the total pore volume measured. The Bowland series saw an increase of pores almost 6.5 times greater between the whole shale and extracted kerogen. This was expected as the Bowland shale also has the lowest organic matter content. Increasing the relative abundance of typically porous material relative to less porous clays produces this signature profile. The pore volume data displayed in Table 24 shows that the abundance of pores is an order of magnitude greater in the kerogens than their respective natural samples.

Table 24| Langmuir isotherm, BET and BJH summary of the natural and extracted kerogen samples from the Bowland Shale, the West Lothian Shale and the Oxford Clay.

	B-N	WL-N	OC-N	B-K	WL-K	OC-K
Surface Area m^2g	26.33	11.92	33.70	38.84	25.03	33.44
Pore Volume cc/g	0.062	0.035	0.09	0.402	0.125	0.218
Pore Radius Å	19.63	19.68	19.36	308.27	19.66	14.84
Analysis time (hr:min)	30:38	12:20	14.13	20.1	23.49	15.52
Langmuir volume (cc/g)	42.16	4.42	55.75	260.32	82.92	140.76
Sample Volume (g)	0.3909	0.1913	0.1846	0.2007	0.4120	0.1849

Pore Observations

Bowland Suite

The total pore volume of the B-N falls in the middle of the natural samples at 0.062 cc/g. The biggest difference in pore size is seen in B-N and B-K. B-K has a pore volume almost 6.5 times greater than its natural counterpart, with B-K pore volumes of 0.402 cc/g. The surface area has increased significantly, up to 38.81 m^2/g from 26.33 m^2/g. The Langmuir sorption volume increases dramatically from 42.16 cc/g to 260.32 cc/g, the largest relative increase out of the 3 sample suites.

Oxford Clay Suite

The total pore volume is the greatest of the natural samples at 0.09 cc/g and the middle value of the extracted kerogens at 0.218 cc/g. The change in the overall pore volume is the smallest between OC-N and OC-K, only 2.4 times greater between natural and extracted samples. The surface area actually decreases marginally between the OC-N and OC-K which was not expected. The change in Langmuir adsorption capacity sees an increase from 55.75 cc/g for the natural sample to 140.76 cc/g in the kerogen. The median pore radius of OC-N is 20nm, similar to B-N.

West Lothian Suite

The total pore volume is the lowest in both the natural and extracted kerogen samples in the West Lothian samples. The increase of pores is about 3.5 times greater between natural and extracted samples. The surface area (SA) measured is also the lowest in both WL samples although the SA does over double between WL-N and WL-K. The Langmuir adsorption capacity increases significantly between WL-N and WL-K, from the lowest value at 4.42 cc/g to the second greatest value at 82.92 cc/g. There is little change in the average pore radius.

It is evident that the West Lothian suite is perhaps not the most typical type I kerogen shale. It was chosen for this research as it was a UK shale. The use of other type I kerogens will be highlighted in the future work section of the conclusions, Chapter 8.

5.4.5 Sample Cell – GC-FID

Gas Extraction Process: Time

Initially the sample data collected was represented in time increments. Data collected in this manor is similar to the production data that would be collected from a shale gas well. Figure 74 shows the change in the C_1-C_2 ratio with sample degassing plotted against each extraction step. In a shale gas well, the data collected cannot be correlated with a given volume of gas extracted, only plotted over time as a production decline curve. However, the nature of this setup allows calculation of the initial volume of gas injected into the cell and the volume of the gas increments that are subsequently extracted. As such, the results will be discussed and presented in terms of volume, not time.

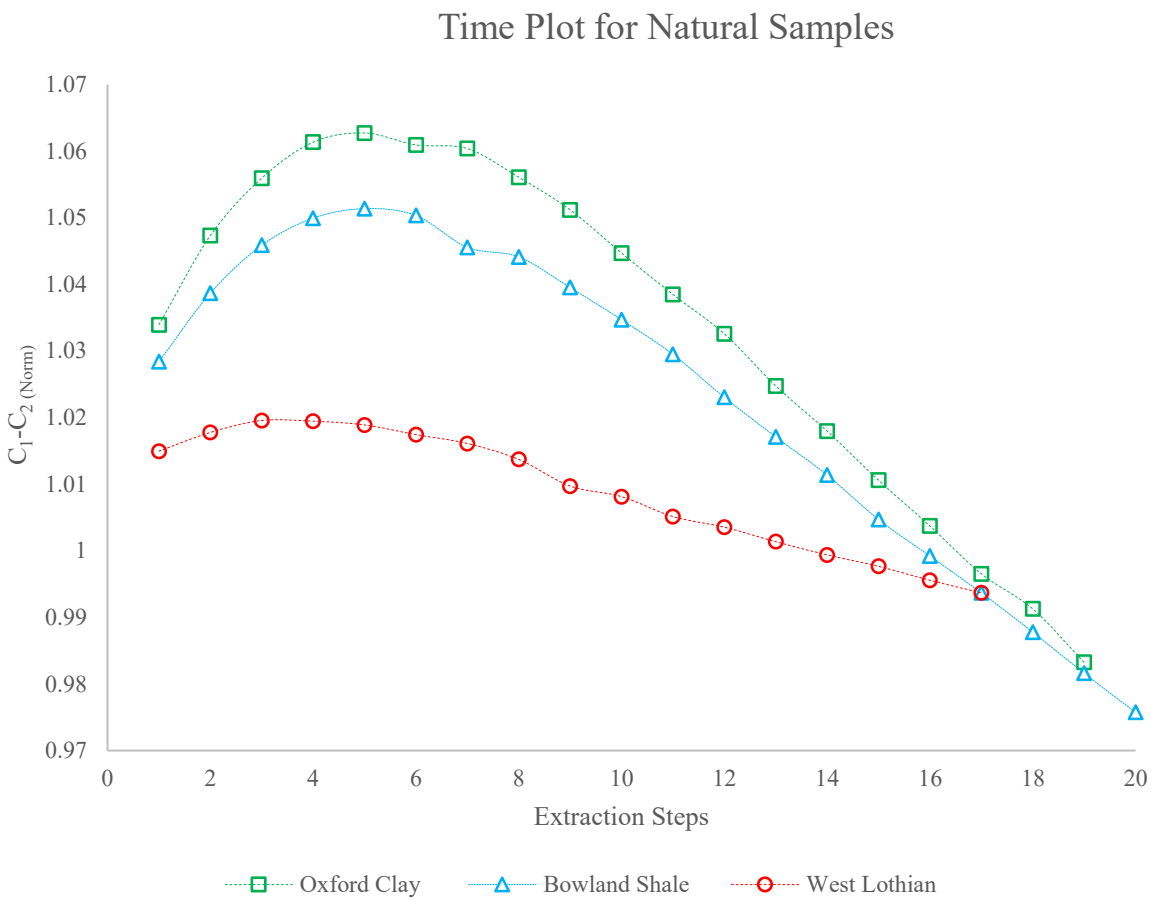


Figure 74| Time plots for the three natural samples. This is the raw data as extracted from the GC-FID. The ratio of C_1-C_2 measured at each extraction step is plotted against the extraction step. The time between each step is approximately 300 seconds.

Gas Extraction Process: Volume

Whilst the time plot in figure Figure 74is useful in highlighting the change in C_1-C_2 ratio with time, the main aim of this experiment was to see how the change in C_1-C_2 ratio relates to the total volume of gas stored within the sample. The cell design and experimental procedure was such that the initial molar volume of the gas injected could be derived, the total number of moles extracted with each step and the number of moles remaining in the cell at the end of the experiment. As these parameters could be calculated, the change in C_1-C_2 ratio could be linked to a specific volume of gas extracted.

To do this, the initial number of moles in the reference cell for each experiment was calculated. As the volume of the reference cell, temperature and pressure of the cell during experimental setup is known, the ideal gas law equation:

$$PV = nRT$$

can be rearranged to give:

$$n = PV/RT$$

where n is the number of moles, P is pressure in pascals, R is the universal gas constant and T is temperature in kelvin. The raw C_1-C_2 data from the GC-FID was plotted against the change in pressure for each extraction step to calculate the number of moles extracted as both absolute values and as a proportion of the total initial gas in place. See Appendix Chapter 5 for the Microsoft Excel spreadsheets containing these data sets.

When discussing the C_1-C_2 fractionation trends, this refers to the change in C_1-C_2 ratio with degassing. An absolute value could be calculated using the equations above however for the purposes of the results section, when discussing the C_1-C_2 fractionation trend, this refers to the ratio of each of the molecules. When the C_1-C_2 ratio is "higher" or "greater", this reflects a higher proportion of methane relative to ethane typically in terms of the bulk gas. When the C_1-C_2 ratio is "lower" or "less than" this reflects a lower proportion of C_1 relative typically to the bulk gas unless stated otherwise.

Figure 75 shows the results of the sample cell- GC-FID and the calculated volume data. The curves displayed by each shale was different when compared to the basic time plot. The WL-N sample still exhibited the least C_1-C_2 fractionation and the B-K the greatest change in C_1-C_2 ratio compared to the reference gas but the shapes of the curves are different. The volume (%) extracted before the peak C_1-C_2 ratio is met is different for each sample. The results of this

is summarised in the table below Table 25. The peak height refers to the “highest” point on each curve, that is to say the curve that has the highest C_1 proportional to C_2. The volume extracted to peak refers to the calculated

Table 26| Whole shale and their isolated kerogen samples, their corresponding C_1-C_2 peak heights and the volume of gas extracted before the C_1-C_2 peak height is met.

Sample Name	C_1-C_2 Peak Height	Volume Extracted to Peak
B-N	1.051	30.6(%)
WL-N	1.019	20.5(%)
OC-N	1.063	30.25(%)
B-K	1.082	24.9(%)
WL-K	1.031	23.7(%)
OC-K	1.061	33.1(%)

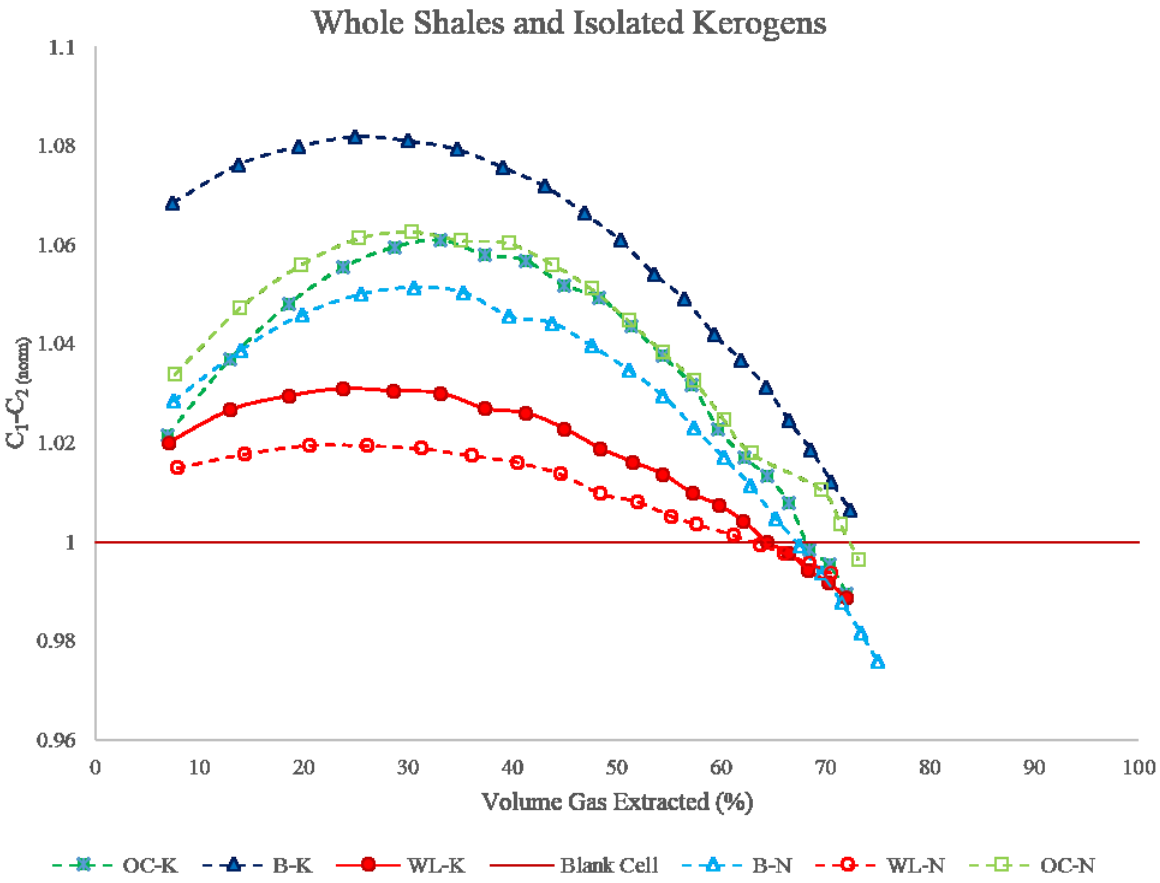


Figure 75| Whole shale samples and isolated kerogens from the three shales: each show a distinctive C_1-C_2 with a given volume of gas extracted.

Volume of Gas Adsorbed

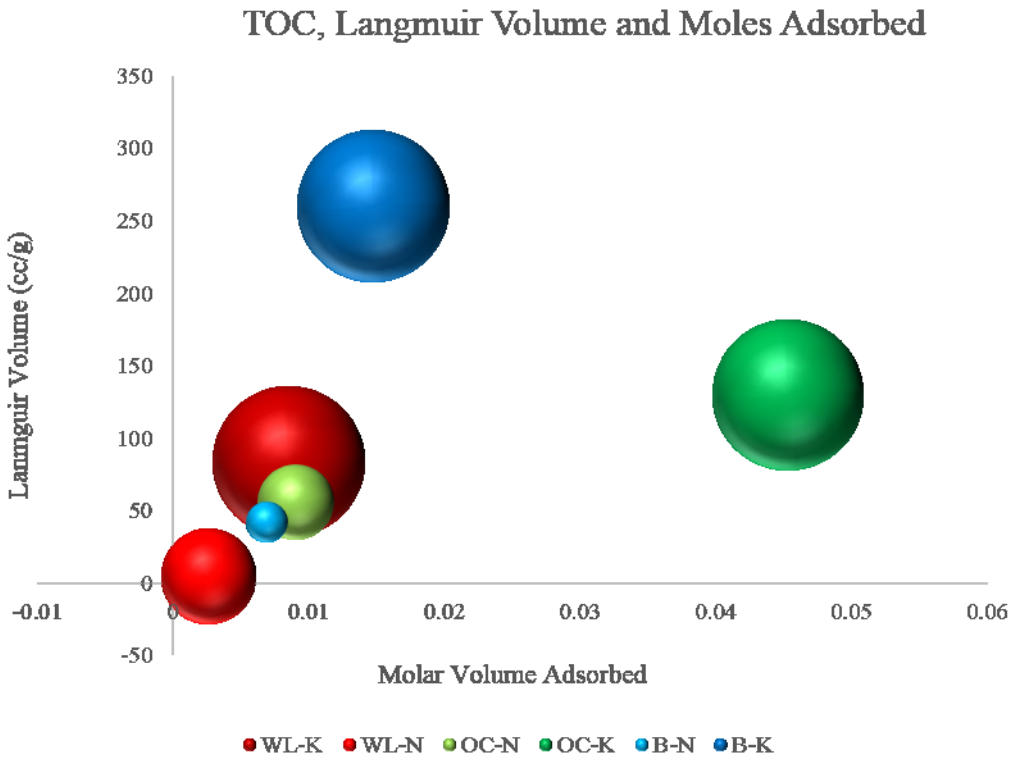


Figure 76| No. of moles adsorbed by each sample, calculated using the custom-built sample cell plotted against the N_2 calculated Langmuir volume shows a linear relationship except for the Oxford Clay isolated Kerogen sample, OC-K. There is no obvious correlation between either of the adsorption measurements and total organic carbon content.

During the initial experimental setup, the volume of gas going into the adsorbed phase can be calculated. This is done by measuring the pressure changes in the sample cell immediately after the gas is expanded from the reference cell (V1-V2) to the sample cell (V1-V3). As gas moves from the free gas stage to the adsorbed stage, there is a drop in pressure. Once the pressure remains stable, the free gas is in equilibrium with the adsorbed gas phase. The number of moles adsorbed in each whole shale sample is shown in Figure 76 WL-N adsorbed the least number of moles which also correlated with the lowest measured Langmuir volume of 4.4 cc/g. OC-K adsorbed the highest number of moles and has the second highest calculate Langmuir volume. The size of the bubbles relates to the total organic carbon contained within the sample. On the whole, the isolated kerogens have a higher Langmuir volume and greater number of moles adsorbed. The number of moles adsorbed calculated using

the pressure change within the cell. Removing OC-K from the series shows a strong correlation between the cell, calculated moles adsorbed and the Langmuir Volume calculated using N_2 adsorption isotherms. This volume does not correlate with TOC which is represented by the bubble size.

5.4.6. Summary of results

Table 27 synthesises the key results taken from the testing of the whole shale samples and their isolated kerogens. All three natural samples show an increase in the calculated Langmuir volume when compared to their isolated kerogens.

Table 27| A summary of the quantitative analysis carried out on each sample. This includes the Langmuir isotherm volume data, the RockEVAL total organic carbon, kerogen type and maturity data, BET surface area and BJH pore size distribution data as well as the data collected as part of the new experimental setup, degassing from the sample cell.

	B-N	**WL-N**	**OC-N**	**B-K**	**WL-K**	**OC-K**
Surface Area m^2g	26.331	11.923	33.698	38.841	25.032	33.436
Pore Volume cc/g	0.062	0.035	0.09	0.402	0.125	0.218
Pore Radius Å	19.634	19.675	19.36	308.269	19.659	14.835
Analysis time (hr:min)	30:38	12:20	14.13	20.1	23.49	15.52
Langmuir volume (cc/g)	42.0	4.40	55.75	260.32	82.92	140.76
Sample Volume (g)	0.3909	0.1913	0.1846	0.2007	0.412	0.1849
TOC (%)	2.9%	15.4%	11%	70%	80%	90%
Maturity	Marginally Mature	Marginally Mature	Marginally Mature			
Surface area/ volume	424.69355	340.657	374.422	96.619	200.256	153.37
C_1-C_2 peak	1.051	1.019	1.063	1.082	1.031	1.061
Volume extracted at C_1-C_2 Peak (%)	30.6	20.5	30.25	24.9	23.7	33.1

5.5 Discussion

5.5.1. Isotherm analysis: adsorption capacity of the materials

The shape of the Langmuir isotherms can give an indication of the dominant pore types present within the material. Figure 68, Figure 69, and Figure 70 show the Langmuir isotherms measured on the natural samples and their isolated kerogens. WL-N exhibits a type III isotherm with moderate type II influences and a marginally unequal adsorption-desorption loop. A type II isotherm is dictated by weak adsorbate-adsorbent interactions whilst a type II isotherm suggests a macroporous adsorbent and unrestricted monolayer adsorption. The shape of the hysteresis loop suggests that, where micropores are present, these pores have a slit-like geometry (Thommes et al., 2015). Even though WL-N has the greatest abundance of TOC, the adsorption capacity is the least and the pore shapes indicated by the isotherm analysis suggests that the gas that is stored within the adsorptive phase is easily desorbed (Wei et al., 2012a). This agrees with the C_1-C_2 volumetric curves in Figure 75. This is substantiated further by studies in the literature which suggest that organic matter pores in lacustrine shales are not the dominant source of porosity or the dominant storage areas (Chen et al., 2019). If the pores were situated within the organic material then a greater C_1-C_2 desorption profile would be observed. This shows unequivocally that it is not just the presence of organic matter in a source rock but the nature of the organic material which facilitates C_1-C_2 fractionation and thus adsorption.

OC-N exhibits an isotherm shape that is pseudo type II - type IV (Trunschke, 2013b). The presence of a hysteresis loops suggest a capillary condensation force where aliquots of the bulk gas form a liquid-like layer on the pore walls in which ink-bottle shaped pores inhibit desorption (Sing and Williams, 2004; Thommes et al., 2015; Trunschke, 2013b)[. These inkbottle pores are dominant at mesopore scale (2-50nm, (Zdravkov et al., 2007).

B-N also exhibits a pseudo type II - type IV isotherm with an evident hysteresis loop of type 3 pore distribution. This suggests porosity in slit-like pores Sing and Williams, 2004.

All three kerogen extracted samples have isotherms which are similar to type III with minor type II influence seen. This is suggesting weak adsorptive-adsorbate interactions between the bulk gas and the organic material (Sing and Williams, 2004).

5.5.2. Observing the influence of kerogen type on material degassed from the custom-built sample cell

The initial aim of this project was to determine whether the change in C_1-C_2 ratio could be used as a geochemical index for volume of gas extracted; is there a change in ratio of C_1-C_2 that occurs with depressurisation of the reservoir and can this be used to calculate shale gas decline curves that are associated to volume of gas instead of time. The change in C_1-C_2 ratio relates to a specific volume of gas extracted. This can then be used to explore a shale-specific recovery factor, based on the composition of the shale sample. Based on the evidence collected in chapter 4, it was apparent that the organic material had the strongest influence on the C_1-C_2 ratio. The overall surface area of the material did not seem to influence the $\Delta C_{1(0)} - C_{1(z)}$. The $\Delta C_{1(0)} - C_{1(z)}$ refers to the overall standard deviation of each C_1-C_2 ($C_{1(z)}$) data point from the bulk gas ($C_{1(0)}$). There did seem to be a relationship however, between the surface area of the samples containing an organic fraction and the $\Delta C_{1(0)} - C_{1(z)}$. Building on this relationship, the samples tested in this chapter contain a range of different TOC (%) and kerogen types. It became apparent that surface area of the organic-bearing material is incredibly important to the $\Delta C_{1(0)} - C_{1(z)}$ and change in C_1-C_2 ratio with degassing. In terms of generating a geochemical index for degassing shales to help predict the recovery factor and location on the production decline curve, the C_1-C_2 ratio is not a function just of the TOC (%) but the associated surface area.

Once it was established that the C_1-C_2 ratio was different for each degassed shale and their extracted kerogens, further investigation into the cause of this fractionation was carried out. Understanding what causes this fractionation has a two-fold benefit. Primarily, if the main contributing factors to changing C_1-C_2 ratio can be determined then a universal volumetric production decline curve can be generated for any shale gas well. By generating a production decline curve that is associated with the total volume of gas in place, a shale gas company could take the necessary measurements from a shale core e.g. surface area and kerogen type and then predict from our degassing method, how much gas may be in place in the reservoir. By calculating the expected volume of gas in place and measuring the C_1-C_2 ratio through production time in the initial stages of gas extraction, a volume decline curve will aid in robust economic forecasting of the well. The cause of fractionation will be discussed in detail in this chapter.

The second benefit to understanding the influencing factors on the C_1-C_2 ratio is understanding what this fractionation relates to i.e. fractionation driven by sorption processes thus being a proxy for volume of gas stored in the adsorbed phase *or* whether the fractionation is driven by diffusive flow through a microporous, tortuous network in which case it is not a proxy for gas adsorbed or some combination of the two. Whilst adsorbed gas to free gas has been the context of many shale gas studies, no consensus has been reached on how much gas is stored as free gas versus adsorbed gas, how to predict the volume of gas adsorbed and how this adsorbed gas is released (Cheng and Huang, 2004b; Han et al., 2016; Li et al., 2015a, 2017; Yuan et al., 2014b; Zou and Rezaee, 2019b). This study aims to approach the degassing shales in a different way, the change in C_1-C_2 ratio may be driven by adsorption-desorption and/or diffusive fractionation processes but the overall change in geochemistry with volume of gas extracted need not relate specifically to either process to be a useful indicator of volume of gas extracted. As the volume-based production decline curves consider total volume of gas in both

the adsorbed, diffused and free gas phase, it becomes secondary to know where the gas is stored. As long as the C_1-C_2 ratio changes related to the total gas volume, it is useful for calculating shale gas production. There is however, scope to infer the adsorption-desorption versus diffusive fractionation trends. In terms of scientific completeness and for considering the potential of a shale to store gas, determining the adsorbed, diffused and free gas is an important characteristic of a shale gas reservoir to understand.

This will be discussed in chapter 7 which will consider adsorption-desorption and diffusion for the entire suite of samples which form the basis of all 4 thesis data chapters. As such, the results discussed in this chapter will be done so in this order:

1. Recap of hypothesis from chapter 4 and expected results from the literature
2. C_1-C_2 ratio as a proxy for volumetrically-derived production decline curves
    a. How does TOC (%) influence the $\Delta C_{1(0)} - C_{1(z)}$?
    b. How does kerogen type influence the $\Delta C_{1(0)} - C_{1(z)}$?
    c. Using the BET, BJH, Langmuir and SEM data, what factor(s) determine the change in C_1-C_2 ratio and $\Delta C_{1(0)} - C_{1(z)}$?
    d. What factors have been suggested in the literature to have an influence but do not appear to in this data
3. How might this geochemical index be put into practice when determining the decline curves?

5.5.3. Literature hypothesis: TOC as a controlling factor on C_1-C_2 fractionation?

It was originally hypothesised that by increasing the total organic carbon % of a shale, there would be a direct and correlatable increase in the storage capacity of that shale (Durand, 1980; Fathi and Akkutlu, 2009b; Ross and Bustin, 2009b). This would be reflected in the molecular weight fractionation between C_1-C_2. The whole shale with the highest TOC (%) -

the West Lothian shale would have the greatest gas storage capacity which would thus induce the greatest fractionation between C_1-C_2 as the stored gas desorbed from the surface of the organic material. A higher volume of kerogen was hypothesised to yield more sorption sites resulting in a bigger change in the C_1-C_2 ratio (Liu et al., 2016a); consequently, the extracted kerogens were hypothesised to have greater adsorption capacities and greater changes in the C_1-C_2 ratio with degassing.

My results show that there is not a simple relationship between the total volume of organic material and the volume of gas adsorbed. The lack of relationship is summarised in Figure 77a, a cross plot showing the 3 natural and 3 extracted samples plotted against their respective TOC (%). The TOC (%) for the kerogens was roughly calculated using the change in organic peaks relative to the inorganic peaks between N and K samples in the FTIR data. There is not a clear relationship between increasing the volume of organic material and increasing the volume of gas adsorbed, contrary to popular belief. This is shown both by the standard Langmuir isotherm analysis and the newly designed experimental setup.

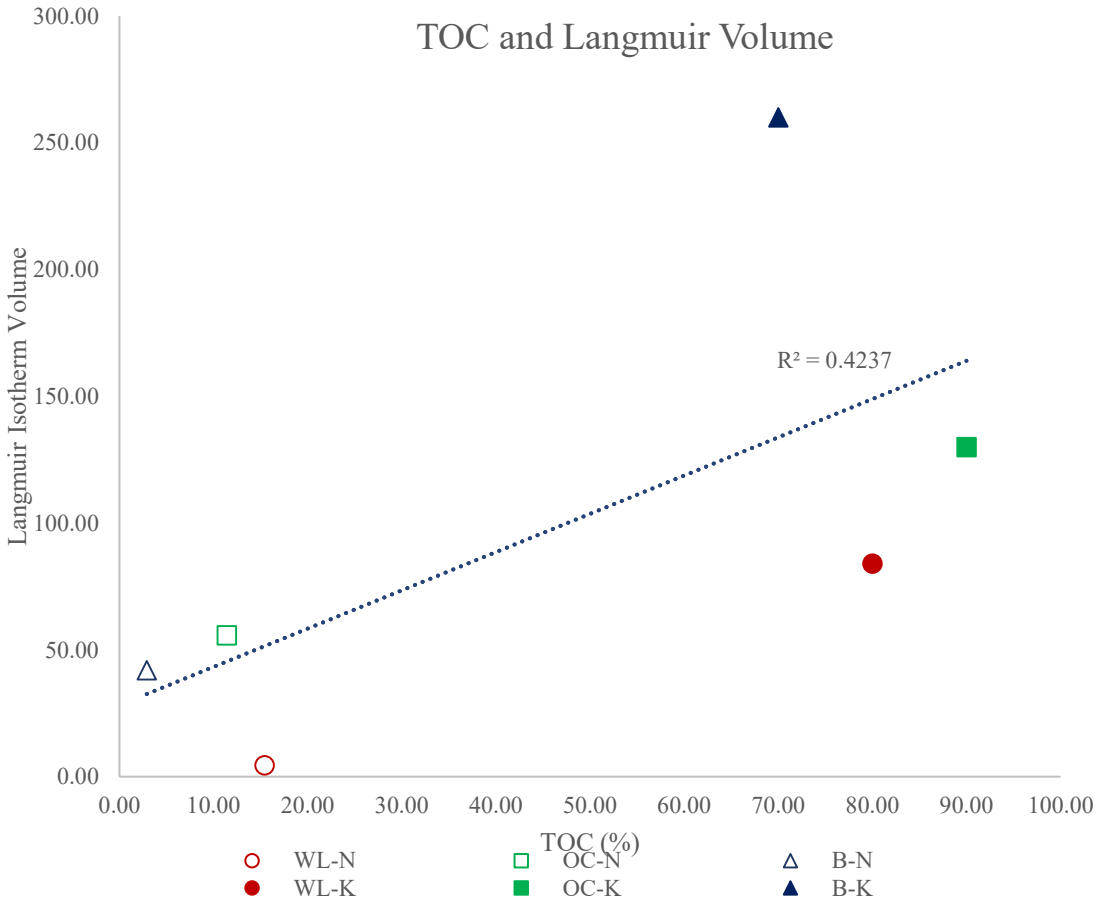


Figure 77| TOC and Langmuir volume for the extracted kerogens and natural samples tested. There is no clear relationship between the volume of organic material and the amount the Langmuir volume measured.

There are two points to consider in terms of the experimental data when looking at Figure 75; the peak change in C_1-C_2 compared to the bulk gas and the volume of gas extracted to reach this peak. The "height" of the curve generated by plotting the C_1-C_2 ratio with degassing relative to the bulk gas is a simply reference point to use when comparing the relative change in C_1-C_2 degassing composition between the samples. This peak height of the C_1-C_2 degassing curve indicates the amount of fractionation that has occurred for that extraction step. C_1-C_2 fractionation is a function of sorption processes and/or diffusional fractionation. The volume of gas extracted until the peak fractionation point is reached indicates the rate at which the fractionation processes are occurring. The volume of sample that is degassing remains constant between each experiment as does the initial volume of gas being injected, the influencing factor is the composition of each shale sample. Based on the results collected in chapter 4, C_1-C_2

fractionation of gas extracted from isolated shale components, it was hypothesised that the TOC would influence both the peak C_1-C_2 height and the volume of gas extracted to peak height. Neither of these two reference points appear to have a simple relationship with TOC, shown in Figure 78 and Figure 79Figure 80. The possible relationships will now be explored.

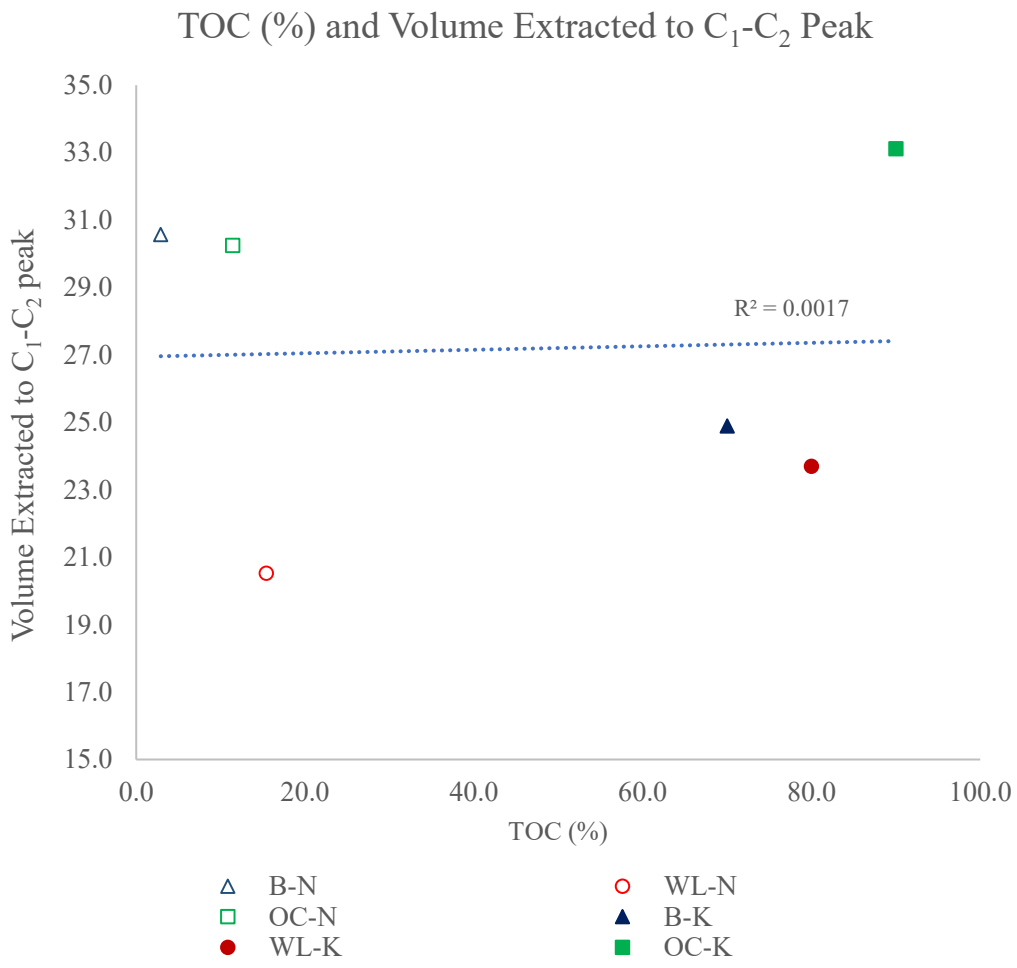


Figure 78| TOC (%) plotted against the cumulative volume of gas extracted before the peak C_1-C_2 ratio was reached for each sample. There is no correlation between the amount of organic material and the amount of gas extracted before peak fractionation is met. The volume-to-peak can be a proxy for the volume of gas stored in the adsorbed phase as the desorption process would contribute to the increments of gas being extracted

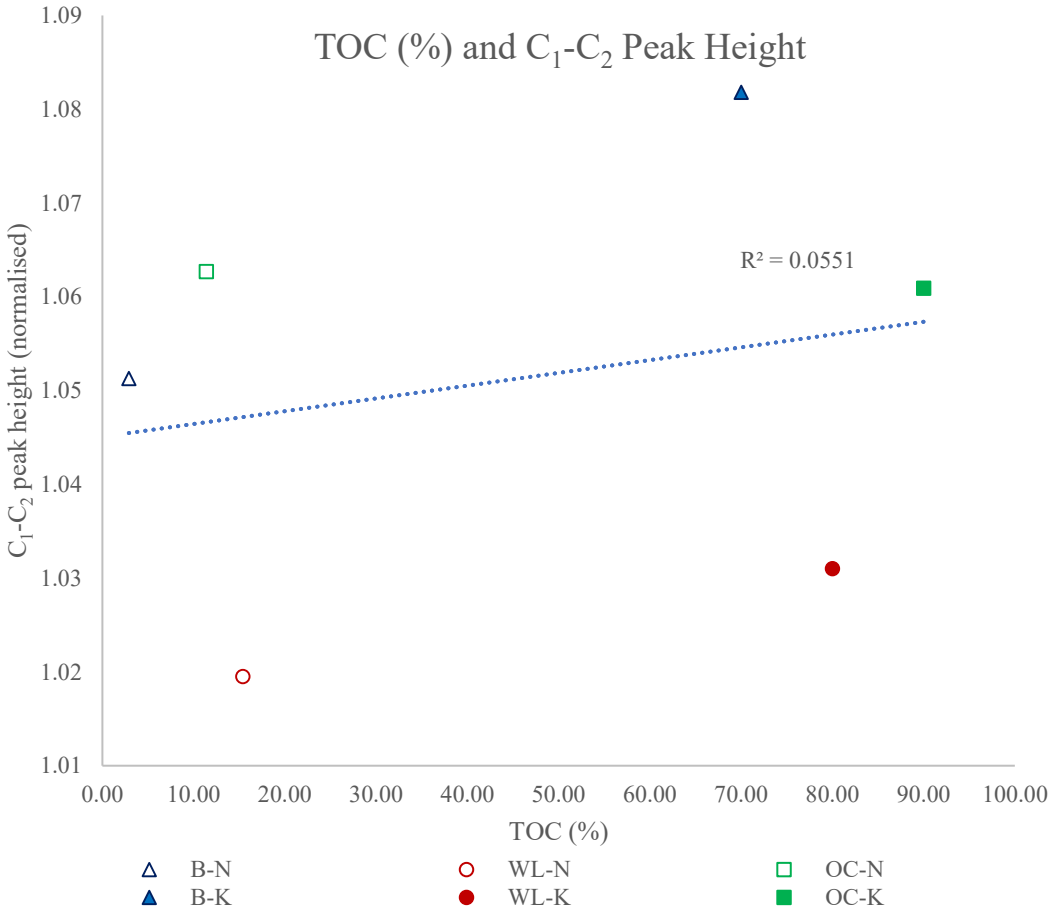


Figure 79| TOC (%) plotted against the C_1-C_2 ratio "peak height". This refers to the point at which the C_1-C_2 ratio deviates the furthest away from the bulk gas was reached for each sample. There is no correlation between the amount of organic material and maximum change in C_1-C_2 ratio of the degassed material to the bulk gas. The magnitude of change in C_1-C_2 ratio compared to the bulk aas can be a proxy for the volume of gas stored in the adsorbed phase as the desorption process would contribute to the increments of gas being extracted or could be influenced by the diffusion processes in which case would be a proxy for distance travelled within the shale.

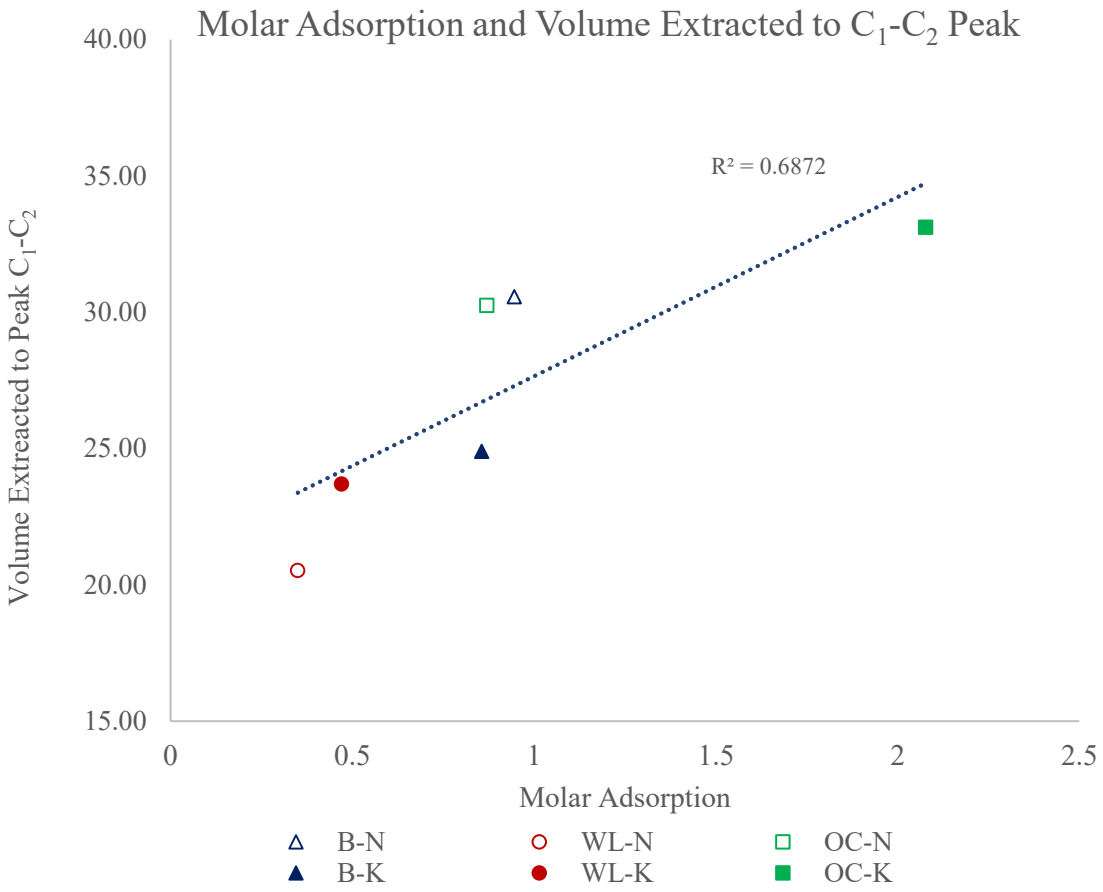


Figure 80| Molar adsorption calculated from the pressure measurements recorded from the sample cell during introduction of gas to the shale or kerogen, plotted against the cumulative volume of gas extracted before the peak C_1-C_2 ratio was reached for each sample. There is a weak correlation between the amount of moles adsorbed and the amount of gas extracted before peak fractionation is met. The volume-to-peak can be a proxy for the volume of gas stored in the adsorbed phase as the desorption process would contribute to the increments of gas being extracted

5.5.4. Other factors that could influence C_1-C_2 fractionation trends

The evidence collected in chapter 4 strongly suggested that TOC would have the greatest influence on the change in C_1-C_2 ratio with gas extraction. To test the influence of TOC three samples of differing TOC and kerogen type were tested. The hypothesis was that the dominant control on the C_1-C_2 ratio would be the amount or organic material present in the shale. The clays have a minor influence and the inert calcite and clay material have a negligible influence. What was shown by the data collected in this chapter however, was that the TOC did not correlate either with the overall $\Delta C_{1(0)} - C_{1(z)}$ or the peak C_1-C_2 height. The height of the peak

and the volume % extracted to peak both relate to the adsorptive-desorptive and the diffusive fractionation with degassing thus were hypothesised to be influenced by the volume of organic material within the sample.

5.5.5 Argument for Surface Area as the controlling factor on C_1-C_2 peak height

Table 27 indicates the other characteristics besides composition that may influence the C_1-C_2 ratio of the extracted gas. Cross plots of these measurements, including surface area, calculated Langmuir volume and porosity, plotted against peak height and volume-to-peak were generated. The data collected and analysed in chapter 4 suggested that surface area of the sample may influence the C_1-C_2 peak height when relating to the surface area of the organic material. Figure 81 shows a significant correlation between the surface area of a given sample and the C1-C2 peak height. The surface area is independent of the total organic carbon content i.e. the WL-N sample contains the greatest volume of TOC but has the lowest BET surface area measured.

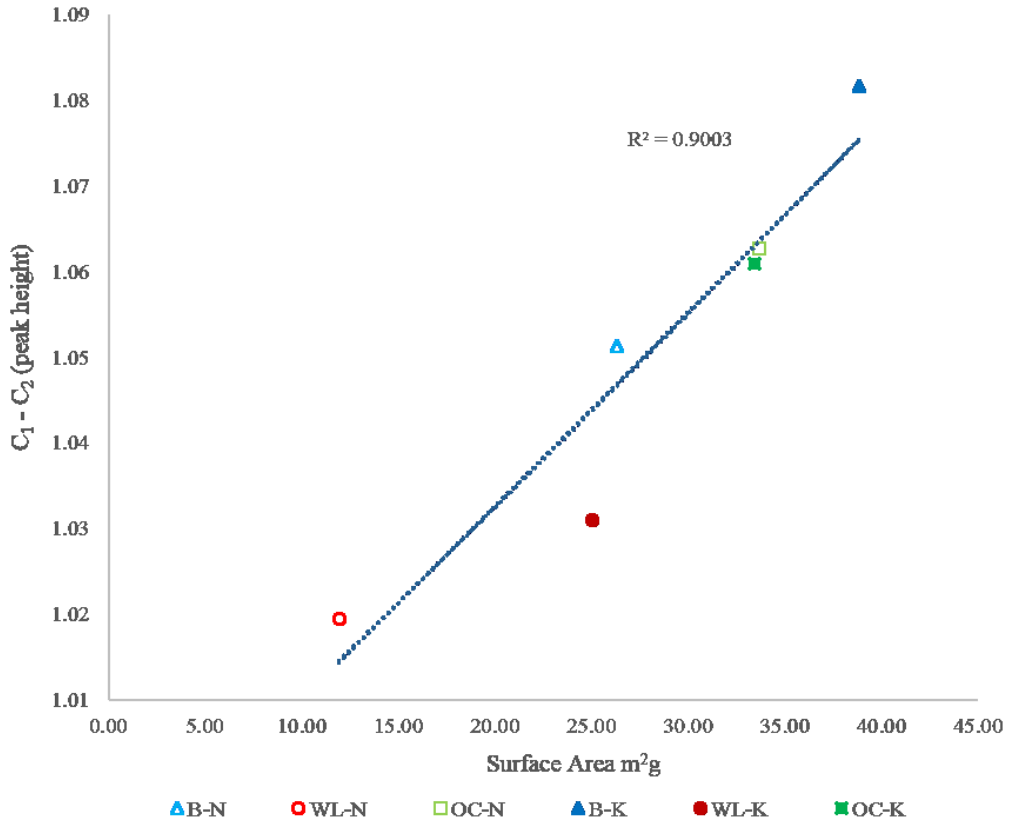


Figure 81| cross plot of the C_1-C_2 peak height and the calculated BET surface area of the three shale samples and their respective extracted kerogens. The R^2 value relates to the proximity of each data point to the regression line, shown by the blue dashed line.

There is a direct correlation between the surface area of each sample and the C1-C2 peak height, shown in Figure 81. Both follow in order from smallest to largest:

W-N < WL-K < B-N < OC-K < OC-N < BK

WL-N WL-K have smallest surface areas at 11.92 m^2/g and 25.03 m^2/g respectively and the smallest C_1-C_2 peak. OC-K and OC-N have very similar surface areas at 33.436 m^2/g and 33.698 m^2/g respectively. OC-N has a slightly greater C_1-C_2 peak which is reflected in the surface area. The greatest surface area is seen in B-K at 38.841 m^2/g which also represents the greatest C_1-C_2 peak. Whilst TOC has dominated previous research into shale as storage capacity, recent papers have suggested that surface area may play the greatest role, independent of the volume of organic material present (Boruah et al., 2019; Kim et al., 2017). This is evident

not only between the kerogen types where type I kerogen, the WL sample, has the highest TOC but smallest deviation of C_1-C_2 degassing compared to the bulk gas but also compared the OC-N sample and its extracted kerogen sample. The TOC increased significantly from the bulk rock to the isolated kerogen but there is not a representative change in surface area.

There are two points to be taken from this. Firstly, the BET surface area of the samples, regardless of the organic content, appeared to have a strong correlation with the C_1-C_2 peak height. There was also a correlation seen between the BET surface area and the overall deviation of the extracted gas from the bulk gas. This $\Delta C_{1(0)} - C_{1(z)}$ and BET surface area correlation is shown in Figure 82.

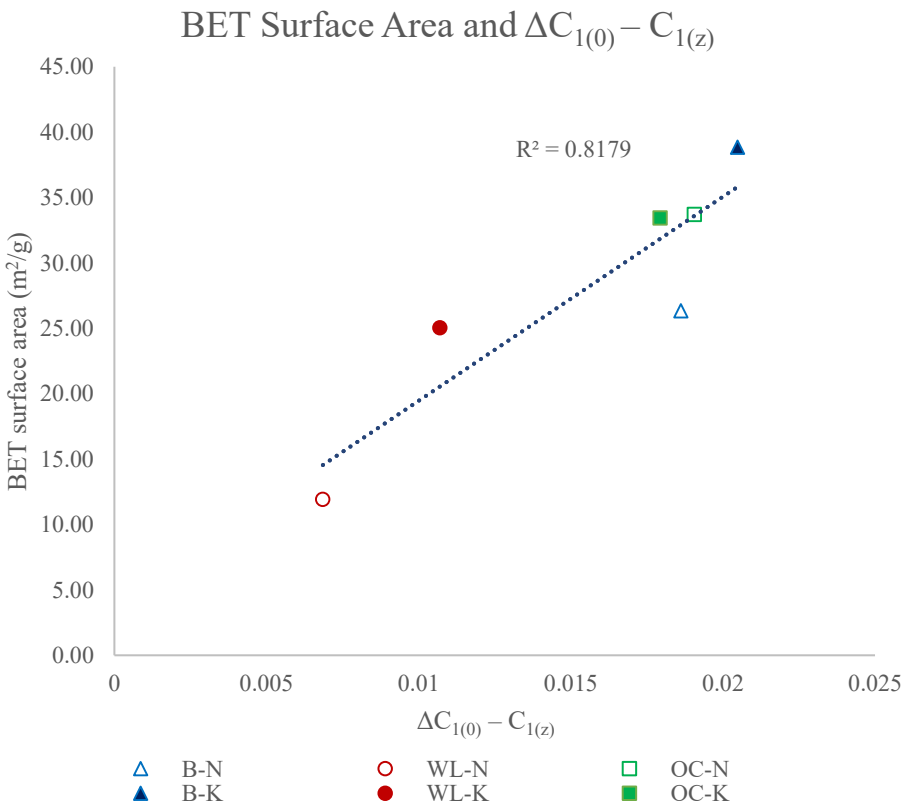


Figure 82| $\Delta C_{1(0)} - C_{1(z)}$ and BET surface area; how much does the extracted gas deviate away from the bulk, in total across the experimental procedure.

Do the surface areas of other minerals contribute to the C_1-C_2 ratio?

Whilst many authors focus solely on the influence of organic material on adsorption capacity of a shale, some authors have studied the effects of clays on methane adsorption. Studies have shown that clay minerals have different adsorption capacities with smectite having the greatest and illite the least (Ji et al., 2012b; Liang et al., 2016). Others have suggested that illite has a strong adsorption capacity whilst kaolinite has little (Busch et al., 2009; Chalmers and Bustin, 2007a; Kuila and Prasad, 2013; Lu et al., 1995; Schettler and Parmoly, 1990b). It may also not simply be the case of clay mineral type effecting adsorption but also on clay diagentic history (Ji et al., 2012b). It is suggested that the surface area of different clays has a direct impact on the volume of gas that can be sorbed (Busch et al., 2009; Liang et al., 2016). Clays may be a potential reason for the lack of relationship between TOC (%) and surface area. However, based on the pervious research carried out in chapter 4, it is evident that, whilst clays have relatively large surface areas, they do not influence greatly the change in C_1-C_2 ratio with sample degassing. The $\Delta C_{1(0)} - C_{1(z)}$ was an order of magnitude smaller between clays and organics. This suggests that the $\Delta C_{1(0)} - C_{1(z)}$ must be influenced by the organic fraction.

5.5.6 Surface area and adsorption capacity

Adsorption capacity is represented by the Langmuir volume. Figure 83 shows the surface area of each sample plotted against the measured adsorption capacity. Figure 77 showed the TOC of each sample plotted against the C_1-C_2 peak. There is no clear relationship between the calculated Langmuir volume, the gas that can be adsorbed by a sample, and the relative amount of C_1-C_2 fractionation seen. Either C_1-C_2 fractionation is not controlled by desorption processes or TOC is not the controlling factor.

Whilst there could be some relationship e.g. WL-N has the lowest capacity for gas storage at 4.40 cc/g and the smallest fractionation trend, this relationship is not seen across all the samples. OC-K has the largest volume of gas that can be adsorbed onto the surface yet a moderate fractionation trend compared to the other samples. B-K, which has the greatest fractionation peak has the second largest Langmuir volume yet this is almost three times smaller than the OC-K. This lack of relationship is seen occasionally in the literature (Kim et al., 2017).

Whilst there was not a direct correlation between the amount of organic material present within the shale sample and the Langmuir volume, there is a correlation between the surface area of the sample and the adsorption capacity. Again, this suggests that the current thinking which tends to consider TOC as a proxy for gas storage is incorrect and surface area, specifically surface area of the organic material is more significant. Furthermore, it is evident that the type of organic material plays a role not only on the overall surface area but also the adsorption capacity of the shale and the $\Delta C_{1(0)} - C_{1(z)}$.

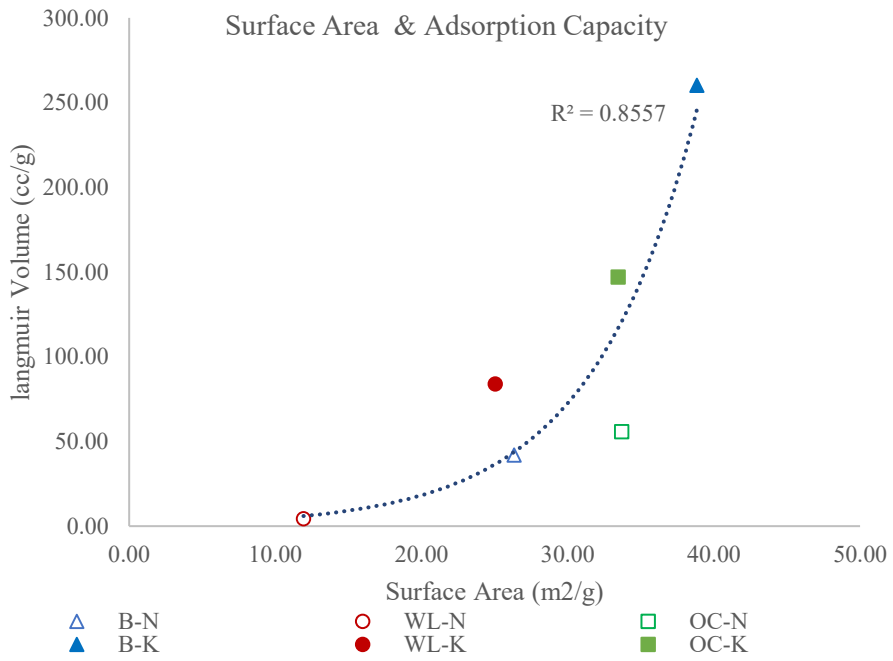


Figure 83| BET surface area (m^2/g) and Langmuir volume (cc/g) for each three samples and their isolated kerogens

5.5.7 Kerogen Type

Some authors have suggested that different kerogen types have varying affinities for adsorbing methane (Gasparik et al., 2014; Ji et al., 2012b; D. Zhang et al., 2016). Type III kerogen has been suggested to have greater affinity for adsorbing methane than type II and type I which in turn would influence the C_1-C_2 degassing trend and must be considered when generating a geochemical index for shale degassing. It is debatable whether the total volume of organic material would become more of a factor when the same kerogen type is considered i.e. 5% type I kerogen compared to 15% type I kerogen. For the WL-N sample and the B-N sample, it is apparent that by increasing the relative abundance of the kerogen, there is an increase in both the adsorption capacity and the C_1-C_2 peak height. This is not the case however for the OC-N sample which sees an increase in the adsorption capacity — shown by the Langmuir volume — but very little change to the surface area and the C_1-C_2 peak height. This suggests that simply increasing the TOC (%) may not yield an increase in gas storage capacity and greater volumes of gas extracted.

5.5.8 Do porosity or pore volumes influence the C_1-C_2 fractionation trend?

B-K has the greatest pore volume by a significant margin, 0.402 cc/g compared to the next greatest pore volume, OC-K, with 0.218 cc/g. Whilst this somewhat correlates with the peak fractionation trends, it does not hold true for the next greatest pore volume, WL-K at 0.125 cc/g and one of the lowest fractionation peaks. There is no obvious correlation between the pore volume and either the C_1-C_2 peak height or the volume of extraction required before this peak is met.

Authors have postulated as to the influence of a bimodal pore size distribution on positive gas storage capacity (Ross and Bustin, 2009; Wang et al., 2015). B-K has by far the greatest average pore radius at 308Å. As B-K is a type III kerogen, there is a larger volume of pores at

the micro- and meso- rather than nanoscale. The fact that there is little increase in the Langmuir volume yet a vast increase in pore radius, combined with a significant increase in the C_1-C_2 height suggests that the role of gas storage in these micropores may have been overlooked in the literature. B-K has one of the most rapid volume extraction times to the peak C_1-C_2 ratio. This may reflect the relative ease in which free gas can escape the sample through these larger pores encouraging desorption. The desorbed gas in turn can easily escape the sample. OC-K has the smallest average pore radius at 14.8 Å. The change in pore radius between the extracted kerogen and whole shale is the greatest in the OC suite and also sees the greater change in Langmuir volume, from 55.24 to 130 cc/g respectively. This does not, however, correlate with a greater C_1-C_2 peak, a proxy for C_1-C_2 storage capacity. The remaining samples have an incredibly similar average pore radius at 19.6 Å and there is no obvious correlation between this and C_1-C_2 storage.

5.5.9 Surface area of the organic material is the controlling factor on C_1-C_2 fractionation with degassing

It was originally hypothesised that by increasing the total organic carbon % of a shale, there would be a direct and correlatable increase in the storage capacity of that shale (Akkutlu et al., 2012; Durand, 1980; Ross and Bustin, 2009a). This would be reflected in the molecular weight fractionation between C_1-C_2. The whole shale with the highest TOC - the West Lothian shale would have the greatest gas storage capacity which would thus induce the greatest fractionation between C_1-C_2 as the stored gas desorbed from the surface of the organic material. A higher volume of kerogen was hypothesised to yield more sorption sites resulting in a bigger change in the C_1-C_2 ratio (Liu et al., 2016b) consequently, the extracted kerogens were hypothesised to have greater adsorption capacities and greater changes in the C_1-C_2 ratio with degassing.

What is shown by the results is that different shales do produce a unique and repeatable C_1-C_2 fractionation trend but the cause of this is not simply related to the TOC The lack of relationship is summarised in Figure 77, a cross plot showing the 3 natural and 3 extracted samples plotted against their respective TOC. The TOC for the kerogens was roughly calculated using the change in organic peaks relative to the inorganic peaks between N and K samples in the FTIR data. There is not a clear relationship between increasing the volume of organic material and increasing the volume of gas adsorbed. This is shown both by the standard Langmuir isotherm analysis and the newly designed experimental setup.

There are two points to consider in terms of the experimental data; the peak change in C_1-C_2 compared to the bulk gas and the volume of gas extracted to reach this peak. The height of the peak indicates the amount of fractionation that has occurred and may relate to purely sorption processes or diffusional fractionation. The volume of gas extracted until the peak fractionation point is reached indicates the speed at which the fractionation processes have occurred and the amount of time that the desorption process is contributing the gas being extracted. Neither factor appear to have a simple relationship with TOC directly but relate to the surface area of the samples (Figure 82).

In conflict with the previously established concepts that imply a correlation between adsorption capacity, fractionation and TOC, the C_1-C_2 fractionation data collected originally in time and then converted to volume % of total gas shows no correlation between TOC content of the sample and the adsorption capacity, C_1-C_2 fractionation peak height or volume of gas extracted before this peak is met.

- The West Lothian shale sample contains the highest volume of organic material, almost 16% yet incites the smallest deviation from the bulk gas with the lowest C_1-C_2 peaks.

- The Bowland shale contains 2.9% total organic carbon but has a greater adsorption capacity than the West Lothian Shale and generates a greater change in C_1-C_2 composition compared to the bulk gas.
- The Oxford Clay contains 11% TOC and exhibits the greatest change in C_1-C_2 fractionation from bulk gas composition.

It was also hypothesised that the extracted kerogens would generate a greater C_1-C_2 fractionation than the bulk gas as more gas should be stored in the adsorbed phase. Whilst this is the case for the B-K and WL-K, it is not the case for the OC-K which actually has a slightly lower C_1-C_2 fractionation peak.

5.5.10 What is the significance of these unique C_1-C_2 fractionation trends?

The aim of this study was to calculate volume of gas extracted from the sample cell and correlate this to a molecular weight fractionation trend. This change in C_1-C_2 ratio corresponds to a specific volume of gas extracted from the total gas in place, thus it also has the potential to function as a proxy of a production decline curve. This allows quantitative analysis of gas volumes, molecular weight composition of reservoir gas for a given amount of total as extracted as well as residual gas, something that has yet to be translated readily to production data. When volumetric calculations carried out, it is evident that the shale degassing signatures are significantly different to the time plots. This highlights the importance of this technique in calculating the volume of total gas extracted and the molecular weight fractionation ratio for a given gas volume.

5.5.11Mass balance: predicting the gas tail

If the peak gas represents a specific volume of gas that has been extracted then the final composition can be predicted. Using the Oxford Clay as an example in Figure 84, the predicted

remaining gas volume is shown by the blue colour graded rectangle. The C_1-C_2 peak for the OC-N sample occurs after 30% of the gas has been extracted. The initial composition can be back-calculated using the peak C_1-C_2 ratio and 30% volume as a marker point. The weighted molar mass for each increment extracted can be calculated as follows:

$$\frac{1}{mv} = \frac{v\%}{mwC_1} + \frac{v\%}{mwC_2}$$

Where *mv* is molar mass, *v* is volume as a % and *mW* is the molecular weight. Assuming a closed system, once the initial composition has been back calculated, the C_1-C_2 composition of the remaining gas can be calculated though mass balancing. Figure 87 shows the graphical worked example for OC-N — the full calculations for this are available in Appendix Chapter 5.

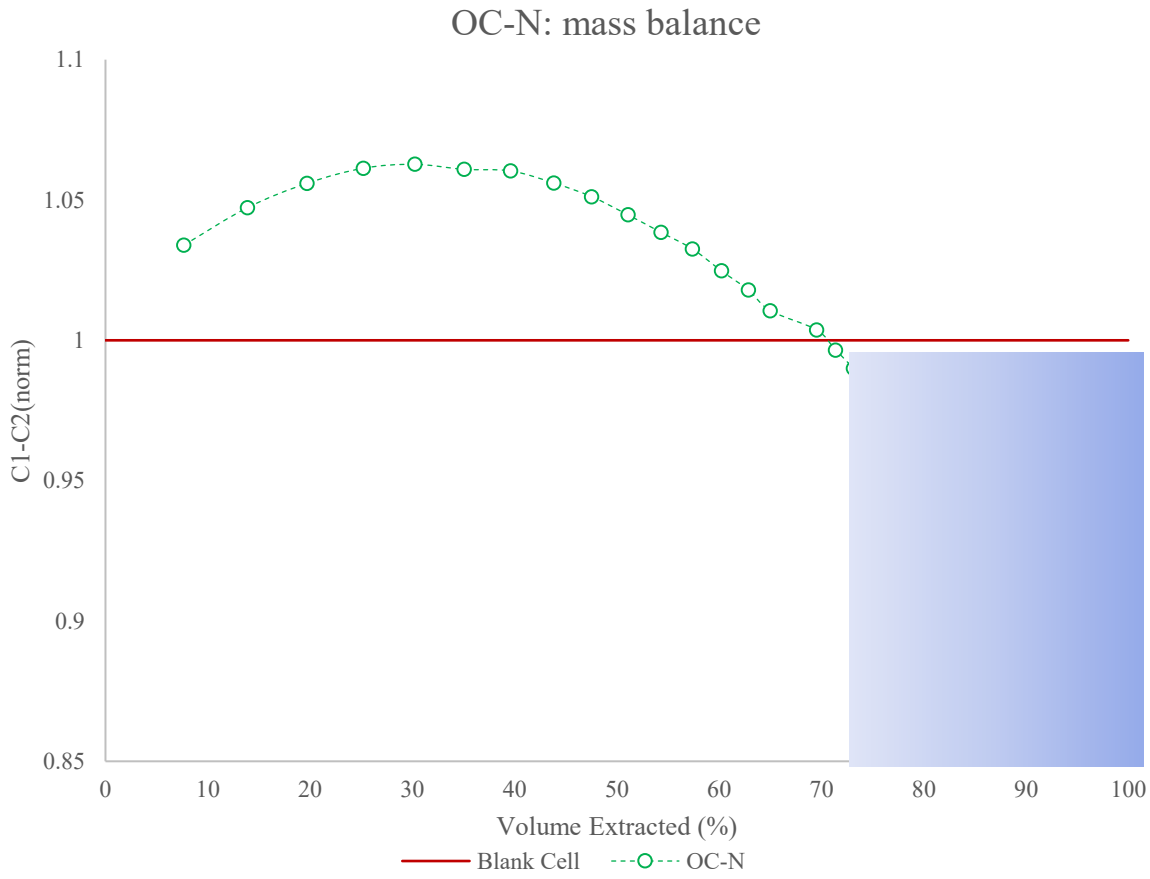


Figure 84| Material balance for the OC-N sample. The sum total of methane molecules and ethane molecules for each extraction step relative to the initial molar volume of methane and ethane injected gives the remaining molar volume of methane and ethane in the cell. The material balance only gives the ratio of methane to ethane left in the cell, not the exact shape of the curve so this is only a prediction. The graph does however show that the final 25% of the gas still trapped in the sample has a higher proportion of ethane relative to ethane than the starting gas.

Mass balance equations were calculated for the three whole shale and isolated kerogen samples; these are shown in Figure 85. As expected, the greater the C_1-C_2 peak, the smaller the final C_1-C_2 ratio. The ability to predict the final composition of the extractable gas generates a full C_1-C_2 compositionally derived volume decline curve. These curves can only predict the shape of the curve based on the composition of the gas remaining in the sample. Ultimately, each sample initially releases gas that has a progressively higher proportion of methane relative to the bulk gas, until it reaches a peak C_1-C_2 ratio. After this point, whilst much of the samples still release gas that has more C_1 relative to the bulk gas, the ratio is constantly dropping towards the bulk gas C_1-C_2 ratio. The residual gas, gas that was not extracted during the experiment, for each sample has a lower C_1-C_2 ratio than the bulk gas.

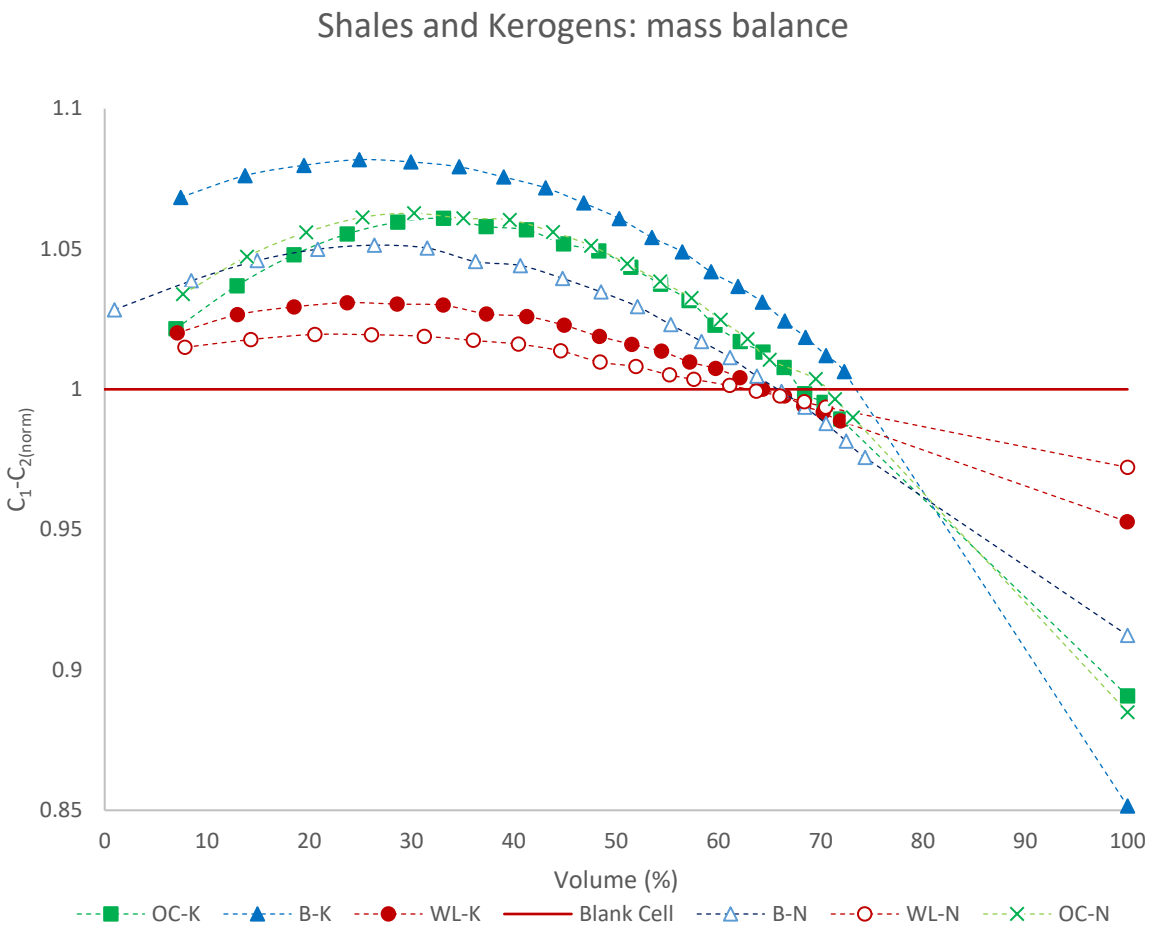


Figure 85| Mass balanced gas tail composition predictions for the three whole shale samples and the isolated kerogen samples.

5.5.12 Summary of C_1-C_2 as a proxy for quantitative production decline

Initially, this work has shown that C_1-C_2 is a viable geochemical index for predicting the total volume of gas in place and predicting the final composition of the reservoir gas thus generating a predicted geochemical decline curve. The basis of this index is as follows; C_1-C_2 fractionation curves reach a peak C_1 enriched maximum after which, the relative proportion of C_2 begins to increase. This C_1-C_2 peak correlates with a specific volume of gas extracted from the reservoir and varies depending on the composition of the shale. By changing the kerogen type and amount of organic material present, there is a corresponding change in volume of gas extracted before the peak height occurs.

Understanding the processes behind this geochemical index is important in terms of building up the fundamental implications of this research; we have shown that changes in the C_1-C_2 ratio is a viable geochemical index for shale gas extraction. The new method developed allows for rapid collection of data which is easily collected and is reproducible, with small error between triplicate runs.

Once the use of C_1-C_2 as an index for volume of gas extracted had been established as a success, the second phase was understand what parameters of the shale can relate to the size and shape of the C_1-C_2 decline curve; what dictates the height of the C_1-C_2 peak and the volume of gas extracted until this peak is met. The preliminary research in chapter 4 as well as many literature studies outlined in the introduction (e.g. Huang et al., 2018; Romero-Sarmiento et al., 2013; Strąpoć et al., 2006) all suggested that the amount of organic matter present in a shale accounts for the majority of the adsorptive and storage capacity of a shale. As the changes in the C_1-C_2 ratio are intrinsically linked to adsorption-desorption processes and/or diffusive flow, if the initial hypothesis held true then there would be a direct correlation between TOC (%) and change in C_1-C_2 ratio. As already outlined, this was not the case. There is no simple relationship between the amount of organic material, volume of gas adsorbed (shown by the on-line adsorption measurements of the sample cell and the Langmuir isotherm analysis, Figure 77 and change in the C_1-C_2 fractionation curve.

5.5.13 Volume-to-peak and $\Delta C_{1(0)} - C_{1(z}$

The volume-to-peak height and $\Delta C_{1(0)} - C_{1(z}$ is shown in Figure 86. The $\Delta C_{1(0)} - C_{1(z}$ numerically shows the degree of fractionation of the degassed material from the bulk gas. There is not a linear relationship between the volume-to-peak height seen and the degree of fractionation exhibited overall by the degassing material. OC-N has the greatest volume of gas extracted before the peak fractionation point is met but not the greatest overall change in geochemistry. This may be indicative of a high volume of gas in sorbed phase, contributing to

the peak height but less diffusive fractionation as the overall fractionation, after the initial peak height, is less. Conversely, B-K has a lower volume of gas extracted to peak height perhaps indicated a smaller contribution from the desorbing gas initially but greater overall fractionation through diffusion and desorption out of the kerogen in the tail part of the degassing curve.

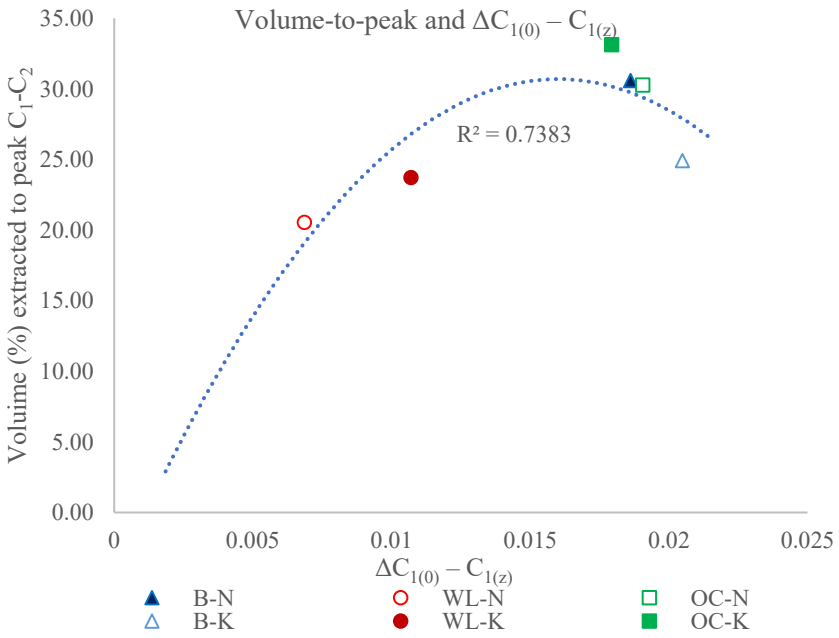


Figure 86| Volume-to-peak height and $\Delta C_{1(0)} - C_{1(z)}$ for the three shale samples and the kerogen samples

5.6 Conclusions

Initially it can be said that this new method functions to isolate the C_1-C_2 ratios through storage and gas transport and that individual shales, regardless of TOC, produce a unique C_1-C_2 fractionation with volume of gas extracted. Each shale and their extracted kerogens produce a unique C_1-C_2 fractionation trend and have different adsorption capacities which do not directly correlate to TOC. Change in C_1-C_2 ratios taken from production data from producing shale gas wells could be used in conjunction with shale composition to:

1. back calculate initial gas in place of a well
2. volume of gas remaining in the well
3. transition from free gas dominated to desorbing gas

The calculated volume of moles initially adsorbed reflect the peak C_1-C_2 values suggesting that this is indeed a proxy for gas storage capacity of a shale and that the sample cell GC-FID setup can provide important understanding of how gas is stored and transported within a shale. TOC is often attributed as the main storage site for shale gas through adsorption. This report however, highlights that the relationship is not as simple as this. Surface area appears to be the dominant control on volume of gas stored and C_1-C_2 fractionation with gas extraction. In the West Lothian Shale and the Bowland shale, increasing the TOC results in a greater surface area yet in the Oxford Clay, this is independent of whether surface area is attributed to organic or inorganic material.

Type of organic material has a significant effect on the amount of gas that can be adsorbed within a shale. The West Lothian type I kerogen sampled showed that the adsorbed gas volume is small and the free gas is extracted rapidly, qualities that would not produce a long-lived shale gas well. Type III kerogen has the greatest adsorption capacity but this peak is reached rapidly. The pores within this sample are by far the greatest. It can be theorized that these larger pores

mean the tortuosity is low and permeability is higher suggesting that, whilst gas storage capacity is high, gas can escape the sample rapidly.

Surface area has the strongest influence on the initial number of moles stored in the sample. The TOC does not have the strongest influence between different kerogen types but does seem to have an influence between type I and type III kerogens.

There is no influence between the TOC of OC-N and OC-K, the type II kerogen. This suggests that another factor is influencing the storage capacity. From literature studies, it seems most likely that the clays have a significant influence on gas storage capacity. This lack of correlation of TOC and porosity and adsorption has also been documented in the type II New Albany Shale (Mastalerz et al., 2013).

6.0 C_1-C_2 Fractionation in degassing shales: artificial maturation

Chapter Aims:

- to further explore the influence of shale organic geochemistry on shale gas geochemistry during gas extraction,
- to investigate the effects of organic matter (kerogen) maturity on C_1-C_2 fractionation during degassing of shale gas reservoirs,
- to characterise the organic matter through BET surface area analysis, Langmuir isotherm analysis and BJH pore size distribution in order to explore the effects on C_1-C_2 fractionation during degassing of shale gas reservoirs.
-

6.1. Introduction

The "boom" of the shale gas industry in the USA since the mid 00's has brought focus to the vast potential of many shales across the world. Throughout the World, there is an estimated 22,016 trillion cubic feet (tcf) of gas, of which at least 5,700 tcf has been determined as technically recoverable across the known shale gas plays (US Dpt of Energy and Kuuskraa, 2011). The development and production of shale gas in the United States of America rose from less than 0.5 tcf in 2004 to almost 5 tcf by 2010 (Energy Information Administration, 2019). There is an estimated 25 tcf of unproven but technically recoverable gas reserves in UK shale reservoirs (EIA, 2015). As the need for energy dependency as well as cleaner hydrocarbons which will allow the gap between renewable and non-renewable energy to be bridged, shale gas may be the answer to the UK's energy requirements which meet the proposed carbon budgeting (US Dpt of Energy and Kuuskraa, 2011).

Economical exploitation of a shale gas reservoir requires understanding not only of how much gas is stored within the shale but where the gas in stored, how much can be extracted and over what timescale this extraction will occur at (Bustin et al., 2008a; Gasparik et al., 2014; Jarvie et al., 2007; Krooss et al., 2010) . Unlike conventional hydrocarbon plays, unconventional reservoirs are characterised by a reservoir, source and cap-rock which are all the same lithological shale unit (Chen and Xiao, 2014; Curtis, 2002; Gasparik et al., 2014; Jarvie et al., 2007). Within unconventional shale gas reservoirs, gas is stored adsorbed onto shale component surfaces, diffused within the nanoporous network and as free gas within any pre-existing macropores or fractures (Guo et al., 2017; Shabro et al., 2011; Zou and Rezaee, 2019b). One of the main complications with understanding a shale gas reservoir is the heterogeneity related to its microstructure (Curtis, 2002). The size and shape of shale pores - effective pore radius, the geometry of pores and apparent permeability will impact the adsorption capacity and desorption effect of a gas within a shale matrix (Löhr et al., 2015; Y. Wang et al., 2016). The adsorption capacity will have an overall influence on the volume of gas that a shale can store which in turn influences how shale gas companies attempt to predict the gas in place (Cheng and Huang, 2004b; Topor et al., 2017).

6.1.1 Why consider artificial maturation?

Chapters 4 and 5 of this thesis consider how TOC (%), kerogen type and surface area of the organic material influence the C_1-C_2 fractionation trend with shale degassing. Regardless of whether this can be used to determine gas storage capacity, an objective of many shale degassing studies, the change in C_1-C_2 ratio has been shown in previous chapters to be a viable geochemical index. This index can inform us on not only the recovery factor (% of the overall initial gas volume that has been extracted) but also the composition of the host reservoir. Knowing the composition of the host reservoir would give a predicted C_1-C_2 fractionation trend, deviations from this could be evidence of gas coming from a shale of a different

composition i.e. draining from a large volume, a greater areal extent away from the drilled well. Changing the surface area of a shale through clay composition, total organic carbon type and total organic matter content can have an effect on how much gas can be stored within a shale and how this gas is extracted. The relationships explored between adsorption capacity in the previous chapters show that it many factors interplay and it is not a simple case of increasing the volume of organic material to increase the gas storage capacity of a shale as often outlined in literature studies (Akkutlu et al., 2012; Etminan et al., 2014b; Gasparik et al., 2014; Kuila et al., 2014a; Liu et al., 2016a; Wei et al., 2012b; Yin et al., 2017a).

Thermal maturation has been outlined in the literature as having the ability to alter organic matter pores (Ambrose et al., 2011c; Curtis et al., 2012; Hu et al., 2015b; Loucks et al., 2009a; Topor et al., 2017; Xiong et al., 2017b). Thermal maturation refers to an increase in temperature of a shale that is typically the product of burial. The Earth's geothermal gradient is approximately 35°C per km so burial of a shale will over several kilometres will move the shale through various hydrocarbon "windows". Often the thermal maturation of a sample can be determined by looking at the vitrinite reflectance of the organic material and placed on a VR_0 scale (British Geological Survey, 2014; Loucks et al., 2009b). The vitrinite reflectance scale is commonly used and requires a polished surface of vitrine which is derived from the cell walls of plants (Cardott, 2012). The percent of incident light reflected off this surface is how we measure the vitrinite reflectance of a piece of organic-material bearing rock (British Geological Survey, 2014). Shales with a VR_0 of than 0.7% are considered in the low end of the hydrocarbon generating window (Loucks et al., 2009b) with 1.5% VR_0 considered as late-mature. The oil window corresponds to the onset of oil generation and has been correlated to a VR of 0.5-0.6% R_0. Between 0.85-1.1 % R_0 is when a hydrocarbon-bearing rock typically enters the gas window (British Geological Survey, 2014). The limitations of VR as a scale is that if a poor-quality sample is used, the data will be poor quality. There are issues with using

outcrop and well cuttings in terms of sample deterioration and cross-contamination, especially from weathering (outcrop samples) and drilling mud additive contamination (well cuttings) (Cardott, 2012). You must also take a certain number of measurements in order to have reliable data, typically more than 20 (Cardott, 2012) .

Different kerogen types will produce oil at different rates, or not at all if they are gas-prone and cannot produce oil (Al-Areeq, 2018). This relates the relative proportions of pristine and phytane, which can refer to the oxidation state of the organic matter and in turn relate to terrestrially-derived, gas prone humic material or oil-prone sapropelic marine or lacustrine material (Al-Areeq, 2018). Type I kerogen is oil-prone at approximately 0.65 R_0% with peak oil generation at 1.1 R_0% before entering the gas window at >1.4 R_0%. For type II kerogen, the most prolific shale source rock, the onset of oil generation is at 0.5 R_0%, entering peak oil generation at an R_0 of 0.8% and finally the gas window at >1.4 R_0%. Type III kerogen tends to be gas prone with a low HI. If any oil is produced it with be at approximately 0.55 R_0 % with "peak" oil at 0.9 R_0%, entering the gas window with an R_0 of >1.4% (Al-Areeq, 2018, p.; British Geological Survey, 2014).

Several literature studies have indicated that by increasing the maturation of a shale, there is a corresponding change in the pore morphology of the organic material (Curtis et al., 2012; Loucks et al., 2009b; Mastalerz et al., 2013b; Topor et al., 2017). If, by changing the pore structure, there is an increase in the relative surface area then it is expected that the shale can adsorb a greater volume of gas. This predicted greater adsorption capacity is based on the preceding chapters of this thesis as well as literature studies which suggests a change in gas storage capacity in the adsorbed phase (Mastalerz et al., 2013b). However, if thermal maturation results in an increased pore size then this reduces the relative volume of gas stored in the sorbed state relative to free gas residing within the void volume (Xiong et al., 2017b). With decreasing pore size there is an overall increase in methane adsorption capacity; so if

pores increase in size through thermal maturation there may indeed be a reduction in the volume of gas stored in the adsorbed phase relative to free gas (Xiong et al., 2017b). Changing the pore size will also perturb fractionation driven by diffusion.

6.1.2 Literature studies: thermal maturity influences gas storage, pore size and gas diffusion

Literature studies conducted on shale samples of varying organic matter maturation suggest that thermal maturation does have an influence on the volume of gas stored within a shale (Chen et al., 2019; Jarvie et al., 2007; Mastalerz et al., 2013b; Song et al., 2019). A change in the volume of pores with thermal maturation of organic matter and its subsequent degradation has been described in key shale gas studies (Jarvie et al., 2007; Löhr et al., 2015). This change in volume of pores has been argued to have a direct influence on the volume of gas that a shale can store (Loucks et al., 2009b).

The effect may not be linear and the development of organic matter pores increases only up until the dry gas window (Song et al., 2019). After this point, the nanopores within the organic material coalesce and overall surface area is reduced (Song et al., 2019). This would mean that a shale of the same clay and total organic carbon volume and composition matured to the dry gas window would store less gas in the adsorbed phase than its wet gas mature counterpart. The change in porosity with thermal maturation is not agreed upon in the literature. Some studies have shown a a decrease in porosity from immature to late mature but then an increase again in post mature (Mastalerz et al., 2013b). These changes in porosity are also accompanied by changes in pore size distributions and relative proportions of nano-, meso- and macro- pores. Other studies have shown that, with initial burial and maturation, the adsorption potential of a shale increases (Li et al., 2015c). With further burial, resulting in an increase in the pressure-temperature regime and thus compaction of the shale, pore size and storage capacity is reduced (Li et al., 2015c). The reduction in pore size reduces the volume of free

gas which reduces the overall storage capacity of a shale but may increase C_1-C_2 fractionation through diffusion (Li et al., 2015c).

There is further debate as to the role of clays in maturation of a shale and whether increasing the thermal maturity of a shale has an influence on the storage capacity and gas extraction potential of a shale. It has been suggested that thermal maturation has an influence on the specific surface area of both organic material and clay material with different correlations seen between shale samples (Chen et al., 2019; Li et al., 2019b). Arguably, when shale samples are collected in situ it cannot be as simple as looking at thermal maturation and porosity. Factors such as compaction during burial, burial history and hydrocarbon generation and expulsion history must also be considered (Li et al., 2019).

These papers argue that whilst the character of the organic matter and mineral composition have an effect on the adsorption capacity of a shale, the maturity of the shale exerts the dominant control.

6.1.3. Literature studies: thermal maturation has no influence on shale gas storage capacity

The role of organic matter maturation in gas storage capacity is not only contentious in how the changes in pore size effect the storage capacity, some authors argue that no effect is seen (Zhang et al., 2012a). It has been shown that, under experimental conditions, differences in thermal maturity showed no significant effect on the total volume of gas stored (Zhang et al., 2012a). Other authors have shown that, whilst there is a change in pore size with thermal maturation, there is no systematic variation between different shales, their levels of thermal maturity and pore size (Fishman et al., 2012; Löhr et al., 2015). This may relate to the presence of bitumen which has the ability to block pores and reduce the measurable porosity of a shale. The direct relationship between total organic carbon and development of organic matter pores is thus in itself, contentious (Löhr et al., 2015).

6.1.4 Aim of this chapter

It is widely accepted that maturation of organic material changes the pore structure of a shale although the direct effects on pore size distribution, pore throat sizes and development of spongey porosity is still in question (Mastalerz et al., 2013). Change in gas storage capacity of a shale with maturation is still being explored. As organic material is cracked and bitumen released, the impact of gas dissolved within this may mask the effects of changing pore sizes (Curtis et al., 2011, Mastalerz et al., 2013).

Chapter 5 highlights the impact of BET surface area of the organic material as a key influence on volume of gas that is adsorbed on the surface of the shale constituents. For the West Lothian and Bowland sample suites, there is a link to increased TOC (%) and increased methane adsorption capacity. For the Oxford Clay series, increasing the TOC (%) did little to alter the methane adsorption capacity. To investigate the effects of organic maturation on gas storage capacity, removing the effects of bitumen, the same GC-FID coupled with custom built sample cell, outlined in chapter 3 is used along with artificially matured samples of the Oxford Clay suite. As highlighted in previous chapters, C_1-C_2 is a viable geochemical index reflecting gas storage locations and, using C_1-C_2 volume curves, could be used to back calculate the initial GIP. The inherent fractionation between methane and ethane through desorption can be used to determine free gas vs adsorbed gas and its relationship to specific, testable variables. In this case, that variable is organic matter maturity.

6.2. Methodology

6.2.1 Samples

The Oxford Clay, as outlined in chapter 5, is Callovian to Oxfordian aged and was sampled from Chickerell, Weymouth in the south of England. Rock-eval analysis of this sample indicates 11.09% total organic carbon (TOC) and a type II marine kerogen. The same Oxford Clay sample, used in chapter 5, was artificially matured in a procedure outlined in the Experimental Parameter section of this chapter.

6.2.2. Experimental Parameters

Sample Preparation

The Oxford Clay sample, once collected, was stored wrapped in aluminium foil in a polythene sample bag. The sample was crushed with a pestle and mortar and sieved to 125-250 µm grain fractions. The sample was not treated with acid or washed with water so as not to alter the original composition of the sample. Prior to experimentation, the sample was kept in a drying box for 24 hours at 38°C. This encourages loss of surface water or any gases adsorbed onto the exposed surfaces of the shale whilst not causing degradation of the kerogen.

BET surface area, Langmuir isotherm and BJH pore analysis

Similar to previous chapters, the surface area, the adsorption capacity and the pore size distribution were measured using the Quantachrome ® ASiQwin ®- Automated Gas Sorption Data Acquisition and Reduction ■ 1994-2017, Quantachrome Instrument version 5.2. The raw data for this is in Appendix chapter 6. A full description of these techniques is outlined in chapter 2, the Methodology.

Hydrous Pyrolysis

To artificially mature the samples, representing oil mature and gas mature, the powdered sample was split into three equally weighted sections. One was kept as the natural sample, representing a marginally mature type II kerogen rich source rock. The remaining two thirds were then prepared for artificial maturation via hydrous pyrolysis.

Hydrous pyrolysis is defined as a laboratory experimental procedure for stimulating the natural formation of hydrocarbons from organic rich material in an environment lacking oxygen but in the presence of liquid water (Lewan, 2017). A schematic example of a hydrous pyrolysis unit is shown in Figure 87. A stainless steel, 100ml volume reactor with a thermal source at the base and a sealed lid and pressure gauge at the head acts as the sample holder. As such, it is a closed reactor system and can generate oil from hydrocarbon bearing source rocks when heated to between 250-374°C. The presence of liquid water is integral to the kerogen cracking procedure and is a more accurate representation of maturation through burial as liquid water is ubiquitous in sedimentary basins (Lewan, 2017)The reactor limit is 374°C, the critical point of distilled water.

In this experimental procedure, no more than 15 g of sample was added at a time due to the size of the reactor. The sample must always remain submerged in liquid water throughout the experimental procedure. To maintain this submersion, around 35 ml of water had to be added. Due to the small reactor size, the remaining volume of the reactor had to be left otherwise there was risk of explosion.

The hydrous pyrolysis bombs were cleaned with de-ionised water and cleaned with brushes to remove any material adhering to the inside. 30 ml of de-ionised water was added to each bomb which was then sealed and heated to 320°C for 24 hours. After the heat cleaning cycle, the sample could safely be added without risk of contamination. The sample was added

to the bomb and covered with 30ml of de-ionised water. The bomb was sealed and then flushed with He to remove air within the bomb. Prior to heating, the bomb contained only the sample, liquid water and He gas. The bomb was then heated to 250°C for the oil-mature samples and 325°C for the gas mature samples over the course of 24 hours. Once cooled, the contents of the bomb was placed in centrifuge tubes and separated into the solid sample and residue which was kept aside for GC-MS analysis. The samples were then transferred to silica glass beakers and loosely covered with aluminium foil to air dry.

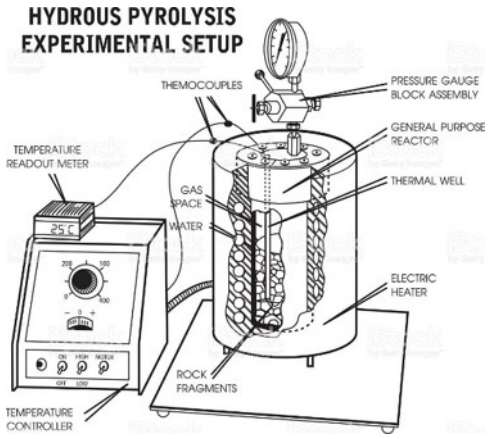


Figure 87| Hydrous Pyrolysis setup (Collard and Blin, 2014). The samples remain submerged in fluid thus are considered pyrolyzed in an aqueous setting.

Sample Cell – GC-FID

A full description of the development of this technique is given in chapter 2, the methodology. An overview is given here.

A sample cell, designed to allow parameters such as initial molar volume of gas injected, sample volume and adsorption capacity of the sample was constructed (see Figure 88). The cell comprises of a reference volume into which the C_1-C_2 mixture is injected. As the reference cell is attached to a pressure transducer, the molar volume of gas can be calculated using the ideal gas law. Direct injection and blank instrument runs allow the ratio of C_1-C_2 in the sample gas to be calculated. As such, the initial volume of C_1-C_2 is known. The gas is then expanded into

the sample chamber which contains a powdered form of the sample to be tested. Change in pressure after the immediate injection of gas into the chamber is evidence of gas moving out of the free gas stage and adsorbing onto the inorganic and organic pore walls. Once equilibrated, the gas is sequentially extracted into PEEK tubing and sent into the GC-FID. The hydrogen flame burns the gas and analyses the amount of hydrocarbon analyte, oxidising the organic molecules to produce particles with an electric charge. These charged particles produce a measurable signature which have different molar response factors which are equal to the number of carbon atoms comprising that specific molecule.

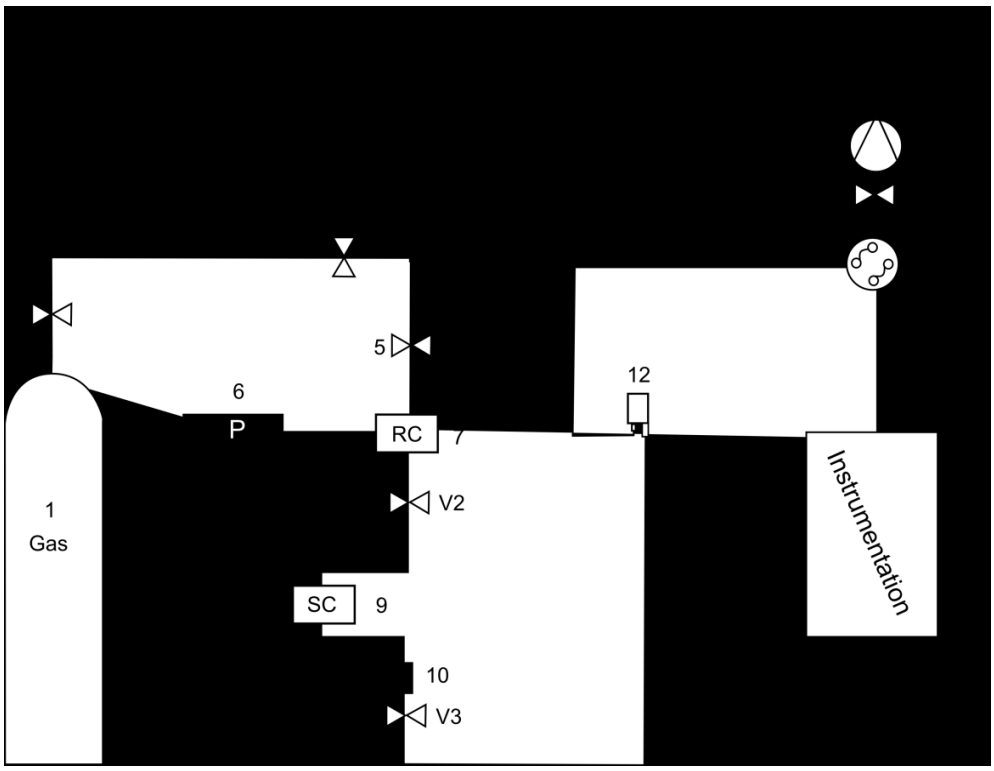


Figure 88| Sample cell – GC-FID configuration.

6.3. Results

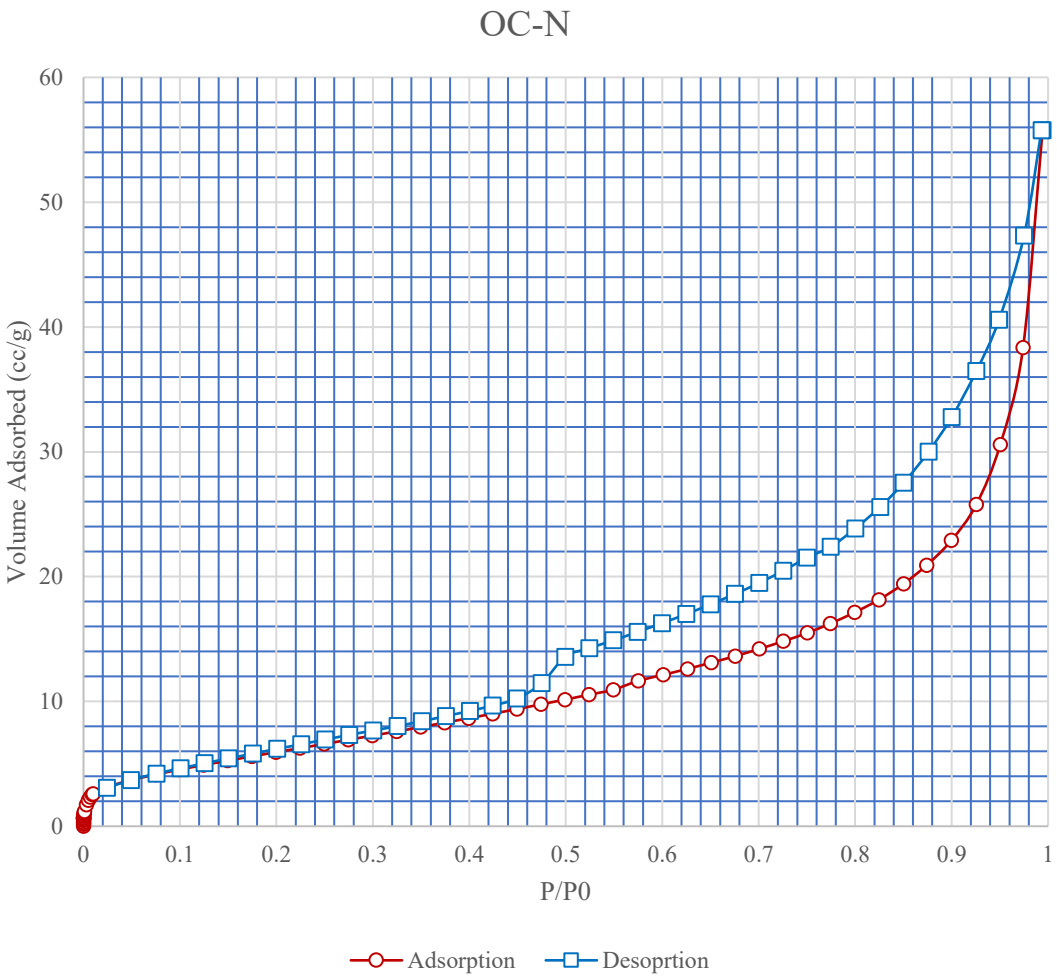
6.3.1. Langmuir Isotherm, BET and BJH Analysis

BET (Brunauer-Emmett-Teller) and BJH (Barrett- Joyner-Halenda) surface area and pore size analysis was carried out by the Quantachrome R ASiQwin R - Automated Gas Sorption Data Acquisition and Reduction ■1994-2017, Quantachrome Instrument version 5.2. This software allows for comprehensive physisorption analysis of a sample. Langmuir isotherms and N_2 adsorption capacity was also calculated for the Oxford sample suite. For a full breakdown of the Langmuir isothermal, BET and BJH analysis for the OC-250 and OC-325 please refer to Appendix Chapter 6.

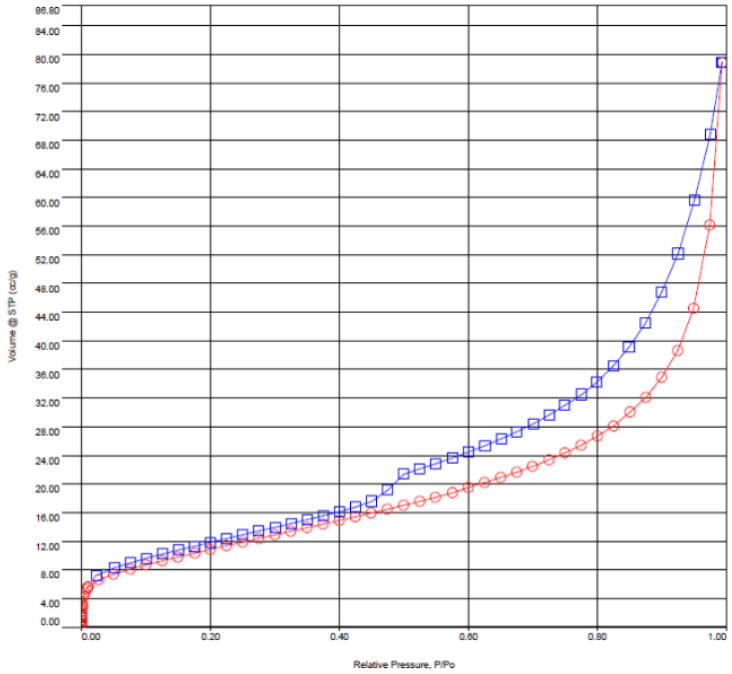
Langmuir Isotherm Analysis

Figure 89 shows the Langmuir isotherms calculated using the iQ3 autosorb Quantachrome Instrument. This software allows for comprehensive physisorption analysis of a sample showing maximum gas adsorption capacity of a sample for monolayer coverage of the sample surface area.

OC-N has the lowest Langmuir adsorption capacity, adsorbing 55.75 cc/g at standard pressure and temperature shown in Figure 89. This increases to 79.3 cc/g for OC-250 and again to 112cc/g for OC-325. The largest increase is evidently between the natural sample and OC-250 which has almost 8 times the adsorption capacity. OC-325 has double the adsorption capacity of OC-N. OC-250 has a Langmuir isotherm with the most significant hysteresis loop. The Langmuir isotherm with a shape most similar to a type IV isotherm with evident hysteresis between the adsorption and desorption curves.


OC-N
Volume Adsorbed (cc/g)
60
50
40
30
20
10
0
0
0.1
0.2
0.3
0.4
0.5
0.6
0.7
0.8
0.9
1
P/P0
Adsorption
Desoprtion

OC-250



OC-325

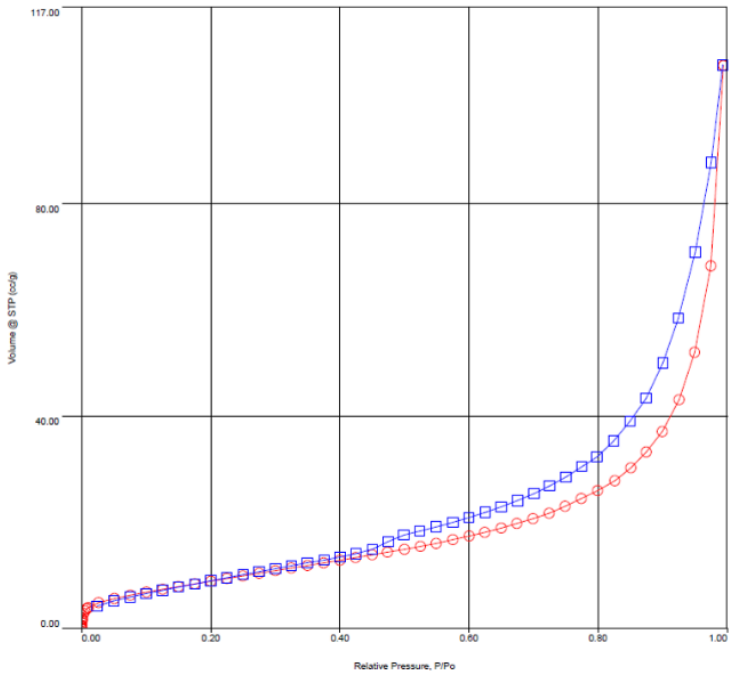
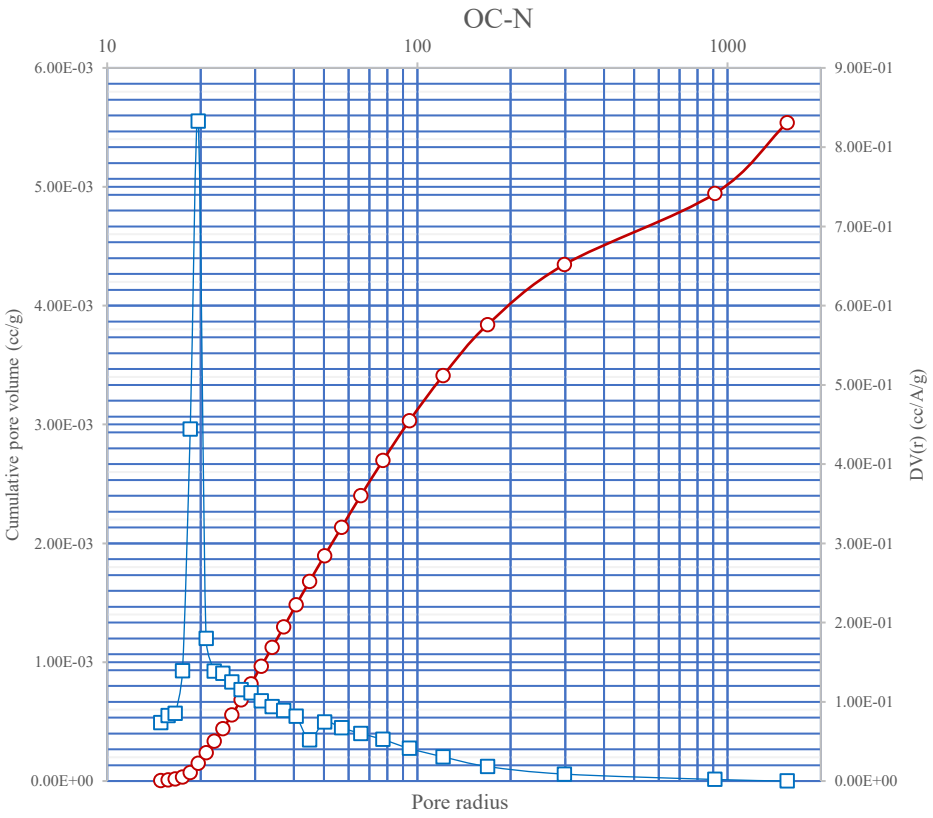


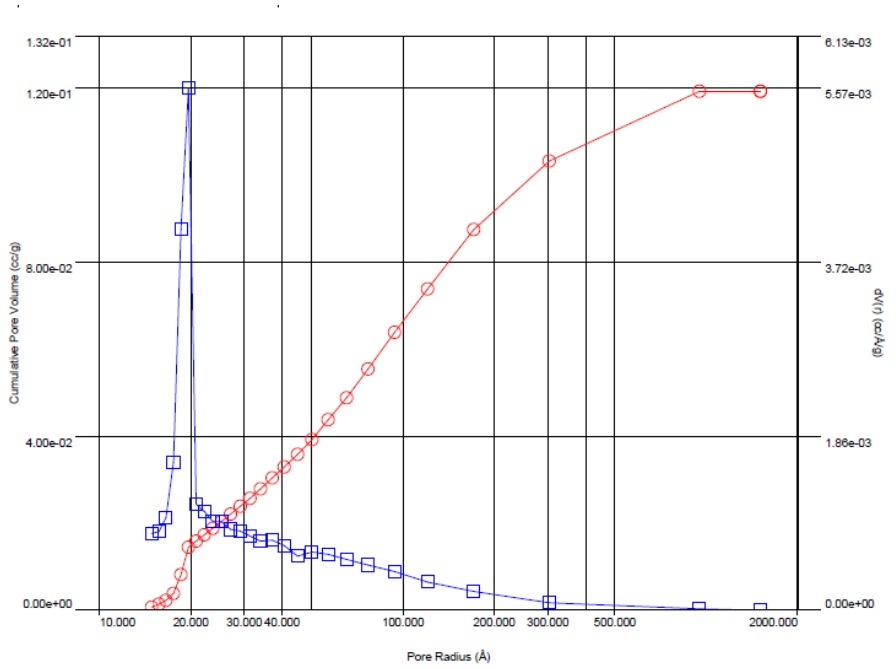
Figure 89| OC-N, OC-250 and OC-325 Langmuir isotherm analysis. The blue line is the adsorption curve and the red lines the desorption curve. Note the scale variations between the plots.

BJH Pore Size Distribution

The figures below (Figure 90) show the pore size distributions for the three shale samples. The peak shapes are similar for all three plots with a peak between 18-20 Å. it is evident that OC-325 has a much greater volume of mesopores (between 20-500 Å) and macropores (> 500 Å) (Zdravkov et al., 2007).



OC-250



OC-325

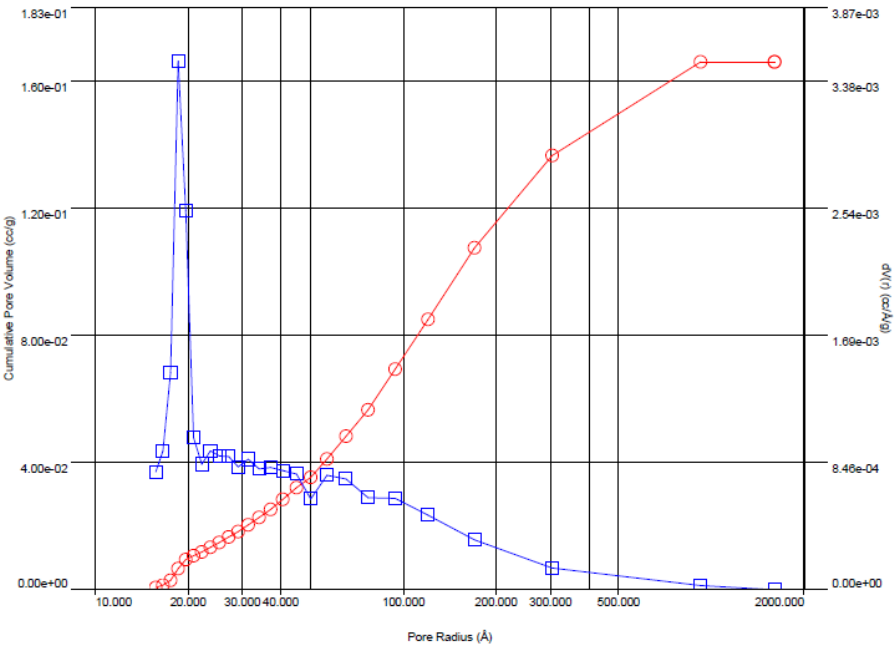


Figure 90| OC-N, OC-250 and OC-325 pore size distributions, note the scale variations between plots.

The data collected from the BJH, BET and Langmuir isotherm experiments are summarised in the Table 28. It is evident that, by artificially maturing the samples, there are

changes in the pore size distributions of the shales, shown graphically in Figure 90 and numerically in Table 28.

Table 28| BET surface area, Langmuir isotherm

	OC-N	OC-250	OC-325
BJH Surface Area m^2g	33.698	42.379	42.942
BET Surface Area m^2g	22.095	42.677	34.405
Pore Volume cc/g	0.09	0.119	0.166
Pore Radius A	19.36	19.655	18.562
Analysis time (hr:min)	14.13	32.48	15.39
Langmuir volume (cc/g)	10.29	79.3	112
Sample Volume (g)	0.1846	0.4127	0.3555
Surface area/volume	374.422	356.126	258.68

Figure 90 shows that the pore volume is greatest in OC-325, shown numerically in Table 28. The average pore radius is the smallest which suggests that the pores are narrow, slit like pores with a small radius but relatively large volume. The BET surface area analysis suggests that OC-325 has a greater surface area than OC-N but a smaller BET surface area than OC-250.

Figure 90 shows has a similar spectrum of pores to OC-N although a greater volume overall. OC-250 has a greater relative abundance of pores < 20Å compared to OC-325 which has a broader shoulder following the initial peak of pores measured at 20Å. The average pore radius is similar to OC-N although marginally larger at 19.65Å compared to 19.36Å. OC-325 has the smallest average pore radius despite being the most mature.

Figure 90 shows the pore distribution and cumulative pore volume for the unheated Oxford Clay sample. OC-N has the smallest volume of pores and the lowest surface area measured both by BJH analysis and BET surface area analysis. The total surface area relative to pore volume is greatest for the OC-N.

6.3.2 BJH and BET Comparison

Artificially maturing the sample has a significant effect on the surface area and the pore volume OC-250 has a very similar measured surface area to OC-325 however the total pore volume is significantly lower, almost the same as OC-N. This indicates that the bulk of the pores are likely to be small with a greater surface area relative to the pores measured in OC-325. Previous research has which focuses on kerogen and change in kerogen structure with maturity suggests that, with maturation, an increase in spongey porosity is seen in organic material. With progressive heating these spongey pores collapse, reducing the overall surface area to pore volume ratio - nanopores coalesce and become meso or macro pores (Dahl et al., 2012; Driskill et al., 2013b; X. Li et al., 2016). Other authors have argued that the greatest pore evolution is seen in the gas window (Mathia et al., 2016). This can be seen in Figure 90 which shows the BJH porosity data for OC-250 and OC-325. Whilst the most common pore size is between 18 and 20 nm for both samples,

OC-325 has a significant shoulder with significantly more pores between 20 and 200 nm. The OC-250 sample has a relatively high pore surface area compared to the other samples in

the OC suite with 41.67 m^2/g however the total pore volume is the relatively small. This suggests that, whilst the surface area is large, the pores themselves are small and do not contribute excessively to the total porosity of the shale. OC-325 however, has a similar pore surface area than it's less mature counterpart yet a greater pore volume. The size, shape and distribution of these pores will have an effect on both the adsorptive capacity of the shale, desorptive fractionation and molecular sieving with gas extraction.

6.3.3 GC-FID Time Plot

Figure 91 shows the change in C_1-C_2 ratio through each gas extraction step (a function of time). It is evident that each OC sample has a unique C_1-C_2 fractionation trend with sample degassing. The change in C_1-C_2 ratio occurs through physical desorption processes where methane will desorb more readily from the surface of a material or through diffusive fractionation where the C_1 is able to navigate through the tortuous nanoporous network more readily than the kinetically larger C_2. The change in the C_1-C_2 ratio can indicate where gas is being stored but what is more important in this study is the factors which may influence the C_1-C_2 ratio in order to create a geochemical index based on easily measurable shale parameters.

It is evident that the least amount of change in C_1-C_2 fractionation relative to the bulk gas is seen in the most mature sample, OC-325. The peak C_1-C_2 height is at 1.03 and the gas drops below the bulk C_1-C_2 ratio prior to the end of the experiment.

The greatest change from the first gas pulse to peak height is seen in OC-250 which changes from a normalised ratio of 1.033 to 1.062. After a sharp rise to peak height at gas extraction step 5, the tail is more gentle, finally falling below the C_1-C_2 ratio of the bulk gas by extraction step 18.

OC-250 has a similar curve shape to OC-325 although with a slightly steeper peak and slightly broader tail. Interestingly, OC-250 has a much higher initial gas pulse and is evidently retaining significantly more ethane than both OC-N and OC-325. It is the only curve which does not result in a C_1-C_2 ratio falling below the bulk gas value.

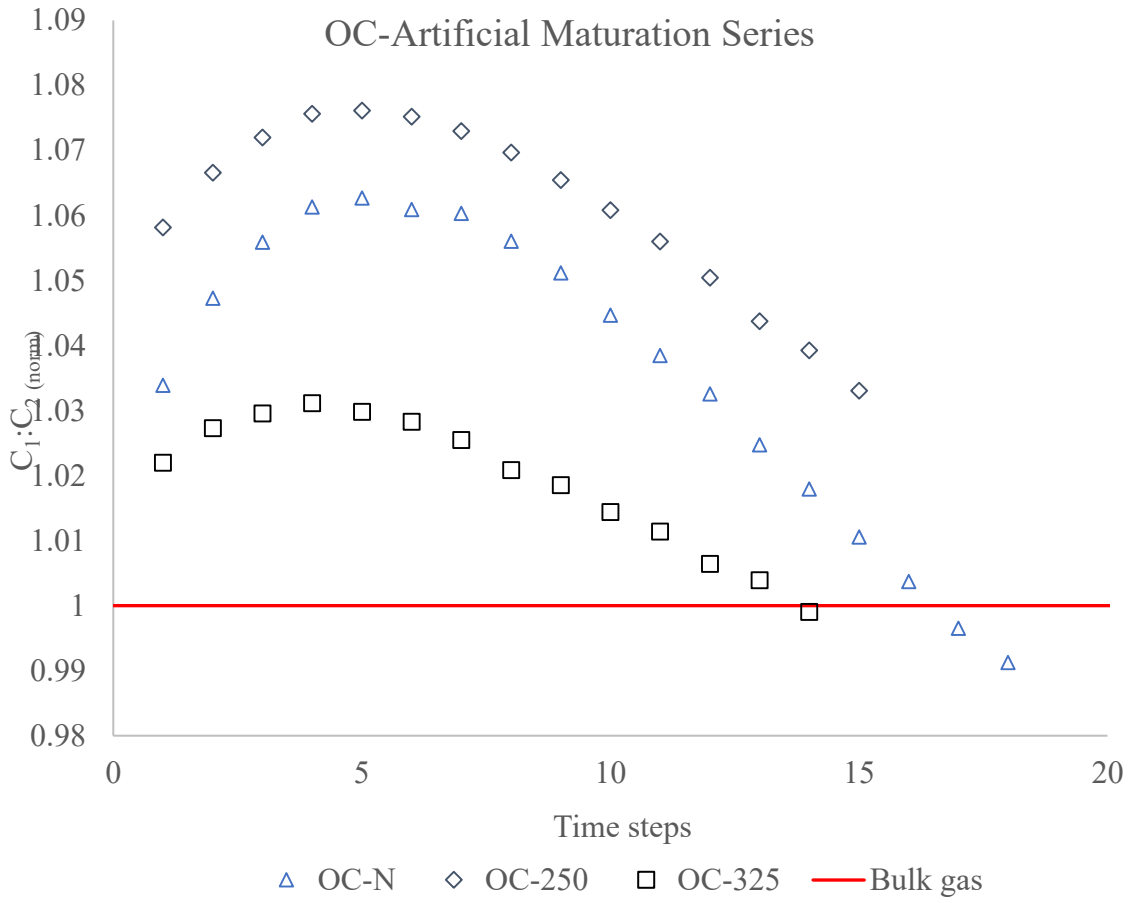


Figure 91| Oxford artificial maturation suite; gas extraction steps plotted against the normalised C_1-C_2 gas fractionation trend

Errors

The experimental error was calculated by running duplicate and triplicate runs of each sample. The standard deviation between the triplicate runs allowed for the reproducibility of the results to be determined. This is highlighted in Appendix Chapter 6.

6.4. Discussion

6.4.1 Volumetric data

Volumetric data could be calculated due to the nature of the sample cell design. The reference cell allowed for calculation of the initial molar volume of gas introduced to the sample. Direct injection into the GC-FID beforehand allowed the initial C_1-C_2 ratio to be determined. With these two factors known, the initial volume of gas introduced to the sample could be calculated. The volume of gas extracted with each extraction step could be calculated whilst the GC-FID measured the relative proportion of C_1 and C_2 with each gas pulse. The calculations for this are in Appendix Chapter 6. Figure 92 shows the change in molecular weight fractionation with progressive gas extraction between the Oxford Clay artificial maturation sample suite. It is evident that each sample produces its own C_1-C_2 fractionation curve with degassing. The magnitude of the change in C_1-C_2 from the baseline (bulk gas) is greatest in the OC-250 sample and the least in the OC-325. None of the three samples degas entirely, leaving over 20% residual gas that was unextractable at the detection limits of the GC-FID.

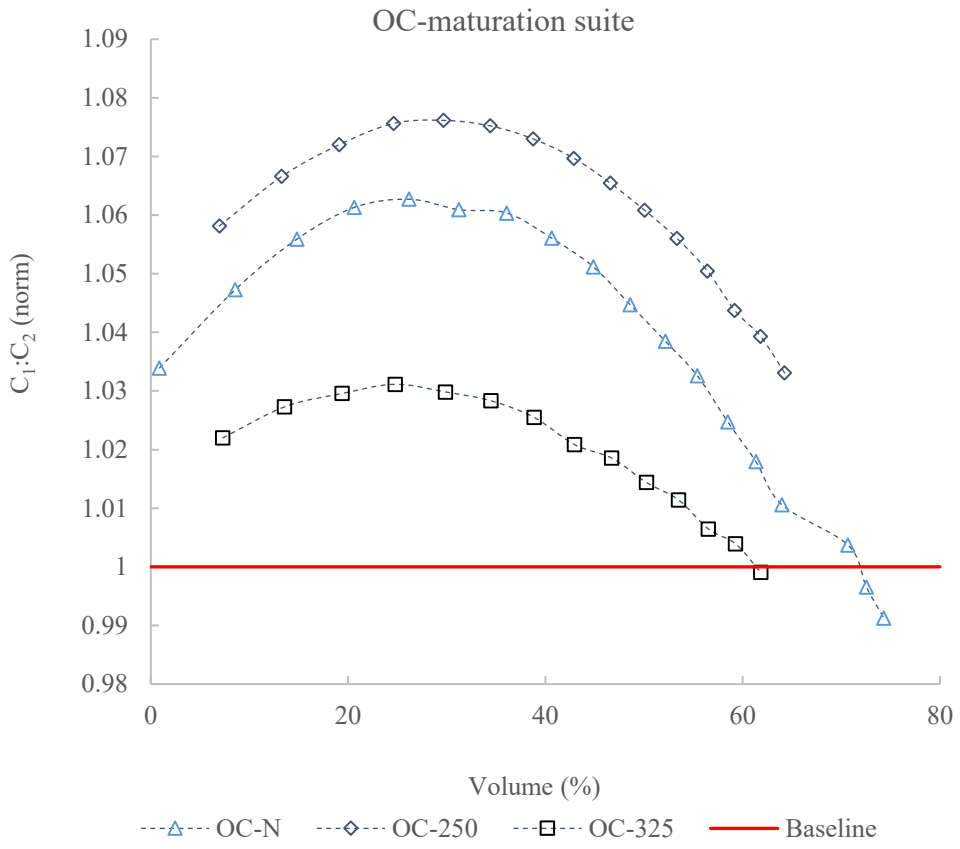


Figure 92|Volumetric data calculated for the OC-artificial maturation suite

OC-N Volumes

The fractionation trend exhibited by the gas extracted from OC-N begins with relatively more methane than the bulk gas composition. The C_1-C_2 gas ratio occurs after around 25% of the gas has been extracted. After this point, the gas extracted becomes more enriched in ethane than this peak point at 25%. After approximately 70% of the gas has been extracted, the remaining gas becomes more enriched in ethane than the bulk gas. Approximately 25% of the gas was unrecoverable in this sample

OC-250 Volumes

OC-250 fractionation trend begins with a relatively high C_1-C_2 ratio relative to bulk gas (dashed line). The gas extracted over the initial 33% of total gas volume becomes increasingly

enriched in methane relative to ethane. Once approximately 33% of the gas has been recovered, a rollover towards a less enriched methane signature is observed. The total ratios remain above that of the bulk gas and initial gas composition. Just over 35% of the gas was unrecoverable in this experiment.

OC-325 Volumes

OC-325 exhibits a distinct trend to both OC-250 and OC-N. The initial gas extracted, whilst enriched in C_1 relative to the bulk gas composition, has the lowest relative proportion of methane to ethane in the initial gas pulse than any other samples tested. The initial 25% of the gas extracted continues in an increasingly enriched methane to ethane fractionation trend. The greatest abundance of methane relative to ethane is see at 25% of total gas extracted, after this point, a rollover is observed. Similar to OC-250, the remaining gas fraction becomes increasingly enriched in C_2 after this rollover point. Unlike OC-250, the gas extracted from OC-325 becomes more enriched in ethane relative to the bulk gas. This occurs after around 60% of the total gas has been extracted. Just over 37% of gas is unrecoverable using this method.

Figure 93 shows how the Langmuir volume compares to the peak C_1-C_2 height. There is very little correlation between the peak height and the amount of gas that can be adsorbed. From Table 28, it is evident that the BET surface area is greatest for the OC-250 sample which also correlates with the greatest peak height, similar to the results seen in chapters 4 and 5. However, OC-325 has a higher surface area than OC-N but still exhibits a greater C_1-C_2 fractionation trend.

The volume of pores is significantly greater in OC-325 than OC-250 and OC-N. The surface area is smaller in OC-325 than OC-250 but the pore volume greater. It may be that, as the organic material matures, the pores generated in this maturation coalesce and create a bigger

void volume but with an overall lower surface area. It may be that the chemical surface properties of the organic material, reducing the adsorptive fractionation potential which in turn reduces the overall C_1-C_2 fractionation trend. A further muting of the C_1-C_2 fractionation trend could be that, as the void volume increases and the overall surface area decreases, the pores are thus larger. This would result in less diffusive fractionation during the gas extraction processes.

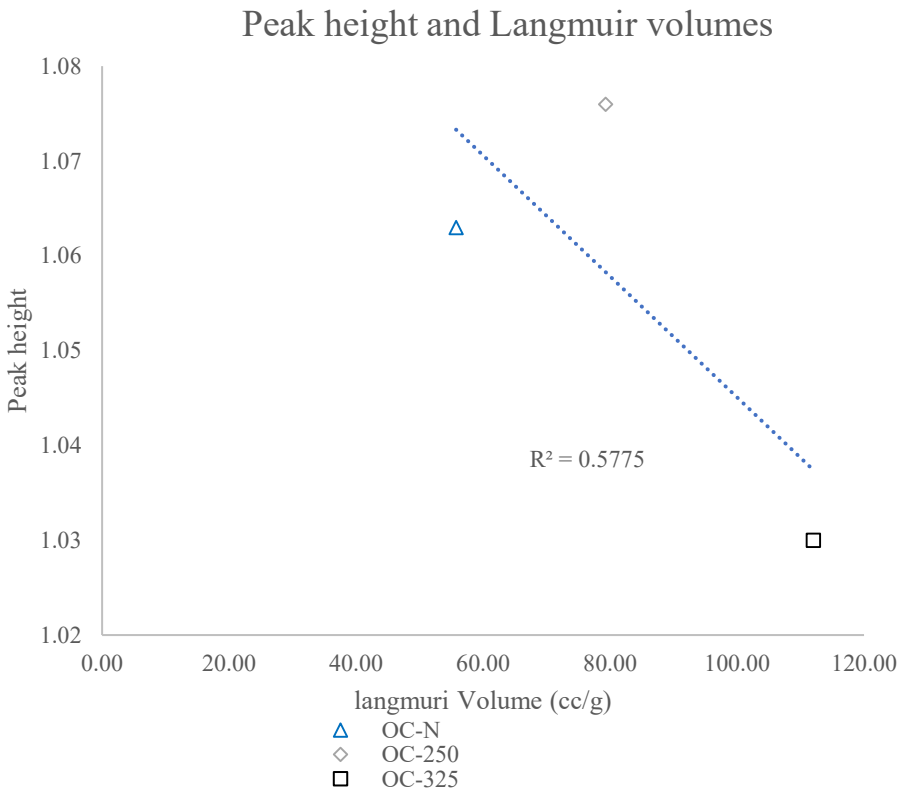


Figure 93| Peak height and Langmuir volumes of the Oxford suite

6.5. Conclusions

- Artificial maturation of organic material alters the surface area and porosity of the shale samples,

- Initially, there is an increase in surface area from OC-N to OC-250 which then decreases when matured to OC-325,

- Unlike the previous two chapters which indicate that surface area of the organic material is the greatest contributing factor to the C_1-C_2 fractionation trend, when considering artificial maturation it seems that the surface area to pore volume has an influence,

- Fractionation may be muted in the OC-325 sample as the larger pore volume and lower surface area suggests less potential for diffusive fractionation during degassing.

7.0 Discussion Applications to Industry

The data collected throughout this thesis has shown that the geochemistry of a shale influences the $\delta^{13}CH$ and C_1-C_2 fractionation during degassing. When considering molecular weight fractionation between C_1-C_2, organic material is the controlling factor in a number of ways. The surface area of the organic material, kerogen type and maturation all influence the C_1-C_2 ratio during shale degassing. The $\delta^{13}CH$ degassing curves however, are influenced both by the clay minerals and organic material. Whilst there was not the scope within this project to compare to production data or complete a suite of numerical models considering the adsorption vs. diffusion processes, this chapter aims to highlight how the data collected could be used to:

a) how gas *may* be fractionated by adsorptive or diffusive processes based of literature studies and how this could inform drilling decisions;

b) create a geochemical index for production data based on changing gas geochemistry which would inform the volume of total gas extracted at a given time.

This chapter aims to summarise the findings of the previous data chapters and show how the findings could be used to inform shale gas reservoir decisions.

Adsorption and diffusion; $\delta^{13}CH$ degassing trends

The changes in the stable carbon isotope ratio and C_1-C_2 molecular weight ratio during shale degassing can tell us several pieces of information about the reservoir. $\delta^{13}CH$ is influenced most strongly by the clay minerals with degassed material becoming progressively isotopically more positive. Organic material on the other hand produces a $\delta^{13}CH$ degassing trend that "rolls over", the final degassing stages producing material that is becoming isotopically more negative.

These results can be compared to papers which focus of isotopic fractionation through diffusion and desorption modelling (Xia and Tang, 2012a). Figure 94 shows a numerical model for adsorption dominated (D*/D=1 and α=1) and diffusion dominated (D*/D =0.999, α=1). For diffusion dominated processes, the degassing trend becomes slightly isotopically more negative before becoming increasingly isotopically more positive. This is seen in the clay samples discussed in chapter 3. The curves, especially for kaolinite have a similar pattern. The Langmuir volumes of the clay minerals suggested that, if adsorption-desorption processes were dominant, montmorillonite would exhibit greater variation in the δ^{13}CH measured.

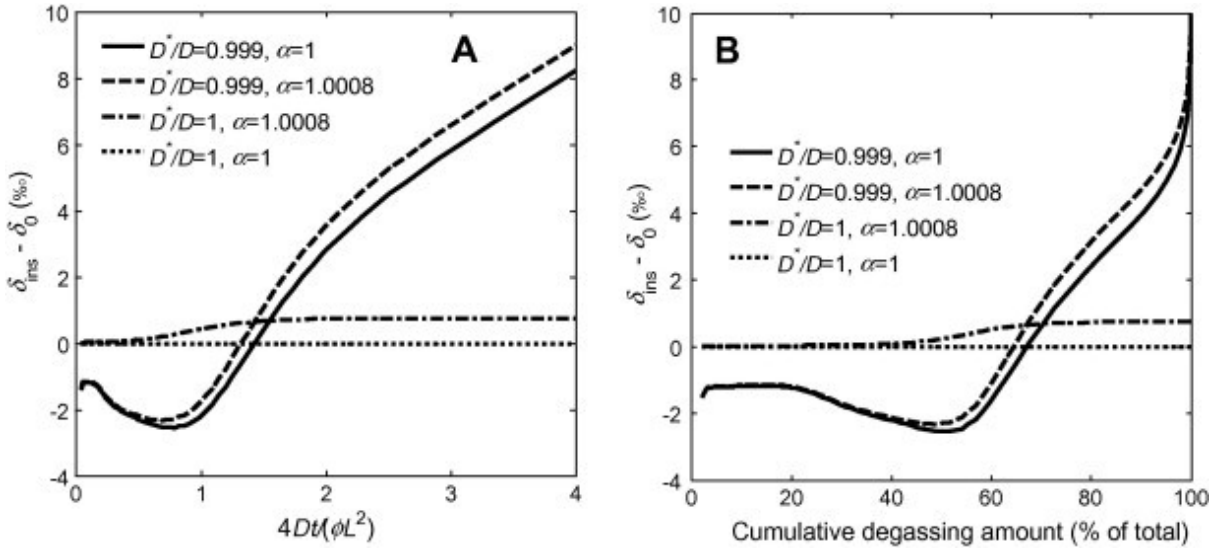


Figure 94| Combined diffusion and desorption fractionation models from when D/D=1 there is only desorptive fractionation through to α =1 (diffusion dominated) (Xia and Tang, 2012).*

Adsorption-desorption modelling in the literature also sites unusual behaviours of δ^{13}CH during degassing, with the isotopic ratios creating a slightly humped curve, shown in Figure 95. Whilst there is not the scope within this body of work to numerically model the diffusion-desorption processes, comparing the data collected in this body of work to the literature suggests that the δ^{13}CH trends seen in the degassed clay minerals relates to diffusive fractionation whilst the organic material may be more influence by desorption processes or at least not simple diffusion.

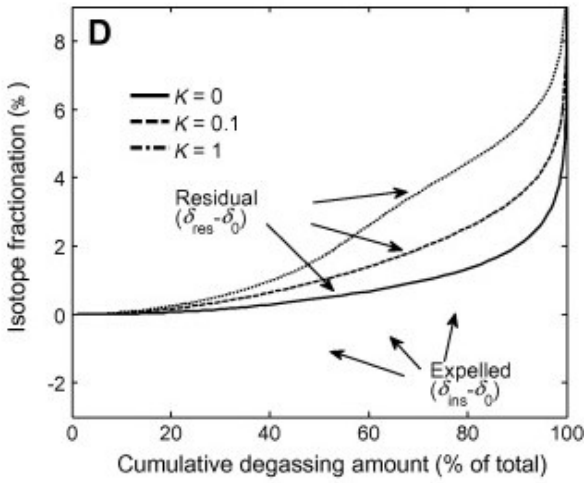


Figure 95| Effect of the sorption processes on the δ^{13}CH. K refers to the desorption coefficient and increases from little effect when K=0 to sorption dominated when K=1 (Xia and Tang, 2012a)

How can δ^{13}CH trends be applied to industry

If indeed the clay minerals cause δ^{13}CH fractionation via diffusion during gas extraction and organic material is more strongly influenced by desorptive processes, this can be used to infer parameters such as drainage area. In clay-rich shale reservoirs, a large drainage area would facilitate increased δ^{13}CH through long transport pathways and increased diffusion potential through clay-rich rocks. A small drainage area would have a less pronounced δ^{13}CH gradient in collected production data

Figure 96 is a map schematic of a shale gas field with the well shown as a vertical line. If the shale was dominated by clays then, from the data collected in this study, the isotopic fractionation trend seen in production data would be the function of diffusive-driven δ^{13}CH fractionation. If the composition of the shale is known and the clay volume known but a shallower gradient in the δ^{13}CH is seen then it suggests that the gas has travelled a short distance and the diffusive fractionation trend is less obvious and may be overprinted by desorption fractionation trends caused by the organic material. If the gas has travelled a greater distance then the δ^{13}CH caused by diffusion would be greater and a steeper gradient seen. A simple schematic of this is shown in Figure 96 where a large volume of gas drained from a small area

has a mixed diffusion-desorption signature driven by diffusion through clays and desorption form the organic material. If the drainage area is large and the gas volume smaller, the diffusive fractionation signature would dominate in a clay rich rock and produce a steep, linear $\delta^{13}CH$ degassing trend.

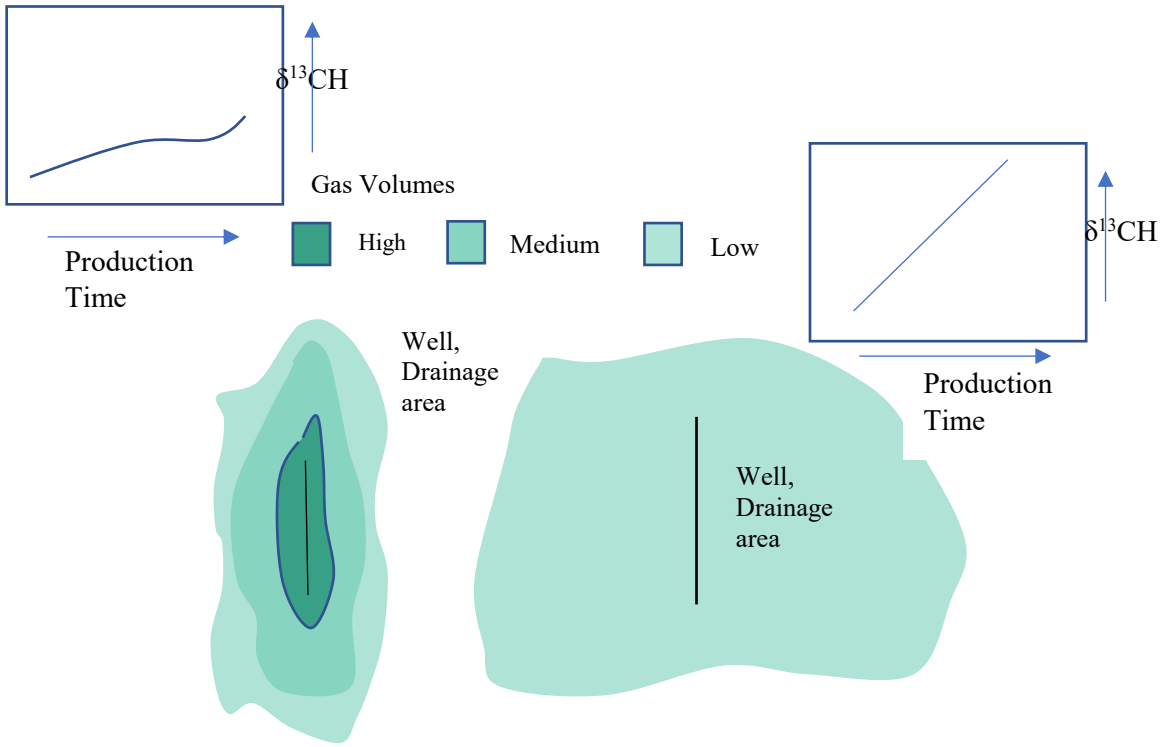


Figure 96|Drainage area: a lot of gas from a large area or the same volume of gas from a much smaller area? A small area with a lot of gas would have minimal diffusion as the distance travelled would be less far.

Sorption and diffusion processes; a combination controlling the C_1-C_2 fractionation trends

When considering molecular weight fractionation, organic material is the dominant controlling factor with minor influence from clays. Similar to the carbon isotopes, literature modelling can inform on whether the fractionation seen in the degassing shale ad kerogen samples is a function of mainly desorption or diffusion driven processes. This modelling is shown in Figure 97, based on Knudsen diffusivity and desorption from literature (Ray and Ramesh, 2000). Whilst in-depth modelling was outside the scope of this thesis, it is evident from the curves that a combination of processes occurred during the degassing of each sample.

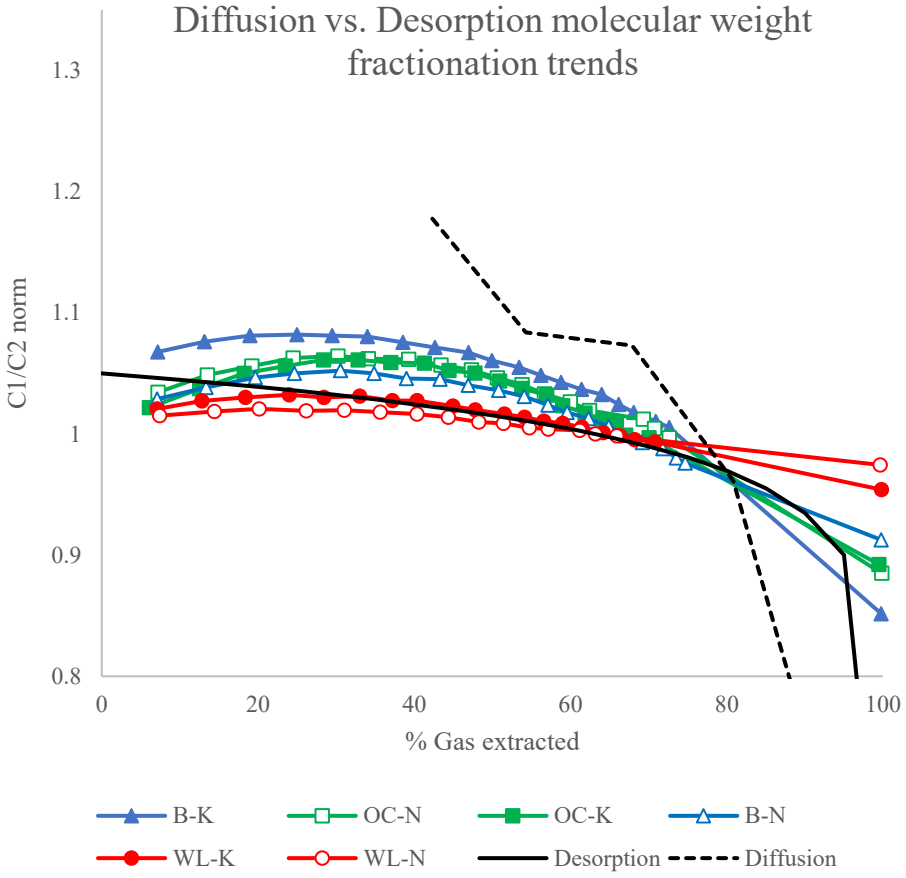


Figure 97| Adsorption and diffusion curves plotted over the data collected in chapter 5 – Diffusion from Ray & Ramesh 2000- and Knudsen diffusivity modelling by Dr Craig Smalley.

Using C_1-C_2 as a proxy for quantitative shale gas production decline

To appreciate the power of the techniques, it is useful to explore a number of scenarios and to predict how shale gas geochemistry can be interpreted to benefit precision and decisions during production

In order to explain how the fact that this change in C_1-C_2 ratio relates to a specific volume can be used to interpret field data, a worked example is shown in Figure 98, Figure 99 and Figure 100.

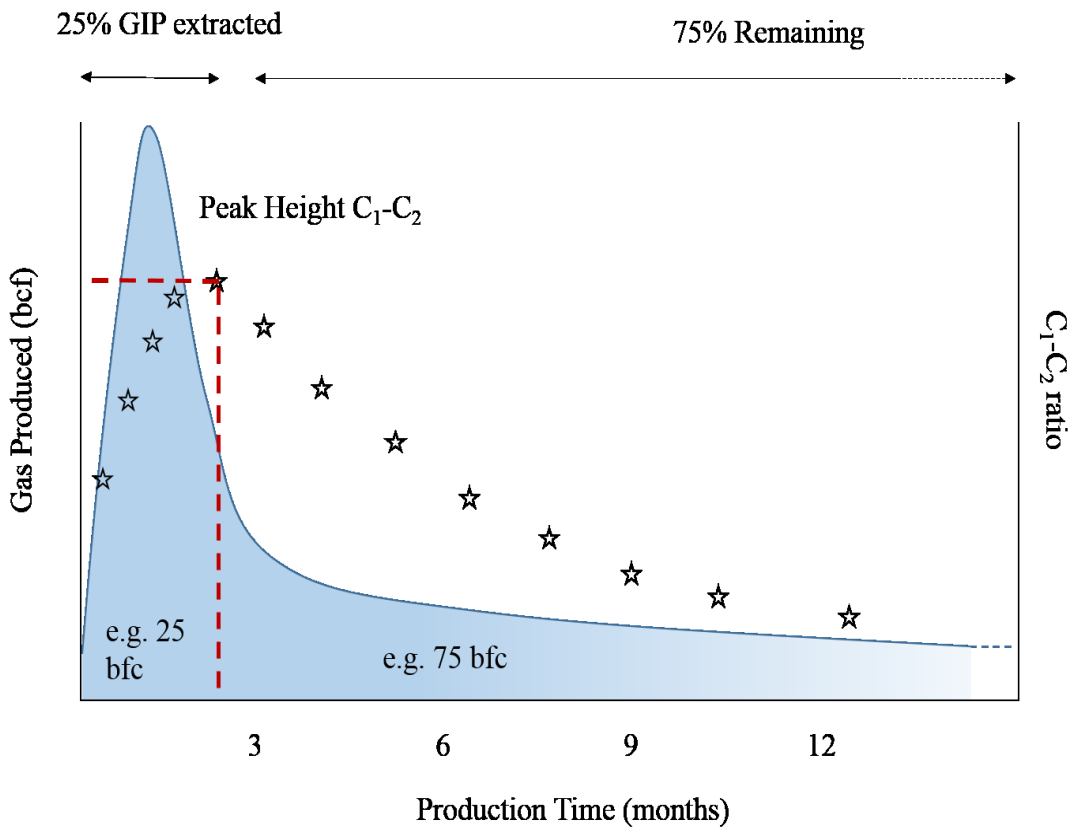


Figure 98| Worked example where, after less than 3 months of production time, the peak C_1-C_2 has been achieved and 25% of the gas has been extracted. This will not be a long-lived well.

3 Months to C_1-C_2

Assuming that a well has been drilled and the shale reservoir cored. It is a type I kerogen of marginal maturity and contains around 15.5% TOC. After almost 3 months of production, the C_1-C_2 ratio, which has been progressively more enriched in methane compared to the first gas samples, begins to become more enriched in ethane. Figure 98 shows the scenario. After 2.7 months, the peak C_1-C_2 has been met. The conditions of the shale are that of the West Lothian sample. This C_1-C_2 peak correlates to 25% of gas having been extracted. This peak can be used as a reference point; the sum total of the volume of gas extracted prior to this peak represents 25% of the total gas in place. This also means that 75% of the gas is still in place within the reservoir. The laboratory experiments also suggest that 30% of the gas cannot be extracted. After 3 months of production, only 45% of the remaining gas volume can be recovered

suggesting that after a year of production, the majority of the recoverable gas will have been extracted and keeping the well online is unlikely to be profitable.

6 Months to C_1-C_2 Peak

Working with the same shale compositional parameters as those outlined in, shows a worked example where the peak height has been met after 6 months of production. The sum of the gas volume extracted prior to this peak is 50 billion cubic feet (b.c.f.). This means that there is 150 b.c.f. of gas remaining in the reservoir. 30% of the total gas volumes cannot be extracted so 60b.c.f. will remain in the shale but 90 b.c.f. is still recoverable. It is likely to be profitable to keep the well online until the 140 b.c.f. of extractable gas has been recovered.

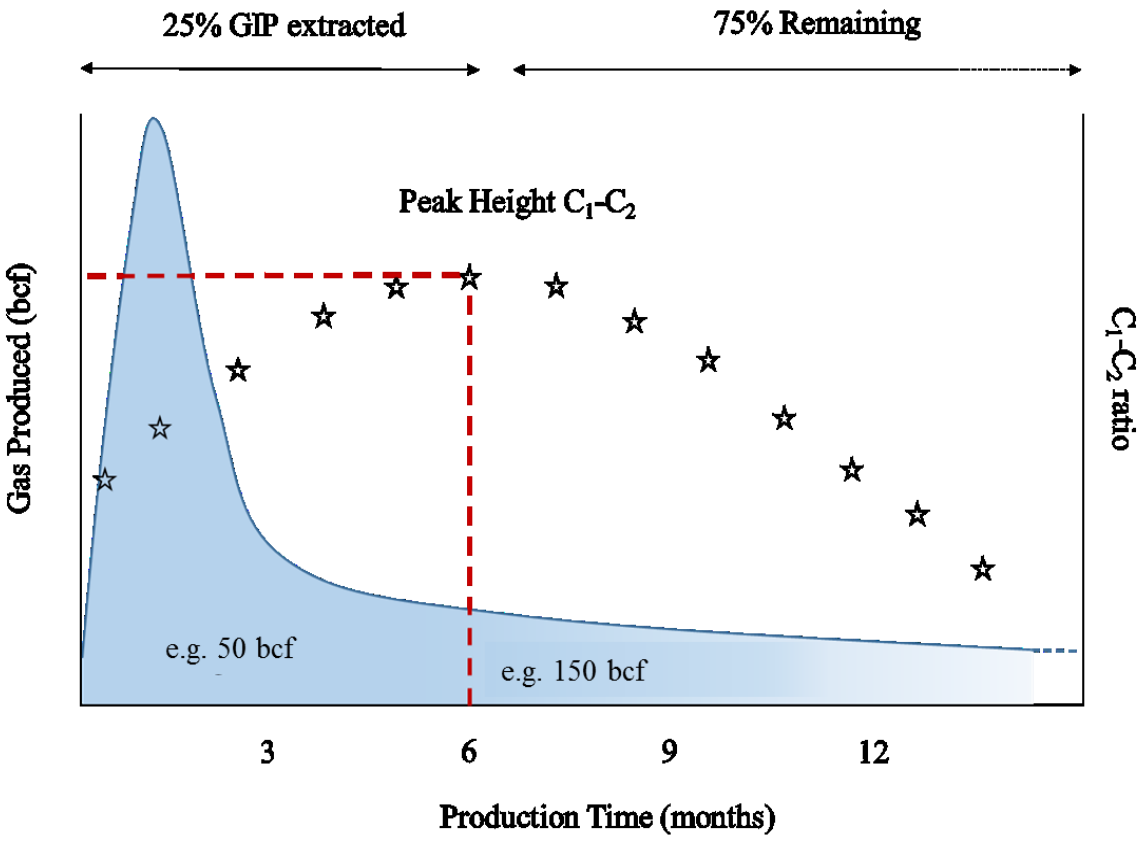


Figure 99| Worked example where, after 6 months of production, the peak to C_1-C_2 was met. The sum total of gas extracted up to this peak point accounts for 25% of the total extractable gas. This well has a long gas tail accounting for 150 billion cubic feet (b.c.f.) so will most likely be profitable to keep open.

12 Months to C_1-C_2 Peak

Again, working with the same shale parameters, Figure 100 shows that the peak C_1-C_2 ratio is met after 12 months of production and again this accounts for 25% of the initial gas in place. The sum total of gas extracted prior to this peak is a mere 25 b.c.f. which, compared to 12 months production in examples Figure 98 and Figure 99 is a relatively small volume of gas. This suggests that the production rate is low and it is likely to be economically viable to re-stimulate the well.

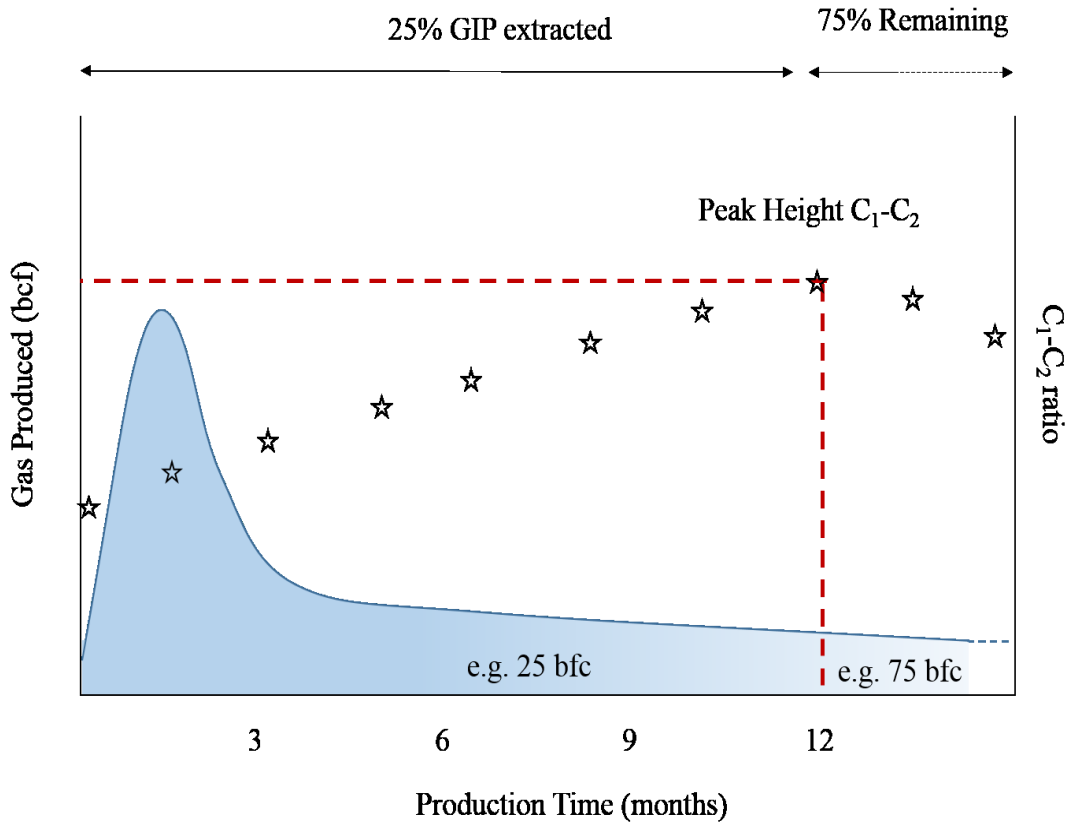


Figure 100 Worked example where, after 12 months of production, the peak to C_1-C_2 ratio has been met. The sum total of gas extracted prior to this peak accounts for 25% of total gas in place. The sum total of gas up to this point is only 25 b.c.f. which suggests a low production rate compared to the previous two worked examples.

How realistic are these examples?

This method produces data collected at standard pressure and temperature regimes, not at reservoir temperatures and depths. The samples used were also powdered samples so the total volumes of gas that are extractable are far greater than those seen in currently producing fields. However, this data shows that using the change in molecular weight between C_1-C_2 is a viable geochemical index which is unique to specific shales of specific compositions. This fundamental result can be used as building blocks for future research that can work towards mimicking reservoir conditions.

8.0 Conclusions

The research conducted within this thesis showed that the stable carbon isotope and C_1-C_2 fractionation seen in degassing shale gas was influenced by the geochemistry of the shale. Our method of measuring the geochemical changes in gas chemistry with shale degassing indicates that different minerals control the stable carbon isotope composition whilst organic material influenced the change in molecular weight with degassing.

This research has shown that C_1-C_2 fractionation and $\delta^{13}CH$ cannot be used as a direct proxy for gas stored in the adsorbed state as fractionation trends measured do not correlate with the maximum adsorption capacity measured in the samples. TOC itself is not the dominant control on gas stored in the adsorbed phase or control of $\delta^{13}CH$ or C_1-C_2 fractionation but the surface area of the TOC, type of organic material and the maturity of the organic material influenced the Langmuir volume and the change in gas geochemistry with gas extraction.

Current methods for predicting the shale gas decline curve are based on mathematical modelling analogue approaches and rarely consider the influence of shale geochemistry whilst this data indicates that composition of a shale can have a significant influence on changing gas geochemistry. As our method allows for calculation of changing gas geochemistry from 100% gas in place to 100% gas extracted, fractionation curves for different minerals and shales of different compositions were produced. These trends, whilst not immediately directly translatable to a shale gas reservoir, can be used as the building blocks for creating a geochemical index where specific isotopic and molecular weight fractionation trends can be predicted for a given shale composition. The change in gas geochemistry measured during production will then inform the predicted percent of the total volume of gas that can be extracted, based on the laboratory curves.

1. Verification and calibration of original GIP estimates

2. Generation of expected geochemical fractionation trend for volume of total gas extracted

3. Calculation of gas volume remaining in the reservoir and what percentage has been produced over a given production time period

4. Enhancement of the predicative capabilities of a shale gas reservoir production life

8.1 Future Work

The basis of this work demonstrates that the composition of a shale, organic matter content, organic matter type and organic matter maturity has a significant influence on the volume of gas that can be absorbed onto shale sorption sites. As previously outlined in the Introduction, there are numerous factors that will also come in to play when considering how gas can be stored within a shale and there is incredible scope for further work. The areas to consider are as follows:

- Number of shale samples tested. Are these shales representative of type I, II and III kerogens? Future work would ideally build up a sample database of several shales from across the globe. This data excellently demonstrates the lack of gas storage capacity in the adsorbed phase of the type I West Lothian shale however it would be ideal to test other type I kerogens to test if this is typical of all type I kerogens.
- Core samples vs outcrop samples. The samples used here were samples collected at outcrop. They were taken at outcrop as we wanted to use immature samples. For future work, it would be beneficial to use core samples which will not have been exposed to erosion and chemical degradation from weathering. The British Geological Survey in Nottingham is a good place to take samples from that will already have been characterised in terms of TOC %, $VR_{0,}$ Tmax and composition.

- Cored samples instead of powdered. It would be ideal to compare powdered samples and cored samples from the same stratigraphic interval. Cored samples will retain the internal pore structure and the gas mixtures will have to navigate out of the tortuous network, increasing the influence of diffusive fractionation through molecular sieving and mass transfer. Comparing this to powdered samples that will not retain the tortuosity will be a proxy for sorption dominated fractionation. I did attempt to core samples but the samples we had were too friable.
- Water saturation. The presence of water and preferential adsorption of water onto sorption sites over hydrocarbon gases will influence the fractionation of C_1-C_2 and other gases. In order to see how fractionation occurs in more realistic reservoir conditions, the influence of water must be considered, at various levels of water saturations. Different minerals have different hydrophilic and hydrophobic properties so composition of the shale may become even more relevant.
- Reservoir pressure and temperate regimes. For simplicity, these experiments were run at standard atmospheric pressure and temperature regimes. In order to understand fractionation effects and gas adsorption in shale gas reservoirs, experiments that reflect shale reservoir pressure-temperature regimes must be conducted. This is particularly pertinent for gas adsorption as , at low pressures methane is only adsorbed in a small fraction and pressures of around 300 bar, whereas these experiments were conducted between 3 and 4 bar, 2 orders of magnitude less than the pressure required to meet equilibrium capacity.
- Complex gas mixtures and a higher C_1-C_2 ratio. Initially, I used a methane-ethane ratio that is unlikely to be found in a real reservoir. This was because we were unsure if we would see any fractionation and I wanted to increase the ratio of ethane in order to see trends. Future experiments should be done with <10% ethane. Experiments could also look at wetter gas reservoirs which would include C_3-C_5 gases.

Akkutlu, I.Y., Fathi, E., others, 2012. Multiscale gas transport in shales with local kerogen heterogeneities. SPE J. 17, 1–002.
Al-Areeq, N.M., 2018. Petroleum Source Rocks Characterization and Hydrocarbon Generation. Open Acess Peer-review.
Amann-Hildenbrand, A., Ghanizadeh, A., Krooss, B.M., 2012. Transport properties of unconventional gas systems. Mar. Pet. Geol. 31, 90–99.
Ambrose, R.J., Clarkson, C.R., Youngblood, J.E., Adams, R., Nguyen, P.D., Nobakht, M., Biseda, B., others, 2011a. Life-cycle decline curve estimation for tight/shale reservoirs, in: SPE Hydraulic Fracturing Technology Conference. Society of Petroleum Engineers.
Ambrose, R.J., Hartman, R.C., Akkutlu, I.Y., others, 2011b. Multi-component sorbed phase considerations for shale gas-in-place calculations, in: SPE Production and Operations Symposium. Society of Petroleum Engineers.
Ambrose, R.J., Hartman, R.C., Akkutlu, I.Y., others, 2011c. Multi-component sorbed phase considerations for shale gas-in-place calculations, in: SPE Production and Operations Symposium. Society of Petroleum Engineers.
Arora, V., Cai, Y., 2014. US natural gas exports and their global impacts. Appl. Energy 120, 95–103.
Arps, J.J., others, 1945. Analysis of decline curves. Trans. AIME 160, 228–247.
Atkins, P., 2010. Atkins' Physical Chemistry, 9th ed. Oxford University Press.
Bello, R.O., Wattenbarger, R.A., others, 2010. Multi-stage hydraulically fractured horizontal shale gas well rate transient analysis, in: North Africa Technical Conference and Exhibition. Society of Petroleum Engineers.
Bernard, S., Horsfield, B., Schulz, H.-M., Schreiber, A., Wirth, R., Vu, T.T.A., Perssen, F., Könitzer, S., Volk, H., Sherwood, N., others, 2010. Multi-scale detection of organic and inorganic signatures provides insights into gas shale properties and evolution. Chem. Erde-Geochem. 70, 119–133.
Berner, U., Faber, E., Scheeder, G., Panten, D., 1995. Primary cracking of algal and landplant kerogens: kinetic models of isotope variations in methane, ethane and propane. Chem. Geol. 126, 233–245.
Binnion, M., 2012. How the technical differences between shale gas and conventional gas projects lead to a new business model being required to be successful. Mar. Pet. Geol. 31, 3–7.
Blumsack, S., 2014. Dash for gas, 21st-century style! Elements 10, 265–270.
Boruah, A., Rasheed, A., Mendhe, V.A., Ganapathi, S., 2019. Specific surface area and pore size distribution in gas shales of Raniganj Basin, India. J. Pet. Explor. Prod. Technol. 9, 1041–1050.
British Geological Survey, 2014. User Guide Vitrinite Data. BGS.
Britt, L.K., Schoeffler, J., others, 2009. The geomechanics of a shale play: what makes a shale prospective, in: SPE Eastern Regional Meeting. Society of Petroleum Engineers.
Busch, A., Alles, S., Krooss, B.M., Stanjek, H., Dewhurst, D., 2009. Effects of physical sorption and chemical reactions of CO2 in shaly caprocks. Energy Procedia 1, 3229–3235.
Busch, A., Gensterblum, Y., Krooss, B.M., Littke, R., 2004. Methane and carbon dioxide adsorption–diffusion experiments on coal: upscaling and modeling. Int. J. Coal Geol. 60, 151–168.
Bustin, A.M., Bustin, R.M., 2012. Importance of rock properties on the producibility of gas shales. Int. J. Coal Geol. 103, 132–147.
Bustin, R., Clarkson, C., 1998a. Geological controls on coalbed methane reservoir capacity and gas content. Int. J. Coal Geol. 38, 3–26.

Bustin, R.M., Bustin, A.M., Cui, A., Ross, D., Pathi, V.M., others, 2008a. Impact of shale properties on pore structure and storage characteristics, in: SPE Shale Gas Production Conference. Society of Petroleum Engineers.
Cao, T., Song, Z., Wang, S., Xia, J., 2015. A comparative study of the specific surface area and pore structure of different shales and their kerogens. Sci. China Earth Sci. 58, 510–522.
Cardott, B., 2012. Introduction to Vitrinite Reflectance as a Thermal Maturity Indicator*. Search Discov. Artic., Standard test method for microscopical determination of the reflectance of vitrinite in a polished specimen of coal: Annual book of ASTM standards: gaseous fuels; coal and coke, 5, 280–283.
Carter, J., Barwick, V., 2011. Good Practice Guide for Isotope Ratio Mass Spectrometry, First Edition. ed. FIRMS.
Chalmers, G.R., Bustin, R.M., 2008. Lower Cretaceous gas shales in northeastern British Columbia, Part I: geological controls on methane sorption capacity. Bull. Can. Pet. Geol. 56, 1–21.
Chalmers, G.R., Bustin, R.M., 2007a. The organic matter distribution and methane capacity of the Lower Cretaceous strata of Northeastern British Columbia, Canada. Int. J. Coal Geol. 70, 223–239.
Chalmers, G.R., Bustin, R.M., Power, I.M., 2012a. Characterization of gas shale pore systems by porosimetry, pycnometry, surface area, and field emission scanning electron microscopy/transmission electron microscopy image analyses: Examples from the Barnett, Woodford, Haynesville, Marcellus, and Doig unitsCharacterization of Gas Shale Pore Systems. AAPG Bull. 96, 1099–1119.
Chareonsuppanimit, P., Mohammad, S.A., Robinson Jr, R.L., Gasem, K.A., 2012a. High-pressure adsorption of gases on shales: Measurements and modeling. Int. J. Coal Geol. 95, 34–46.
Chen, F., Lu, S., Ding, X., He, X., 2018. Shale gas reservoir characterization: A typical case in the Southeast Chongqing of Sichuan Basin, China. PloS One 13, e0199283.
Chen, J., Xiao, X., 2014. Evolution of nanoporosity in organic-rich shales during thermal maturation. Fuel 129, 173–181.
Chen, L., Jiang, Z., Liu, Q., Jiang, S., Liu, K., Tan, J., Gao, F., 2019. Mechanism of shale gas occurrence: Insights from comparative study on pore structures of marine and lacustrine shales. Mar. Pet. Geol. 104, 200–216.
Chen, Y., Zou, C., Mastalerz, M., Hu, S., Gasaway, C., Tao, X., 2015c. Applications of micro-fourier transform infrared spectroscopy (FTIR) in the geological sciences—a review. Int. J. Mol. Sci. 16, 30223–30250.
Cheng, A.-L., Huang, W.-L., 2004a. Selective adsorption of hydrocarbon gases on clays and organic matter. Org. Geochem. 35, 413–423.
Civan, F., Rai, C.S., Sondergeld, C.H., 2011. Shale-gas permeability and diffusivity inferred by improved formulation of relevant retention and transport mechanisms. Transp. Porous Media 86, 925–944.
Clarkson, C., Bustin, R., 1999. The effect of pore structure and gas pressure upon the transport properties of coal: a laboratory and modeling study. 1. Isotherms and pore volume distributions. Fuel 78, 1333–1344.
Clarkson, C.R., Solano, N., Bustin, R.M., Bustin, A., Chalmers, G., He, L., Melnichenko, Y.B., Radliński, A., Blach, T.P., 2013a. Pore structure characterization of North American shale gas reservoirs using USANS/SANS, gas adsorption, and mercury intrusion. Fuel 103, 606–616.
Clayton, C., 1991. Carbon isotope fractionation during natural gas generation from kerogen. Mar. Pet. Geol. 8, 232–240.

Collard, F.-X., Blin, J., 2014. A review on pyrolysis of biomass constituents: Mechanisms and composition of the products obtained from the conversion of cellulose, hemicelluloses and lignin. Renew. Sustain. Energy Rev. 38, 594–608.
Coplen, T.B., 1994. Reporting of stable hydrogen, carbon, and oxygen isotopic abundances (technical report). Pure Appl. Chem. 66, 273–276.
Cui, X., Bustin, A., Bustin, R.M., 2009. Measurements of gas permeability and diffusivity of tight reservoir rocks: different approaches and their applications. Geofluids 9, 208–223.
Curiale, J., Curtis, J.B., 2016. Organic geochemical applications to the exploration for source-rock reservoirs – A review. J. Unconv. Oil Gas Resour. 13, 1–31. http://dx.doi.org/10.1016/j.juogr.2015.10.001
Curtis, J.B., 2002. Fractured shale-gas systems. AAPG Bull. 86, 1921–1938.
Curtis, M.E., Cardott, B.J., Sondergeld, C.H., Rai, C.S., 2012. Development of organic porosity in the Woodford Shale with increasing thermal maturity. Int. J. Coal Geol. 103, 26–31.
Dahaghi, A.K., others, 2010. Numerical simulation and modeling of enhanced gas recovery and CO2 sequestration in shale gas reservoirs: A feasibility study, in: SPE International Conference on CO2 Capture, Storage, and Utilization. Society of Petroleum Engineers.
Dahl, J., Moldowan, J., Walls, J., Nur, A., DeVito, J., 2012. Creation of porosity in tight shales during organic matter maturation, in: AAPG Annual Convention and Exhibition, Volume Search and Discovery Article.
Dawson, W.C., Almon, W.R., 2010. Eagle Ford Shale variability: Sedimentologic influences on source and reservoir character in an unconventional resource unit.
Dayal, A., 2017. Shale, in: Shale Gas. Elsevier, pp. 1–11.
Department or Energy and Climate Change, 2013. THE UNCONVENTIONAL HYDROCARBON RESOURCES OF BRITAIN'S ONSHORE BASINS - SHALE GAS (No. 1). BGS.
Diamond, S., 1970. Pore size distributions in clays. Clays Clay Miner. 18, 7–23.
Diamond, W.P., Schatzel, S.J., 1998. Measuring the gas content of coal: a review. Int. J. Coal Geol. 35, 311–331.
Driskill, B., Walls, J., DeVito, J., Sinclair, S.W., 2013a. 11 Applications of SEM Imaging to Reservoir Characterization in the Eagle Ford Shale, South Texas, USA.
Durand, B., 1980. Sedimentary organic matter and kerogen. Definition and quantitative importance of kerogen. Kerogen Insoluble Org. Matter Sediment. Rocks 13–34.
Dutrow, B., 1997. X-Ray Powder Diffraction: Geochemical Instrumentaton adn Analysis (Webpage). Louisiana State University.
Ehrenberg, S., Nadeau, P., 2005. Sandstone vs. carbonate petroleum reservoirs: A global perspective on porosity-depth and porosity-permeability relationships. AAPG Bull. 89, 435–445.
EIA, 2015. Natural gas explained: where our natural gas comes from, U.S. Energy Information Administration.
Emmerich, K., 2013. "Full Characterisation of Smectites" in Developments in Clay Science. Elsevier.
Energy Information Administration, 2019. World Shale Gas Resources. Geology.
Espitalie, J., Ungerer, P., Irwin, I., Marquis, F., 1988. Primary cracking of kerogens. Experimenting and modelling C1, C2–C5, C6–C15 and C15+ classes of hydrocarbons formed. Org. Geochem. 13, 893–899.
Estep, P.A., Kovach, J.J., Karr Jr, C., 2008. Quantitative infrared multicomponent analysis of minerals occurring in coal. Pet Sci Eng 60, 1–17.

Etminan, S.R., Javadpour, F., Maini, B.B., Chen, Z., 2014a. Measurement of gas storage processes in shale and of the molecular diffusion coefficient in kerogen. Int. J. Coal Geol. 123, 10–19.
Fan, Z., Hou, J., Ge, X., Zhao, P., Liu, J., 2018. Investigating influential factors of the gas absorption capacity in shale reservoirs using integrated petrophysical, mineralogical and geochemical experiments: A case study. Energies 11, 3078.
Fathi, E., Akkutlu, I.Y., 2009a. Matrix heterogeneity effects on gas transport and adsorption in coalbed and shale gas reservoirs. Transp. Porous Media 80, 281.
Fishman, N.S., Hackley, P.C., Lowers, H.A., Hill, R.J., Egenhoff, S.O., Eberl, D.D., Blum, A.E., 2012. The nature of porosity in organic-rich mudstones of the Upper Jurassic Kimmeridge Clay Formation, North Sea, offshore United Kingdom. Int. J. Coal Geol. 103, 32–50.
Follows, B., Tyson, R.V., 1998. Organic facies of the Asbian (early Carboniferous) Queensferry beds, lower oil shale group, South Queensferry, Scotland, and a brief comparison with other Carboniferous North Atlantic oil shale deposits. Org. Geochem. 29, 821–844.
Freeman, C., Moridis, G., Blasingame, T., 2011. A numerical study of microscale flow behavior in tight gas and shale gas reservoir systems. Transp. Porous Media 90, 253.
Freeman, C., Moridis, G.J., Michael, G.E., Blasingame, T.A., 2012. Measurement, modeling, and diagnostics of flowing gas composition changes in shale gas wells, in: SPE Latin America and Caribbean Petroleum Engineering Conference. Society of Petroleum Engineers.
Fuex, A., 1980. Experimental evidence against an appreciable isotopic fractionation of methane during migration. Phys. Chem. Earth 12, 725–732.
Gandossi, L., others, 2013. An overview of hydraulic fracturing and other formation stimulation technologies for shale gas production. Eur Commisison Jt Res Cent Tech Rep. 26347.
Gasparik, M., Bertier, P., Gensterblum, Y., Ghanizadeh, A., Krooss, B.M., Littke, R., 2014. Geological controls on the methane storage capacity in organic-rich shales. Int. J. Coal Geol. 123, 34–51.
Gensterblum, Y., Ghanizadeh, A., Cuss, R.J., Amann-Hildenbrand, A., Krooss, B.M., Clarkson, C.R., Harrington, J.F., Zoback, M.D., 2015a. Gas transport and storage capacity in shale gas reservoirs–A review. Part A: Transport processes. J. Unconv. Oil Gas Resour. 12, 87–122..
Gross, D., Sachsenhofer, R.F., Bechtel, A., Pytlak, L., Rupprecht, B., Wegerer, E., 2015. Organic geochemistry of Mississippian shales (Bowland Shale Formation) in central Britain: Implications for depositional environment, source rock and gas shale potential. Mar. Pet. Geol. 59, 1–21.
Guo, H., Jia, W., Peng, P., Zeng, J., He, R., 2017. Evolution of organic matter and nanometer-scale pores in an artificially matured shale undergoing two distinct types of pyrolysis: A study of the Yanchang Shale with Type II kerogen. Org. Geochem. 105, 56–66.
Guo, K., Zhang, B., Wachtmeister, H., Aleklett, K., Höök, M., n.d. Characteristic Production Decline Patterns for Shale Gas Wells in Barnett.
Guo, Q., Ji, L., Rajabov, V., Friedheim, J.E., Portella, C., Wu, R., 2012. Shale gas drilling experience and lessons learned from Eagle Ford, in: SPE Americas Unconventional Resources Conference. Society of Petroleum Engineers.
Guo, Z., Li, X.-Y., Liu, C., Feng, X., Shen, Y., 2013. A shale rock physics model for analysis of brittleness index, mineralogy and porosity in the Barnett Shale. J. Geophys. Eng. 10, 025006. https://doi.org/10.1088/1742-2132/10/2/025006

Han, H., Yan Cao, Chen, S.-J., Lu, J., Huang, C., Zhu, H., Zhan, P., Gao, Y., 2016. Influence of particle size on gas-adsorption experiments of shales: Anexample from a Longmaxi Shale sample from the Sichuan Basin, China. Fuel 186, 750–757.
Hao, F., Zou, H., Lu, Y., 2013. Mechanisms of shale gas storage: Implications for shale gas exploration in China. AAPG Bull. 97, 1325–1346.
Hartman, R.C., Ambrose, R.J., Akkutlu, I.Y., Clarkson, C.R., 2011. Shale gas-in-place calculations part II-multicomponent gas adsorption effects, in: North American Unconventional Gas Conference and Exhibition. Society of Petroleum Engineers.
Heath, G.A., O'Donoughue, P., Arent, D.J., Bazilian, M., 2014. Harmonization of initial estimates of shale gas life cycle greenhouse gas emissions for electric power generation. Proc. Natl. Acad. Sci. 111, E3167–E3176.
Heller, R., Zoback, M., 2014a. Adsorption of methane and carbon dioxide on gas shale and pure mineral samples. J. Unconv. Oil Gas Resour. 8, 14–24.
Holditch, S.A., 2013. Unconventional oil and gas resource development–Let's do it right. J. Unconv. Oil Gas Resour. 1, 2–8.
Höök, M., Davidsson, S., Johansson, S., Tang, X., 2014. Decline and depletion rates of oil production: a comprehensive investigation. Philos. Trans. R. Soc. Math. Phys. Eng. Sci. 372, 20120448.
Horvath, Z., Jackson, K.S., 1982. Procedure for the isolation of kerogen from sedimentary rocks. Bur. Miner. Resour. Geol. Geophys.
Hou, Y., He, S., Harris, N.B., Yi, J., Wang, Y., Zhang, J., Cheng, C., 2017. The effects of shale composition and pore structure on gas adsorption potential in highly mature marine shales, Lower Paleozoic, central Yangtze, China. Can. J. Earth Sci. 54, 1033–1048.
Hsu, S.-C., Nelson, P.P., 2002. Characterization of eagle ford shale. Eng. Geol. 67, 169–183.
Hu, H., 2014a. Methane adsorption comparison of different thermal maturity kerogens in shale gas system. Chin. J. Geochem. 33, 425–430.
Hu, H., 2014b. Methane adsorption comparison of different thermal maturity kerogens in shale gas system. Chin. J. Geochem. 33, 425–430.
Hu, H., Zhang, T., Wiggins-Camacho, J.D., Ellis, G.S., Lewan, M.D., Zhang, X., 2015a. Experimental investigation of changes in methane adsorption of bitumen-free Woodford Shale with thermal maturation induced by hydrous pyrolysis. Mar. Pet. Geol. 59, 114–128.
Huang, L., Ning, Z., Wang, Q., Qi, R., Zeng, Y., Qin, H., Ye, H., Zhang, W., 2018. Molecular simulation of adsorption behaviors of methane, carbon dioxide and their mixtures on kerogen: Effect of kerogen maturity and moisture content. Fuel 211, 159–172.
Hubbert, M.K., Willis, D.G., 1972. Mechanics of hydraulic fracturing.
Hunt, J., 1995. Petroleum Geochemistry and Geology, Second. ed. W.H.Freeman & Co Ltd.
IEA, 2019. World Energy Outlook 2019 (Flagship Report). IEA, Paris.
J Rouquerol, Llewellyn, P., Rouquerol, F., 2007. Is the bet equation applicable to microporous adsorbents? Stud. Surf. Sci. Catal. 160, 49–56. https://doi.org/10.1016/S0167-2991(07)80008-5
Jarvie, D., Pollastro, R., Hill, R., Bowker, K., Claxton, B., Burgess, J., 2004. Evaluation of hydrocarbon generation and storage in the Barnett shale, Ft. Worth basin, Texas, in: Ellison Miles Memorial Symposium, Farmers Branch, Texas, USA. pp. 22–23.
Jarvie, D.M., Hill, R.J., Ruble, T.E., Pollastro, R.M., 2007. Unconventional shale-gas systems: The Mississippian Barnett Shale of north-central Texas as one model for thermogenic shale-gas assessment. AAPG Bull. 91, 475–499.

Javadpour, F., Fisher, D., Unsworth, M., others, 2007. Nanoscale gas flow in shale gas sediments. J. Can. Pet. Technol. 46.
Ji, L.M., Qiu, J.L., Zhang, T.W., Xia, Y.Q., 2012a. Experiments on methane adsorption of common clay minerals in shale. Diqiu Kexue-Zhongguo Dizhi Daxue XuebaoEarth Sci.-J. China Univ. Geosci. 37, 1043–1050.
Ji, W., Song, Y., Rui, Z., Meng, M., Huang, H., 2017. Pore characterization of isolated organic matter from high matured gas shale reservoir. Int. J. Coal Geol. 174, 31–40.
Jing, W., Haishan, L., Huiqing, L., Jie, L., Liwen, L., Wenxin, L., 2016. Influences of adsorption/desorption of shale gas on the apparent properties of matrix pores. Pet. Explor. Dev. 43, 158–165.
Kershaw, J.R., 1989. Spectroscopic analysis of coal liquids.
Kim, J., Kim, D., Lee, W., Lee, Y., Kim, H., 2017. Impact of total organic carbon and specific surface area on the adsorption capacity in Horn River shale. J. Pet. Sci. Eng. 149, 331–339.
King, G.E., others, 2010. Thirty years of gas shale fracturing: What have we learned?, in: SPE Annual Technical Conference and Exhibition. Society of Petroleum Engineers.
Krooss, B.M., Amann, A., Gensterblum, Y., Han, F., Littke, R., Weniger, P., 2010. Gas Transport and Sorption Processes in Coals and Shales: New Insights and Concepts from Laboratory Experiments. Search Discov. Artic. 110127.
Kuila, U., McCarty, D.K., Derkowski, A., Fischer, T.B., Topór, T., Prasad, M., 2014a. Nano-scale texture and porosity of organic matter and clay minerals in organic-rich mudrocks. Fuel 135, 359–373.
Kuila, U., Prasad, M., 2013. Specific surface area and pore-size distribution in clays and shales. Geophys. Prospect. 61, 341–362.
Lancaster, D., Hill, D., 1993. A multilaboratory comparison of isotherm measurements on Antrim shale samples, Otsego County, Michigan. SCA Pap. 15.
Lane, H., Watson, A., Lancaster, D., others, 1989a. Identifying and estimating desorption from Devonian shale gas production data, in: SPE Annual Technical Conference and Exhibition. Society of Petroleum Engineers.
Langmuir, I., 1918. The adsorption of gases on plane surfaces of glass, mica and platinum. J. Am. Chem. Soc. 40, 1361–1403.
Law, C., 1996. Handbook of Petroleum Geology: Exploring for Oil and Gas Traps. Chapter 6: Evaluating Source Rocks (AAPG Special Volumes No. 6), Treatise of Petroleum Geology. AAPG.
Levi, M., 2013a. Climate consequences of natural gas as a bridge fuel. Clim. Change 118, 609–623.
Lewan, M.D., 2017. Hydrous Pyrolysis. Encycl. Pet. Geosci. 1–7.
Li, F., Wang, M., Liu, S., Hao, Y., 2019a. Pore characteristics and influencing factors of different types of shales. Mar. Pet. Geol. 102, 391–401.
Li, J., Yan, X., Wang, W., Zhang, Y., Yin, J., Lu, S., Chen, F., Meng, Y., Zhang, X., Chen, X., 2015a. Key factors controlling the gas adsorption capacity of shale: A study based on parallel experiments. Appl. Geochem. 58, 88–96.
Li, Jijun, Huang, K., Zhang, Y., Ma, Y., Yin, J., Lu, S., Xue, H., Li, Junqian, Yang, J., 2017. Chemical and Isotopic Fractionation of Shale Gas During Adsorption and Desorption. J. Nanosci. Nanotechnol. 17, 6395–6403.
Li, P., Jiang, Z., Zheng, M., Bi, H., Chen, L., 2016. Estimation of shale gas adsorption capacity of the Longmaxi Formation in the Upper Yangtze Platform, China. J. Nat. Gas Sci. Eng. 34, 1034–1043.

Li, X., Chen, G., Chen, Z., Wang, L., Wang, Y., Dong, D., Lü, Z., Lü, W., Wang, S., Huang, J., others, 2016. An insight into the mechanism and evolution of shale reservoir characteristics with over-high maturity. J. Nat. Gas Geosci. 1, 373–382.
Liang, L., Xiong, J., Liu, X., Luo, D., 2016. An investigation into the thermodynamic characteristics of methane adsorption on different clay minerals. J. Nat. Gas Sci. Eng. 33, 1046–1055.
Liu, Y., Zhang, J., Tang, X., 2016a. Predicting the proportion of free and adsorbed gas by isotopic geochemical data: A case study from lower Permian shale in the southern North China basin (SNCB). Int. J. Coal Geol. 156, 25–35.
Löhr, S., Baruch, E., Hall, P., Kennedy, M., 2015. Is organic pore development in gas shales influenced by the primary porosity and structure of thermally immature organic matter? Org. Geochem. 87, 119–132.
Lorant, F., Prinzhofer, A., Behar, F., Huc, A.-Y., 1998. Carbon isotopic and molecular constraints on the formation and the expulsion of thermogenic hydrocarbon gases. Chem. Geol. 147, 249–264.
Loucks, R.G., Reed, R.M., Ruppel, S.C., Jarvie, D.M., 2009a. Morphology, genesis, and distribution of nanometer-scale pores in siliceous mudstones of the Mississippian Barnett Shale. J. Sediment. Res. 79, 848–861.
Lu, J., Larson, T.E., Smyth, R.C., 2015. Carbon isotope effects of methane transport through Anahuac Shale — A core gas study. J. Geochem. Explor. 148, 138–149. https://doi.org/10.1016/j.gexplo.2014.09.005
Lu, X.-C., Li, F.-C., Watson, A.T., 1995. Adsorption measurements in Devonian shales. Fuel 74, 599–603.
Mac Kinnon, M.A., Brouwer, J., Samuelsen, S., 2018. The role of natural gas and its infrastructure in mitigating greenhouse gas emissions, improving regional air quality, and renewable resource integration. Prog. Energy Combust. Sci. 64, 62–92.
Macquaker, J.H.S., Gawthorpe, R.L., 1993. Mudstone lithofacies in the Kimmeridge Clay Formation, Wessex Basin, southern England; implications for the origin and controls of the distribution of mudstones. J. Sediment. Res. 63, 1129–1143.
Mango, F.D., Hightower, J., 1997. The catalytic decomposition of petroleum into natural gas. Geochim. Cosmochim. Acta 61, 5347–5350.
Mastalerz, M., Hampton, L., Drobniak, A., Loope, H., 2017. Significance of analytical particle size in low-pressure N2 and CO2 adsorption of coal and shale. Int. J. Coal Geol. 178, 122–131.
Mastalerz, M., Schimmelmann, A., Drobniak, A., Chen, Y., 2013a. Porosity of Devonian and Mississippian New Albany Shale across a maturation gradient: Insights from organic petrology, gas adsorption, and mercury intrusion. AAPG Bull. 97, 1621–1643.
Mathia, E.J., Bowen, L., Thomas, K.M., Aplin, A.C., 2016. Evolution of porosity and pore types in organic-rich, calcareous, Lower Toarcian Posidonia Shale. Mar. Pet. Geol. 75, 117–139.
Mayerhofer, M.J., Richardson, M.F., Walker Jr, R.N., Meehan, D.N., Oehler, M.W., Browning Jr, R.R., 1997. Proppants? We don't need no proppants, in: SPE Annual Technical Conference and Exhibition. Society of Petroleum Engineers.
McCarthy, K., Rojas, K., Niemann, M., Palmowski, D., Peters, K., Stankiewicz, A., 2011. Basic petroleum geochemistry for source rock evaluation. Oilfield Rev. 23, 32–43.
McGlade, C., Speirs, J., Sorrell, S., 2013. Unconventional gas–a review of regional and global resource estimates. Energy 55, 571–584.
Medlin, W.L., 1976. Hydraulic fracturing method for creating horizontal fractures. Google Patents.

Middleton, R.S., Gupta, R., Hyman, J.D., Viswanathan, H.S., 2017. The shale gas revolution: Barriers, sustainability, and emerging opportunities. Appl. Energy 199, 88–95.
Morris, K.A., 1980. Comparison of major sequences of organic-rich mud deposition in the British Jurassic. J. Geol. Soc. 137, 157–170.
Mosher, K., He, J., Liu, Y., Rupp, E., Wilcox, J., 2013. Molecular simulation of methane adsorption in micro-and mesoporous carbons with applications to coal and gas shale systems. Int. J. Coal Geol. 109, 36–44.
Mullen, J., 2010. Petrophysical characterization of the Eagle Ford Shale in south Texas, in: Canadian Unconventional Resources and International Petroleum Conference. Society of Petroleum Engineers.
Neuzil, C., 1994. How permeable are clays and shales? Water Resour. Res. 30, 145–150.
Newsham, K., Rushing, J., others, 2001. An integrated work-flow model to characterize unconventional gas resources: Part I-Geological Assessment and Petrophysical Evaluation, in: SPE Annual Technical Conference and Exhibition. Society of Petroleum Engineers.
Pancost, R., Bull, I., 2014. Short course on compound specific isotope ratio mass spectrometry.
Peters, K.E., 1998. Rock Eval-Pyrolysis. In: Geochemistry. Encylopedia of Earth Science. Kluwer Academic Publishers.
Prinzhofer, A., Pernaton, É., 1997. Isotopically light methane in natural gas: bacterial imprint or diffusive fractionation? Chem. Geol. 142, 193–200. https://doi.org/10.1016/S0009-2541(97)00082-X
Prinzhofer, A.A., Huc, A.Y., 1995. Genetic and post-genetic molecular and isotopic fractionations in natural gases. Chem. Geol. 126, 281–290.
Psarras, P., Holmes, R., Vishal, V., Wilcox, J., 2017. Methane and CO2 adsorption capacities of kerogen in the Eagle Ford shale from molecular simulation. Acc. Chem. Res. 50, 1818–1828.
Ray, J.S., Ramesh, R., 2000. Rayleigh fractionation of stable isotopes from a multicomponent source. Geochim. Cosmochim. Acta 64, 299–306.
Rexer, T.F., Benham, M.J., Aplin, A.C., Thomas, K.M., 2013. Methane adsorption on shale under simulated geological temperature and pressure conditions. Energy Fuels 27, 3099–3109.
Rexer, T.F., Mathia, E.J., Aplin, A.C., Thomas, K.M., 2014. High-pressure methane adsorption and characterization of pores in Posidonia shales and isolated kerogens. Energy Fuels 28, 2886–2901.
Rice, D.D., Claypool, G.E., 1981. Generation, accumulation, and resource potential of biogenic gas. AAPG Bull. 65, 5–25.
Romero-Sarmiento, M.-F., Ducros, M., Carpentier, B., Lorant, F., Cacas, M.-C., Pegaz-Fiornet, S., Wolf, S., Rohais, S., Moretti, I., 2013a. Quantitative evaluation of TOC, organic porosity and gas retention distribution in a gas shale play using petroleum system modeling: Application to the Mississippian Barnett Shale. Mar. Pet. Geol. 45, 315–330.
Rooney, M.A., Claypool, G.E., Chung, H.M., 1995. Modeling thermogenic gas generation using carbon isotope ratios of natural gas hydrocarbons. Chem. Geol. 126, 219–232.
Ross, D.J., Bustin, R.M., 2009a. The importance of shale composition and pore structure upon gas storage potential of shale gas reservoirs. Mar. Pet. Geol. 26, 916–927.
Sandrea, R., Sandrea, I., 2014. New well-productivity data provide US shale potential insights. Oil Gas J. 112, 66–66.

Sandvik, E.I., Young, W.A., Curry, D.J., 1992. Expulsion from hydrocarbon sources: the role of organic absorption. Org. Geochem. 19, 77–87. https://doi.org/10.1016/0146-6380(92)90028-V
Scanlon, B.R., Reedy, R.C., Nicot, J.-P., 2014. Comparison of water use for hydraulic fracturing for unconventional oil and gas versus conventional oil. Environ. Sci. Technol. 48, 12386–12393.
Schettler Jr, P., Parmely, C., others, 1991. Contributions to total storage capacity in Devonian shales, in: SPE Eastern Regional Meeting. Society of Petroleum Engineers.
Schettler, P., Parmely, C., Lee, W., others, 1989a. Gas storage and transport in Devonian shales. SPE Form. Eval. 4, 371–376.
Schettler, P., Parmoly, C., 1990a. The measurement of gas desorption isotherms for Devonian shale. GRI Devonian Gas Shale Technol. Rev. 7, 4–9.
Schloemer, S., Krooss, B.M., 2004. Molecular transport of methane, ethane and nitrogen and the influence of diffusion on the chemical and isotopic composition of natural gas accumulations. Geofluids 4, 81–108.
Schoell, M., 1980. The hydrogen and carbon isotopic composition of methane from natural gases of various origins. Geochim. Cosmochim. Acta 44, 649–661.
Scotchman, I.C., 2016. Shale gas and fracking: exploration for unconventional hydrocarbons. Proc. Geol. Assoc. 127, 535–551.
Sevcik, J.G., 2011. Detectors in gas chromatography, First. ed. Elsevier.
Shabro, V., Torres-Verdin, C., Javadpour, F., others, 2011. Numerical simulation of shale-gas production: from pore-scale modeling of slip-flow, Knudsen diffusion, and Langmuir desorption to reservoir modeling of compressible fluid, in: North American Unconventional Gas Conference and Exhibition. Society of Petroleum Engineers.
Sigal, R.F., others, 2015. Pore-size distributions for organic-shale-reservoir rocks from nuclear-magnetic-resonance spectra combined with adsorption measurements. SPE J. 20, 824–830.
Sing, K.S., 1985. Reporting physisorption data for gas/solid systems with special reference to the determination of surface area and porosity (Recommendations 1984). Pure Appl. Chem. 57, 603–619.
Sing, K.S., Williams, R.T., 2004. Physisorption hysteresis loops and the characterization of nanoporous materials. Adsorpt. Sci. Technol. 22, 773–782.
Smith, D.M., Williams, F.L., others, 1984a. Diffusional effects in the recovery of methane from coalbeds. Soc. Pet. Eng. J. 24, 529–535.
Smith, D.M., Williams, F.L., others, 1984b. Diffusional effects in the recovery of methane from coalbeds. Soc. Pet. Eng. J. 24, 529–535.
Snowdon, L.R., 2001. Natural gas composition in a geological environment and the implications for the processes of generation and preservation. Org. Geochem. 32, 913–931.
Solomon, P.R., Carangelo, R.M., 1988. FT-ir analysis of coal: 2. Aliphatic and aromatic hydrogen concentration. Fuel 67, 949–959.
Sone, H., Zoback, M.D., 2013. Mechanical properties of shale-gas reservoir rocks—Part 1: Static and dynamic elastic properties and anisotropy. Geophysics 78, D381–D392.
Song, L., Martin, K., Carr, T.R., Ghahfarokhi, P.K., 2019. Porosity and storage capacity of Middle Devonian shale: A function of thermal maturity, total organic carbon, and clay content. Fuel 241, 1036–1044.
Soroush, E., Mesbah, M., Shokrollahi, A., Bahadori, A., Ghazanfari, M.H., 2014. Prediction of methane uptake on different adsorbents in adsorbed natural gas technology using a rigorous model. Energy Fuels 28, 6299–6314.

Steiner, S., Ahsan, S.A., Raina, I., Dasgupta, S., Lis, G.P., 2016. Interpreting Total Organic Carbon TOC in Source Rock Oil Plays, in: Abu Dhabi International Petroleum Exhibition & Conference. Presented at the Abu Dhabi International Petroleum Exhibition & Conference, Society of Petroleum Engineers, Abu Dhabi, UAE. https://doi.org/10.2118/183050-MS

Stolper, D., Lawson, M., Davis, C., Ferreira, A., Neto, E.S., Ellis, G., Lewan, M., Martini, A.M., Tang, Y., Schoell, M., others, 2014. Formation temperatures of thermogenic and biogenic methane. Science 344, 1500–1503.

Strąpoć, D., Schimmelmann, A., Mastalerz, M., 2006a. Carbon isotopic fractionation of CH4 and CO2 during canister desorption of coal. Org. Geochem. 37, 152–164.

Tan, L., Zuo, L., Wang, B., 2018. Methods of decline curve analysis for shale gas reservoirs. Energies 11, 552.

Tang, X., Jiang, Z., Jiang, S., Wang, P., Xiang, C., 2016. Effect of organic matter and maturity on pore size distribution and gas storage capacity in high-mature to post-mature shales. Energy Fuels 30, 8985–8996.

Tang, X., Ripepi, N., Luxbacher, K., Pitcher, E., 2017. Adsorption models for methane in shales: Review, comparison, and application. Energy Fuels 31, 10787–10801.

Tang, X., Zhou, X., Peng, Y., 2019. Molecular simulation of methane adsorption within illite minerals in the Longmaxi Formation shale based on a grand canonical Monte Carlo method and the pore size distribution in southeastern Chongqing, China. J. Nat. Gas Geosci. 4, 111–119.

Tang, Y., Xia, D., 2011. Predicting original gas in place and optimizing productivity by isotope geochemistry of shale gas, in: AAPG Hedberg Research Conference—Natural Gas Geochemistry: Recent Developments, Applications and Technologies.

Thommes, M., Kaneko, K., Neimark, A.V., Olivier, J.P., Rodriguez-Reinoso, F., Rouquerol, J., Sing, K.S., 2015. Physisorption of gases, with special reference to the evaluation of surface area and pore size distribution (IUPAC Technical Report). Pure Appl. Chem. 87, 1051–1069.

Topor, T., Derkowski, A., Ziemianski, P., 2017. The effect of organic matter maturation and porosity evolution on methane storage potential in the Baltic Basin (Poland) shale-gas reservoir. Int. Journ. of Coal Geology 180, 46–56. https://doi.org/10.1016/j.coal.2017.07.005

Trunschke, A., 2013a. Surface area and pore size determination. Mod. Methods Heterog. Catal. Res. 4.

US Dpt of Energy, Kuuskraa, V., 2011. World shale gas resources: an initial assessment of 14 regions outside the United States, EIA Administration Report.

U.S. Energy Information Administration, 2019. Annual Energy Outlook 2019, with projections to 2050. U.S. Department of Energy.

Wang, S., Feng, Q., Javadpour, F., Yang, Y.-B., 2016. Breakdown of fast mass transport of methane through calcite nanopores. J. Phys. Chem. C 120, 14260–14269.

Wang, S., Song, Z., Cao, T., Song, X., 2013. The methane sorption capacity of Paleozoic shales from the Sichuan Basin, China. Mar. Pet. Geol. 44, 112–119.

Wang, X., Li, X., Wang, Xiangzeng, Shi, B., Luo, X., Zhang, L., Lei, Y., Jiang, C., Meng, Q., 2015. Carbon isotopic fractionation by desorption of shale gases. Mar. Pet. Geol. 60, 79–86.

Wang, Y., Liu, L., Zheng, S., Luo, Z., Sheng, Y., Wang, X., 2019. Full-scale pore structure and its controlling factors of the Wufeng-Longmaxi shale, southern Sichuan Basin, China: Implications for pore evolution of highly overmature marine shale. J. Nat. Gas Sci. Eng. 67, 134–146.

Wang, Y., Tsotsis, T.T., Jessen, K., 2015a. Competitive sorption of methane/ethane mixtures on shale: measurements and modeling. Ind. Eng. Chem. Res. 54, 12187–12195.
Wang, Y., Zhu, Y., Liu, S., Zhang, R., 2016. Pore characterization and its impact on methane adsorption capacity for organic-rich marine shales. Fuel 181, 227–237.
Wei, X., Wei, G., Honglin, L., Shusheng, G., Zhiming, H., Farong, Y., 2012a. Shale reservoir characteristics and isothermal adsorption properties. Nat. Gas Ind. 32, 113–116.
Weijermars, R., Drijkoningen, G., Heimovaara, T.J., Rudolph, E.S.J., Weltje, G.J., Wolf, K., 2011. Unconventional gas research initiative for clean energy transition in Europe. J. Nat. Gas Sci. Eng. 3, 402–412.
Wignall, P.B., 1989. Sedimentary dynamics of the Kimmeridge Clay: tempests and earthquakes. J. Geol. Soc. 146, 273–284.
Wright, M.C., Court, R.W., Kafantaris, F.-C.A., Spathopoulos, F., Sephton, M.A., 2015. A new rapid method for shale oil and shale gas assessment. Fuel 153, 231–239.
Xia, X., Chen, J., Braun, R., Tang, Y., 2013. Isotopic reversals with respect to maturity trends due to mixing of primary and secondary products in source rocks. Chem. Geol. 339, 205–212.
Xia, X., Tang, Y., 2012a. Isotope fractionation of methane during natural gas flow with coupled diffusion and adsorption/desorption. Geochim. Cosmochim. Acta 77, 489–503.
Xiong, J., Liu, X., Liang, L., Zeng, Q., 2017a. Adsorption of methane in organic-rich shale nanopores: An experimental and molecular simulation study. Fuel 200, 299–315.
Yaalon, D., 1962. Mineral composition of the average shale. Clay Miner. Bull. 5, 31–36.
Yang, Y., Burke, N., Ali, S., Huang, S., Lim, S., Zhu, Y., 2017. Experimental studies of hydrocarbon separation on zeolites, activated carbons and MOFs for applications in natural gas processing. RSC Adv. 7, 12629–12638.
Yin, Y., Qu, Z., Zhang, J., 2017a. An analytical model for shale gas transport in kerogen nanopores coupled with real gas effect and surface diffusion. Fuel 210, 569–577.
Yuan, W., Pan, Z., Li, X., Yang, Y., Zhao, C., Connell, L.D., Li, S., He, J., 2014a. Experimental study and modelling of methane adsorption and diffusion in shale. Fuel 117, 509–519.
Zapušek, A., Marsel, J., 1998. Measurement of the composition of gas desorbed from coal by gas chromatography. Chromatographia 48, 154–155.
Zdravkov, B.D., Čermák, J.J., Šefara, M., Jank\uu, J., 2007. Pore classification in the characterization of porous materials: A perspective. Cent. Eur. J. Chem. 5, 385–395.
Zhang, D., Ranjith, P.G., Perera, M.S.A., 2016. The brittleness indices used in rock mechanics and their application in shale hydraulic fracturing: A review. J. Pet. Sci. Eng. 143, 158–170.
Zhang, M., Tang, Q., Cao, C., Lv, Z., Zhang, T., Zhang, D., Li, Z., Du, L., 2018. Molecular and carbon isotopic variation in 3.5 years shale gas production from Longmaxi Formation in Sichuan Basin, China. Mar. Pet. Geol. 89, 27–37.
Zhang, T., Ellis, G.S., Ruppel, S.C., Milliken, K., Yang, R., 2012a. Effect of organic-matter type and thermal maturity on methane adsorption in shale-gas systems. Org. Geochem. 47, 120–131.
Zhang, T., Krooss, B.M., 2001a. Experimental investigation on the carbon isotope fractionation of methane during gas migration by diffusion through sedimentary rocks at elevated temperature and pressure. Geochim. Cosmochim. Acta 65, 2723–2742.
Zhang, X., Myhrvold, N.P., Hausfather, Z., Caldeira, K., 2016. Climate benefits of natural gas as a bridge fuel and potential delay of near-zero energy systems. Appl. Energy 167, 317–322.

Zhong, J., Chen, G., Lv, C., Yang, W., Xu, Y., Yang, S., Xue, L., 2016. Experimental study of the impact on methane adsorption capacity of continental shales with thermal evolution. J. Nat. Gas Geosci. 1, 165–172.
Zou, J., Rezaee, R., 2019a. A Prediction Model for Methane Adsorption Capacity in Shale Gas Reservoirs. Energies 12, 280.
Zumberge, J., Ferworn, K., Brown, S., 2012. Isotopic reversal ('rollover') in shale gases produced from the Mississippian Barnett and Fayetteville formations. Mar. Pet. Geol. 31, 43–52.